Metamaterials with Active Circuits

A dissertation

submitted by

Wangren Xu

In partial fulfillment of the requirements

for the degree of

Doctor of Philosophy

in

Electrical Engineering

Tufts University

May 2013

ADVISER: Dr. Sameer Sonkusale

© Copyright 2013 by Wangren Xu

Abstract

The focus of this dissertation is on embedding active circuits into metamaterials to mitigate some of their intrinsic problems such as losses and to create new hybrid metamaterial devices. The dissertation can be divided into four distinct contributions.

For the first contribution, an experimental demonstration of loss compensation in metamaterials using embedded active transistor based circuits is described. Each unit cell of the metamaterial is embedded with a cross-coupled transistor pair based negative differential resistance circuit to cancel these losses. Design, simulation and experimental results for Split Ring Resonator (SRR) metamaterials with and without loss compensation are presented. Results indicate that the quality factor (Q) of the SRR improves by over 400% at 1.6GHz, showing the effectiveness of the approach.

In the second contribution, we demonstrate an example of a metamaterial absorber (MMA) detector array that enables room-temperature, narrow-band detection of gigahertz (GHz) radiation in the S-band (2-4 GHz). The system is implemented with a commercial printed circuit board process and we characterize the detector sensitivity and angular dependence. A modified MMA geometry allows for each unit cell to act as an isolated detector pixel and to collectively

form a focal plane array (FPA). Each pixel can have a dedicated microwave receiver chain and functions together as a hybrid device tuned to maximize the efficiency of detected power. The demonstrated sub-wavelength pixel shows detected sensitivity of -77 dBm, corresponding to a radiation power density of 27 nW/m^2, with pixel to pixel coupling interference below -14 dB at 2.5 GHz.

For the third contribution, a diode switchable metamaterial reflector/absorber is demonstrated as another application of metamaterials with active circuits. We embed diodes as active circuit elements within the metamaterial array to implement a switchable metamaterial reflector/absorber at microwave frequencies. Diodes are placed in series with the unit cells of the metamaterial array. This results in just a pair of control lines to actively tune all the diodes in an array. Tuning the diodes switches the function of the metamaterial array between a perfect absorber and a reflector. The design, simulation and experimental results of a switchable reflector/absorber in 2-6 GHz range are presented in this dissertation.

Lastly, we explore the utilization of CMOS technology for making metamaterials. CMOS is the mainstream fabrication technology featuring low cost, high yield and fast throughput. Continued scaling in CMOS process has resulted in available feature sizes of tens of nanometers. It offers all the elements needed to build new hybrid metamaterial devices including the multiple layers of metal, the *via*s connecting them, diodes, resistors, capacitors, transistors, etc. Several 2D and 3D metamaterial devices on CMOS are designed and simulation results are presented that verify the feasibility of implementing metamaterials on CMOS.

As proof of concept, a metamaterial enhanced mid-IR detector array on CMOS is fabricated and tested. We scaled the metamaterial enhanced detector design down to μm dimensions to make it operational in the mid-IR band. Row/column decoder and readout circuits are implemented with the metamaterial enhanced detector array monolithically on a commercial 45nm CMOS chip. The simulation result verifies the design and the preliminary test results validate the electronic circuits. Recommendations are made for future prospects of IR based imager in CMOS process.

Acknowledgements

My advisor, Dr. Sameer Sonkusale has provided me with patient guidance and firm support that has helped me make the difficult transition from a student to a researcher. I am thankful to him for providing me the opportunity to conduct my PhD research in his Nanoscale Integrated Sensors and Circuits Laboratory (NanoLab) at Tufts University. His detailed guidance with problems and optimism during unexpected results in an experiment encouraged me to think critically and creatively to solve the problem.

I am grateful to Prof. Willie Padilla from Boston College who helped me bridge the gap between circuits and metamaterials that I have tried to fill in my interdisciplinary research. His expertise and knowledge of the physics of metamaterials and its application in my research helped me overcome several difficulties during experiments. His attention greatly improved the quality of my research.

I would also like to thank Dr. Sonkusale, Dr. Padilla, Dr. Chorng Hwa Chang (Electrical Engineering, Tufts University) and Prof. Qiaobing Xu (Biomedical Engineering, Tufts University) for serving on my dissertation committee and providing essential guidance to complete a well-rounded thesis.

My fellow graduate researcher David Shrekenhamer provided me with much needed technical support in the use of CST for simulating the metamaterial structures. I would like to thank him for his detailed assistance in helping me

understand many intricate theories in metamaterial design.

I shared several interesting discussion sessions with Xianliang Liu and Wenchen Chen at Boston College on metamaterials and CST simulations. These discussions were extremely helpful especially when I needed the motivation to think and solve a particular problem.

Saroj Rout provided me with great advice and help while testing my chip. He enlightened me of several issues that could come up during measurements. This helped me avoid many mistakes and saved me a lot of time. I could not have asked for any better discussions regarding measurements than those I had with Saroj.

I would specially like to thank Samuel MacNaughton. He spent a lot of time working on post-processing my chip and gave me countless bits of technical support.

Most importantly, I appreciate the continuous support I got from my parents. It is their love and care that has helped me persist in doing research.

Contents

List of Tables **x**

List of Figures **xi**

1 Introduction **1**

1.1 Introduction 1

1.2 Scope of the thesis 3

2 Fundamentals of Metamaterials **6**

3 Metamaterials as Circuit Elements **18**

3.1 Derivation of equivalent circuit model of Metamaterial from electromagnetic theory 18

3.2 Distributed circuit and reflection coefficient 23

3.3 Extraction of Equivalent Circuit from Reflection Coefficient 24

3.4 Interface between Metamaterial Design and Active Circuits Design 32

3.5 Reflection Coefficient based Systematic Design Flow 33

3.6 Summary 35

4 Loss Compensation in Metamaterials through Embedding of Active Tran-

sistor based Negative Differential Resistance Circuits **36**

4.1 Background . . . 37

4.2 Negative Differential Resistance (NDR) . . . 39

4.3 Embedding of NDR circuit into ELC resonator . . . 41

4.4 Loss Compensation in ELC resonator . . . 44

4.5 Effective electromagnetic parameter retrieval of metamaterials . . . 52

4.6 Embedding of NDR circuit into SRR . . . 59

4.6.1 Measurement . . . 64

4.6.2 Effective permeability retrieval of SRR embedded with NDR . . . 67

4.7 Summary . . . 68

5 Experimental Realization of a Metamaterial Detector Focal Plane Array **71**

5.1 Background . . . 71

5.2 Metamaterial absorber (MMA) . . . 73

5.2.1 Electromagnetic wave absorber . . . 73

5.2.2 Metamaterial perfect absorber . . . 77

5.3 Metamaterial absorber (MMA) based microwave detector focal plane array . 85

5.3.1 Overview . . . 85

5.3.2 Implementation . . . 88

5.3.3 Measurement . . . 100

5.4 Summary . . . 108

6 Diode Switchable Metamaterial Reflector/Absorber **110**

6.1 Background . . . 110

6.2 Design and implementation . . . 113

6.2.1 Principle of proposed approach . . . 113

6.2.2 Design . . . 113
6.2.3 PIN diodes . . . 116
6.2.4 Implementation and simulation . . . 118
6.3 Measurement . . . 121
6.4 Results and Summary . . . 121

7 CMOS Based Metamaterial - Theory, Design and Simulations 124
7.1 Typical 45nm CMOS Process . . . 125
7.1.1 Physical Properties of Metal and Dielectrics at Optical Frequencies . 128
7.2 Case studies . . . 135
7.2.1 Single layer metamaterial operating at 100μm . . . 135
7.2.2 Multi-layer metamaterial . . . 139
7.2.2.1 Stacking of metamaterial layers with different architectures . 139
7.2.2.2 Stacking of metamaterial layers with same architectures at mid-IR band . . . 143
7.2.2.3 IR absorber . . . 146
7.2.2.4 Twisted rod pair based circular polarizer at near infrared . . 150
7.2.2.5 Short wire pair based band pass filter type metamaterial . . 154
7.2.2.6 3D Metamaterial . . . 160
7.3 Summary . . . 163

8 Metamaterial Enhanced Mid-IR Detector Array 164
8.1 Background . . . 164
8.2 Design . . . 167
8.2.1 Architecture of Metamaterial enhanced IR detector and EM simulation of it . . . 167

8.2.2 Design and Simulation of CMOS based Metamaterial Unit Cell . . . 170
8.2.3 Detector and readout circuit . . . 172
8.3 Measurements . . . 182
8.3.1 Optical setup . . . 182
8.3.2 Electrical setup for image acquisition . . . 185
8.3.3 Measurement result . . . 187
8.3.3.1 Blackbody source test . . . 187
8.3.3.2 Polarization dependent signal test . . . 190
8.3.3.3 High power tunable IR laser test . . . 191
8.3.3.4 Lock in amplifier test . . . 196
8.3.4 Post-hoc analysis . . . 199
8.4 Summary . . . 203

9 Conclusion **205**

Bibliography **209**

List of Tables

7.1 **Vertical dimensions of metal and dielectric layers in commercial CMOS process employed** 127

List of Figures

2.1 ϵ and μ coordinate system to categorize materials (15) 10

2.2 RHM is constituted when ϵ and μ are greater than zero simultaneously (17) 12

2.3 LHM is constituted when ϵ and μ are less than zero simultaneously (17) . . . 13

2.4 Dispersion diagram of LHM and RHM (20) 14

2.5 Typical negative ϵ and μ values of metamaterials versus frequency (21). ϵ is shown in solid blue lines while the μ is shown in dashed red lines (a) shows the real part of ϵ and μ (b) shows the imaginary part of ϵ and μ (21) 14

2.6 Early metamaterial or LHM composed of wire array and SRRs (1) 15

2.7 Research activities in the metamaterial area are shown as apples on a tree (24) 17

3.1 (a)Edge coupled SRR(EC-SRR) (b)equivalent circuit model (37) 20

3.2 ELC resonator 20

3.3 SRR resonator 21

3.4 Typical transmission of ELC resonator 22

3.5 Labyrinth resonator (43) 22

3.6 Equivalent circuit model of Labyrinth resonator (43) 23

3.7 ELC resonator with a opening slit in the center. All units are in mm. $a = 27.3, b = 24, c = 4, d = 2, g_1 = 1, g_2 = 0.5$. The dielectric substrate is a 5 mm thick FR4 layer, the real part of its permittivity is 4.5 and the loss tangent is 0.06 at 2 GHz. The metallic structures are made of 0.03 mm thick gold layer, which has an electric conductivity of 4.561e+007 S/m. 25

3.8 Waveguide port 1 and 2 defined in CST to simulate ELC resonator. The polarization of incident EM wave is also depicted. 26

3.9 Port 3 is in the gap of ELC resonator 27

3.10 Simulated S_{33} of ELC resonator in CST 27

3.11 Topology of equivalent circuit model of the ELC resonator, S_{11} is the reflection coefficient looking into the input the equivalent circuit model 28

3.12 Reflection coefficient S_{11} of equivalent circuit model and S_{33} of ELC resonator 29

3.13 The schematic of a FSS based on square loop arrays and wire grid. The square loop array implemented on the top layer is shown in grey while the wire grid fashioned on the bottom layer is shown in black. Capacitors are embedded to connect the neighboring square loops (47) 30

3.14 Proposed equivalent circuit model for one unit cell of the FSS (47) 31

3.15 Comparison between the equivalent circuit model simulation and 3D full wave finite element method (FEM) simulation (47) 32

3.16 Reflection coefficient of a metamaterial resonator embedded with active circuit 34

4.1 simplified equivalent circuit model: The SRR is modeled by an RLC parallel circuit, in which the R stands for the loss of the resonator. Negative Differential Resistance (NDR) circuit provides loss compensation that is bias tunable. 40

4.2 ELC resonator, all units are in mm. $a = 27.3, b = 24, c = 4, d = 2, g_1 = 1$. The dielectric substrate is a 5 mm thick FR4 layer, the real part of its permittivity is 4.5 and the loss tangent is 0.06 at 2 GHz. The metallic structures are made of 0.03 mm thick gold layer, which has an electric conductivity of 4.561e+007 S/m. 42

4.3 Waveguide port 1 and 2 defined in CST to simulate ELC resonator. The polarization of incident EM wave is also depicted. 43

4.4 FDTD simulation of transmission of ELC resonator without the active NDR circuit 43

4.5 Surface current distribution on the ELC resonator at the resonant frequency 45

4.6 ELC resonator with a opening slit in the center. All units are in mm. $a = 27.3, b = 24, c = 4, d = 2, g_1 = 1, g_2 = 0.5$. 45

4.7 The transmission of ELC resonator with a opening slit in the center 46

4.8 Simulated $|S_{33}|$ in dB of ELC resonator in CST 47

4.9 The implementation of the NDR circuit and its connection to the ELC resonator. Q1 and Q2 are pseudomorphic HEMT (pHEMT) transistors connected as cross coupled transistor pair. R1, R2, L1 and L2 are on chip resistors and inductors providing the required phase of reflection coefficient and bias voltage, respectively. R1, L1, Q1 are identical to R2, L2, Q2, respectively. C1 is a 20 pF on-chip capacitor. Q3 is the current sink, whose bias current is controlled by voltage signal Vbias 49

4.10 The 3D layout of the implemented active negative differential circuit in TriQuint TQPED 0.5 μm pHEMT process. Area I are L1 and L2, which are identical on chip spiral inductors, each of which has 2.5 turns and occupies 200 μm $\times$ 200 μm. Area II shows GaAs pHEMT transistors Q1, Q2 and Q3. Area III shows the on-chip capacitor C1, which is a 20 pF and occupies 200 μm $\times$ 120 μm. Area IV shows a pair of identical on- chip resistors R1 and R2, each of which is 100 Ω and occupies 11 μm $\times$ 22 μm, they are relatively small compared with other components in the figure. The entire design occupies 520 μm $\times$ 420 μm 50

4.11 The magnitude of reflection coefficient S_{11} of the NDR circuit. 51

4.12 The phase of reflection coefficient S_{11} of the NDR circuit. 51

4.13 transmission of the original ELC resonator (blue curve) and the ELC resonator embedded with the active loss compensation circuit (red curve) 52

4.14 Definition of S_{11} and S_{21} in terms of scattering characteristics of a metamaterial slab. Its thickness is l. (69) 54

4.15 Definition of S_{22} and S_{12} in terms of the scattering characteristics of a metamaterial slab. Its thickness is l. (69) 55

4.16 The real and imaginary part of permittivity, ϵ' and ϵ'' of original ELC resonator without embedded active loss compensation circuit 59

4.17 The real and imaginary part of permittivity, ϵ' and ϵ'' of ELC resonator with embedded active loss compensation circuit, ϵ'' become negative when the active loss compensation circuit is embedded 60

4.18 Dimension of SRR in the test. All units are in millimeter. a=2, b=16, c=12, d=1.5 61

4.19 Implementation of active negative differential resistance circuit and its connection to SRR. 62

4.20 Simulated $|S_{11}|$ in dB of SRR with and without active loss compensation circuit 63

4.21 Measurement setup to measure the reflection. Area I shows the active NDR circuit implemented on the printed circuit board. Area II shows the SRR. Area III shows the loop antenna. The circuit in area I could be integrated into single chip in future, with dimensions much smaller than the size of each unit cell. 65

4.22 Measured $|S_{11}|$ in dB of loop antenna by itself and SRR with and without embedded active NDR circuit. When the bias voltage V_{bias} is set to 0.350V, the current flowing in the active circuit is 3.6mA. The DC power supply voltage is 3.1V. 66

4.23 Measured $|S_{11}|$ in dB of SRR with and without embedded active NDR circuit after the auxiliary 2 Ohm resistors are removed. 67

4.24 Retrieved complex permeability $\mu = \mu' + i \cdot \mu''$ of SRR excited by plane wave and their Lorentz oscillation model. Osc. model 1 is the Lorentz oscillator model used to fit the μ curve of SRR without NDR circuit. Osc. model 2 is the Lorentz oscillator model used to fit the μ curve of SRR embedded with the NDR circuit. 69

5.1 Quarter-wave transformer (77) 74

5.2 SRR (a) and the EM radiation impinged on it (b) (91) 79

5.3 ELC resonator (a) and the EM radiation impinged on it (b) (91) 80

5.4 ELC resonator with dielectric and ground plane (a) and the EM radiation impinged on it (b) (91) 82

5.5 Dimensions of the metamaterial absorber (a) Dimension of the ELC resonator, all units in mm, $a_1 = 4.2$, $a_2 = 12$, $W = 4$, $G = 0.6$, $t = 0.6$ (b) dimension of the split wire on the back, $L = 1.7$, $H = 11.8$) (c) polarization of the incident EM wave (87) 83

5.6 Measurement result (shown in blue) and simulation result (shown in red) of transmissivity $T(\omega)$ and reflectivity $R(\omega)$ for the MMA. (a) The inset is the reflection experiment setup where BS is the beam splitter. (b)the inset is the photographs of the both sides of the MMA. (87) 84

5.7 Simulation of ohmic and dielectric losses in MMA. (87) 85

5.8 The dimensions utilized for the metamaterial absorber design in the FPA, all units in mm. (a)dimension of the MM unit cell and ground plane. MM unit cell is shown in bright yellow and the ground plane is shown in dark yellow. The grey area in the ground plane is an opening to let the *via* holes go through (b)back view. A discrete port called 'port 3' is defined across the end of *via*s. 88

5.9 System architecture of my metamaterial microwave power detector array. (a) Radiation is incident from port 1 with electric field polarization as depicted. A schematic of the full device is shown (exploded view) and the layers shown from top to bottom are: the ELC, Rogers dielectric spacer, patterned ground plane, and microwave power receiver circuit. (b) Photo of an individual pixel, i.e. an ELC unit cell with dimensions of $a = 27.3$, $l = 24$, $w = 3.5$, and $g = 4$; all in millimeters. (c) Photo of the circuit layer with *vias* indicated. The *vias* transport the received signal (port 3) to the microwave power receiver circuit underneath each unit cell where the different highlighted regions are: (I) balun, (II) impedance matching circuit, (III) low noise amplifier, and IV) microwave power detector. 90

5.10 Numerical simulations of metamaterial absorber. Simulated results of the free space reflection (S_{11} dashed blue curve), transmission (S_{31} green curve), and reflection coefficient (S_{33} red curve). 92

5.11 Simulated current densities shown directly underneath the ELC (left) and above the ground plane (right) at the simulated design frequency of 2.0 GHz. 93

5.12 Simulated electric field magnitude shown directly underneath the ELC (left) and above the ground plane (right) at the simulated design frequency of 2.0 GHz. 93

5.13 How the impedance moves on smith chart when series/shunt L/C are added (104) 95

5.14 The schematic of the impedance matching circuit 95

5.15 The schematic of a realistic model of a capacitor at RF/microwave frequency. (105) 97

5.16 The magnitude of S_{33} at the output of the metamaterial loaded with impedance matching circuit 99

5.17 The schematic of a realistic model of an inductor at RF/microwave frequency (107) R_p and C_p are the parasitic resistance and capacitance, respectively (107) 100

5.18 Measurement setup inside anechoic chamber 101

5.19 Experimental measurements in anechoic chamber for the center pixel on the MMA / FPA. S- parameter data shows the reflection coefficient (S_{33} red curve) and the transmission (S_{31} green curve) with the dashed grey line at 2.5 GHz, which is the resonant frequency. 102

5.20 Adjusted impedance matching circuit after measurement 103

5.21 System architecture consists of three boards with board 1 which contains the metamaterial connecting through the *vias*, traces and balun out through a ultraminiature coax connector (UMCC) designated as port 3. The UMCC cable connects to board 2 containing both the impedance matching circuit and low noise amplifier (LNA) with output labeled as port 4. The third board consists of only the microwave power detector providing a DC voltage output signal. 104

5.22 S-parameter data shows the transmission without (S_{31} blue curve) and with (S_{41} gold curve) the addition of the impedance matching and low noise amplifier (LNA) with the dashed grey line at 2.5 GHz the frequency for sensitivity and off-angle measurements. 105

5.23 Experimental measurements in anechoic chamber for mutual coupling (MC) between neighboring metamaterial pixels located parallel (gold curve), perpendicular (blue curve), and diagonal (grey curve) with respect to the electric field polarization. 106

5.24 Experimental measurements in anechoic chamber for sensitivity characterization with the output of microwave power detector of single pixel as function of incident power, and is sensitive as indicated by dashed red line down to -77 dBm at 2.5 GHz. 107

5.25 Off-angle performance characterization of the MMA / FPA at 2.5 GHz for both the electric field vector perpendicular (TE) and parallel (TM) to the floor of the chamber. The ELC resonator's are rotated between the correct polarization (E-field perpendicular the split gap) and the cross polarization (E-field parallel to the gap). 108

6.1 Schematic of our diode switchable MM reflector and the dimension of one unit cell. Dimensions of unit cell are in mm. w_1=0.6, w_2=0.3, w_3=0.35, l_1=7.4 , l_2=4.5, g_1=0.13, a_1=9, a_2=8.4. 114

6.2 The typical I-V characteristic of diodes (130) 116

6.3 The resistance of PIN diodes versus DC bias current (131) 117

6.4 Numerical simulation of metamaterial reflector/absorber shows the reflections $|S_{11}|$ in dB. The blue curve shows the $|S_{11}|$ of metamaterial reflector when diodes are turned off while the red curve shows $|S_{11}|$ when diodes are turned on. 119

6.5 Numerical simulation of metamaterial reflector/absorber (a) shows electric field magnitude at "off resonance" (4.1 GHz) when diodes are turned off (b) shows electric field magnitude at "on resonance" (4.785 GHz) when diodes are turned on. 120

6.6 The fabricated PCB, the inset shows two neighboring unit cells and diodes connecting them. All units are in millimeter. a=9, b=21, c=199.9, d=109.98 120

6.7 The measured $|S_{11}|$ of metamaterial reflector. The black curve shows the measured $|S_{11}|$ when there is not bias voltage applied across the metamaterial reflector array. The red curve shows the measured $|S_{11}|$ of metamaterial reflector when a 9.6 V DC voltage is applied across the positive and negative bias lines. 122

7.1 The cross section view of CMOS metal stack. The thickness of each metal and dielectric layer is named after the letter in the parenthesis and defined in table 7.1. 126

7.2 Solid lines show the Drude model of Al (143) 132

7.3 Solid lines show the Drude model of Cu (143) 133
7.4 The IR absorption spectrum of TEOS. Adapted from (144) 134
7.5 The IR absorption spectrum of BCB. Adapted from (145) 135
7.6 The IR absorption spectrum of SiO_2. Adapted from (146) 136
7.7 Dimensions of a ELC resonator metamaterial implemented on the top metal layer M10 in CMOS metal stack. All units are in μm. l_1=14, l_2=16, g=1.4, w=0.8, a=20 137
7.8 Simulated transmissivity T and reflectivity R of an ELC resonator metamaterial implemented on the top metal layer M10 in CMOS metal stack 138
7.9 Electric field distribution of an ELC resonator metamaterial implemented on the top metal layer M10 in CMOS metal stack 138
7.10 Surface current distribution of an ELC resonator metamaterial implemented on the top metal layer M10 in CMOS metal stack 139
7.11 3D view of a two-layer metamaterial composed of ELC resonator on M10 layer and SRR resonator on M9 layer 140
7.12 Dimensions of SRR resonator metamaterial implemented on the metal layer M9 in CMOS metal stack. All units are in μm. l_1=19, l_2=18, g=0.8, w=0.8, a=22 141
7.13 Transmissivity T and reflectivity R of SRR resonator on M9. 141
7.14 Transmissivity T and reflectivity R of a two layer metamaterial composed of ELC resonator on M10 and SRR resonator on M9. 142
7.15 3D view of a two-layer metamaterial composed of ELC resonator on M8 layer and ELC resonator on M6 layer 143
7.16 Transmissivity T and reflectivity R of a single layer metamaterial composed of ELC resonators on M8. 144

7.17 Transmissivity T and reflectivity R of a single layer metamaterial composed of ELC resonators on M6. 145

7.18 Transmissivity T and reflectivity R of a two layer metamaterial composed of a smaller ELC resonators on M8 and larger ELC resonator on M6. 145

7.19 Dimensions of a metamaterial absorber implemented on the top two metal layers in CMOS metal stack. All units in μm. l_1=14, l_2=16, g=1.4, w=3, a=20 147

7.20 $|S_{11}|$ in dB of a metamaterial absorber implemented on the top two metal layers in CMOS metal stack 148

7.21 Absorptivity A, transmissivity T and reflectivity R of a metamaterial absorber implemented on the top two metal layers in CMOS metal stack 149

7.22 Dimensions of rod on M1 layer, All units are in μm. l=0.75, w=0.18, a=0.9 (156) 152

7.23 3D view of the stacked twisted rod layers (156) 153

7.24 Transmission of a circular polarizer implemented on the bottom two metal layers in CMOS metal stack 154

7.25 Top view of short wire pairs with cut-wires implemented on M3 and M1 metal layers in CMOS metal stack and their dimensions (158) 156

7.26 3D view of short wire pairs with cut-wires implemented on M3 and M1 metal layers in CMOS metal stack (158) 156

7.27 The simulated transmission and reflection in dB of short wire pair implemented on M3 and M1 metal layers in CMOS metal stack 157

7.28 The retrieved complex permittivity $\epsilon = \epsilon' + i\epsilon''$ of short wire pair implemented on M3 and M1 metal layers in CMOS metal stack 158

7.29 The retrieved complex permeability $\mu = \mu' + i\mu''$ of short wire pair implemented on M3 and M1 metal layers in CMOS metal stack 159

7.30 The retrieved complex refractive index $n = n' + in''$ of short wire pair implemented on M3 and M1 metal layers in CMOS metal stack 159

7.31 (a)Perspective (b)bottom (c)top view of 3D metamaterial in CMOS. the circle in (b) and (c) indicate the *via*s (161) 161

7.32 The simulated transmission of this 3D chiral metamaterial 162

8.1 Cross section of Metamaterial (ELC resonator) enhanced mid-IR detector. Our design is inspired by the antenna coupled THz detector proposed in (166) 168

8.2 Dimensions of ELC resonator on chip. All units in μm. l_1=1.4, l_2=1.6, g=0.14, w=0.3, a=2.5 169

8.3 Simulation result of the magnitude of reflection $\mid S_{11} \mid$ in dB of the ELC resonator 170

8.4 Simulation result of the magnitude of power transfer $\mid S_{21} \mid$ of the ELC resonator 171

8.5 The power flow in the IR metamaterial coupled detector at the resonant frequency 172

8.6 Schematic of metamaterial coupled IR detector followed by integrator 173

8.7 Ideal integrator output with pixel current of IR detector as input 174

8.8 The schematic of OTA (167) 175

8.9 The schematic of bias voltage generator 176

8.10 The schematic of the first stage of OTA (167) 177

8.11 Schematic of the metamaterial enhanced IR detector array. Part of the figure is adapted from (169) 181

8.12 Layout of a single pixel, a is 3.3 μm. T1 is the IR detector. T2 is the row selection transistor 182

8.13 The microphotograph of the fabricated chip and layout of the system drawn in cadence . . . 183

8.14 A scanning electron microscope (SEM) picture showing exposed 4 by 4 metamaterial pixel array . . . 184

8.15 The typical radiation of blackbody source over the spectrum (171) . . . 184

8.16 The radiation profile of blackbody source at 1050 degree (174) . . . 185

8.17 The architecture of the hardware/software platform to read out an image from the IR image sensor . . . 186

8.18 The output voltage of the integrator on-chip without IR radiation . . . 188

8.19 The output voltage of the on-chip integrator after the chip is exposed to IR radiation for 5 minutes . . . 189

8.20 Histogram of element-wise difference array $c[1, 2, ..., 40]$ between correct and cross polarization . . . 192

8.21 The histogram of differences in pixels' output between reference and mid-IR radiated cases . . . 194

8.22 The histogram of differences in pixels' output between cross polarization and correct polarization cases . . . 195

8.23 Improve the SNR by using lock-in amplifier in the IR laser test (176) . . . 197

8.24 Simulation result of $|S_{21}|$ when the imaginary part of dielectrics' permittivity is doubled . . . 199

8.25 Simulation result of $|S_{11}|$ in dB when the imaginary part of dielectrics' permittivity is doubled . . . 200

8.26 Simulation result of $|S_{21}|$ in dB when the dimensions of ELC resonator and openings in ground plane have -50% variation . . . 201

8.27 Simulation result of $|S_{11}|$ in dB when the dimensions of ELC resonator and openings in ground plane have -50% variation 202

1

Introduction

1.1 Introduction

Metamaterials are artificially structured composites that exhibit exotic and unique electromagnetic (EM) properties, which have found wide applications in demonstrating negative index of refraction (1, 2), invisible cloaking (3), and perfect lensing (4). In the past decade, the interest in metamaterials and the research efforts made to develop matematerial theory and application have increased drastically because the exotic electromagnetic properties of metamaterials are not available in naturally occurring materials. However, the first paper that laid the theoretical foundation of metamaterials appeared in 1968 (5), where Veselago proposed substances with simultaneously negative values of permittivity ϵ and and permeability μ (5). The research area remained inactive for three decades because no experimental work could prove Veselago's idea was feasible. Sir John Pendry renewed this area and proposed theoretically to construct a negative refractive index material by providing negative permittivity using wire array and negative permeability using Split Ring Resonator, respec-

tively (4, 6). An experimental demonstration was expected to validate this unconventional idea. The first experimentally demonstrated metamaterial that exhibited both negative values of permittivity ϵ and permeability μ was presented by David Smith's group (2). Smith's work proved that both the permittivity ϵ and and permeability μ of a material can be tuned by engineering the structure made of metal and dielectric material instead of engineering constituent properties of atoms and molecules (2). Smith's paper ignited the metamaterial area because it showed that many previously unheard of electromagnetic(EM) properties of materials can be created by designing certain patterns of metallic inclusions in dielectric medium. These designs are only limited by imagination and fabrication technique (7). The new EM properties of metamaterials and theory to guide the design of them have been developed and presented in many papers since then.

The metamaterials whose EM properties are tailored by designing their structures are termed passive metamaterial. The properties of passive metamaterials typically do not change with time and cannot be tuned. The active metamaterials, on the other hand, are the metamaterials with some extrinsic, or intrinsic action being added to the original passive design enabling time-varying response (8). For example, the action can be performed by an intrinsic source providing energy to compensate for loss (9), or embedded component whose EM properties changes with an externally applied excitation (10). Many unprecedented EM properties can be achieved by embedding electronic devices and circuits into metamaterials, for example ones that can modulate, tune, detect or harvest power from the metamaterials. Moreover, circuit design techniques can be applied in active metamaterials to overcome their inherent problems that have challenged the metamaterial community for a long time (e.g. loss, lack of tunability).

This dissertation focuses on embedding active circuits into metamaterials to demonstrate

practical metamaterial based devices, tune the EM properties of metamaterials and mitigate the intrinsic problems of metamaterials such as dielectric and ohmic losses.

1.2 Scope of the thesis

Appropriate consideration will be directed to the fundamentals of metamaterials in chapter 2, although the dissertation concentrates on embedding active electronic circuits into metamaterials. Deep understanding of the theory and properties of metamaterials are necessary to design the embedding circuits.

Metamaterials are electromagnetic field devices that have an engineered response to incident radiation. It is difficult, however, to visualize metamaterials from the perspective of circuit theory when designing the embedding circuit for metamaterials. Therefore, it is critical to convert the metamaterials from an EM wave device to an equivalent circuit model that describes the EM properties of metamaterials using circuit elements. Chapter 3 derives the equivalent circuit model of metamaterials and serves as a bridge over the gap between the EM field and circuit design field and opens the gate to the systematic design of metamaterials with active circuitry. Starting from this point, metamaterials can be considered as equivalent circuit models and many existing circuit design techniques can be applied to it to achieve functionality and properties not available in passive metamaterials.

In chapter 4, an all-electronic approach for mitigating the inherent problem of metamaterials, which is the losses in metamaterials, is presented. Each unit cell of the metamaterial is embedded with a cross-coupled transistor pair based negative differential resistance circuit to cancel these losses. The design, simulation and experimental results are provided in details to show the effectiveness of the approach.

In chapter 5, receiver circuits are embedded into metamaterials to make a practical device. Embedded circuits are used to detect narrow-band microwave(2-4 GHz) signals focused by the metamaterial absorbers (MMA) at room temperature. A modified MMA geometry allows for each unit cell to act as an isolated detector pixel and to collectively form a focal plane array (FPA). Each pixel has a dedicated microwave receiver chain and functions together as a hybrid device tuned to maximize the efficiency of detected power.

In chapter 6, active circuit elements are embedded into metamaterial absorbers to make it tunable between two states of perfection absorption and reflection, which is impossible for passive metamaterials. Switchable metamaterial absorber/reflectors are useful in many applications. We embed diodes as active circuit elements within the metamaterial array to enable switchable microwave reflector/absorber applications. By placing diodes in series with unit cells of the metamaterials, we mitigate the issue of routing control lines to turn the diodes on/off. The design, simulation and experimental results of switchable reflector/absorber in 2-6 GHz range with just two control lines are demonstrated.

In chapter 7, a variety of metamaterials are implemented in CMOS. The simulation results prove that it is feasible to fabricate matematerials with nanometer dimensions in CMOS. CMOS is the ideal option of mass production of metamaterials because it features low cost, high yield and fast throughput.

In chapter 8, we employ a similar metamaterial coupled detector architecture as that in chapter 5 but scale the design to operate in mid-IR frequency band and implemented the system on a commercial 45 nm CMOS process. Although the simulation results validate our design, the fabricated chip was not able to detect the incident IR radiation in a series of tests. The post-hoc analysis is elaborated and the directions and guidelines for future design are given.

The dissertation concludes in chapter 9. All the previous work presented is summarized. The discussion and suggestions for potential improvement of these work are also provided.

2

Fundamentals of Metamaterials

In this chapter, the basic aspects of electromagnetic theory are laid out to help readers understand the metamaterials. All of the electromagnetic phenomena, including the propagation of EM wave and the response of materials to external EM field, can be explained by Maxwell's equations. Therefore, we will briefly introduce Maxwell's equations first and derive the metamaterials' EM properties from them. Maxwell's equations describe the relations between charges, current, electric field $\vec{E}$ and magnetic field $\vec{H}$, which are both functions of position $\vec{r}$ and time t.

In free space, Maxwell's equations give (11):

$$\nabla \times \vec{H} = \epsilon_0 \frac{\partial \vec{E}}{\partial t} \tag{2.1}$$

$$\nabla \times \vec{E} = -\mu_0 \frac{\partial \vec{H}}{\partial t} \tag{2.2}$$

$$\nabla \cdot \vec{E} = 0 \tag{2.3}$$

$$\nabla \cdot \vec{H} = 0 \tag{2.4}$$

In these four equations, $\vec{E}$ is the vector of electric field and $\vec{H}$ is the magnetic field. ϵ_0 is the vacuum permittivity and μ_0 is the vacuum permeability .

The first equation means the time-varying electric field generates curl of magnetic field. The second equation indicates that the time-varying magnetic field causes curl of electric field. The third equation means there is no electric charge in free space that emits electric flux. The last equation states that there is no magnetic charge in space that emits magnetic flux.

The EM properties of dielectric medium are different from those of free space because it has distinct response to the external electric and magnetic field. The external electric field applied across the dielectric medium induces electric dipole moments in it, which is termed polarization (12). While magnetization describes the fact that an external magnetic field applied across the dielectric material induces magnetic dipole moments in it (12). In the dielectric medium where there is no free charge or current, Maxwell's equation becomes (11)

$$\nabla \times \vec{H} = \frac{\partial \vec{D}}{\partial t} \tag{2.5}$$

$$\nabla \times \vec{E} = -\frac{\partial \vec{B}}{\partial t} \tag{2.6}$$

$$\nabla \cdot \vec{D} = 0 \tag{2.7}$$

$$\nabla \cdot \vec{B} = 0 \tag{2.8}$$

where "$\vec{D}$ is electric flux density and $\vec{B}$ is the magnetic flux density" (12). These two variables are introduced into Maxwell equations to take into account the polarization and magnetization effect of dielectric medium.

The permittivity ϵ and polarization density $\vec{P}$ characterize $\vec{E}$ and $\vec{D}$ relation (12):

$$\vec{D} = \epsilon_0 \vec{E} + \vec{P} \tag{2.9}$$

where permittivity is a measure of how easily the charges in an electromagnetic dielectric material can be polarized as the result of externally exerted $\vec{E}$ (13).

The relation between magnetic field intensity $\vec{H}$ and magnetic flux density $\vec{B}$ is defined with μ and magnetization density $\vec{M}$ (12):

$$\vec{B} = \mu_0 \vec{H} + \mu_0 \vec{M} \tag{2.10}$$

where permeability is the measure of how much magnetic field can be established internally as the consequence of an externally exerted $\vec{H}$(14).

If the $\vec{P}$ and $\vec{E}$ have a linear relation, dielectric medium respond to the exterior EM field with no delay, the relation between $\vec{P}$ and $\vec{E}$ is the same in the entire dielectric medium and

the direction of $\vec{E}$ does not change its relation with $\vec{P}$, then we obtain (11):

$$\vec{P} = \epsilon_0 \chi \ \vec{E} \tag{2.11}$$

which means $\vec{P}$ and $\vec{E}$ always have the same direction and linear relation. χ is termed electric susceptibility (11).

If we substitute equation 2.11 into equation 2.9, the following equation is obtained (11)

$$\vec{D} = \epsilon_0(1+\chi)\vec{E} = \epsilon \ E \tag{2.12}$$

Using a similar method, we can obtain the relation between $\vec{B}$ and μ (11):

$$\vec{B} = \mu\vec{H} \tag{2.13}$$

The most accurate and complete parameters that characterize the electromagnetic properties of metamaterials are permittivity and permeability. All materials can be categorized into 4 groups according to the combination of the polarities of their ϵ and μ as indicated in the coordinate system in Fig. 2.1 (15).

As shown in Fig. 2.1, most of the dielectric media fall into the first quadrant where both ϵ and μ are positive, which is termed 'right-handed medium' (RHM) (16). Materials in the second quadrant are also common in nature (16), for example, plasma medium such as ionized gas, or metals at optical and infrared frequencies fall into the second quadrant (16). Representative of media in the fourth quadrant is the ferromagnetic materials with strong magnetic interaction near ferromagnetic resonance (16). The only category of materials

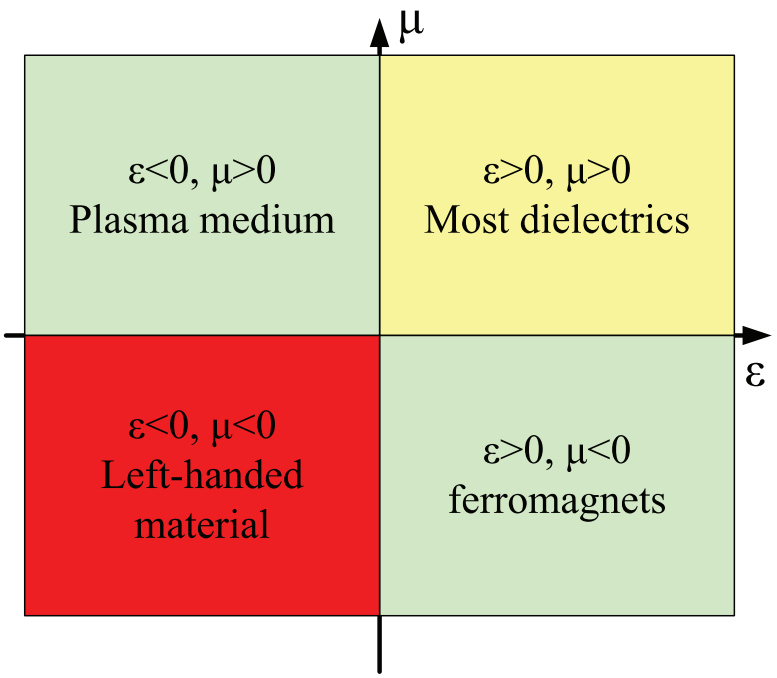

Figure 2.1: ϵ and μ coordinate system to categorize materials (15)

that cannot be found in nature are the material with simultaneous negative permittivity and negative permeability (16). The question anyone would ask at this point is whether the EM wave propagation in this kind of medium is different from the wave propagation in regular medium that falls in the first, second and fourth quadrants in Fig. 2.1 (16). The other interesting question is how to implement a left-handed medium if it is not available in nature (16).

The first question was answered by Veselago in 1968 (5) and it is briefly reviewed here. Let us consider Maxwell's equations of source-free dielectric medium shown in equation 2.5. If we assume the EM wave is a plane wave and monochromatic, then $\vec{E}$ and $\vec{H}$ have the subsequent dependency on position $\vec{r}$ and time t (17):

$$\vec{E} = \vec{E_0} e^{-j\vec{k}\cdot\vec{r}+j\omega\ t} \tag{2.14}$$

$$\vec{H} = \vec{H_0} e^{-j\vec{k}\cdot\vec{r}+j\omega\ t} \tag{2.15}$$

where $\vec{E_0}$ and $\vec{H_0}$ represent complex amplitude vectors of $\vec{E}$ and $\vec{H}$ (17). $\vec{k}$ is the wave vector (17).

By re-organizing equation 2.14 and 2.15, we can reduce them to (17):

$$\vec{k} \times \vec{E} = \omega\mu\vec{H} \tag{2.16}$$

$$\vec{k} \times \vec{H} = -\omega\epsilon\vec{E} \tag{2.17}$$

When permittivity ϵ and and permeability μ are positive, if we extend the index finger of our right hand towards the direction of $\vec{E}$ and point the middle finger towards the direction of $\vec{H}$, then the thumb of our right hand points to the direction of wave vector $\vec{k}$ as shown in Fig. 2.2 (16, 17). The media where the EM wave with such $\vec{E}$, $\vec{H}$ and $\vec{k}$ propagates is defined as a "Right-handed media (RHM)" (16, 17).

However, the relation between $\vec{E}$,$\vec{H}$ and $\vec{k}$ becomes (16, 17):

$$\vec{k} \times \vec{E} = -\omega \mid \mu \mid \vec{H} \tag{2.18}$$

$$\vec{k} \times \vec{H} = \omega \mid \epsilon \mid \vec{E} \tag{2.19}$$

when ϵ and μ are negative. Now if we extend the index finger of our left hand towards the

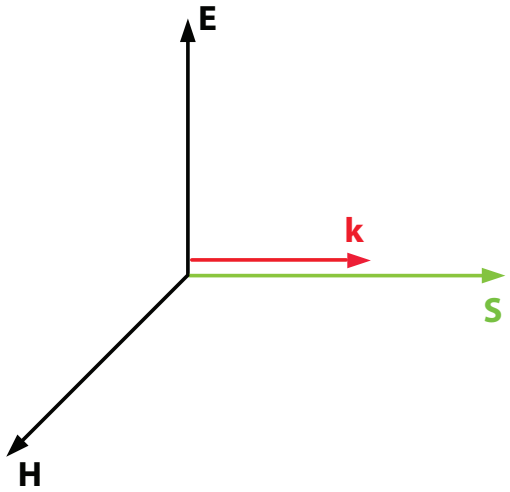

Figure 2.2: RHM is constituted when ϵ and μ are greater than zero simultaneously (17)

direction of $\vec{E}$ and point the middle finger towards the direction of $\vec{H}$, then the thumb of our left hand point to the direction of wave vector $\vec{k}$ as shown in Fig. 2.3 (16, 17). The media where the EM wave with such $\vec{E}$, $\vec{H}$ and $\vec{k}$ propagates is defined as a "Left-handed media (LHM)" (5, 16, 17, 18).

The direction of energy flux of EM wave is described by the Poynting vector as (17):

$$\vec{S} = \frac{1}{2}\vec{E} \times \vec{H}^{*} \tag{2.20}$$

This equation shows that the direction of energy flux $\vec{S}$ is unrelated to the polarity of ϵ and μ (17). Therefore, the relation among the direction of $\vec{S}$, $\vec{E}$ and $\vec{H}$ remain the same in both RHM and LHM, as shown in Fig. 2.2 and 2.3 (17). In LHM, the plane wave wavefront is propagating forward while its energy flux $\vec{S}$ is moving backward (17, 19). This phenomenon is termed "backward-wave propagation" (17, 19). Backward-wave propagation is the basis of all the exotic EM properties of metamaterials (17). The dispersion diagram of LHM shows negative slope in the relation between propagation constant and frequency, as shown in Fig.

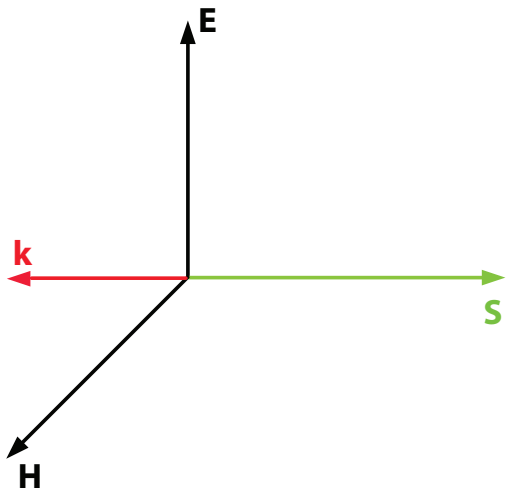

Figure 2.3: LHM is constituted when ϵ and μ are less than zero simultaneously (17)

2.4, because of the back-wave propagation (20).

Typical negative ϵ and μ values of metamaterials versus frequency are plotted in Fig. 2.5 (21). ϵ is shown in solid blue lines while the μ is shown in dashed red lines (a) shows the real part of ϵ and μ (b) shows the imaginary part of ϵ and μ (21).

If the LHM is theoretically feasible, the subsequent question is how to implement LHM and demonstrate it experimentally. The research area of LHM kept silence for three decades since Veselago's paper was published because of the difficulty in realizing the negative permittivity ϵ and negative permeability μ concurrently (22). Materials with negative permittivity has been demonstrated in the history using plasmas below the plasma frequency (23). It has also been shown that the negative permittivity at microwave frequency is achieved through implementing a thin wire array (22). However, negative permeability was not readily available because none of the naturally occurring materials exhibits such a property (23). Implementation of material with negative permeability was the last hurdle on the road leading to the LHM. Finally, in the year 1999, Pendry proposed to utilize the strong negative permeability of the Split Ring Resonator (SRR) above its resonant frequency (6). It provided promise to

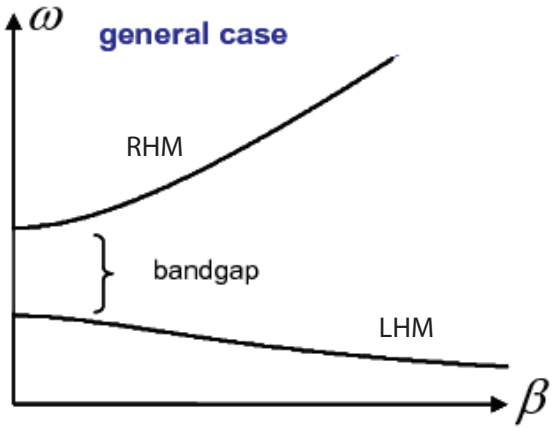

Figure 2.4: Dispersion diagram of LHM and RHM (20)

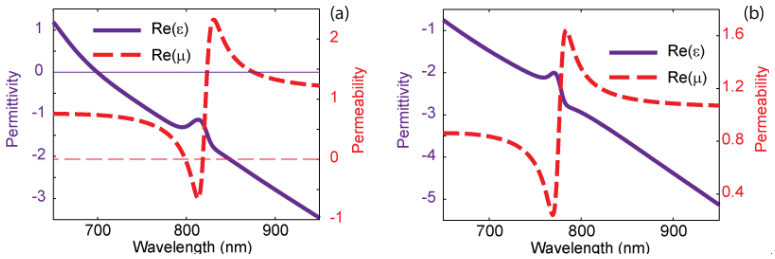

Figure 2.5: Typical negative ϵ and μ values of metamaterials versus frequency (21). ϵ is shown in solid blue lines while the μ is shown in dashed red lines (a) shows the real part of ϵ and μ (b) shows the imaginary part of ϵ and μ (21)

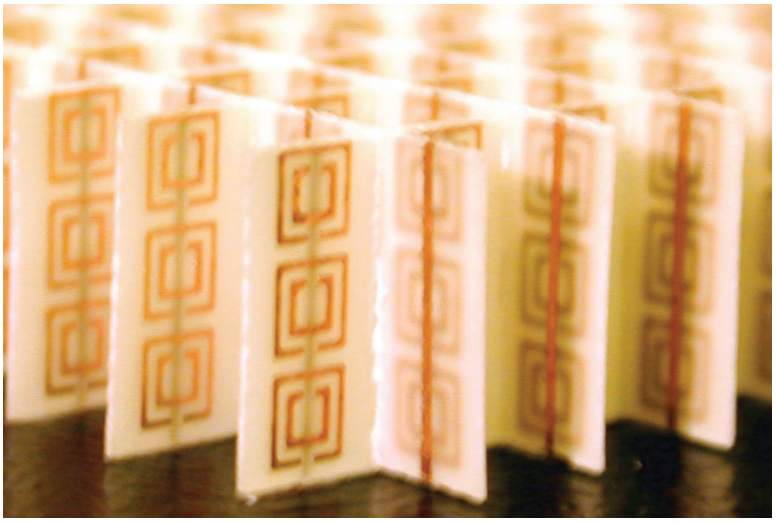

Figure 2.6: Early metamaterial or LHM composed of wire array and SRRs (1)

remove the last hurdle. That promise came true when David Smith's group demonstrated the first composite material with both negative permittivity and permeability experimentally using thin wires and SRRs (2). It verified the feasibility of implementing LHM using artificially engineered composites and triggered an explosion of interest of LHM and inspired many other important advances in this area in the past decade. An early version of the LHM is shown in Fig. 2.6 (1). It is composed of wire arrays and SRRs that are implemented on printed circuit boards(PCB).

Research activities in the metamaterial area are shown as apples on a tree in Fig. 2.7 (24). In Fig. 2.7, the research area of chiral metamaterials, negative index metamaterials and artificial magnetism are depicted as big, red apples that have fallen to ground (24). It means these fields have been investigated thoroughly and become saturated (24). The golden ripe apples hanging in the middle of tree show the research areas of transformation optics, designer dispersion and high/low value of epsilon (24). A great deal of research efforts go into these areas, which produce many publications each year (24). The small green apples on the top of the tree represent the open problems that are piquing many people's interest

(24). These problems include switchable metamaterials, amplifying metamaterials, sensor metamaterials, nonlinear metamaterials, quantum metamaterials (24). This tree predicts the focus of research efforts will shift from investigating the physics essence of metamaterials to experimentally demonstration of applications of metamaterials (24). All of the research work presented in this dissertation fall into the "small green apple" category, or more specifically, the areas of switchable metamaterials, nonlinear metamaterials, sensor metamaterials and loss compensated/amplifying metamaterials.

As of today, LHM/Metamaterials have been demonstrated for practical devices in the general area of transformation optics (25, 26) with applications such as negative index of refraction (1), perfect lens (27), superlens (28) , electrically small antennas (29) and perfect absorbers (30, 31, 32).

Many different names, such as negative index materials (NIM), have been used in place of LHM for this rapid growing area. Now the most widely accepted terminology is metamaterials, which will be used throughout the dissertation.

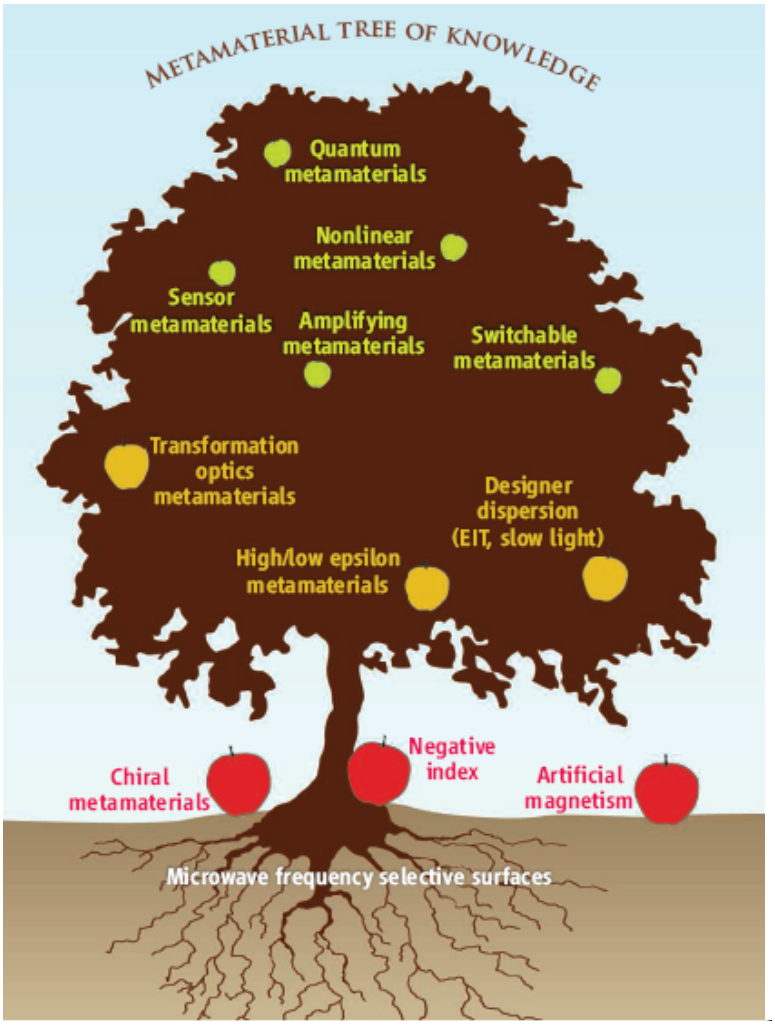

Figure 2.7: Research activities in the metamaterial area are shown as apples on a tree (24)

3

Metamaterials as Circuit Elements

3.1 Derivation of equivalent circuit model of Metamaterial from electromagnetic theory

The accurate electromagnetic (EM) response of metamaterial resonators can be analyzed with electromagnetic field theory. Design of a more complicated metamaterial based devices/system requires higher level understanding of the each component including metamaterial resonators. Equivalent circuit model can help us understand the essence of metamaterial resonators qualitatively from the perspective of circuit theory. It helps us obtain clear understanding and rational and systematic design of metamaterial based devices.

Modeling a metamaterial resonator as circuit elements also facilitates the EM-circuit co-simulation in the circuit simulation tool that enables us to simulate the metamaterial and embedded circuits as a complete system much faster than using the 3D full wave simulation tool. Accurate quantitative analysis of 3D electromagnetic field effects of metamaterials can be carried out in commercial numerical full wave simulation tool such as CST microwave

studio subsequently to verify modeling.

Because metamaterials root in the Frequency Selective Surface (FSS), the history of the circuit modeling of metamaterial should be traced back to early days' of FSS research. In 1983, Langley and Parker proposed a simple equivalent circuit model composed of two inductors and capacitors for their double square array FSS (33). Bayatpur then proposed to use lumped LC together with a transformer to model a "loop-wire miniaturized-element FSS" and achieved very accurate results (34). On the metamaterial side, Wu *et. al* proposed a compact equivalent circuit model for SRR using 4 pairs of parallel LC circuit (35). Chen *et. al* proposed a general equivalent circuit model for different types of SRRs taking into account not only the inductance of each unit cell but also the mutual coupling between adjacent unit cells using transformers (36).

The lumped circuit model of edge coupled SRR is built and explained here as an example. Metamaterial resonators such as edge coupled SRR can be modeled as parallel RLC circuit roughly to the first order (37). As shown in Fig. 3.1, only three passive circuit components are employed in equivalent circuit model, namely, resistors, capacitors and inductors (37).

In this particular example of edge coupled SRR, the narrow slit between the inner and outer ring contributes to the capacitor C in the equivalent circuit model (37). While the inductor L in the equivalent circuit model is attributed to the surface current flowing in the rings (37). The resistor R in the equivalent circuit model arises from the ohmic loss of the metallic rings and the dielectric loss in the substrate. Using the similar method, RLC equivalent circuit model can also be derived from the EM properties of other metamaterial resonators such as electric-coupled LC resonator (ELC) (3) or Split Ring Resonators (SRRs) (38). Schematics of typical ELC and SRR resonators are shown in Fig. 3.2 and 3.3, respectively (3, 38).

ELC resonators exhibit strong coupling to applied electric field and negligible coupling to

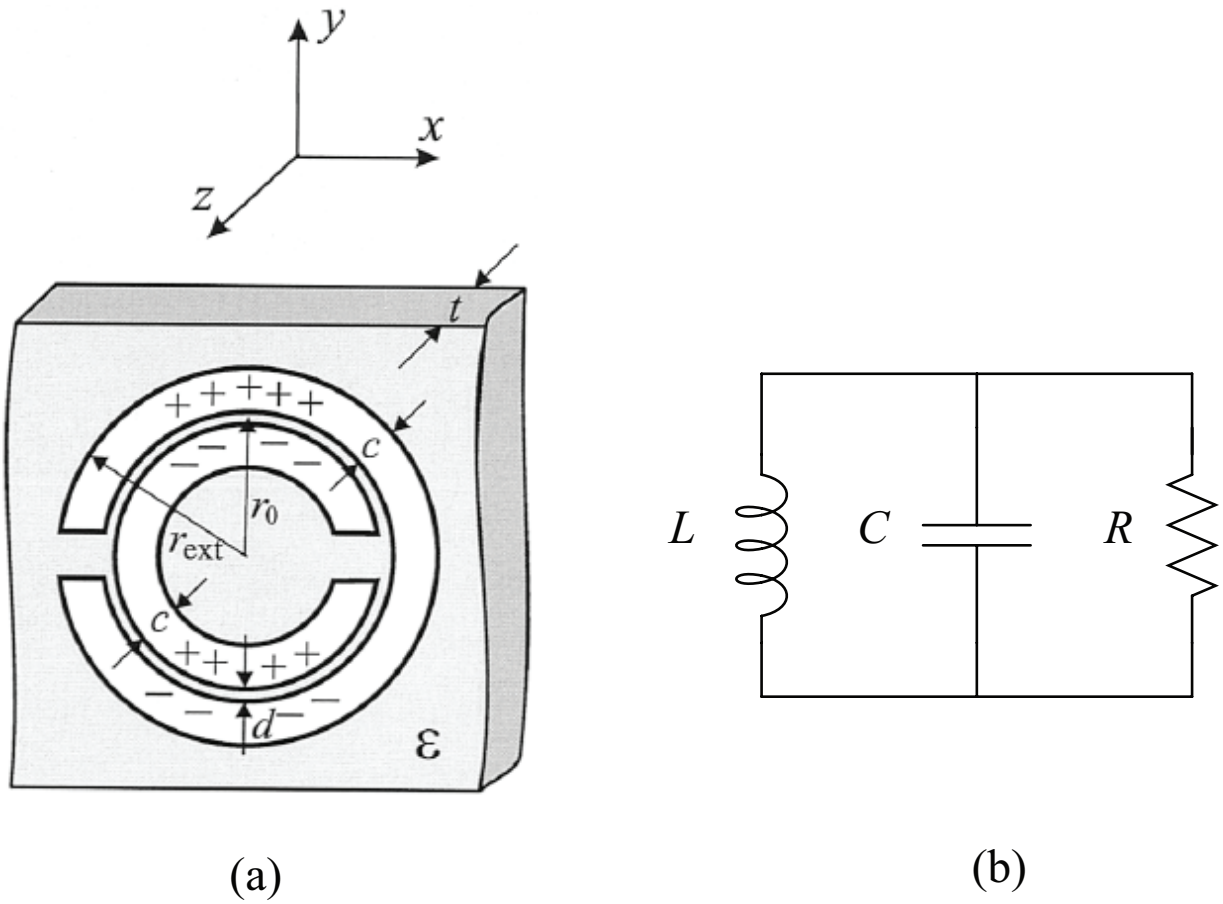

Figure 3.1: (a)Edge coupled SRR(EC-SRR) (b)equivalent circuit model (37) -

Figure 3.2: ELC resonator

Figure 3.3: SRR resonator

the magnetic field (3). ELC resonators have been used as a negative index material (39), dual-resonant terahertz metamaterial (40), a high speed terahertz modulator (41) and an omnidirectional EM absorber (42). The SRR structure couples to both electric and magnetic field (38) and have been a very popular choice with practical demonstrations of negative permeability (1). RLC equivalent circuit models will be used to represent these metamaterial resonators directly in the following chapters to facilitate analysis and illustration.

At the resonant frequency of the metamaterial, $\omega = \frac{1}{\sqrt{LC}}$, the strength of the resonance is strongly dependant on its loss R. The typical resonance of ELC resonator is shown in Fig. 3.4. The sharpness of the resonance is characterized by the quality factor Q, which is inversely proportional to its loss R. Its loss R dampens the resonance of the metamaterials.

More complicated equivalent circuit models have been proposed in literature for other types of metamaterials. One example is the Labyrinth resonator (43). Its schematic and equivalent circuit model are shown in Fig. 3.5 and 3.6 (43).

L^{LR} models the inductance caused by the outer perimeter of the labyrinth resonator (43). C^{LR} models the total capacitance of the labyrinth resonator (43). It is composed of a series

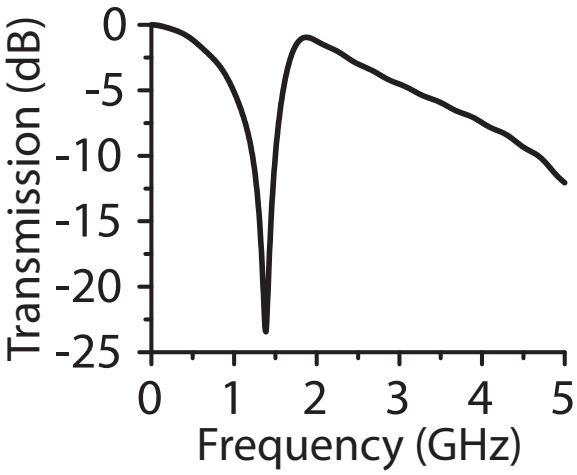

Figure 3.4: Typical transmission of ELC resonator

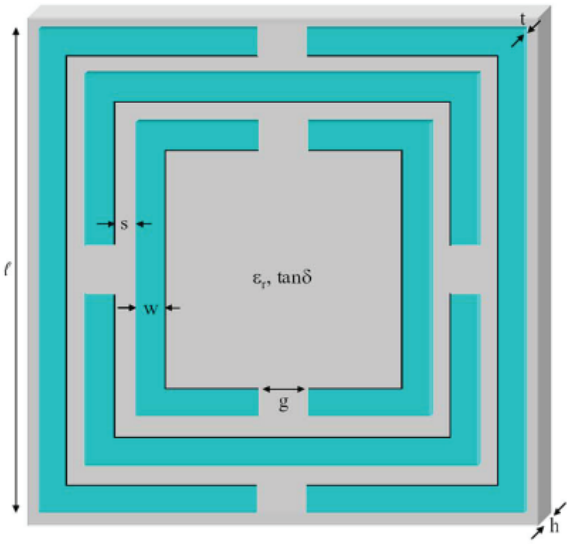

Figure 3.5: Labyrinth resonator (43)

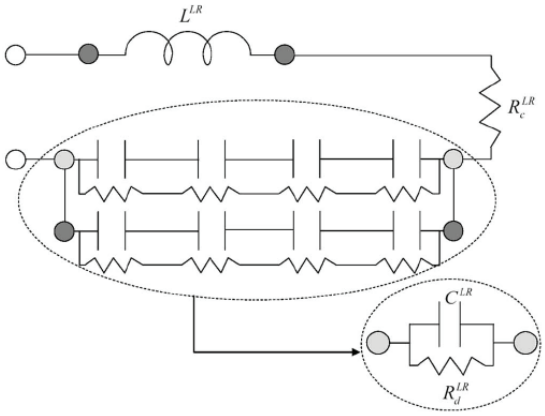

Figure 3.6: Equivalent circuit model of Labyrinth resonator (43)

of distributed capacitors that represent the coupling capacitance between neighboring rings and capacitance in the gap (43). R_c^{LR} models the series resistance that arises from the ohmic losses in the metallic traces (43). R_d^{LR} is the dielectric losses incurred by the dielectric substrate (43). The modeling of this complicated labyrinth resonators requires much more passive circuit components than ELC and SRR resonators.

3.2 Distributed circuit and reflection coefficient

The resistor, capacitor and inductors we used to build the equivalent circuit model of metamaterial resonator are lumped components. However, analysis of circuits at higher frequencies such as radio frequency, microwave, infrared and above are more accurately treated if they are considered as distributed in space. For example, a piece of wire is considered lossless at low frequency. However, for a high frequency signal when the length of the wire is comparable to the wavelength of the incident EM wave, this piece of wire becomes a distributed circuit composed of many identical unit length segments (44). This piece of wire has resistance R, conductance G, capacitance C and inductance L and their values are dictated by the length of wire. Usually we define the value of resistance, conductance, capacitance and

inductance per unit length of wire instead of a fixed value (44). The voltage and current propagates on this piece of wire as waves that have dependence on both time and position on the wire (45). The characteristic impedance of this piece of wire is defined as the ratio between the voltage and current propagating on it (44). If this piece of wire is terminated by a load with different impedance from its characteristic impedance, a large portion or all of the voltage and current signal are reflected from the load, depending on the exact value of the load impedance. One useful metric, namely, the reflection coefficient is defined as "the ratio of the reflected to the incident wave" along the wire (45).

The reflection coefficient is a very powerful metric because it describes the behavior of a complicated high frequency circuit numerically across the frequency band of interest even if we do not know the exact circuit topology and component values. We can treat any unknown high frequency circuit or system as a 'black box' and simulate the reflection coefficient of it to understand its behavior within the frequency band of interest. Because we can measure the reflection coefficient with Vector Network Analyzer (VNA), the measurement result is commonly used to examine the simulation result to ensure the simulation result is reliable.

3.3 Extraction of Equivalent Circuit from Reflection Coefficient

As discussed in section 3.2, any circuit element working at high frequency must be regarded as a distributed circuit. A lumped equivalent circuit model of this circuit element is just an approximation and cannot reflect its accurate EM properties. Metamaterials are not an exception. However, a lumped equivalent circuit model can aid the design of active circuit embedded into the metamaterial.

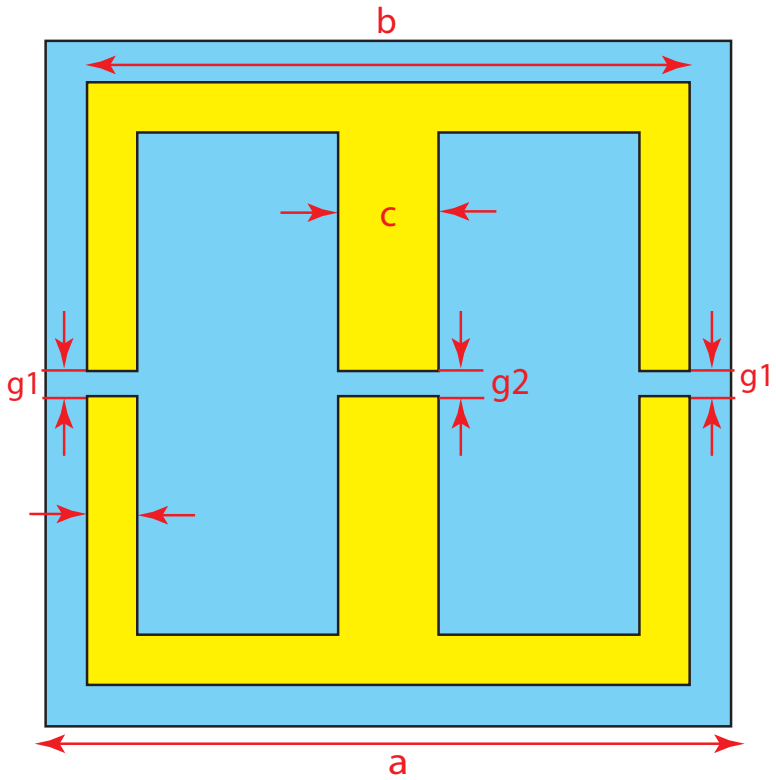

Figure 3.7: ELC resonator with a opening slit in the center. All units are in mm. $a = 27.3, b = 24, c = 4, d = 2, g_1 = 1, g_2 = 0.5$. The dielectric substrate is a 5 mm thick FR4 layer, the real part of its permittivity is 4.5 and the loss tangent is 0.06 at 2 GHz. The metallic structures are made of 0.03 mm thick gold layer, which has an electric conductivity of 4.561e+007 S/m.

In order to make the lumped equivalent circuit model as accurate as possible, we can try to match its reflection coefficient with that of the metamaterial through curve fitting. An example of extracting the parameters of the lumped equivalent circuit model of an electrically coupled LC (ELC) resonator (3) is shown here. The same parameter extraction method can be applied to other kinds of metamaterial resonators. The dimensions of the ELC resonator example are shown in Fig. 3.7. The dielectric substrate is a 5 mm thick FR4 layer, the real part of its permittivity is 4.5 and the loss tangent is 0.06 at 2 GHz. The metallic structures are made of 0.03 mm thick gold layer, which has an electric conductivity of 4.561e+007 S/m.

We simulated the ELC resonator in CST microwave studio. We define port 1 and 2 as free

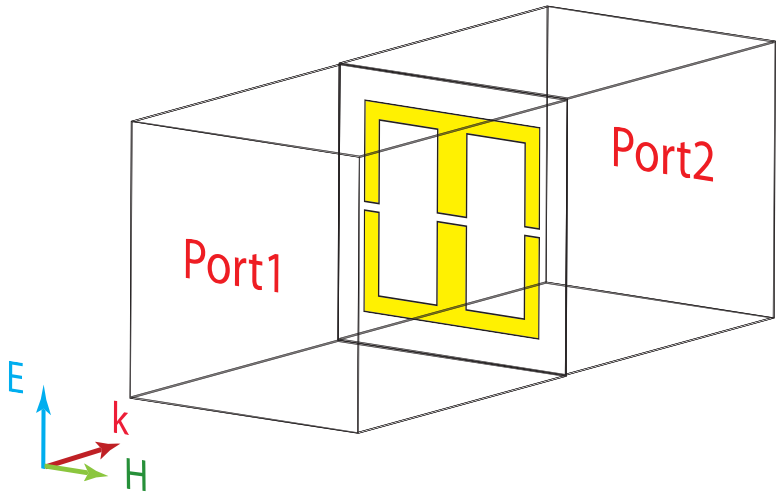

Figure 3.8: Waveguide port 1 and 2 defined in CST to simulate ELC resonator. The polarization of incident EM wave is also depicted.

space waveguide ports in front of and behind ELC resonator, respectively, as shown in Fig. 3.8. The polarization of incident EM wave generated by the waveguide ports are also shown in this figure. Port 3 is a discrete port in the gap as shown in Fig. 3.9. The simulated reflection coefficient at port 3 is denoted as S_{33} and is shown in Fig. 3.10.

The initial circuit topology employed is a RLC circuit. L models the inductance induced by the surface current flowing on the edge and central arm of the ELC resonator. The high electric field focused in the gap justifies a shunt capacitance C. A series resistance R_2 models the ohmic losses incurred by the metallic strips in the ELC resonator. A shunt resistance R_1 models the dielectric losses associated with strong electric field focused in the gap capacitance C. In general, wires parallel to electric field polarization can be modeled as inductors. Gaps in parallel to the electric field polarization usually contains focused electric field and can be modeled as capacitors. Two parallel patches separated by a dielectric that are stacked up in the direction of the wave propagation should be modeled as series capacitor (46). Two parallel wires placed close to each other always have a coupling capacitor between them. Two adjacent rings usually have inductive coupling that should be modeled as transformer

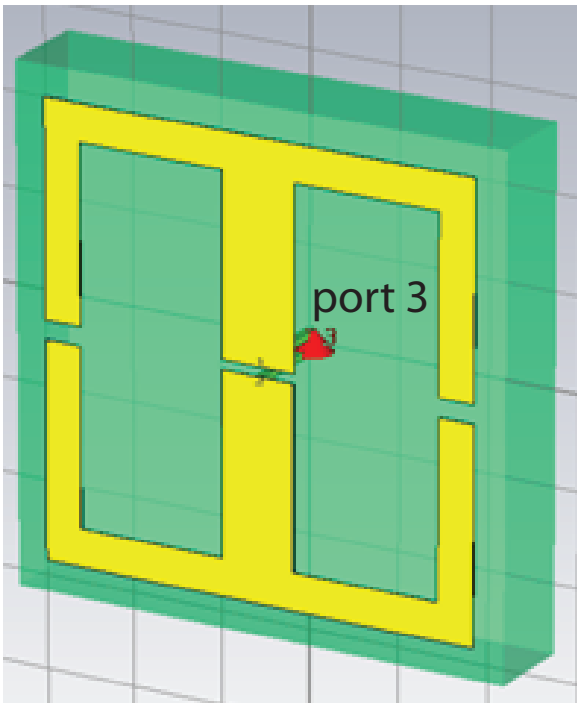

Figure 3.9: Port 3 is in the gap of ELC resonator

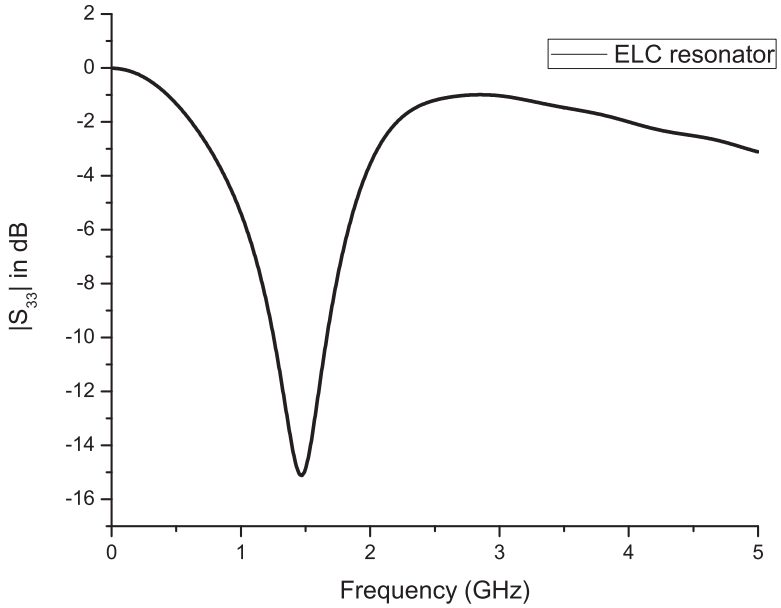

Figure 3.10: Simulated S_{33} of ELC resonator in CST

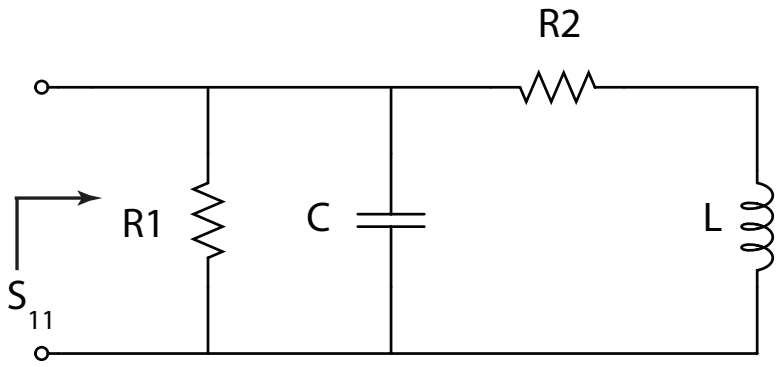

Figure 3.11: Topology of equivalent circuit model of the ELC resonator, S_{11} is the reflection coefficient looking into the input the equivalent circuit model

(36).

This equivalent circuit model is only expected to provide basic, qualitative understanding of the metamaterial resonators. A clearer and more precise model of metamaterial resonators are provided by reflection coefficient. In this particular example, the only goal is to match the resonant frequency of this lumped circuit model to that of the reflection coefficient. A more complex circuit topology may fit the resonance response better to that of the reflection coefficient.

If a more accurate circuit model is desired, one has to include transformer along with RLC to sometimes make a complete model (34). Transformers capture mutual coupling between wire traces from magnetic induction. The polarization of the incident EM radiation also changes the model. An equivalent circuit model of the ELC resonator is designed accordingly and its topology is shown in Fig. 3.11.

In the beginning, we make a guess on the values of R_1, C, R_2, L components in the circuit as the initial values. Then we simulate the reflection coefficient S_{11} of the equivalent circuit model in Advanced Design System (ADS). In order to make the equivalent circuit model approximate the ELC resonator, we compared its reflection coefficient S_{11} with the reflection

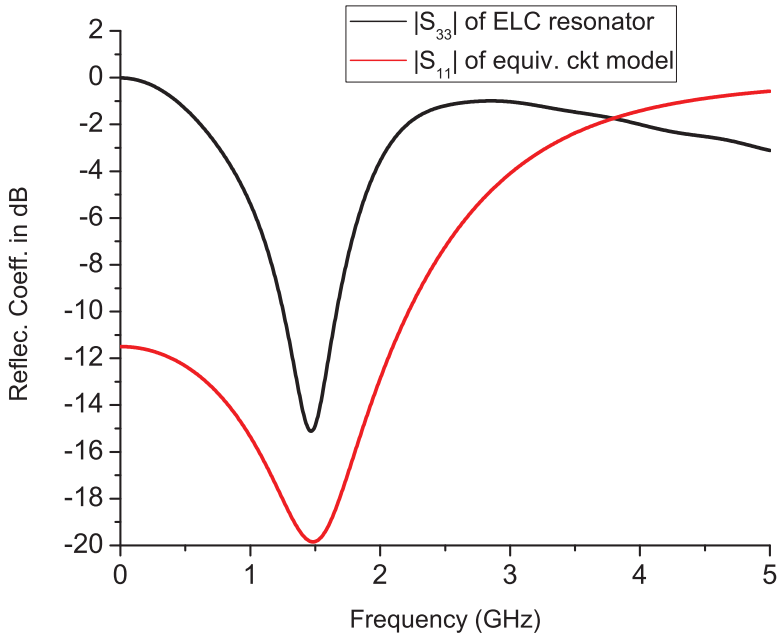

Figure 3.12: Reflection coefficient S_{11} of equivalent circuit model and S_{33} of ELC resonator

coefficient S_{33} of the metamaterial ELC resonator. Then we tune the values of R_1, C, R_2, L to reduce the difference between S_{11} of equivalent circuit model and S_{33} of ELC resonator. It takes tens of iterations to find R_1, C, R_2, L values that makes the S_{11} curve approximate the S_{33} curve. The curve fitting cannot be accurate because we use a lumped first order equivalent circuit to model the ELC resonator. The final values of circuit elements in the equivalent circuit model chosen are $R_1 = 40k\Omega, C = 1.5pF, R_2 = 29\Omega, L = 3nH$. The S_{11} of equivalent circuit model with these parameters and the S_{33} of the ELC resonator are shown in the same figure in Fig. 3.12.

This curve fitting is not perfect but at least the resonant frequency of the equivalent circuit model matches that of the ELC resonator. It helps us decide the operating frequency of embedded active circuit, which has to match that of the ELC resonator in order to make the embedded active circuit and metamaterial work as a system. A more accurate equivalent circuit model can be built with more circuit elements, more complicated topology and more

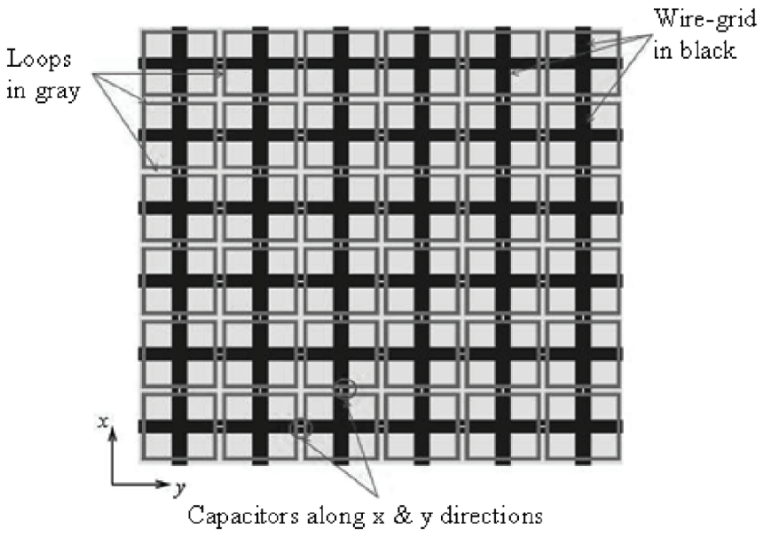

Figure 3.13: The schematic of a FSS based on square loop arrays and wire grid. The square loop array implemented on the top layer is shown in grey while the wire grid fashioned on the bottom layer is shown in black. Capacitors are embedded to connect the neighboring square loops (47)

iterations of circuit elements tuning for curve fitting.

The trial of each circuit topology takes much time and computational resources when the circuit topology becomes more complicated because there are many more combinations of component values. But it is not the focus of this dissertation to build an accurate lumped circuit model of metamaterials. All the designs presented in this dissertation are based on reflection coefficient.

However, it is beneficial to refer to the equivalent circuit modeling of frequency selective surface (FSS) because its modeling method gives us a guideline of how to build a more accurate equivalent circuit model for metamaterials. A lumped equivalent circuit model for a FSS consisting of loop arrays and wire grid is proposed by Bayatpur using a transformer as well as LC components (47). The schematic of this FSS is shown in Fig. 3.13 (47).

The square loop array implemented on the top layer is shown in grey while the wire grid

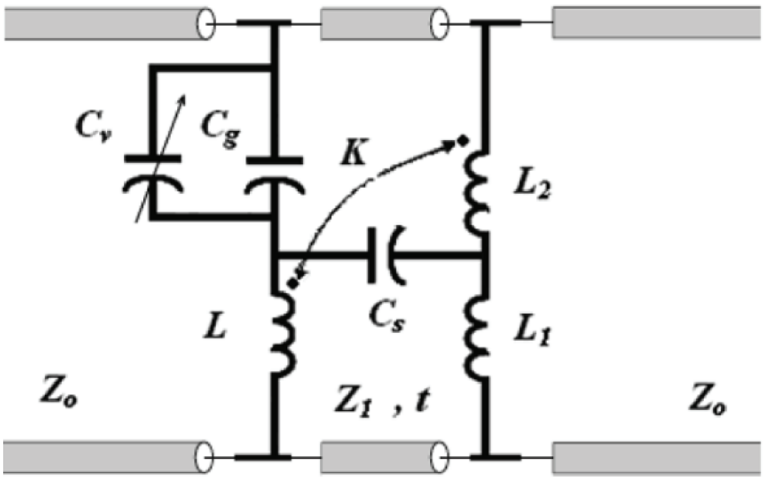

Figure 3.14: Proposed equivalent circuit model for one unit cell of the FSS (47)

fashioned on the bottom layer is shown in black (47). Capacitors are embedded to connect the neighboring square loops (47). Its proposed equivalent circuit model is shown in Fig. 3.14 where the losses are ignored (47).

As mentioned earlier, the incident EM wave excites currents flowing in the wire grid when the wires are in parallel to the E electric field vector (47). These currents induce magnetic field around wires and thus the wire grid is modeled as inductors L_1 and L_2 in Fig. 3.14 (47). In the layer of square loop array, the gap between neighboring loops form a capacitance C_g and the embedded capacitor placed in the gap is named C_v (47). Currents are induced in the square loop trace by the EM wave, which justifies the square loop to be modeled as inductor L (47). The coupling between the square loop array and wire grid is captured by the mutual inductance K in Fig. 3.14 (47). The constituent traces of square loop that are in parallel to the wires in wire grid causes a series capacitor C_s (47). The small transmission line with characteristic impedance Z_1 models the dielectric medium with thickness t between square loop array and wire grid (47). The transmission line with characteristic impedance Z_0 represents the free space over and under the FSS (47). The component parameters of the

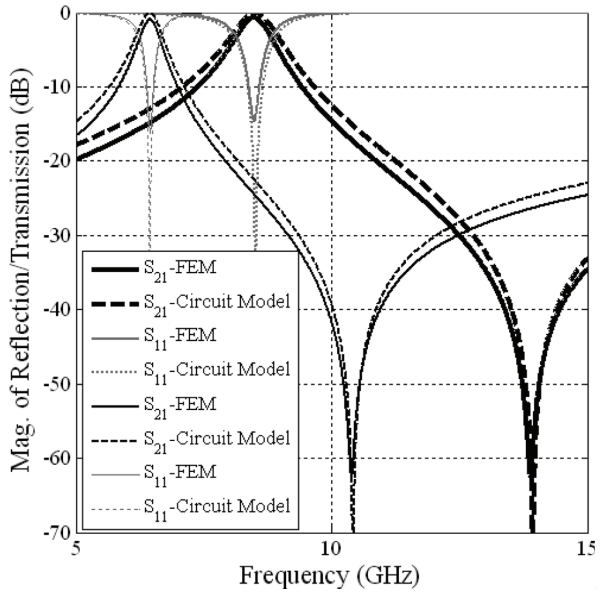

Figure 3.15: Comparison between the equivalent circuit model simulation and 3D full wave finite element method (FEM) simulation (47)

circuit model are L_1=0.523nH, L_2=0.0565nH, C_s=58.75fF, K=-0.97,C_g=8.41fF, L=0.755nH (47). The circuit model simulation result and 3D full wave simulation result are shown in Fig. 3.15 for comparison when C_v are 0.3 and 0.15pF (47).

3.4 Interface between Metamaterial Design and Active Circuits Design

The inherent problem of metamaterial with active circuit design is how to come up with a systematic design flow for such a hybrid system. Full wave electromagnetic (EM) solver such as Microwave CST provides accurate numeric analysis for any intricate 3D structure using Finite-difference time-domain (FDTD) method or finite element method (FEM). But the object under analysis must be decomposed into miniaturized meshes first and boundary conditions have to be defined. Any active circuit cannot meet these conditions and

thus it is impossible to analyze/design active circuits in the full wave EM solver. In contrast, although sophisticated commercial circuit solvers have powerful functions to analyze complicated active circuits, they cannot simulate 3D metamaterial structures.

The EM and circuit solver are working with different methods but both of them are needed for a rational and systematic design of metamaterial with active circuits. The solution is to find an interface between them to facilitate the exchange of design information between them. This interface is found to be the reflection coefficient in S parameter format. With the help of this interface, we can design the active circuits in circuit solver first with a rich body of existing circuit design techniques. Then its reflection coefficient in S parameter format is calculated and imported into EM solver to design the system of metamaterial with active circuit. Or, we can design the metamaterials in the EM solver first and then export its reflection coefficient in S parameter format into circuit solver to complete the system design.

3.5 Reflection Coefficient based Systematic Design Flow

The following reflection coefficient based design flow is followed throughout the dissertation when we design a system of metamaterial with active circuits. The system diagram of the metamaterial with active circuit is illustrated in Fig. 3.16. The design flow is:

- The first step is to simulate the reflection coefficient of the metamaterial resonator, which is denoted as Γ_{MM} in Fig. 3.16 to understand its frequency response. This simulation can be performed in a full wave 3D electromagnetic (EM) simulator such as CST microwave studio. This simulation/measurement is done at the desired port where the metamaterial will interface with the circuit element. Reflection coefficient is typically captured at this port. We expect the frequency response at this port to be consistent with the free space frequency response

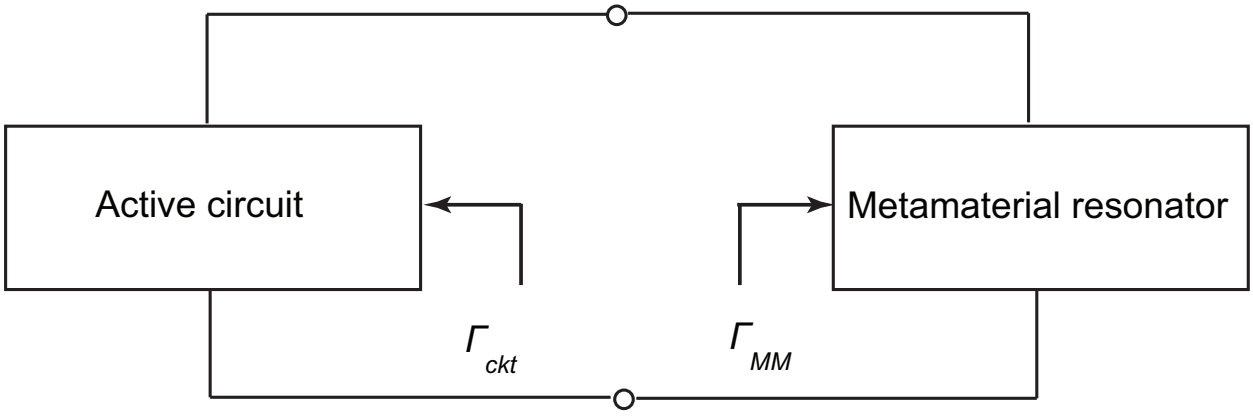

Figure 3.16: Reflection coefficient of a metamaterial resonator embedded with active circuit -

- The active circuit is designed according to its expected function, such as compensating for the losses of metamaterial resonators or receiving signal from metamaterial. Design of the circuit is based on the S-parameters (or reflection coefficients) information provided by the simulation of the metamaterial resonator.

- The next step is to simulate the reflection coefficient of the embedding active circuit, which is shown as Γ_{ckt} in Fig. 3.16, in a circuit simulation software such as Agilent Advanced Design System (ADS).

- Once the Γ_{MM} and Γ_{ckt} are available, they are fed into the full wave 3D electromagnetic simulator and the EM response of the entire system of the active circuit embedded metamaterial is obtained.

- After the metamaterial and active circuits are implemented, Γ_{MM} and Γ_{ckt} of them are measured using the VNA. Their models are refined in simulation to make it closer to measurement results.

3.6 Summary

In this chapter, we discuss an alternative way of understanding metamaterials through modeling them as circuit elements. Modeling metamaterials as circuit elements bridges the gap between metamaterials design and circuit design. Metamaterials can be described either by reflection coefficients or lumped circuit models. The history of modeling FSS and metamaterials using lumped circuit elements is briefly reviewed. Then the theoretical foundation of modeling metamaterials as lumped circuit elements is laid out using electromagnetic theory. An example of extraction of lumped circuit model from reflection coefficients is presented. A general guideline of how to model the constituent elements of the metamaterial resonators as distinct circuit elements is provided. It is very difficult to build an accurate lumped circuit model of metamaterials. Reflection coefficients are more accurate to characterize metamaterials and are naturally compatible with existing simulation software and measurement instruments. Reflection coefficients of metamaterial resonators are selected to guide our design of embedding active circuit into metamaterials. The simulation of the metamaterial with an embedded circuit as a system is facilitated by grouping their reflection coefficient together and calculate their overall response to incident EM radiation. This design and simulation methodology is employed in all of the following chapters to demonstrate a variety of active circuit embedded metamaterials.

4

Loss Compensation in Metamaterials through Embedding of Active Transistor based Negative Differential Resistance Circuits

In this chapter, the active circuit is designed and embedded into metamaterials to resolve one of the most challenging issues in metamaterials design: losses. Losses have plagued the metamaterial community since metamaterial was first demonstrated experimentally. It is explained why the EM properties of metamaterials are vulnerable to losses, where losses in metamaterials arise from and how to compensate for losses through the embedding of active transistor based negative differential resistance circuits into metamaterials. The reflection coefficient design methodology discussed in the previous chapter is employed to design, simulate and measure the embedded active transistor based negative differential resistance

circuits for loss mitigation.

4.1 Background

Metamaterials derive their exotic electromagnetic (EM) properties from their engineered structure made of metal and dielectric material instead of constituent properties of atoms and molecules (4, 5, 6). A number of metamaterial unit cell structures have been explored theoretically by numerical simulation and experimentally by testing. They include, but not limited to, electric-coupled LC resonator (ELC) (3), Split-Ring Resonator (SRR) (2), etc. Passive metamaterials are made by populating an array of identical unit cells such as ELC or SRR. We design the structure of metamaterial unit cells to ensure a maximum current or charge in the unit cell is induced by the incident electromagnetic radiation near the resonant frequency (48). The induced current or charge creates magnetic or electric dipole moments which contribute to the exotic electromagnetic properties of metamaterials (48). But the induced current or charge is closely related to the resonant response of metamaterials, which incurs a lot of losses and is dependent on the resonant frequency (48). As a matter of fact, all these passive metamaterials are made from metal meshes and dielectric substrate and therefore suffer from metallic and dielectric losses, which eventually limit their overall performance. One example is the super lens that relies on the evanescent wave enhancement property (48). The evanescent wave carries high resolution information that are lost in the conventional lenses because the evanescent wave decays quickly from the surface of lenses (49, 50). Super lens can enhance evanescent waves and make it propagate to the detector at far-field so that a high resolution image can be recovered (50). The evanescent wave enhancement property is very vulnerable to losses and any small losses in metamaterials would corrupt the performance of super lens (51, 52). In general, this issue of loss is exac-

erbated in 3D metamaterials where there is more interaction between the electromagnetic waves and the bulk metamaterial (53). Loss mitigation approaches are needed for 2D and 3D metamaterial devices to be practical for real applications. One approach for loss compensation is to introduce a gain medium into metamaterials (53, 54). This idea originates from the laser literature, where the gain medium is used to provide the optical gain (55). An optical pumping source moves the atom from a lower energy state to a higher energy state. By external stimulation, the atom may be induced to emit another electron when it falls from the higher energy state to the lower energy state, which results in the gain (55). This gain can help to compensate for the losses. However, it was noted in (56) that this optical pumping based method for loss compensation may be highly impractical and unscalable because it is too bulky and power consuming (56). Instead, an electrical approach for loss compensation that works by injecting electrical current from a semiconductor into a chunk of metamaterial may be more suitable (56). One example of an electronic method for loss compensation, recently shown for Split Ring Resonators (SRRs), is to insert additional smaller SRRs with an amplifier signal chain to sense, amplify and inject amplified signal into the metamaterial to compensate for its losses (48, 57). However, additional antenna elements affect the original metamaterial response and add design complexity especially at shorter wavelengths with reduced dimensions. Another Field-Effect Transistor (FET) based solution was proposed for a single ring resonator at 100MHz (58) using a single-ended circuit network with complex biasing and tuning circuit, with mediocre improvement in reflection coefficient $|S_{11}|$ of just -1.55dB. An operational amplifier based solution with no experimental results was also proposed in (59); this approach has been used for broadening metamaterial response (60, 61) and not for loss compensation. Another method for loss compensation utilized the negative resistance region in non-linear diodes (62) without practical implementation. The paper (62) also acknowledged that "such diodes bring with them the risk of

instability arising from parasitic oscillations".

A practical realization of a loss compensation circuitry using cross-coupled transistor pair is proposed and implemented which provides Negative Differential Resistance (NDR) to metamaterials. The circuit is fully symmetrical, which can be readily integrated into a standard CMOS process to reduce its size and provides a tunable bias control to adjust impedance and guarantee stability.

4.2 Negative Differential Resistance (NDR)

An active-transistor embedding approach for loss compensation is presented here. The embedded circuitry provides a Negative Differential Resistance (NDR) to compensate for the loss in each unit cell. The concept of NDR is explained as follows. By definition, NDR circuit exhibits a negative value for differential impedance $\frac{\Delta V}{\Delta I}$, while keeping a positive value for impedance $\frac{V}{I}$, where V and ΔV are the voltage phasor and its variation across the network, and I and ΔI represent the corresponding current phasor and its variation flowing into the NDR network respectively ($|\Delta V| < |V|$, $|\Delta I| < |I|$). ΔV and ΔI represent the voltage and current induced by the incident EM radiation and $\Delta I = \frac{\Delta V}{R}$ where resistance R models the undesirable ohmic and dielectric loss in the equivalent RLC representation of the metamaterial as shown in Fig. 4.1. At the resonant frequency of the metamaterial, $\omega = \frac{1}{\sqrt{LC}}$, the strength of the resonance is affected by its loss R. This also affects the (ϵ, μ) parameters of the effective medium. Connecting a NDR circuitry in parallel with the metamaterial RLC circuit will inject a current $\Delta I = -|\frac{\Delta V}{R}|$ that essentially compensates for current through the lossy resistor R. Thus, NDR circuit provides an effective NDR of value $-R$ at the resonant frequency. While this concept of NDR has been applied for the first time in metamaterials, it has been widely used in circuits community. For example,

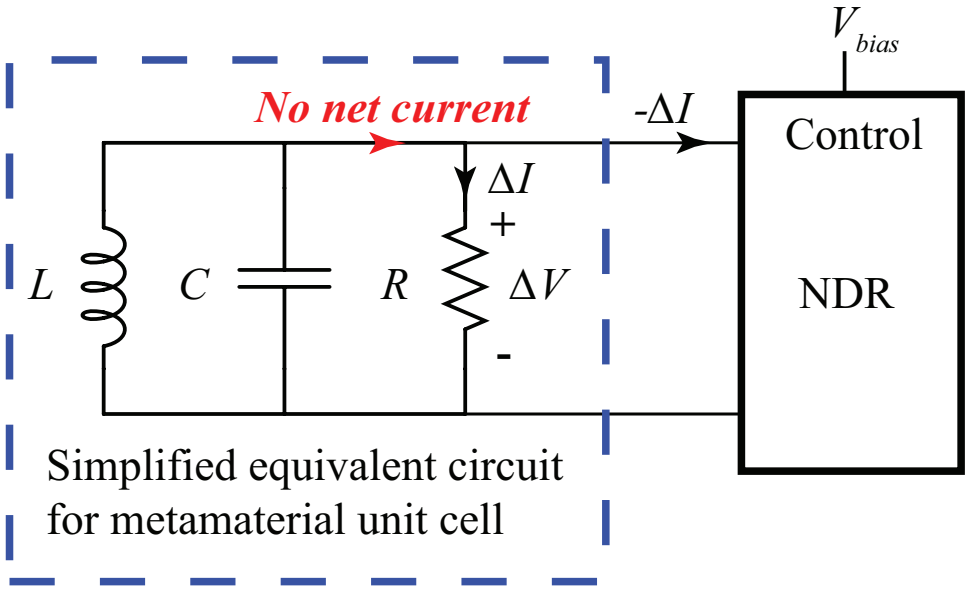

Figure 4.1: simplified equivalent circuit model: The SRR is modeled by an RLC parallel circuit, in which the R stands for the loss of the resonator. Negative Differential Resistance (NDR) circuit provides loss compensation that is bias tunable.

oscillations in Voltage Controlled Oscillators (VCO) are prevented from decaying out using NDR circuits (63, 64). NDR circuits can be implemented using very few active and passive components that can all be potentially integrated into a monolithic chip with size negligible compared to the metamaterial unit cell with low power dissipation. Aggressive scaling of the semiconductor technology to nanometer dimensions where transistors are reaching maximum oscillation frequencies f_{max} and transit-time frequencies f_T of terahertz values (65) allows for such a prospect. A terahertz modulator based on embedding of GaAs High Electron Mobility Transistors (HEMT) in metamaterial was recently demonstrated (41).

This approach of loss compensation can be applied to any planar metamaterials. The following two sections will demonstrate how to embed the NDR circuit into ELC resonators and Split Ring Resonators (SRR) for loss compensation as two examples. The ELC resonator is the typical example of a group of metamaterial resonators that are excited by external electric field. The Split Ring Resonator (SRR) is the typical example representing the group

of metamaterials that are excited by the external magnetic field.

4.3 Embedding of NDR circuit into ELC resonator

The NDR circuit is embedded into the ELC resonator (3) based single layer planar metamaterial to demonstrate proposed active loss compensation approach. ELC resonators exhibit strong coupling to applied electric field and negligible coupling to the magnetic field (3).

ELC resonators have been used as negative index material (39), dual-resonant terahertz metamaterial (40), high speed terahertz modulator (41) and an omnidirectional EM absorber (42), with performance that is also limited by the losses in the metal and dielectric layers. The design, simulation and implementation of the ELC based metamaterial with and without loss compensation is discussed below.

The dimensions of the ELC resonator used is shown in Fig. 4.2. The dielectric substrate is a 5 mm thick FR4 layer, the real part of its permittivity is 4.5 and the loss tangent is 0.06 at 2 GHz. The metallic structures are made of 0.03 mm thick gold layer, which has an electric conductivity of 4.561e+007 S/m.

The ELC resonator was simulated with the commercial finite difference time domain (FDTD) solver CST Microwave Studio. The definition of waveguide ports and polarization of incident EM wave is shown in Fig. 4.3.

The simulated transmission of this ELC resonator is shown in Fig. 4.4. The quality factor Q is low because of the losses in metal and dielectric, and we would like to compensate for them.

An important question to ask now is where to embed the NDR circuit. The NDR circuit is designed to inject power into the structure (such as the proposed ELC resonator) to

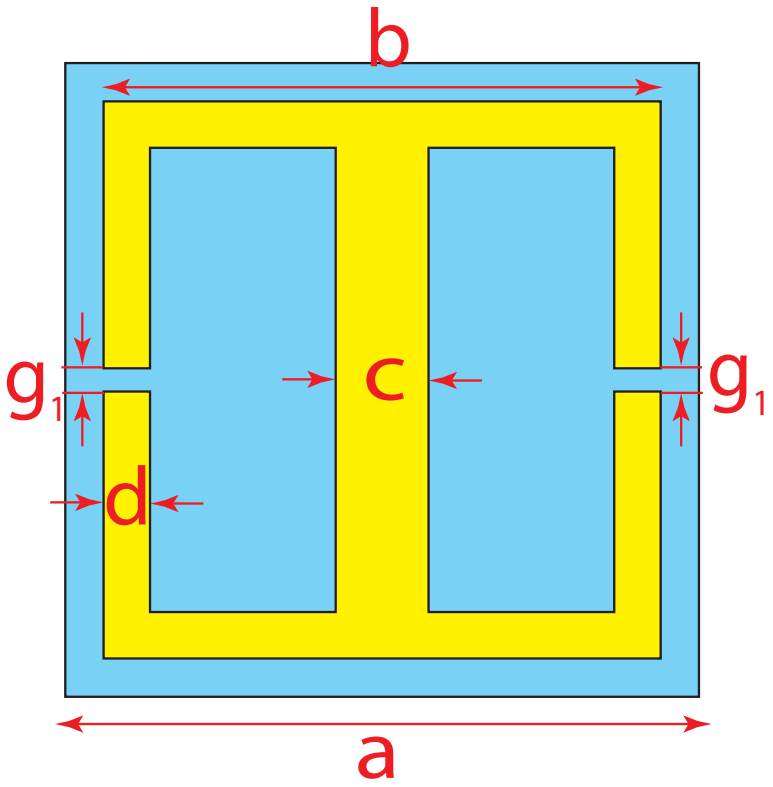

Figure 4.2: ELC resonator, all units are in mm. $a = 27.3, b = 24, c = 4, d = 2, g_1 = 1$. The dielectric substrate is a 5 mm thick FR4 layer, the real part of its permittivity is 4.5 and the loss tangent is 0.06 at 2 GHz. The metallic structures are made of 0.03 mm thick gold layer, which has an electric conductivity of 4.561e+007 S/m.

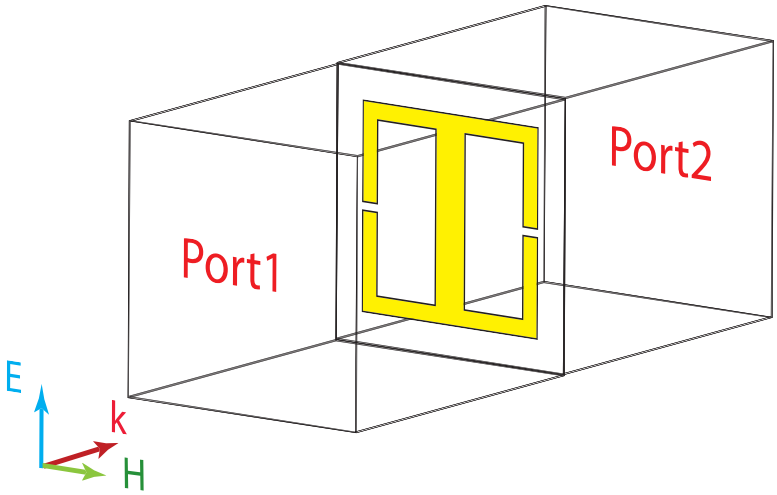

Figure 4.3: Waveguide port 1 and 2 defined in CST to simulate ELC resonator. The polarization of incident EM wave is also depicted.

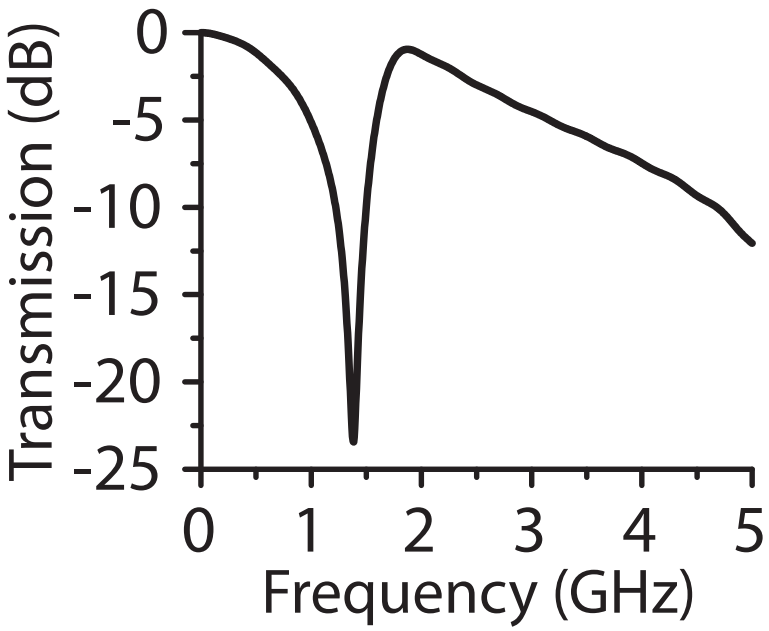

Figure 4.4: FDTD simulation of transmission of ELC resonator without the active NDR circuit

compensate for the loss. This is achieved by sensing the loss current in the system and injecting signal current that is equal and opposite in phase with the loss component. But how to guarantee maximum power transfer from the NDR circuit to the ELC resonator? The solution is to find a feeding or insertion gap in the ELC resonator to connect the NDR circuit. The insertion point is chosen where the reflection coefficient has a strong resonance at the same resonant frequency as that of the free space transmission of the ELC resonator. The insertion points are either capacitive gaps or inductive paths, where either the electric field is maximum or the surface current is densest. One can easily plug in the NDR circuitry without changing the metamaterial geometry when using the capacitive gap as its insertion point. In case of inductive paths where surface current is densest, one may need to cut open a slit in the inductive metal trace to insert the NDR circuitry. In this chapter, we will show both methods for insertion of NDR circuitry. The second method is applied to embed the NDR circuit into the ELC resonator here and the first method is employed to embed the NDR circuit into the SRR resonator, which is discussed in the next section.

4.4 Loss Compensation in ELC resonator

At the resonant frequency of this ELC resonator, it is observed that the surface current is densest on the central arm, as shown in Fig. 4.5.

We open a slit in the middle of the ELC resonator, as shown in Fig. 4.6, and embed the NDR circuit for more effective compensation of loss.

The FDTD simulation of the transmission of the ELC resonator with an open slit in the central arm is shown in Fig. 4.7. The resonance strength is reduced and the transmission rolls off faster above the resonant frequency. The resonance is damped because the opened slit in the central arm splits the ELC resonator into two halves and surface current cannot

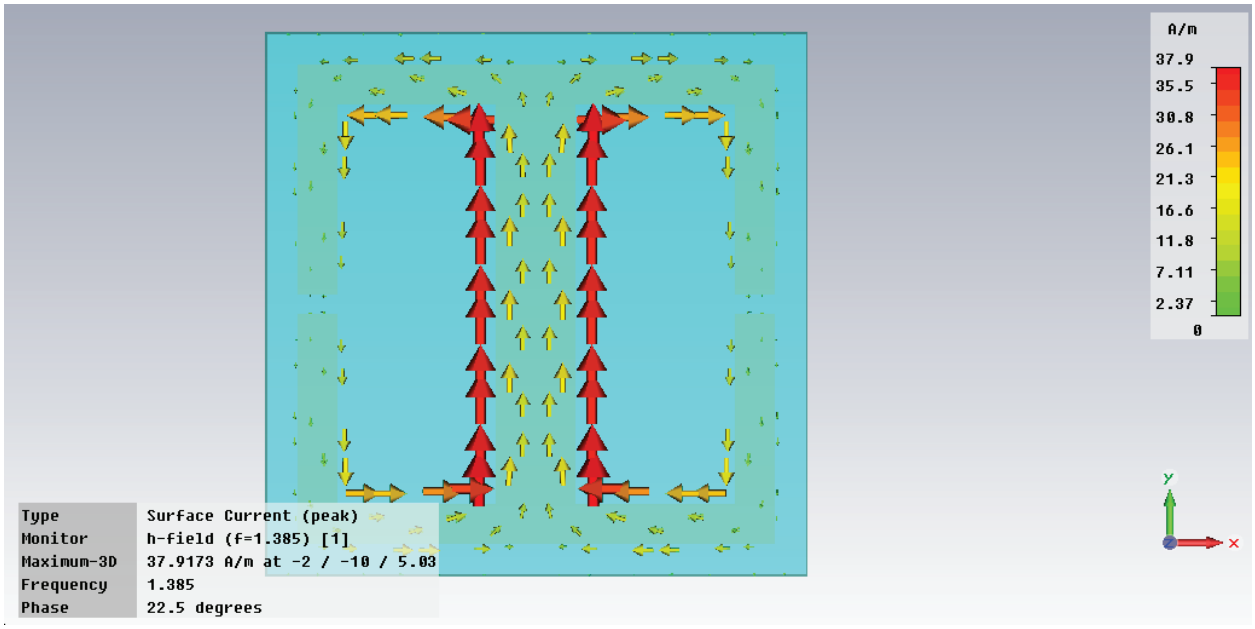

Figure 4.5: Surface current distribution on the ELC resonator at the resonant frequency

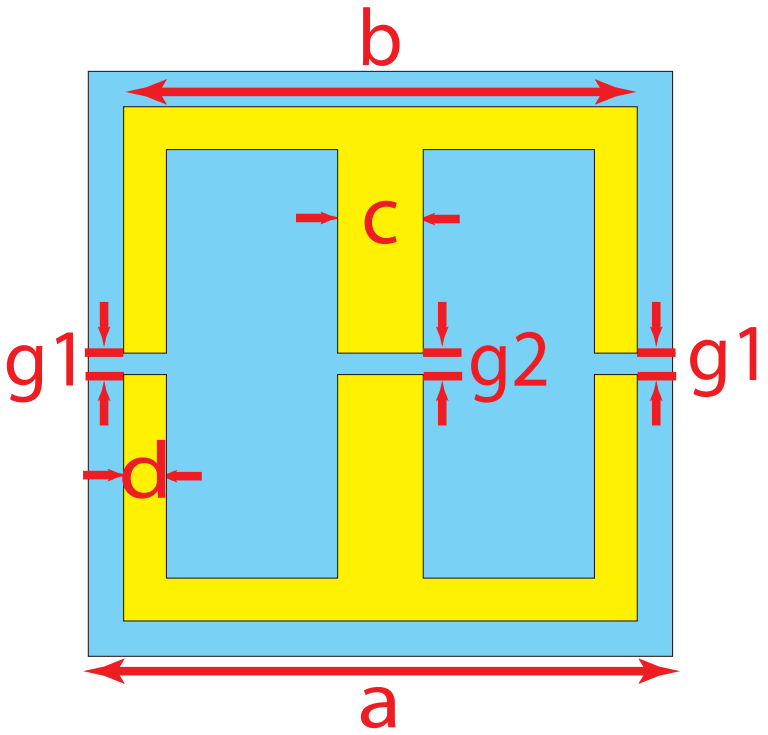

Figure 4.6: ELC resonator with a opening slit in the center. All units are in mm. $a = 27.3, b = 24, c = 4, d = 2, g_1 = 1, g_2 = 0.5$.

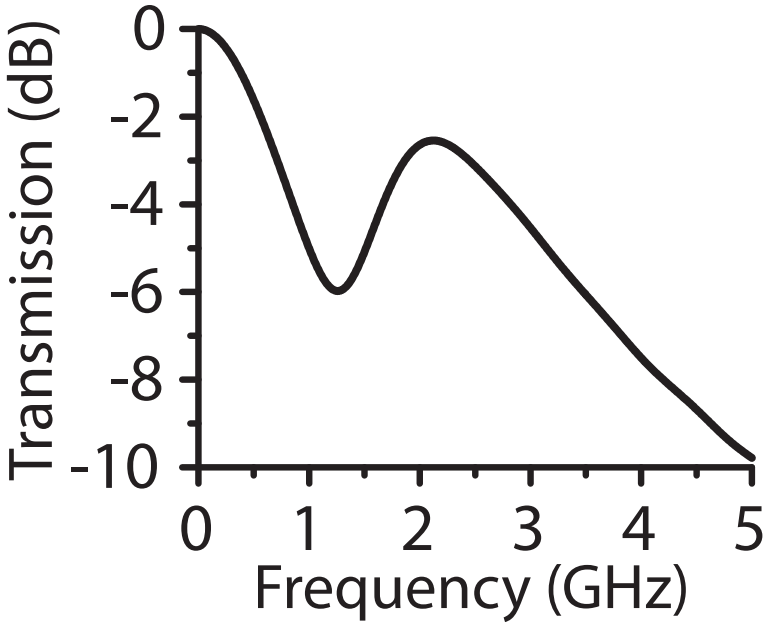

Figure 4.7: The transmission of ELC resonator with a opening slit in the center

flow between them. This problem will disappear after the NDR circuit is embedded into the slit in the central arm.

A discrete port is put in the slit in central arm to extract the reflection coefficient S_{33} of the ELC resonator to help design the NDR circuit. The S_{33} of the ELC resonator is shown in Fig. 4.8. The S_{33} of the ELC resonator has a strong resonance at the same resonant frequency as the free space transmission of the ELC resonator. It means that the ELC resonator with an open slit in the middle can absorb power efficiently around the resonant frequency from any circuit that is connected to its slit in the central arm. Therefore, the power provided by the NDR circuit that is embedded into the slit in the central arm of the ELC resonator will be transferred into the ELC resonator efficiently.

If metamaterial can be implemented as one layer of the printed circuit board or using one metal layer in a semiconductor process, one could utilize *via* holes to connect the two sides of

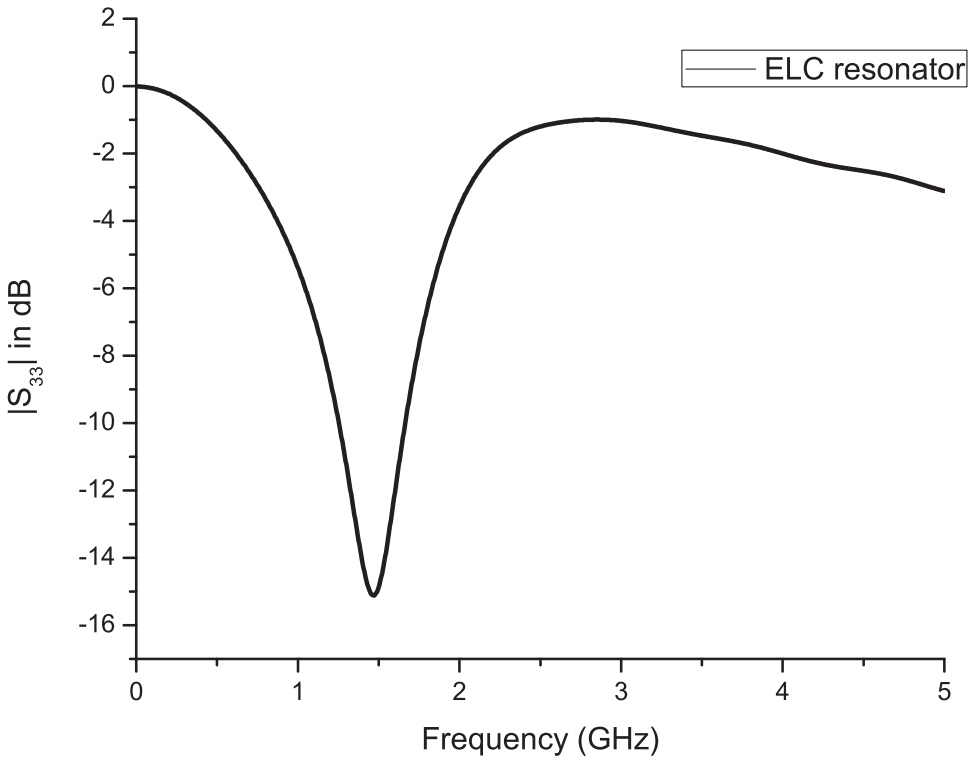

Figure 4.8: Simulated $|S_{33}|$ in dB of ELC resonator in CST

the opened slit in the center arm of the ELC resonator to the integrated active NDR circuit. The surface current is guided towards the active circuit through these *vias*.

The implementation of the NDR circuit and its connection to the ELC resonator is shown in Fig. 4.9.

For this simulation, we propose an integrated circuit process to realize a compact single chip solution for NDR circuitry. The process we use is TriQuint TQPED 0.5 μm pHEMT GaAs process (66). We chose the pHEMT GaAs process for demonstration since it is ideally suited for millimeter wave and terahertz applications due to its higher saturated electron velocity and higher electron mobility compared to traditional silicon based transistors (67).

The implemented NDR circuit consists of just 3 transistors, 1 capacitor, 2 resistors and 2 inductors. In principle, this circuit is a cross-coupled transistor pair consisting of Q1 and Q2. L1 and L2 are identical on chip spiral inductors, each of which has two and a half turns and occupies 200 μm $\times$ 200 μm. R1 and R2 are resistors to bias the transistors Q1 and Q2. R1 and R2 are identical on chip resistors, each of which is 100 Ω and occupies 11 μm $\times$ 22 μm. C1 is a 20 pF on-chip capacitor, which occupies 200 μm $\times$ 120 μm. Q3 is a current sink whose current can be tuned by its gate voltage V_{bias}. In our implementation, Q1, Q2 and Q3 were pseudomorphic HEMT (pHEMT) and could also have been Metal Oxide Semiconductor Field Effect Transistors (MOSFET) or Bipolar Junction Transistors (BJT). The active NDR circuit can be regarded as a one-port network looking into the drains of transistor Q1 and Q2 and connected across the slit in the central arm of the ELC resonator. When appropriately biased, the circuitry imparts NDR to small signal variations across the slit, equal and opposite in polarity to the loss R. The negative impedance imparted by this cross-coupled NDR circuitry can be approximated by $-\frac{2}{g_m}$, where g_m is the small-signal transconductance of Q1 or Q2 and is related to their aspect ratios and bias currents (68).

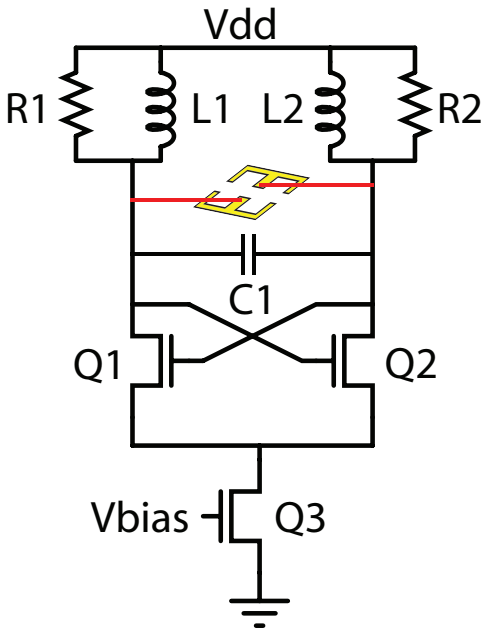

Figure 4.9: The implementation of the NDR circuit and its connection to the ELC resonator. Q1 and Q2 are pseudomorphic HEMT (pHEMT) transistors connected as cross coupled transistor pair. R1, R2, L1 and L2 are on chip resistors and inductors providing the required phase of reflection coefficient and bias voltage, respectively. R1, L1, Q1 are identical to R2, L2, Q2, respectively. C1 is a 20 pF on-chip capacitor. Q3 is the current sink, whose bias current is controlled by voltage signal Vbias

We can tune the NDR by changing the aspect ratio of transistors during the design phase or by tuning the bias voltage of current sink Q3. The active NDR circuit also provides a reactive component for the ELC resonator, whose value can be tuned by changing L1 and L2 in Fig. 4.9.

The layout of the active loss compensation circuit in this process is shown in Fig. 4.10. The total area of the circuit is 520 μm $\times$ 420 μm, which is only $\frac{1}{3412}$ of the area of a metamaterial unit cell. Due to the incredibly small size of the custom loss compensation circuit, it has minimal parasitic effect on the metamaterial response.

The NDR circuit is simulated in the Agilent Advanced Design System (ADS) and its reflection coefficient is extracted as a touchstone format S parameter file. The reflection coefficient

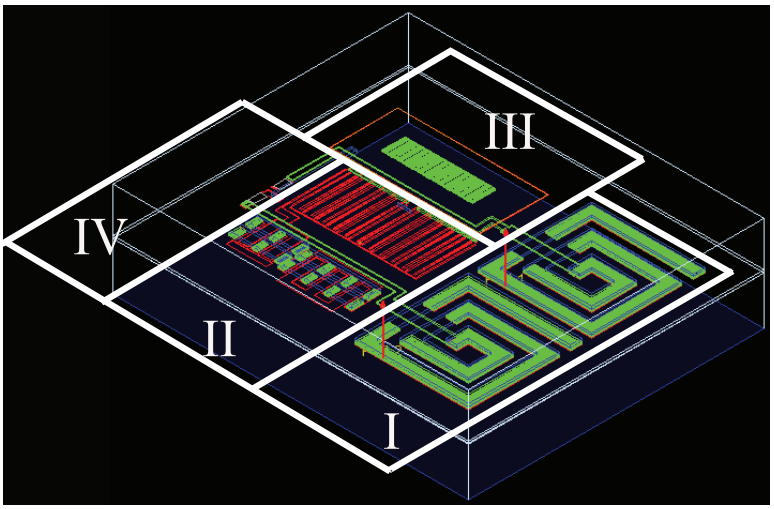

Figure 4.10: The 3D layout of the implemented active negative differential circuit in TriQuint TQPED 0.5 μm pHEMT process. Area I are L1 and L2, which are identical on chip spiral inductors, each of which has 2.5 turns and occupies 200 μm $\times$ 200 μm. Area II shows GaAs pHEMT transistors Q1, Q2 and Q3. Area III shows the on-chip capacitor C1, which is a 20 pF and occupies 200 μm $\times$ 120 μm. Area IV shows a pair of identical on- chip resistors R1 and R2, each of which is 100 Ω and occupies 11 μm $\times$ 22 μm, they are relatively small compared with other components in the figure. The entire design occupies 520 μm $\times$ 420 μm

is simulated at port 1 where the ELC resonator is connected. Therefore, S_{11} is used to denote the reflection coefficient of the NDR circuit. The magnitude and phase of S_{11} is shown in 4.11 and 4.12, respectively. At the resonant frequency of ELC resonator, the magnitude of S_{11} of NDR circuit is above 1 and its phase is around 170 degree in the vicinity of the resonant frequency of ELC resonator. This means the NDR circuit provides gain to any circuit module connected to it including the ELC resonator in this case, in the vicinity of the resonant frequency of ELC resonator.

Then the reflection coefficient of the NDR circuit is imported into the microwave CST studio and the ELC resonator embedded with the NDR circuit in the central slit is simulated in CST. Such an EM-circuit co-simulation gives us the transmission of the original ELC resonator and the ELC resonator embedded with the NDR circuit, as shown in the Fig. 4.13.

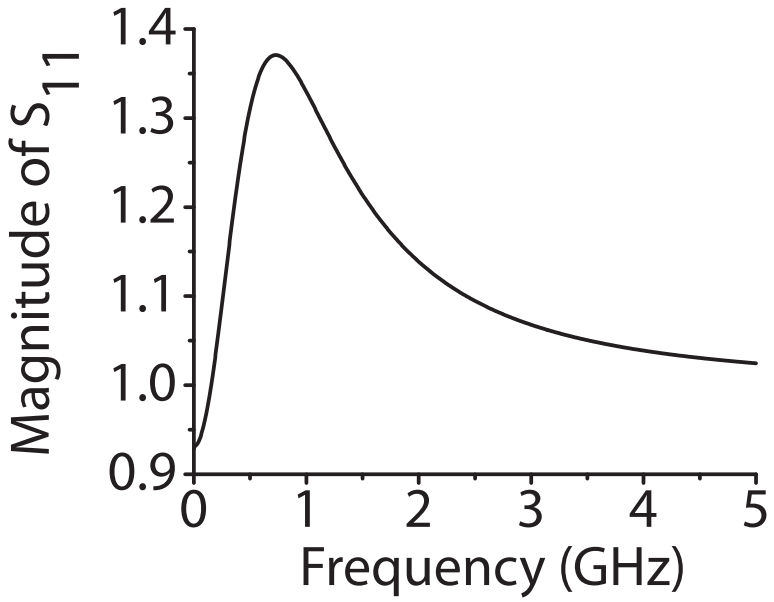

Figure 4.11: The magnitude of reflection coefficient S_{11} of the NDR circuit.

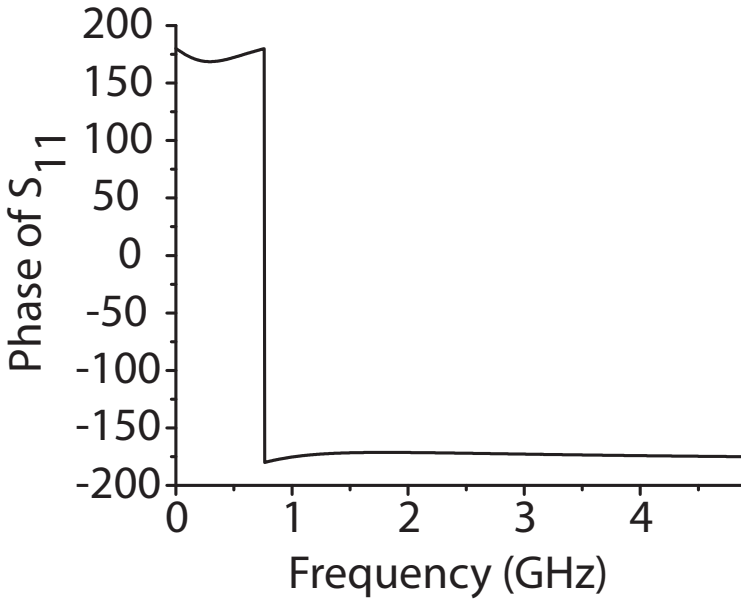

Figure 4.12: The phase of reflection coefficient S_{11} of the NDR circuit.

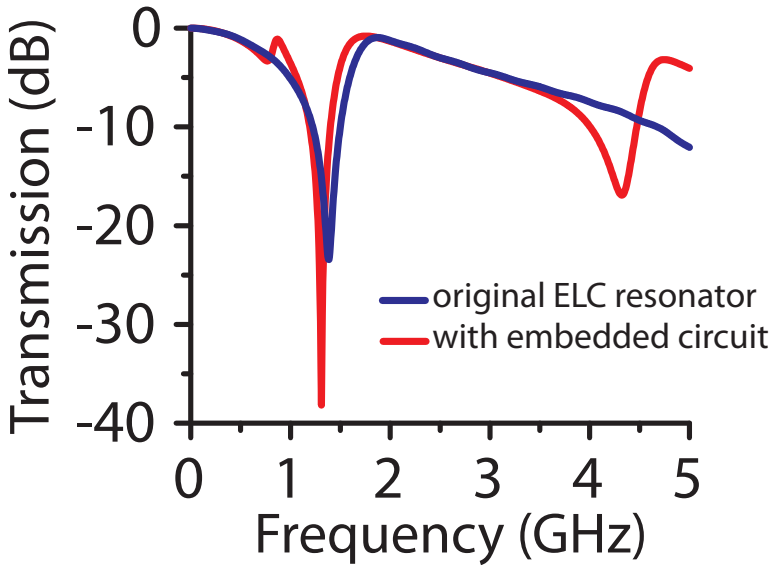

Figure 4.13: transmission of the original ELC resonator (blue curve) and the ELC resonator embedded with the active loss compensation circuit (red curve)

As shown in Fig. 4.13, the transmission of the ELC resonator is improved from -23dB to -39dB at the resonant frequency by embedding the NDR circuit into the central slit in the ELC resonator. This proves that the embedded NDR circuit has compensated for the losses of the ELC resonator at the resonant frequency effectively.

4.5 Effective electromagnetic parameter retrieval of metamaterials

In section 4.4, the transmission of the ELC resonator with and without embedded NDR circuit is simulated. However, transmission is not the best parameter to characterize the electromagnetic property of any homogeneous material. Instead, frequency dependent complex ϵ and frequency dependent complex μ are standard parameters to characterize electromagnetic property of homogeneous material. However, metamaterials are essentially inhomogeneous

because they are composed of periodic metallic inclusions in dielectric materials. Technically speaking, we cannot apply the macroscopic form of Maxwell's equations on the inhomogeneous materials and solve it to get the electromagnetic properties of the entire material slab (69). The relations between electric field, magnetic field, charge and current distribution vary across the inhomogeneous material (69). We have to solve the Maxwell's equation for each local part to obtain a distributed electromagnetic properties (69).

However, we can simplify our calculation and solve the macroscopic Maxwell's equation for the entire metamaterial if we assume that all the unit cells have the same response to the incident electromagnetic wave, the applied electric and magnetic field are static and the coupling between the neighboring cells are negligible (70). Therefore, the metamaterials are replaced by equivalent homogeneous materials with the same thickness in our analysis, which are called effective media (71). This method of simplification is called *imhomogenization* process, which is essentially averaging (69). It is noted in (72) that this assumption is valid beyond the effective medium theory limit and even to the point where meta-particle's size is on the same order of magnitude as the free space wavelength (72).

One way to verify the equivalence between the metamaterials and the homogeneous effective medium is to show there is no or little difference in the scattered waves that transmit through and reflect back from them (69). The scattering properties of materials are characterized by S parameters. Let us assume that there are two waveguide ports placed on the left-hand and right-hand side of metamaterial slab, which is illustrated in Fig. 4.14 (69). If port 1 excites EM radiation onto metamaterial slab and port 2 receives the EM wave propagating through the metamaterial slab, then we can define S_{21} and S_{11}. The latter number 1 in the subscript denotes that the source port is port 1. S_{21}, which is called transmission, denotes the ratio between the power of the transmitted wave and that of the incident wave. S_{11},

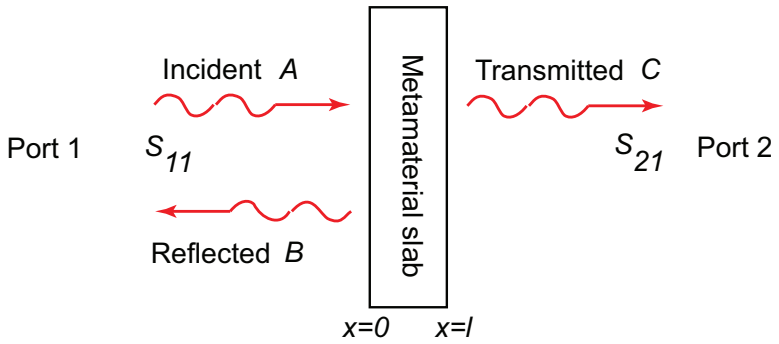

Figure 4.14: Definition of S_{11} and S_{21} in terms of scattering characteristics of a metamaterial slab. Its thickness is l. (69)

which is called reflection, represents the ratio between the power of reflected wave and that of the incident wave. The definitions of S_{21} and S_{11} are illustrated graphically in Fig. 4.14 (69).

Let us assume that the incident wave, which comes from source port 1, has the power of A, the reflected wave, which is reflected by the metamaterial slab and propagate towards source port 1, has the power of B and the power of the transmitted wave is C. Then S_{21} and S_{11} are

$$S_{11} = \frac{B}{A} \tag{4.1}$$

$$S_{21} = \frac{C}{A} \tag{4.2}$$

In order to obtain all the information about the scattering properties of the metamaterial slab, we should move the excitation source such as a waveguide port to the right hand side of metamaterial slab and calculate the transmission and reflection coefficient again because metamaterials are composed of multiple layer and are asymmetric. This time port 2 excites

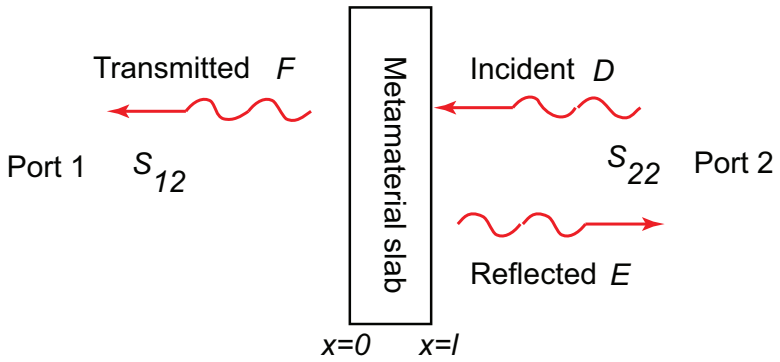

Figure 4.15: Definition of S_{22} and S_{12} in terms of the scattering characteristics of a metamaterial slab. Its thickness is l. (69)

EM radiation onto metamaterial slab and port 1 receives the EM wave propagating through the metamaterial slab, then we can define S_{12} and S_{22}. The latter number 2 in the subscript denotes that the source port is port 2. The diagram of this definition is illustrated in Fig. 4.15.

In Fig. 4.15, the excitation source such as a waveguide port is located port 2. Let us assume that the incident power, which is excited by source port 2 and propagates towards the metamaterial slab, has the power of D. The reflected wave, which is bounced back from metamaterial slab and propagates towards source port 2, has the power of E. The power of the transmitted wave is F. Then S_{22} and S_{12} are

$$S_{22} = \frac{E}{D} \tag{4.3}$$

$$S_{12} = \frac{F}{D} \tag{4.4}$$

These 4 S parameters can be acquired from numerical simulation or measurement. They have been used to characterize the unknown material in the EM measurement decades ago

and have become a standard method since then (73, 74).

The transmission coefficient T has the following relation with the S_{21} (75):

$$S_{12} = Te^{ik_0 l} \tag{4.5}$$

where "k_0 is the wavenumber of incident wave in free space and l is the thickness of metamaterial slab" (75).

The relation between the electric and magnetic field at Port 1 and 2 in Fig. 4.14 and 4.15 can be described by a transfer matrix $\mathbf{T}$ as follows (76):

$$\begin{pmatrix} E_1 \\ H_1 \end{pmatrix} = \mathbf{T} \begin{pmatrix} E_2 \\ H_2 \end{pmatrix}$$

E_1, H_1 are "the amplitude of complex electric field and magnetic field at port 1, respectively". E_2, H_2 are "the amplitude of complex electric field and magnetic field at port 2, respectively" (69). The transfer matrix $\mathbf{T}$ is given by the formula (69):

$$\mathbf{T} = \begin{pmatrix} cos(nkl) & -\frac{z}{k}sin(nkl) \\ \frac{k}{z}sin(nkl) & cos(nkl) \end{pmatrix}$$

where z is the impedance of effective medium and n is the index of refraction of the effective media (69). The relation between z, n and ϵ μ are described in the following formulas (11):

$$n = \epsilon z \tag{4.6}$$

$$n = \frac{\mu}{z} \tag{4.7}$$

The relation between the transfer matrix **T** and the S parameter matrix is governed by the following formulas (69, 77):

$$S_{21} = \frac{2}{T_{11} + T_{22} + (ikT_{12} + \frac{T_{21}}{ik})} \tag{4.8}$$

$$S_{11} = \frac{T_{11} - T_{22} + (ikT_{12} - \frac{T_{21}}{ik})}{T_{11} + T_{22} + (ikT_{12} + \frac{T_{21}}{ik})} \tag{4.9}$$

$$S_{22} = \frac{T_{22} - T_{11} + (ikT_{12} - \frac{T_{21}}{ik})}{T_{11} + T_{22} + (ikT_{12} + \frac{T_{21}}{ik})} \tag{4.10}$$

$$S_{12} = \frac{2}{T_{11} + T_{22} + (ikT_{12} + \frac{T_{21}}{ik})} \tag{4.11}$$

By substituting the transfer matrix equation into these equations, we get (69)

$$n = \frac{1}{kl} cos^{-1}[\frac{1}{2S_{21}}(1 - S_{11}^2 + S_{21}^2)] \tag{4.12}$$

$$z = \sqrt{\frac{(1 + S_{11})^2 - S_{21}^2}{(1 - S_{11})^2 - S_{21}^2}} \tag{4.13}$$

$$\epsilon = \frac{n}{z} \tag{4.14}$$

$$\mu = nz \tag{4.15}$$

Therefore, we can calculate the value of ϵ and μ from the S parameters, which is readily available through numerical simulation or measurement.

However, there is ambiguity problem in this algorithm arises from the cos^{-1} function in Eq. 4.12 (69). cos^{-1} is a multivalued function (78). For example, in equation (78)

$$cos^{-1}(y) = x \tag{4.16}$$

there are multiple values of y that gives the same value of x: $cos^{-1}(\frac{\pi}{2}) = 0$ and $cos^{-1}(\frac{3\pi}{2}) = 0$ (78). Multiple values of ϵ and μ are obtained from the same S parameters using this algorithm. This ambiguity problem is called branch problem in (69). One solution to resolve this problem is to maintain the smooth continuation of the retrieved ϵ and μ because the other branches of cos^{-1} always show an abrupt change in value compared with the neighboring data points.

We retrieve the effective permittivity $\epsilon = \epsilon' + i \cdot \epsilon''$ of the ELC resonator with and without embedded active NDR circuit using the aforementioned algorithm. The ϵ' and ϵ'' of ELC resonator without embedded NDR circuit is shown in Fig. 4.16. The ϵ' and ϵ'' of ELC resonator embedded with NDR circuit is shown in Fig. 4.17. After the active loss compensation circuit is embedded into the ELC resonator, the resonant peak of both ϵ' and ϵ'' become much sharper. The metric characterizing the sharpness of the resonance is quality factor Q, which is inversely proportional to the losses R. The smaller losses result in higher Q and sharper resonance. After the loss compensation circuit is embedded, the peak value

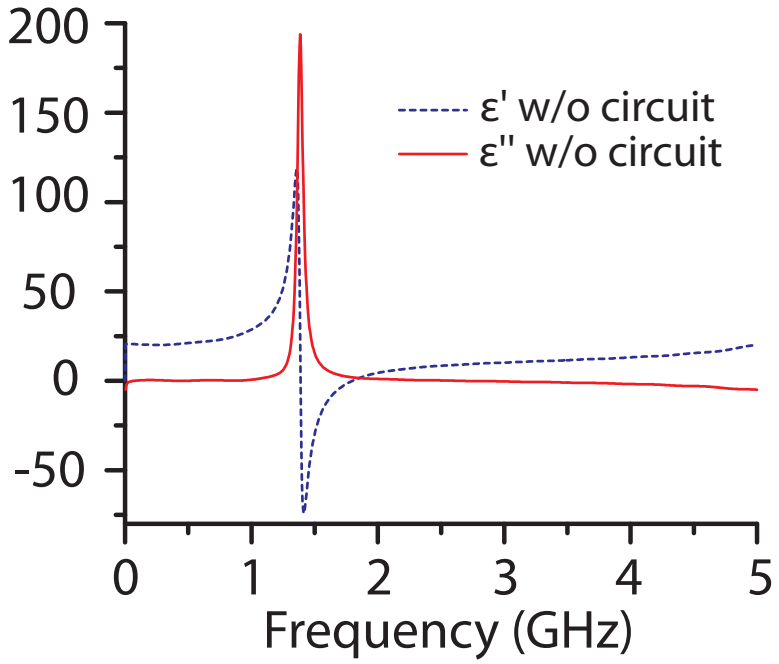

Figure 4.16: The real and imaginary part of permittivity, ϵ' and ϵ'' of original ELC resonator without embedded active loss compensation circuit

of ϵ'' rises from 200 to 900. These changes verify the ability of the embedded NDR circuit to compensate for the losses of the ELC resonator.

4.6 Embedding of NDR circuit into SRR

Now this approach of loss compensation is demonstrated for a class of planar metamaterials based on single-split SRR. The SRR structure couples to both the electric and magnetic field (38) and have been a very popular choice with practical demonstrations of negative permeability (1). Their performance is limited by the ohmic and dielectric losses.

For this work, we implemented SRR with dimensions shown in Fig. 4.18. The metallic split ring is made of 1.4 mil thick copper (1 mil=0.00254 cm). The dielectric substrate is a 62 mil FR4 substrate. The real part of its permittivity is 4.8 and the loss tangent is 0.027 at

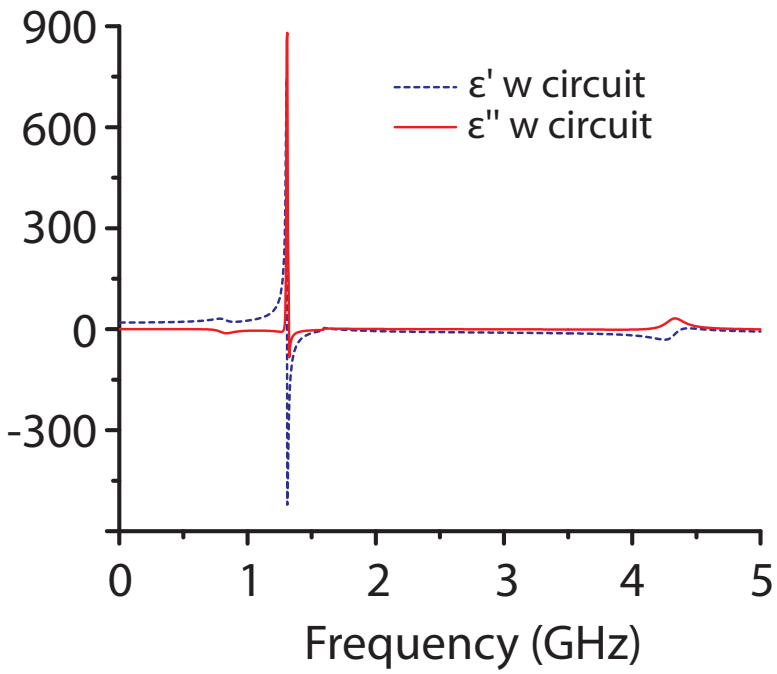

Figure 4.17: The real and imaginary part of permittivity, ϵ' and ϵ'' of ELC resonator with embedded active loss compensation circuit, ϵ'' become negative when the active loss compensation circuit is embedded

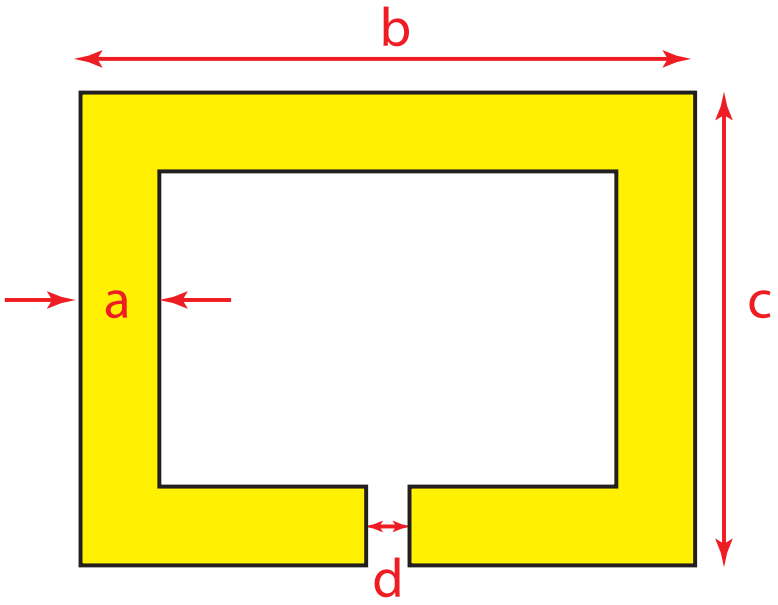

Figure 4.18: Dimension of SRR in the test. All units are in millimeter. a=2, b=16, c=12, d=1.5

2GHz. The equivalent circuit model of SRR can be characterized at the gap of the SRR by measuring the reflection coefficient. The SRR was simulated using Microwave Studio by CST. For experimental verification, SRR was excited by the loop antenna (79), which is discussed later.

We embed the NDR circuit in the existing gap where electric field is maximum.

The implementation of the NDR circuit and its connection to the SRR is shown in Fig. 4.19. The circuit is similar to Fig. 4.9. It consists of just 3 transistors, 2 resistors and 2 inductors. In principle, this circuit is a cross-coupled transistor pair consisting of Q1 and Q2, Lc is a high Q inductor and Rc is a resistor to bias the transistors Q1 and Q2. Q3 is a current sink whose current can be tuned by its gate voltage V_{bias}. In our implementation, Q1, Q2 and Q3 were discrete pseudomorphic HEMT (pHEMT) and could also have been Metal Oxide Semiconductor Field Effect Transistors (MOSFET) or Bipolar Junction Transistors (BJT).

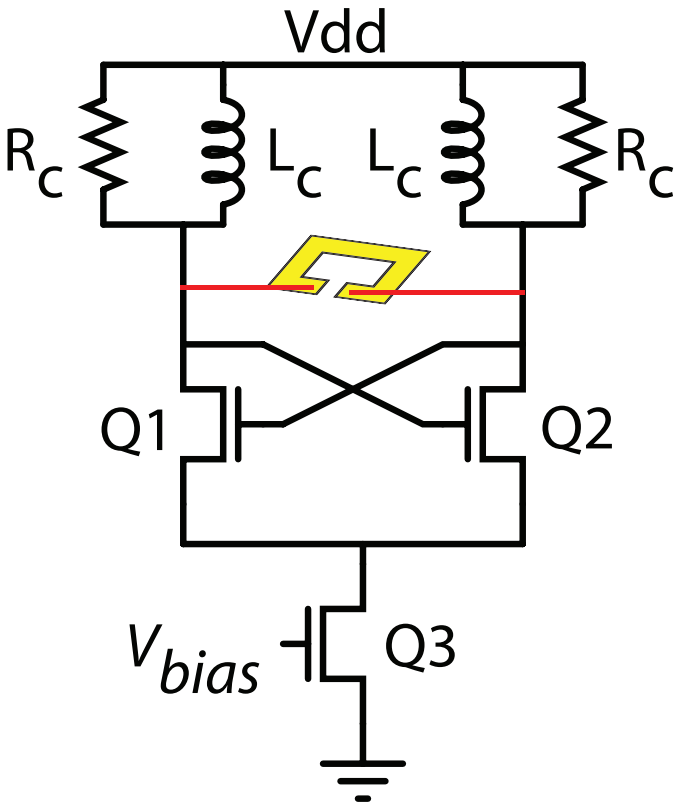

Figure 4.19: Implementation of active negative differential resistance circuit and its connection to SRR.

The active NDR circuit can be regarded as a one-port network looking into the drains of transistor Q1 and Q2 and connected across the gap of the SRR. When appropriately biased, the circuitry imparts NDR to small signal variations across the gap, equal and opposite in polarity to the loss R. The negative impedance imparted by this cross-coupled NDR circuitry can be approximated by $-\frac{2}{g_m}$, where g_m is the small-signal transconductance of Q1 or Q2 and is related to their aspect ratio and bias current (68). We can tune the NDR by changing the aspect ratio of transistors during the design phase or by tuning the bias voltage of current sink Q3. The active NDR circuit also provides a reactive component for the SRR, whose value can be tuned by changing Lc in Fig. 4.19.

The SRR is simulated alone in the CST microwave studio to obtain the reflection coefficient

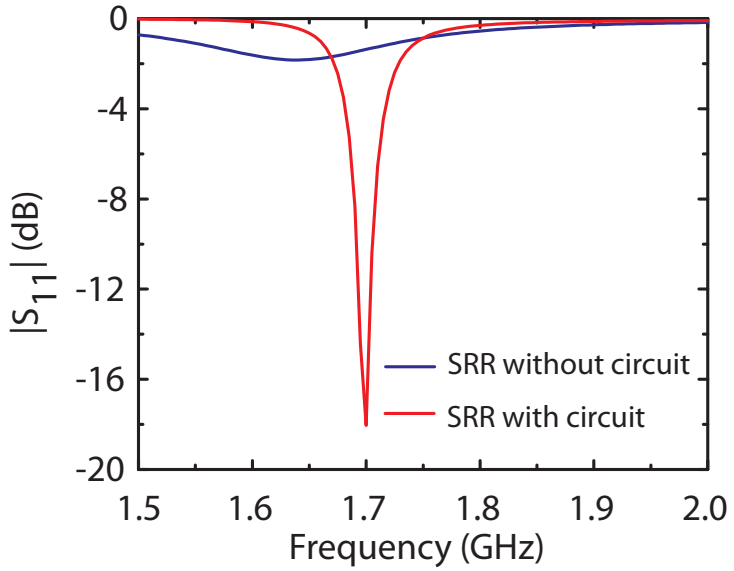

Figure 4.20: Simulated $|S_{11}|$ in dB of SRR with and without active loss compensation circuit

S_{33} at its gap. Then the NDR circuit is simulated in Agilent ADS and the reflection coefficient between the drains of Q1 and Q2 in Fig. 4.19 is obtained. The next step is to import the reflection coefficient of the NDR circuit into the CST microwave studio and run an EM-circuit co-simulation. The reflection $|S_{11}|$ of SRR is acquired and shown in Fig. 4.20. In Fig. 4.20, the reflection $|S_{11}|$ is -2dB for the SRR without active circuit at the resonant frequency of 1.68GHz and -18dB for the SRR with active circuit at the slightly shifted resonant frequency of 1.7GHz. The slight frequency shift is due to process variations and parasitics of Q1 and Q2, which can be incorporated by pre-embedding the parasitics during the design phase. This issue may be exacerbated at higher frequencies where more than one iteration may be needed to correct for parasitics.

One of the important design considerations is the stability of the closed loop system formed by the SRR metamaterial and the active NDR circuit. Based on the well-known Barkhausen's stability criteria for oscillations in linear electronic circuits, the proposed network with SRR

and NDR circuit will not oscillate, i.e. it is stable, as long as the net resistance across the SRR remains positive. However, since we also expect the net resistance to be close to zero for perfect loss compensation, one needs to provide enough margin to account for component tolerances and temperature variations. The proposed circuit provides a convenient mechanism to adjust the negative resistance across the SRR given by $-\frac{2}{g_m}$ and also the margin for stability, by tuning the current I with the cross coupled transistor pair, through V_{bias} control of Q3 in Fig. 4.19; the g_m is a function of operating point of a transistor (I, V_g), where I is the current and V_g is the gate voltage (68).

4.6.1 Measurement

Next we provide measurement results for loss compensation in SRR. For the SRR shown in Fig. 4.19, the resonance frequency is measured around 1.7 GHz. The circuit topology of the loss compensation circuit is shown in Fig. 4.19. Q1, Q2 and Q3 are implemented using Avago ATF-54143 low noise enhancement mode pHEMT transistors in a surface mount plastic package. Lc is a high-Q 1nH surface mount inductors. Rc is a surface mount 100Ω resistor. We intentionally added more loss by introducing 2 surface mount 1Ω resistors in series at two ends of the SRR to test how much loss our NDR circuit can compensate. It is like a worst case scenario test. The loss of bulk metamaterials and 3D metamaterials, which are the realistic applications of SRRs, is much larger than the loss in this thin planar single unit cell SRR. Another example is that people are using a multiple turn coil in each material unit cell in order to reduce the dimension of each unit cell, which increases the resistance of the coil and unit cell greatly (58, 80). It is like a worst case scenario test.

Excitation was provided using a loop antenna as proposed in (79). We made the loop antenna with tinned copper wire, slightly larger than the SRR and placed at a distance of 2 mm over

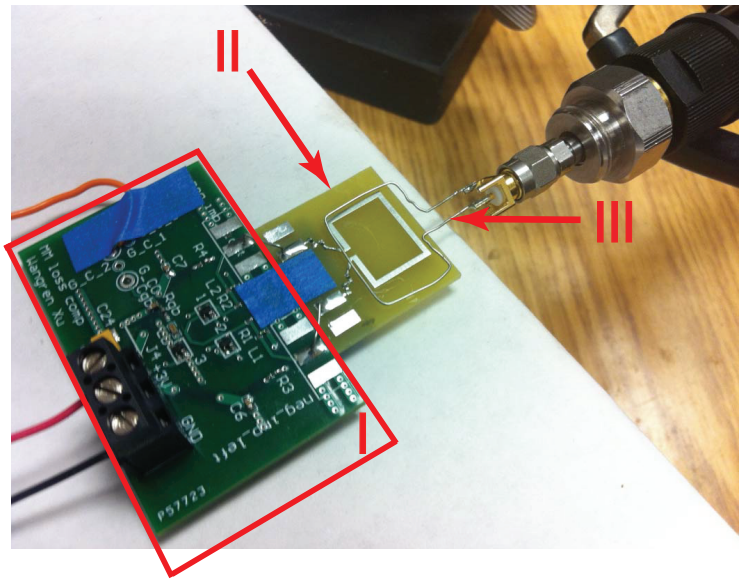

Figure 4.21: Measurement setup to measure the reflection. Area I shows the active NDR circuit implemented on the printed circuit board. Area II shows the SRR. Area III shows the loop antenna. The circuit in area I could be integrated into single chip in future, with dimensions much smaller than the size of each unit cell.

the SRR. Measurements were taken with vector network analyzer Agilent HP8510C. The loop antenna has a self-resonant frequency at 3.9 GHz, much higher than the expected metamaterial resonance. The SRR with loss compensation circuitry is mounted underneath the loop antenna and an expected resonance at around 1.7GHz in $|S_{11}|$ is measured. The bias voltage V_{bias} of the current sink Q3 of the active NDR circuit is set to two values, which are 0V (no loss compensation) and 0.350V (maximum loss compensation). The current in the active circuit is measured to be just 3.6mA when V_{bias} is set to 0.350V. The measurement setup is shown in Fig. 4.21.

The measurement results in Fig. 4.22 show that resonance strength has been improved from -8dB to -32dB, which also agrees well with simulation in Fig. 4.20. Our NDR circuit makes marked improvement of $|S_{11}|$ of the SRR with added large loss in the measurement, which demonstrates that our NDR circuit is robust and has the ability to compensate for larger

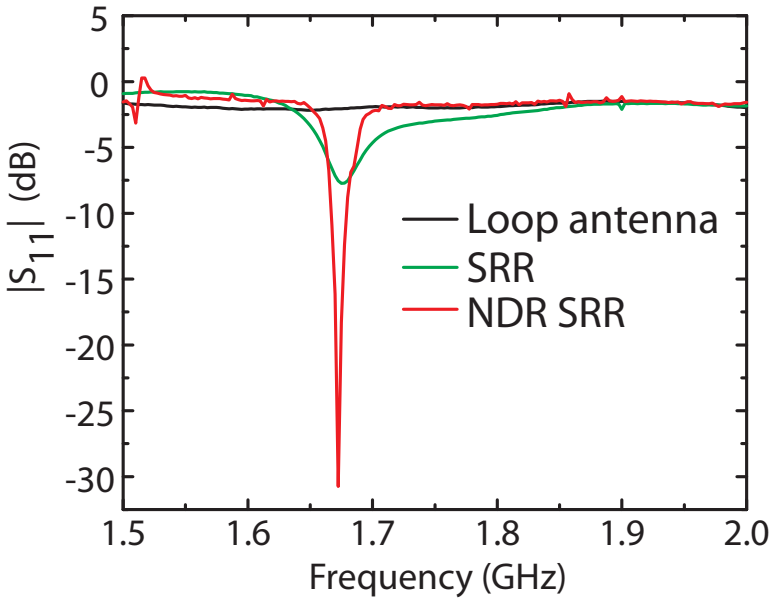

Figure 4.22: Measured $|S_{11}|$ in dB of loop antenna by itself and SRR with and without embedded active NDR circuit. When the bias voltage V_{bias} is set to 0.350V, the current flowing in the active circuit is 3.6mA. The DC power supply voltage is 3.1V.

losses in metamaterials. The resonant frequency was shifted slightly because of the parasitics of the active and passive components. Experiments confirm that the network becomes unstable if V_{bias} is increased further; increasing g_m increases the negative conductance and causes self-oscillations. One could easily tune V_{bias} real-time to ensure stability.

The auxiliary 2Ω resistors in series with the SRR are taken out, the NDR circuit is slightly adjusted and the measurement of the $|S_{11}|$ is conducted again. The result is shown in Fig. 4.23. As expected, the SRR without auxiliary 2Ω resistors has stronger resonance due to the smaller losses. The NDR can improve the resonance of realistic SRR better than that of the SRR with auxiliary 2Ω resistors, which add a large loss to the realistic SRR.

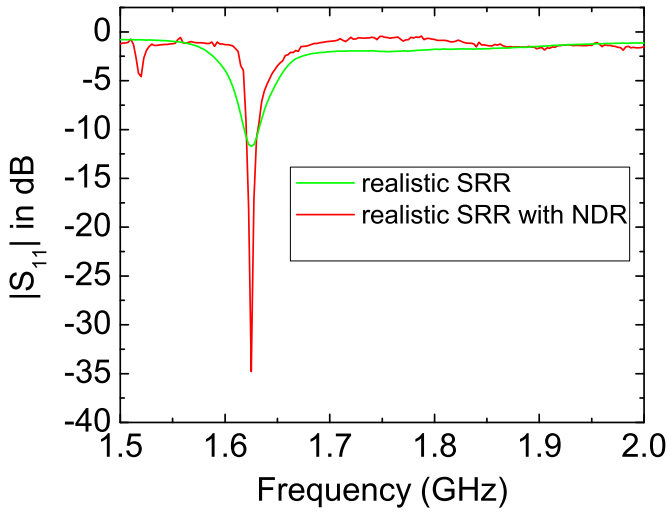

Figure 4.23: Measured $|S_{11}|$ in dB of SRR with and without embedded active NDR circuit after the auxiliary 2 Ohm resistors are removed.

4.6.2 Effective permeability retrieval of SRR embedded with NDR

We also retrieved the effective permeability of the SRR simulated with plain wave excitation in CST using the electromagnetic parameter retrieval algorithm explained in section 4.5.

The equations used to retrieve the effective permeability (69) are

$$\mu = [\frac{(1+S_{11})^2 - S_{21}^2}{(1-S_{11})^2 - S_{21}^2}]^{1/2} \times \frac{1}{kd} \arccos[\frac{1}{2S_{21}}(1 - S_{11}^2 + S_{21}^2)] \tag{4.17}$$

where d is the thickness of the slab (18 mm), k is the wave number of the incident wave, S_{11} is the reflection coefficient and S_{21} is related to the transmission coefficient T by $S_{21} = T\exp(ikd)$ (75).

The extracted permeability of original SRR and SRR embedded with loss compensation circuit are shown in Fig. 4.24. We used the Lorentz oscillator model, which are shown in dashed lines in Fig. 4.24, to fit the curve of extracted μ. The equation of Lorentz oscillator model is

$$\mu = 1 + \frac{\omega_p^2}{\omega_0^2 - \omega^2 - i\gamma\omega} \tag{4.18}$$

, in which ω_p is the plasma frequency, ω_0 is the resonance frequency and γ is the damping parameter. The quality factor Q is defined as

$$Q = \frac{\omega_0}{\gamma} \tag{4.19}$$

We calculated the Q of the SRR based on the Lorentz model. The Q of the SRR is increased by 401.3% when the loss compensation circuit is embedded into SRR. Metamaterial arrays designed using this unit cell with NDR circuitry will also exhibit loss compensated response.

4.7 Summary

In conclusion, a method of loss compensation in metamaterials through embedding of active transistor based NDR circuit directly into each metamaterial unit cell is provided. This approach is valid for any metamaterial construct that are based on patterned metallic in-

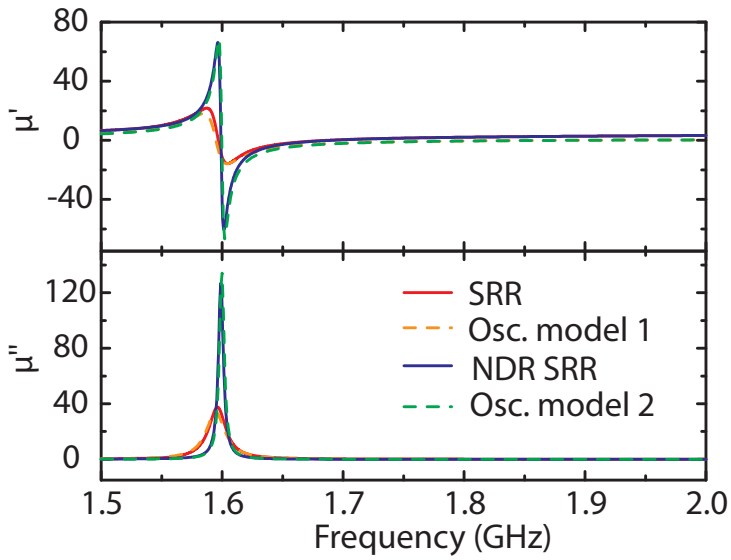

Figure 4.24: Retrieved complex permeability $\mu = \mu' + i \cdot \mu''$ of SRR excited by plane wave and their Lorentz oscillation model. Osc. model 1 is the Lorentz oscillator model used to fit the μ curve of SRR without NDR circuit. Osc. model 2 is the Lorentz oscillator model used to fit the μ curve of SRR embedded with the NDR circuit.

clusions in the dielectric medium. Because of the negligible size of the embedded circuit, it does not interfere the EM response of the metamaterial. It was also shown that the NDR value can be tuned off-chip and this will allow one to guarantee stability of the circuitry and also accommodate for any process and environmental variations. The resonance frequency of the metamaterial can also be tuned through additional on chip varactors in the active NDR circuit. As semiconductor technology scales to nanometer dimensions, the proposed electronic method for loss compensation can be utilized in metamaterials from RF to terahertz frequencies. Since continued transistor scaling also comes with reduced power consumption, the overall power consumption for loss compensation circuits will be amenable for practical implementations. This approach can be combined with current approaches based on gain medium that have only been applied at infrared and visible frequencies to achieve loss compensation in metamaterials over a broad frequency range. The proposed loss compensation can be used in bulk metamaterials to make ideal absorbers, cloaks, perfect lens, modulators, phase shifters, etc. with applications in radar imaging, cellular mobile communications, satellite communications, antennas and security screening.

5

Experimental Realization of a Metamaterial Detector Focal Plane Array

5.1 Background

Microwave imaging and millimeter wave imaging have been used widely in air defense, surveillance, non-destructive inspections and astronomical systems (81, 82). Microwave imaging systems working below 30 GHz has been used for decades for remote sensing and radio astronomy, but they usually employ apertures of several meters (83). This raises a big issue when it is desirable to pack a large number of antennas and receivers into a small focal plane

region. The other problem of the conventional microwave focal plane array is the mutual coupling between neighboring pixels when they are placed close to each other to increase the resolution of the image (84, 85, 86). Another challenging problem of microwave imaging system is how to increase the power transfer efficiency from free space radiation to the input of the receiver. An imaging system with higher power transfer efficiency can detect weaker incident EM radiation.

One of the most important features of metamaterials is its sub-wavelength unit cells. The compact size of the metamaterial unit cells can be utilized to reduce the volume of the microwave imaging system. A large number of metamaterials unit cells can be readily integrated with receivers in a small focal plane region. Metamaterial absorbers (MMA) features high absorption of incident EM wave energy(87). In MMA, the majority of incident electromagnetic energy is focused in the metamaterial gap and converted to dielectric and / or ohmic loss (88). Here, however, the metamaterial perfect absorber can be utilized to guide the electromagnetic radiation to a receiver detection circuit and thus measure incident microwave power. The strong power absorption ability improves the power transfer efficiency from free space to detector. The electrically coupled LC resonator (ELC) resonators (38) are employed as the sensing element in each pixel to reduce the mutual coupling between the adjacent pixels .

In this chapter, a metamaterial absorber array (MMA) that operates as a detector array of microwave radiation is presented. The theory, implementation, and characterization of conventional MMA are elaborated in the following section before presenting the MMA based microwave detector.

5.2 Metamaterial absorber (MMA)

5.2.1 Electromagnetic wave absorber

Due to burgeoning wireless personal communication industry, there are much more undesired electromagnetic (EM) wave radiation in the environment than decades ago that disturbs electronic devices, circuits and systems. This problem is called electromagnetic interference (EMI) and has garnered growing concerns and interests because EMI degrades the performance of electronic systems severely. For example, EMI increases clutter on radar, gives rise to total loss of data in the communication (89) and causes the medical implanted devices, such as pacemakers, to malfunction (90). That is why the wireless personal communication devices are not allowed in either the airplane when it is taking off or landing or the hospital where a lot of implanted medical devices are vulnerable to EMI (89). One approach to reduce or suppress EMI is to use EM wave absorbers to absorb the undesired EMI signal (89). EM wave absorber is the type of device that allow the incident radiation to be reflected or transmitted through over a broad frequency band except one frequency, which is called the operating frequency. At the operating frequency of the absorber, all the incident EM wave is absorbed and dissipated in some form in the absorber. There has been a lot of research efforts about developing EM wave absorbers since 1970's (91). One of the most important application of EM wave absorbers is to reduce radar cross section (RCS) so that the radar signal bounced back by the targeted object is reduced and the targeted object becomes invisible to the radar (92). Absorbers are also used in wireless communication (93), thermal imagers (94) and solar cells (95).

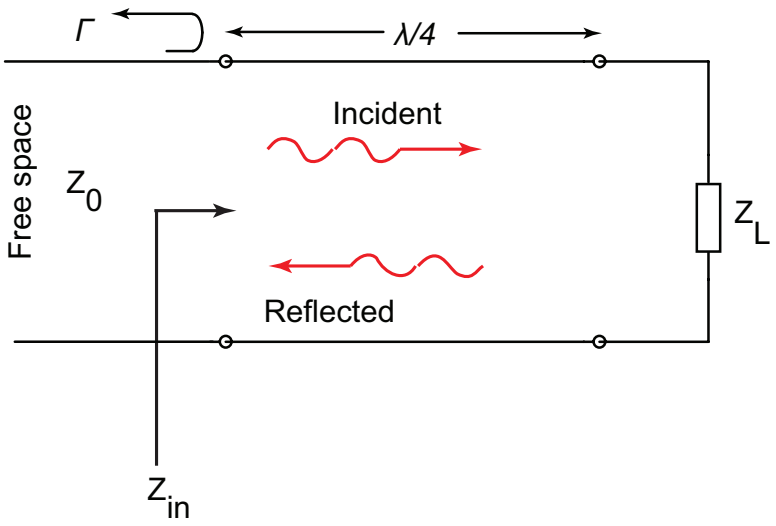

Figure 5.1: Quarter-wave transformer (77)

In the literature, we can find two groups of EM absorber, namely, broadband absorber and resonant absorber (96). Broadband absorbers rely on the unique properties of the materials that they are composed of to absorb the incident radiation over a broad frequency spectrum (91). They do not have frequency selectivity. In contrast to broadband absorbers, resonant absorbers have very high frequency selectivity and absorb incident EM wave only at the resonant frequency where they have strong interaction with the the incident radiation (91).

The early versions of resonant absorbers such as Salisbury screen utilized the quarter-wave transformer to convert the impedance of a metal plate, which is zero, to infinity (97). A resistive sheet with surface resistance of 377Ω is then placed on top of the quarter-wave transformer to match that of the free space so that all the incident EM radiation is absorbed (97). The quarter-wave transformer used in these early designs are lossless dielectrics with the thickness of quarter wavelength. Theoretically, the quarter-wave transformer can convert any load impedance to the free space impedance as explained in the Fig. 5.1 (77)

In Fig. 5.1, the free space is modeled as a feed line with the characteristic impedance of

$$Z_0 = 377\Omega \tag{5.1}$$

The load impedance Z_L is given by the load of the Quarter-wave transformer. Quarter-wave transformer is modeled as a lossless transmission line which is $\lambda/4$ long. Its characteristic impedance is Z_1, which is unknown.

The goal is to make the impedance at the input of the quarter-wave transformer, which is denoted as Z_{in}, to be the same as characteristic impedance of free space Z_0. So the reflection coefficient Γ at the input of the transformer becomes zero.

The transmission line theory gives (77):

$$Z_{in} = Z_1 \frac{Z_L + jZ_1 tan(\beta\ l)}{Z_1 + jZ_L tan(\beta\ l)} \tag{5.2}$$

where $\beta\ l$ is the electrical length, which is $\frac{\pi}{2}$ for the quarter wavelength transmission line. So, we can obtain(77) :

$$Z_{in} = \frac{Z_1^2}{Z_L} \tag{5.3}$$

If we tune the quarter-wave transformer and make its impedance to be (77):

$$Z_1 = \sqrt{Z_0 Z_L} \tag{5.4}$$

Then we'll obtain

$$Z_{in} = Z_0 \tag{5.5}$$

$$\Gamma = 0 \tag{5.6}$$

which means all the incident radiation is absorbed by the device.

Broadband absorbers, which are mostly used in anechoic chambers, employ pyramid like structures to guide the incident radiation into the lossy material and dissipate the incident radiation power in the process of guiding (96).

These days EM wave absorbers have found wide applications in wireless communication industry. For example, the burgeoning personal wireless communication devices demand compact antennas with high directivity to save power and reduce the harmful spurious radiation and interference (98). EM wave absorbers can help suppress the undesired spurious

radiation and improves the directivity of antenna (93). However, the biggest drawback of the traditional EM wave absorber is that its thickness has to be at least quarter wavelength, which is prohibitively large for any consumer electronic products. The other problem of the traditional EM wave absorber is that the EM properties of the absorber rely on the properties of the constituent material completely, which limits the design freedom.

5.2.2 Metamaterial perfect absorber

Metamaterials provide new options to build the EM wave absorbers with smaller thickness. Metamaterials exhibit exotic EM properties that arise from the artificially engineered geometry of their unit cell instead of the constituent molecules or atoms (99). Hence, metamaterials offer more design freedom to the EM wave absorber based on metamaterials.

Metamaterials absorbers employ different principle from the quarter-wave transformer used in the traditional resonant absorbers to program their impedance in order to absorb all of the incident EM wave energy (100). The impedance of the metamaterials absorbers $Z(\omega)$ is (100)

$$Z(\omega) = \sqrt{\frac{\mu(\omega)}{\epsilon(\omega)}} \tag{5.7}$$

where $\mu(\omega)$ and $\epsilon(\omega)$ are the complex permeability and permittivity of metamaterial absorbers, respectively (100). By tuning the $\mu(\omega)$ and $\epsilon(\omega)$ independently and then combining them together, we can program its impedance and make it equal to the impedance of the

free space (100).

For example, if an EM wave is impinged onto the SRR shown in Fig. 5.2(a), there will be a magnetic Drude-Lorentz type resonant response in SRR (91). The analytical expression of this magnetic Drude-Lorentz type resonant response is (91)

$$\widetilde{\mu}_r(\omega) = \mu_\infty + \frac{\omega_{p,m}^2}{\omega_{0,m}^2 - \omega^2 - i\gamma_m\omega} \tag{5.8}$$

where $\omega_{p,m}$ is termed plasma frequency, $\omega_{0,m}$ is the resonant frequency of the oscillator, γ_m is the damping frequency and μ_∞ is the static permeability (91).

Similarly, the ELC resonator shown in Fig. 5.3 (a) exhibits an electric Drude-Lorentz type resonant response when an EM wave radiation with polarization shown in Fig. 5.3(b) is impinged onto it (91). The electric Drude-Lorentz type resonant response can be described as (91):

$$\widetilde{\epsilon}_r(\omega) = \epsilon_\infty + \frac{\omega_p^2}{\omega_0^2 - \omega^2 - i\gamma_e\omega} \tag{5.9}$$

where ω_p is termed plasma frequency, ω_0 is termed the resonant frequency of the oscillator, ϵ_∞ is termed static permittivity while γ_e is termed damping frequency (91).

It is possible to obtain both electric and magnetic Drude-Lorentz type resonant response in a

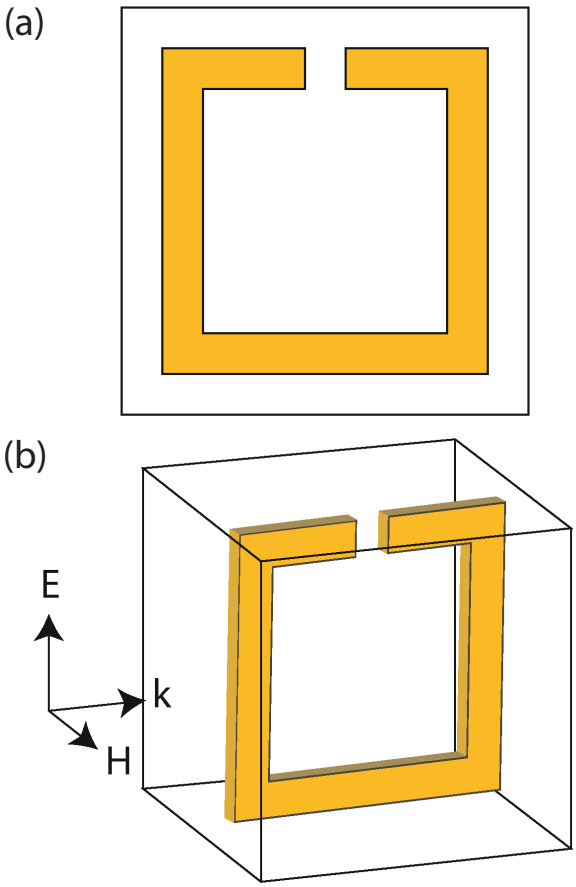

Figure 5.2: SRR (a) and the EM radiation impinged on it (b) (91)

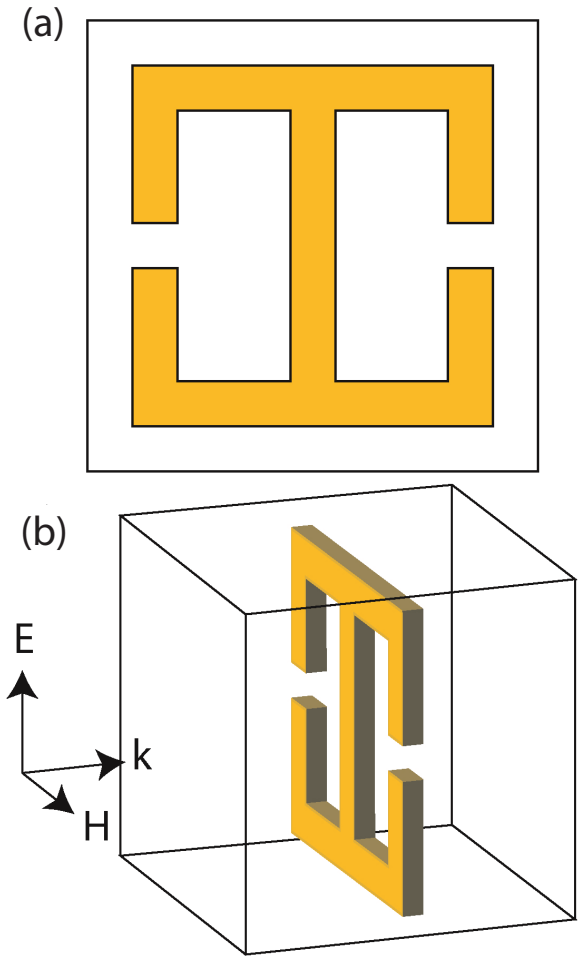

Figure 5.3: ELC resonator (a) and the EM radiation impinged on it (b) (91)

single metamaterial device, which gives us more design freedom. One such example is shown in Fig. 5.4 (91), where a dielectric spacer is sandwiched between the ELC resonator and a metal plate (91). The currents flowing in the ELC resonator and the metal plate underneath the ELC resonator have the same magnitude and opposite direction, which results in the magnetic Drude-Lorentz type resonance (100). When the EM wave is impinged on the ELC resonator with ground plane, the H field of the EM wave induces these currents in the loop formed by the ELC resonator and ground plane (100). The induced effective $\mu(\omega)$ can be tweaked by changing the thickness of the dielectric spacer while the induced effective $\epsilon(\omega)$ can be tuned by changing the geometry of the ELC resonator (91). Thus, we increase the chance to make this metamaterial device's impedance 377Ω, which is the free space impedance, by tuning $\mu(\omega)$ and $\epsilon(\omega)$ separately (100). It provides a much larger degree of freedom in design than the traditional absorbers whose $\mu(\omega)$ and $\epsilon(\omega)$ are dictated by the constitutive dielectric material. For example, it has been proven that metamaterial absorbers can be made ultra-thin in (100, 101).

The first practical metamaterial perfect absorber is reported by Landy *et. al* in (87). It employs split wire instead of the metal plate on the back of the substrate to provide antiparallel current with the ELC resonator on the top (87). The electric Drude-Lorentz type resonant response is still provided by the ELC resonator (87). The structure and dimension of this metamaterial perfect absorber is shown in Fig. 5.5 (87).

The simulated and measured results of this metamaterial absorber (MMA) are shown in Fig. 5.6 (87). The photos of the measurement setup used to characterize it and the fabricated device are also shown in Fig. 5.6 (87). The transmissivity $T(\omega)$ is almost zero in the entire frequency spectrum under observation as we expected (87). The reflectivity $R(\omega)$ is close

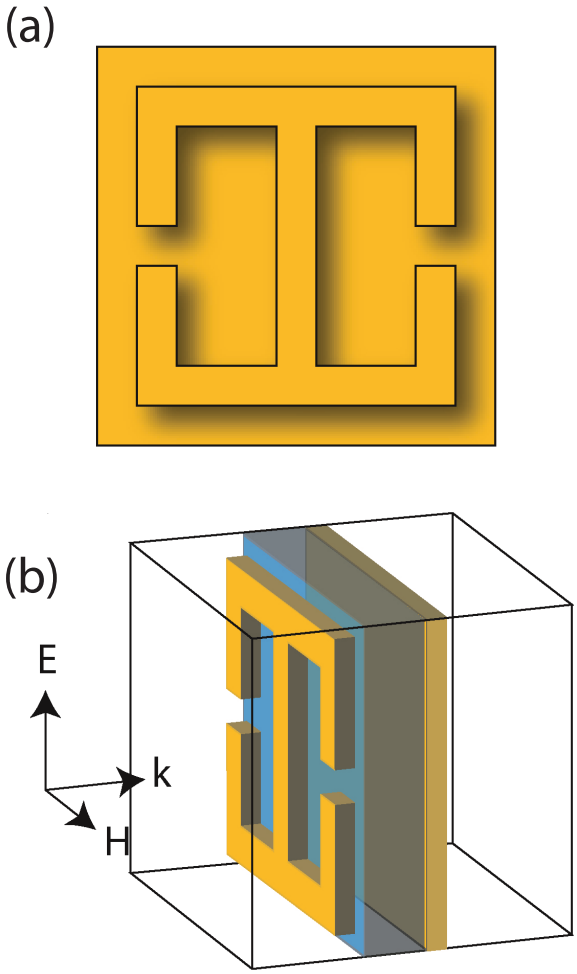

Figure 5.4: ELC resonator with dielectric and ground plane (a) and the EM radiation impinged on it (b) (91)

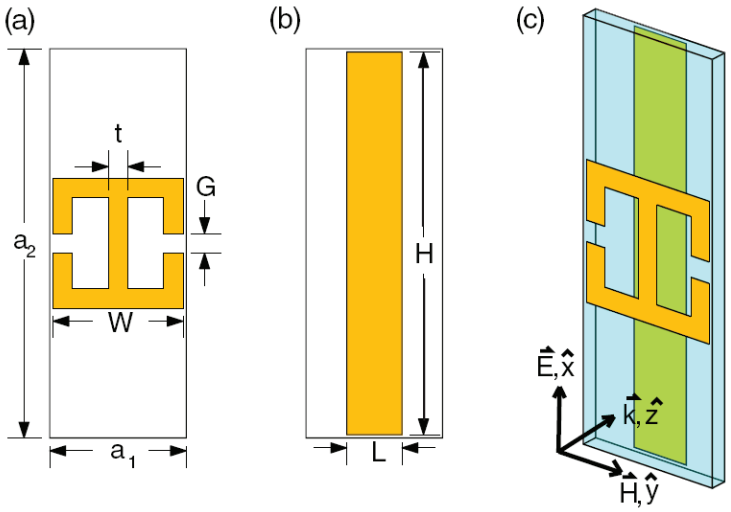

Figure 5.5: Dimensions of the metamaterial absorber (a) Dimension of the ELC resonator, all units in mm, $a_1 = 4.2$, $a_2 = 12$, $W = 4$, $G = 0.6$, $t = 0.6$ (b) dimension of the split wire on the back, $L = 1.7$, $H = 11.8$) (c) polarization of the incident EM wave (87)

to 1 in the entire frequency band of interest except an narrow band around the resonant frequency where reflectivity $R(\omega)$ drops to almost zero (87). Therefore, the absorptivity A is almost 1 in the narrow band around the resonant. The measurement and simulation results prove that the metamaterial absorber can absorb almost all of the incident EM wave power in narrow band around the resonant frequency (87). If we stack multiple MMA, we can improve the absorptivity A to 1 (87), making MMA a perfect absorber (87).

But an interesting question to ask is where does the absorbed EM wave power go? Numerical simulation reveals that the absorbed EM wave power is dissipated as the ohmic and dielectric losses in the metamaterial absorber (87). In this metamaterial absorber shown in Fig. 5.5, the central conducting arm in the ELC resonator is the dominant source of ohmic losses (87). The two gaps in the ELC resonator where the electric field is concentrated are the dominant source of dielectric losses (87). The simulation results to support this conclusion is shown in Fig. 5.7. In Fig. 5.7, the ohmic loss is simulated at the surface of ELC resonator while

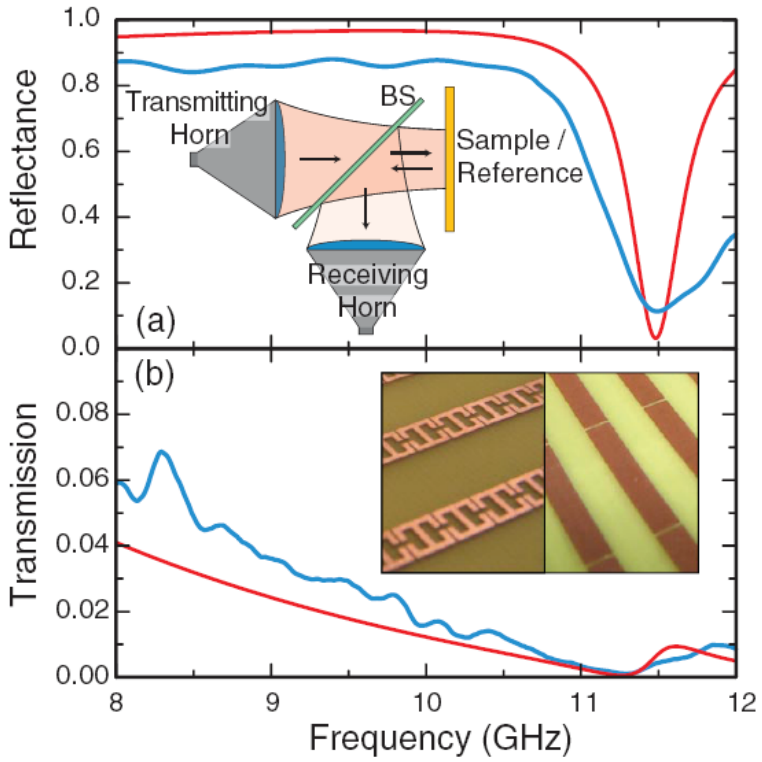

Figure 5.6: Measurement result (shown in blue) and simulation result (shown in red) of transmissivity $T(\omega)$ and reflectivity $R(\omega)$ for the MMA. (a) The inset is the reflection experiment setup where BS is the beam splitter. (b)the inset is the photographs of the both sides of the MMA. (87)

the dielectric loss is simulated for the volume of the MMA including the dielectric spacer in between the ELC resonator and the split wire on the back (87). The numerical investigation also reveals that the dielectric loss is 10 times, or more, as large as the ohmic loss, which means that the majority of the incident EM wave power is converted into dielectric losses in the MMA (87). The analysis of traditional frequency selective surface shows a similar result (102).

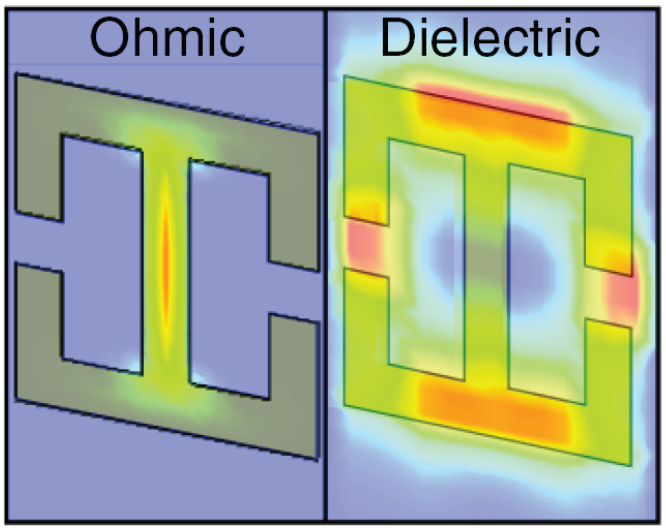

Figure 5.7: Simulation of ohmic and dielectric losses in MMA. (87)

5.3 Metamaterial absorber (MMA) based microwave detector focal plane array

5.3.1 Overview

In the previous section, the ability of metamaterial unit cells to completely absorb incident electromagnetic energy with effectively zero reflected signal is presented. One key design feature afforded by metamaterials is the ability to engineer materials for matching the impedance of the MMA to that of free space. The resonant nature of the MMA structures generates high electric fields in the gap, completely dissipating the incident energy into a combination of dielectric and ohmic losses (100, 103). If we can modify the MMA design in order to instead transfer the incident energy into a detector circuit, then we will improve

the power transfer efficiency from free space to the detector and the detectivity.

An ideal metamaterial detector focal plane array is the one in which all EM wave radiation impinged upon its surface is received and transferred to detector circuit. Detection of the absorbed energy can be accomplished by a number of means and one particular approach undertaken is detailed below.

A metamaterial enhanced single pixel detector for room-temperature detection of gigahertz (GHz) radiation is proposed first. Successful demonstration of a single pixel GHz detector would be an important milestone towards development of a focal plane array detector for active imaging with video frame rate capability. A variety of detection schemes have been compared, keeping in mind what is most easily, rapidly and inexpensively fabricated. Thus initially, one method for thermal detection, rectification of the electrical energy within the metamaterial gap is investigated. This and other various detection methods offer different advantages, and several are considered to determine which is best suited for the goal. Parameters affecting performance of FPA such as: cross talk, polarization dependency, off-angle performance, etc are explored to yield maximum performance.

Detection of electric energy of the trapped electromagnetic field in the metamaterials is demonstrated below. A sensitive circuit is designed and fabricated for detection of electric field generated by each unit cell in a metamaterial perfect absorber in the low gigahertz frequency range. The metamaterial is expected to have a very high-Q at the specified gigahertz frequency of absorption, which should achieve a high signal to noise ratio. The overall detection limit will be restricted by the input referred noise of the detector. Design of the 2 GHz Focal Plane Array (FPA) was performed. The FPA consists of array of square

unit cells of 27.3 mm side length. Metamaterials (MMs) were utilized due to their high Q and subwavelength properties. A conventional ELC resonator unit cell (see Fig. 5.8) was combined with a ground plane in order to generate an impedance matched layer at the target frequency. Each ELC resonator is placed at the center of each pixel and conductive *via*s connects the front ELC resonator layer to a circuit layer on the back side. The MM was computationally designed with commercially available software - Microwave Studio by CST. The objective was to obtain high detectivity at 2 GHz with narrow band response. We also designed a detection circuit which uses a balun to convert the balanced MM output signal into an unbalanced signal. This was followed by an impedance matched circuit to provide both frequency tuning and to sharpen the Q of the EM response. A microwave receiver circuit was implemented to convert the received EM wave signal INto DC signal. We utilized so-called Ultraminiature Coax Connectors (UMCCs) to permit characterization of both the MM response and access for a secondary detection board. The detector board consists of a low noise amplifier (LNA) and radio frequency (RF) detector for DC measurement characterization.

As mentioned, an ELC unit cell was utilized and this has been shown to possess the high Q and sub-wavelength properties necessary for the proposed work. The physical dimensions of the MM (See Fig. 5.8) were designed to be compatible with the tolerances of the printed circuit board (PCB) manufacturing companies, as well as to tune the resonant frequency and bandwidth to meet our objectives. The MM absorber utilized a ground plane for impedance match at the resonant frequency. In this work the MM serves as an electric resonator that concentrates the electric field into its gap at the resonant frequency when EM wave radiation is impinged onto it. The loop formed by the MM and the ground plane produces an effective magnetic response to the incident EM wave radiation. When the optical constants of our

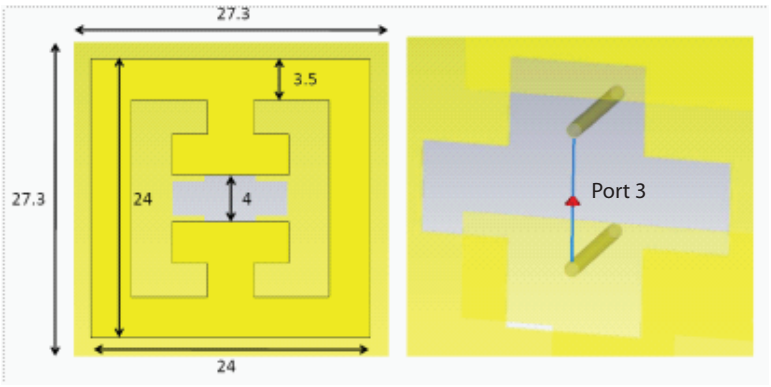

Figure 5.8: The dimensions utilized for the metamaterial absorber design in the FPA, all units in mm. (a)dimension of the MM unit cell and ground plane. MM unit cell is shown in bright yellow and the ground plane is shown in dark yellow. The grey area in the ground plane is an opening to let the *via* holes go through (b)back view. A discrete port called 'port 3' is defined across the end of *via*s.

device and free space are equal, there is an impedance matched condition such that there is zero reflection - implying that all incident radiation flows into the metamaterial unit cell where it may be detected.

5.3.2 Implementation

The metamaterial and the detector circuit was designed to be compatible with the published physical dimensions and tolerances of the manufacturer - Hughes Circuits . The total board consisted of a 11 by 11 MM array (121 total unit cells) which roughly measured a total of 11 inches on a side. This utilized a Rogers 4003 dielectric substrate with one ounce copper metal in a 4 layer standard stack up with board thickness of 0.213". We bypassed the second metal layer to create additional spacing between the MM and ground plane in order to have sufficient distance to couple magnetically at 2 GHz. A cut-through in the ground plane was designed in order to connect the center of the front metamaterial resonator

through to the circuit layer, as depicted in Fig. 5.8. The opening in the ground plane was increased to minimize the coupling between *via*s and ground plane as well as tune the magnetic response. The ground plane also helps to prevent any undesirable coupling effects between the circuit components and the metamaterial electromagnetic response. A 3D view of the system architecture of my metamaterial microwave power detector array is shown in Fig. 5.9(a), where the layers shown from top to bottom are: the ELC resonators, Rogers dielectric spacer, patterned ground plane, and microwave power receiver (circuit layer).

Fig. 5.9(b) shows a photo of a single pixel with dimensions. Fig. 5.9(c) shows a photo of the circuit layer with *vias* indicated.

The material stack up contains three core boards, each with 60 mil thickness of Rogers 4003 dielectric ($\tilde{\varepsilon} = \varepsilon_1 + i\varepsilon_2 = 3.38 + i0.007$), between the MM and the ground plane. Prepreg layers of Rogers 4450f ($\tilde{\varepsilon} = \varepsilon_1 + i\varepsilon_2 = 3.52 + i0.004$) are placed between each pair of core layers as well as between the core and ground plane for adhesion. The circuit layer is separated from the ground plane by two 4 mil sheets of Rogers 4003 dielectric. One ounce copper sheets were used for all metal layers (30.5 μm thick).

The entire unit cell was modeled using a commercial package, CST's Microwave Studio. Materials are modeled using the built-in library values for copper with a DC conductivity equal to 5.8E7 S/m. The real part of the Rogers 4003 dielectric constant was modeled as 3.38 (frequency independent) - obtained from data sheet published by the Rogers Corporation. We utilized the frequency solver to allow access to tetrahedral meshing which discretizes the cylindrically *via*s much more accurately than with other meshing option, i.e. hexahedral meshing. Perfect electric and magnetic boundaries replicate an infinite array. We place a

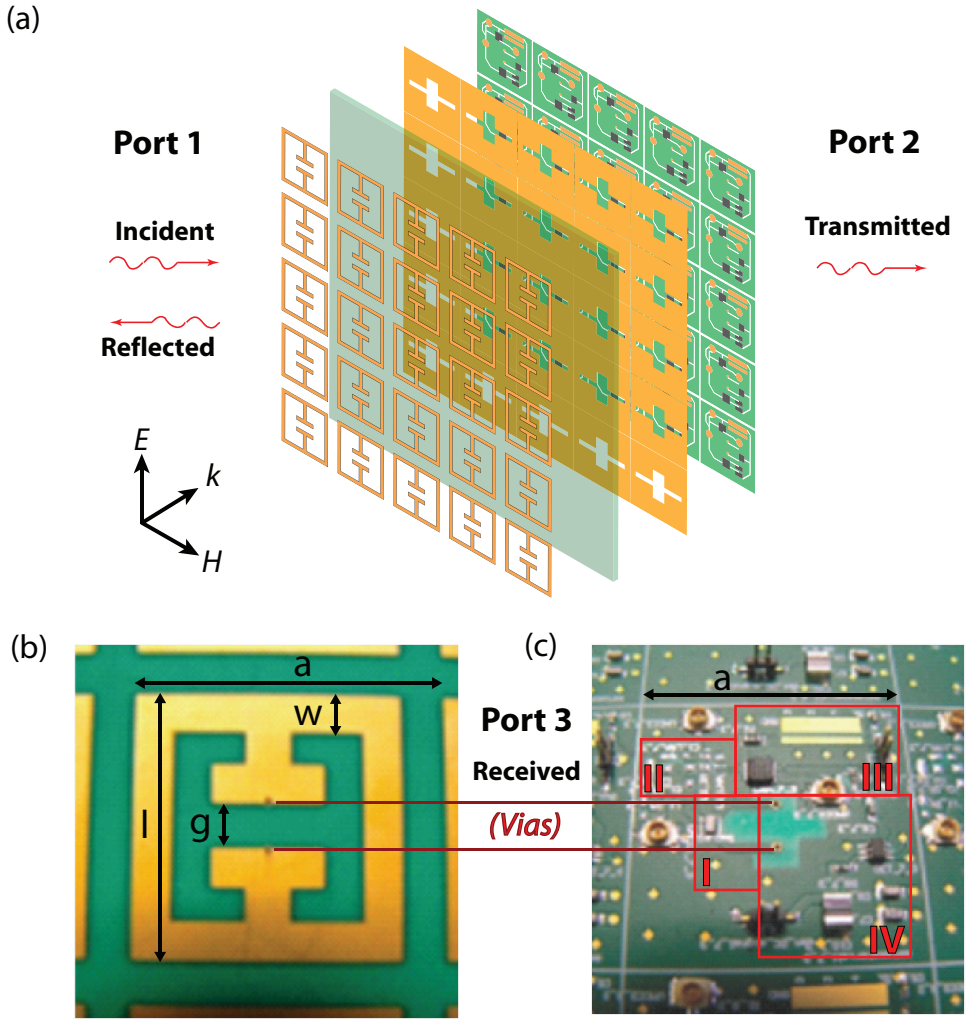

Figure 5.9: System architecture of my metamaterial microwave power detector array. (a) Radiation is incident from port 1 with electric field polarization as depicted. A schematic of the full device is shown (exploded view) and the layers shown from top to bottom are: the ELC, Rogers dielectric spacer, patterned ground plane, and microwave power receiver circuit. (b) Photo of an individual pixel, i.e. an ELC unit cell with dimensions of $a = 27.3$, $l = 24$, $w = 3.5$, and $g = 4$; all in millimeters. (c) Photo of the circuit layer with *vias* indicated. The *vias* transport the received signal (port 3) to the microwave power receiver circuit underneath each unit cell where the different highlighted regions are: (I) balun, (II) impedance matching circuit, (III) low noise amplifier, and IV) microwave power detector.

discrete port (100 Ohms) called port 3 across the ends of *via*s at the back of the device, which is the circuit layer. If we define a pair of discrete ports instead, each of which is defined across the end of each *via* and the edge of cutout opening in the ground plane, then the ground plane would not be a sufficient ground as the cutout opening created for the *via*s to pass through has a significant effect on the impedance between the terminations of the two discrete ports at the ground plane. The single discrete port removed the additional impedance added by the ground plane with cutout opening, which is the specified input impedance into the balun. The cutout opening in the ground plane was shaped as a cross to avoid coupling with the *via*s.

A waveguide port denoted as port 1 is defined to generate a TEM wave for free space characterization. The waveguide port allows for a closer resemblance to experiment as the setup allows for maximizing the transmission from a free space wave to the measured output through the balun.

The metamaterial was configured to maximize the transfer of energy into port 3, i.e. S_{31}, while at the same time minimize both the free space reflection coefficient S_{11} and reflection coefficient S_{33} at 2.0 GHz. We simulated the scattering parameters and the results are shown in Fig. 5.10 over a frequency range of 0 to 4 GHz. We demonstrates that a maximum in transmission S_{31} corresponds with the minima of both reflection coefficients S_{11} and S_{33} at 2.0 GHz. As mentioned, the MMA design typically utilizes the dielectric and ohmic losses within the constituent components in order to achieve a minimum in S_{11}. In contrast, the design presented here achieves S_{31}= 0.986, indicating that over 97% of the incident intensity is transmitted into the detector circuit. By minimizing the reflection coefficient we are able to maximize absorption of incident radiation at the operational frequency.

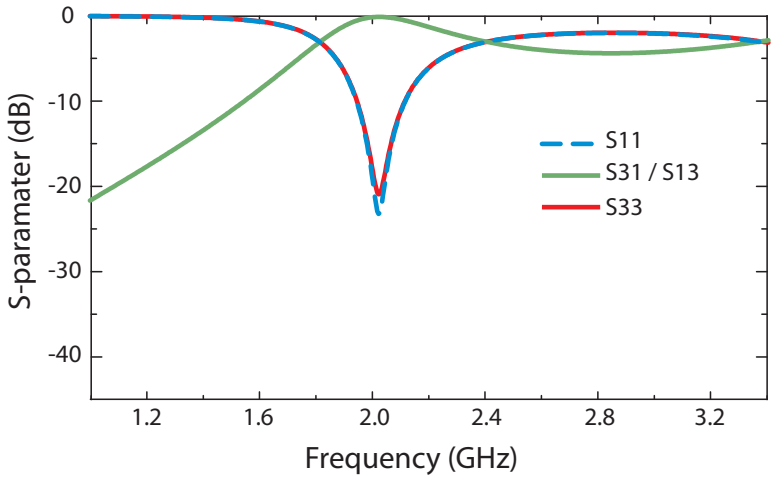

Figure 5.10: Numerical simulations of metamaterial absorber. Simulated results of the free space reflection (S_{11} dashed blue curve), transmission (S_{31} green curve), and reflection coefficient (S_{33} red curve).

In Fig. 5.11, we plot the surface current density at the resonant frequency and find that our MMA achieves a response similar to prior designs (38).

Fig. 5.12 shows the magnitude of the electric field and, as can be observed, the electric field is focused into the ELC split gap (right panel) and the *vias* are sufficiently decoupled from the ground plane.

The received microwave signal across the end of *via*s is a balanced signal. But most of the commercial-off-the-shelf(COTS) circuits are unbalanced and more importantly, our vector network analyzer (VNA) only has unbalanced input. A Murata balun is used to convert the balanced received signal to unbalanced signal for measurement and processing. The output of the balun is fed into the impedance matching circuit and following stages. The impedance matching circuit compensates for ELC resonator and other component's variances in the fabrication process, and tunes the resonance frequency and resonance strength of metamaterial.

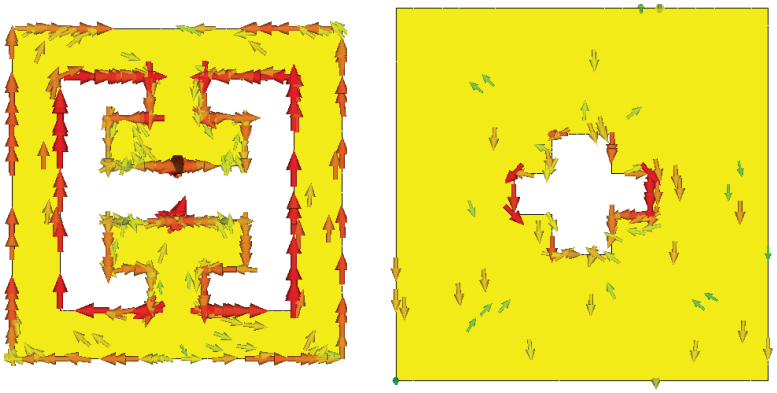

Figure 5.11: Simulated current densities shown directly underneath the ELC (left) and above the ground plane (right) at the simulated design frequency of 2.0 GHz.

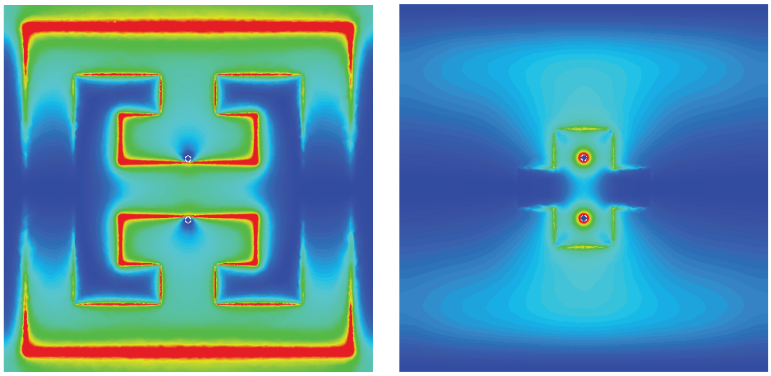

Figure 5.12: Simulated electric field magnitude shown directly underneath the ELC (left) and above the ground plane (right) at the simulated design frequency of 2.0 GHz.

CST's circuit design studio permits export of the frequency dependent S-matrix data, as a Touchstone file. Specifics of the Murata balun were also incorporated into this circuit file. From this point, the MM can be treated as a circuit element in the circuit simulation tool, such as Agilent Advanced Design System (ADS), by importing its frequency dependent S-matrix data in Touchstone format into the circuit simulation tool. The S-matrix data in Touchstone format serves as bridge between the EM simulation and circuit simulation and enables EM-circuit co-simulation.

Now the impedance matching circuit designed for providing maximum power transfer from ELC resonator to detector is presented below. The ZY smith chart can be used in the design process. Ideally, the effect of adding a series reactance element or a shunt susceptance element will move the impedance of metamaterial on a constant resistance or conductance circle, respectively. By choosing the appropriate topology for construction of an impedance matching circuit, and the value of reactance / susceptance element, we can achieve a very low reflection coefficient at the target frequency. This is illustrated in Fig. 5.13 (104).

The metamaterial impedance at the output of the balun before the impedance matching circuit is added at 1.945 GHz is 50*(1.011+j1.247) Ω. If the metamaterial is directly connected to the the circuit stage, which has 50 Ω input impedance, a significant portion of the received signal power will be reflected to the metamaterial instead of being transferred to the detector circuit as the impedance of metamaterial at 1.945 GHz contains a large inductive component.

A Tee network was selected for the impedance matching topology because of its superior frequency selecting ability. It can boost the Q or the resonance strength of the metamaterial.

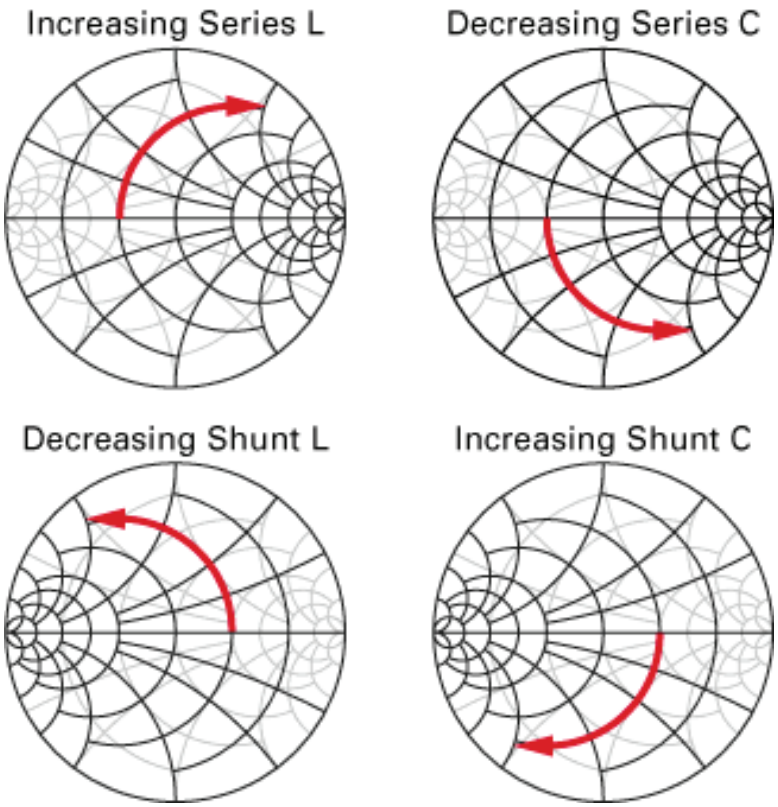

Figure 5.13: How the impedance moves on smith chart when series/shunt L/C are added (104)

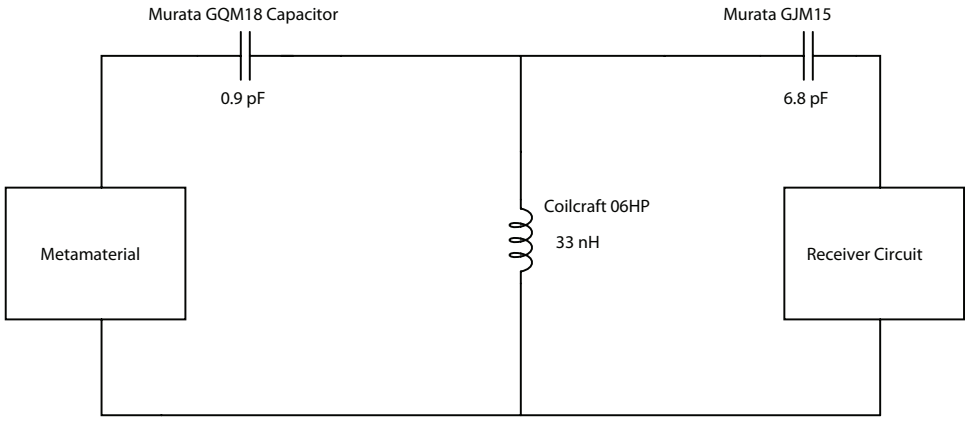

Figure 5.14: The schematic of the impedance matching circuit

The impedance is moved downward to the horizontal axis in the smith chart along a constant resistance circle first. This requires a small series capacitor. However, commercial off the shelf (COTS) capacitors often contain equivalent series inductances and equivalent series resistances, which must be carefully considered. An equivalent series inductance cancels part of the capacitance and equivalent series resistance moves the impedance of the metamaterial off the constant resistance circle. The larger the equivalent series resistance, the farther away it is moved from the desired constant resistance circle.

There are many different kinds of capacitors in the market such as aluminum, film, ceramic, tantalum, etc (105). What we need in our project are capacitors with high Q, low loss, and a compact package. Multi-Layer Ceramic Capacitors (MLCC) are chosen because they are specially designed for RF, microwave applications with low loss and high Q (105). A real capacitor contains an "equivalent series resistor (ESR)", which is caused by imperfections of dielectric material in the capacitor (105). The impedance of capacitor becomes (105):

$$Z_c = \frac{1}{j\omega\ c} + R_{ESR} \tag{5.10}$$

As the operating frequency approaches infinity, the reactance term gets closer to zero and resistance becomes dominant.

There are usually two pins in the package of COTS capacitor to be connected to the pads on printed circuite boards. These pins causes undesired parasitic inductance in series with the capacitor, which is termed "equivalent series inductance (ESL)"(105). Capacitance is

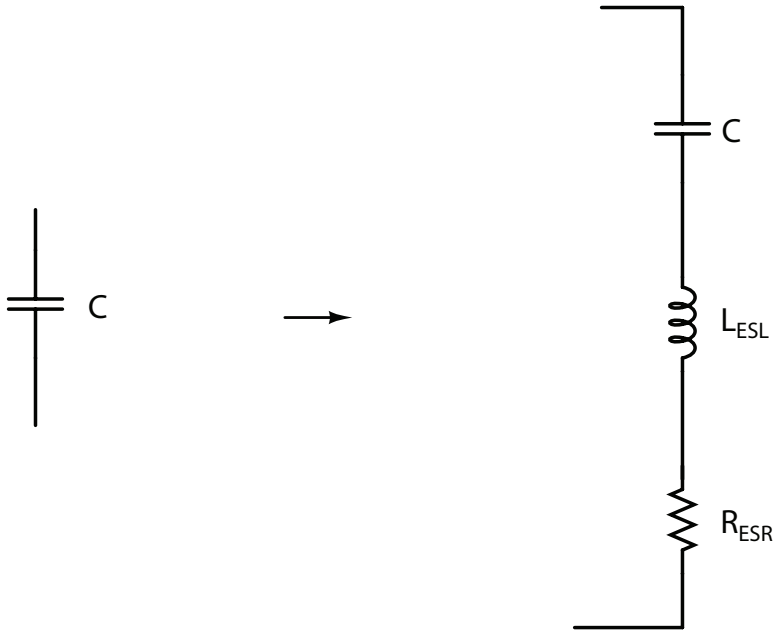

Figure 5.15: The schematic of a realistic model of a capacitor at RF/microwave frequency. (105)

canceled by inductance at a certain frequency called "Self Resonant Frequency (SRF)" if we sweep the operating frequency of the capacitor (105), and the capacitor is actually turned into a inductor at frequencies above SRF (105). The schematic of a realistic model of a capacitor is shown in Fig. 5.15 at RF/microwave frequency (105).

The net result of the aforementioned non-idealities related to capacitors, is that the value of the capacitance changes with frequency and the capacitor turns into an inductor beyond the SRF (105). An accurate model of capacitor across the band of interest is crucial in circuit design. Here we used the S parameters of the capacitor provided by the manufacturer, and utilized the circuit simulation tool - Agilent Advanced Design System (ADS) to simulate it.

The analytical expression of this circuit model of the capacitor is (105)

$$Z_c = \frac{1}{j\omega\ c} + R_{ESR} + j\omega\ L_{ESL} \tag{5.11}$$

A 0.9 pF Murata GQM18 capacitor was chosen based on the S parameter model provided by the manufacturer. We then moved the impedance upward along a constant conductance circle until it hit the 50 Ω resistance circle. This was done by adding a shunt inductor with relatively large inductance and small equivalent series resistance, which moves the impedance off the constant conductance circle.

The parasitics in an inductor cause the value of the inductance changes with frequency and the inductor to turn into a capacitor beyond the SRF (106). An accurate model of inductor across the band of the interest is crucial in circuit design. Here we used the S parameters of the inductor provided by the manufacturer, and utilized the circuit simulation tool - Agilent Advanced Design System (ADS) to simulate it.

We resolved to use a value of 33 nH based on the S parameter model provided by the manufacturer. The last step is to move the impedance downward along the 50Ω constant resistance circle. We added a series 6.8 pF Murata GJM15 capacitor for this purpose. The entire impedance matching circuit is shown in Fig. 5.14. The impedance of the MM has been transformed to 50Ω at the resonant frequency of 1.945 GHz. The magnitude of S_{33} is shown in Fig. 5.16.

There are many constraints in circuit design, including a lack of availability of components in the manufacturer's catalog. In initial designs, parts listed in the manufacturers' catalog

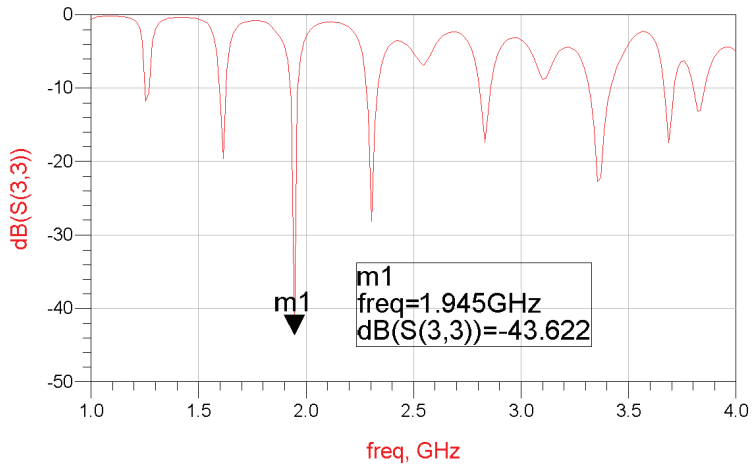

Figure 5.16: The magnitude of S_{33} at the output of the metamaterial loaded with impedance matching circuit

are used and good simulation results are obtained. It was later found out that these parts, however, are not readily available, with a long lead time. A new impedance matching circuit is thus built, as shown in Fig. 5.14, which employs in-stock parts only. Another issue is related to the discrete values of available inductors/capacitors, and the relatively large tolerances, ranging from 5% to 10%. Tolerance may sometimes significantly reduce the performance, as the metamaterial is a narrow band device. As a final consideration, modeling of each part may not be accurate enough, which may cause discrepancy between simulation and measurement.

In reality the actual circuit is much more complicated than the Tee network shown above in Fig. 5.14 as each component in the circuit is a network composed of numerous parasitic inductors, capacitors and resistors, which are illustrated in Fig. 5.15 and 5.17. By organizing component level networks properly, it is possible to cancel these undesirable effects. It can also reduce component size tolerance effects to a certain extent. However, both of these advantages rely on the accuracy of the S parameter component models provided by the

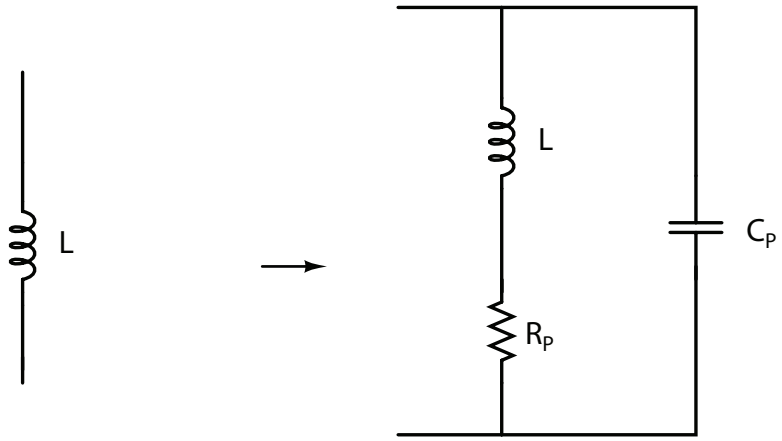

Figure 5.17: The schematic of a realistic model of an inductor at RF/microwave frequency (107) R_p and C_p are the parasitic resistance and capacitance, respectively (107)

manufacturer, which are not reliable in real life because of the process variation in PCB and the tolerances in components (108).

5.3.3 Measurement

Although simulations presented above indicate that a high performance MMA unit cell may be used as a detector of incident radiation, tolerances in both the component values and the geometry can occur in the fabrication process and may thus alter the ideal electromagnetic response shown in Fig. 5.10. Characterization of S_{11} is not possible with our experimental setup. However, simulations presented in Fig. 5.10 indicate that S_{33} is a reasonable approximation of S_{11}. Thus we measure S_{33} in order to investigate the resonant properties of the fabricated MMA.

Free space measurements of the center pixel were performed within an anechoic chamber. We use a HP 8510B vector network analyzer (VNA) with a double ridge guide horn antenna

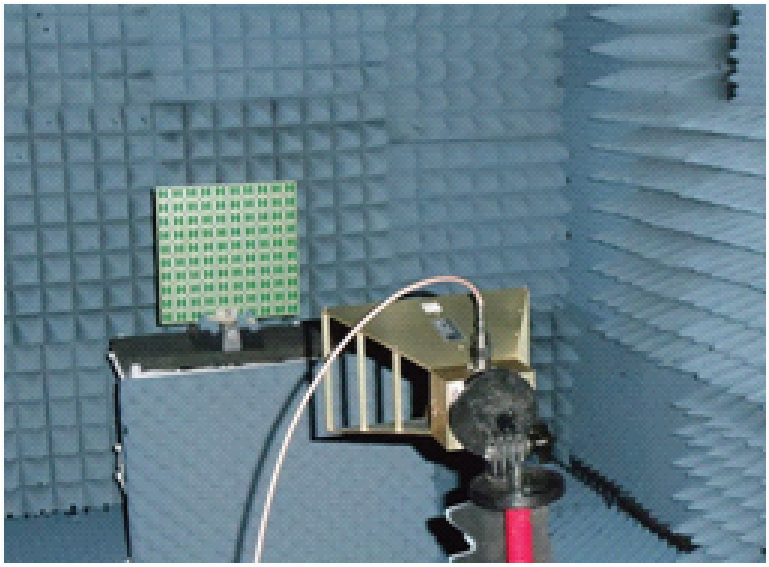

Figure 5.18: Measurement setup inside anechoic chamber

(700 MHz - 18 GHz range) as a transmitter. The horn was connected to a port of the VNA which provided a power level of -3 dBm. Another port of the VNA was directly connected following the unbalanced signal output of the balun on the center single pixel of the MMA / FPA. Both ports of the VNA were calibrated by the short, open, load and through (SOLT) method. The measurement setup in the anechoic chamber is shown in Fig. 5.18. The resulting S-parameters measured were for only this center pixel with all neighboring unit cells having 50 Ω terminations following their respective balun output connections. The MMA / FPA was placed 1.75 m away from the horn antenna to be in the far field of the horn's radiating field pattern. In Fig. 5.19, the green S_{31} curve shows a peak about 2.5 GHz overlapping with the minimum observed in S_{33}, which is the red curve in Fig. 5.19.

We observe a high reflection coefficient across the range investigated but notably minima occur at 2.5 and 3.15 GHz, with values of -33 dB and -29 dB, respectively. The simulated minimum in S_{33} occurring at 2.0 GHz has shifted to 2.5 GHz, which we attribute to the

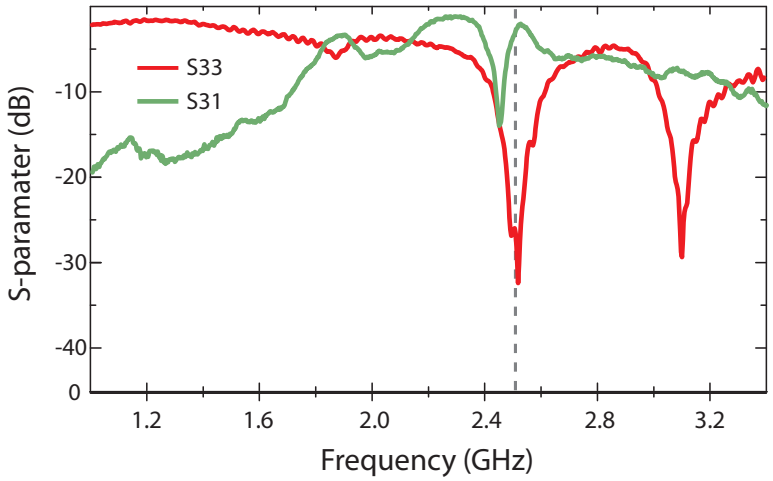

Figure 5.19: Experimental measurements in anechoic chamber for the center pixel on the MMA / FPA. S- parameter data shows the reflection coefficient (S_{33} red curve) and the transmission (S_{31} green curve) with the dashed grey line at 2.5 GHz, which is the resonant frequency.

variation in the fabrication from the simulated design. We characterized various parameters of our device and found errors that include: layer thickness, *via* dimensions, layer alignment (registration), balun impedance, and dielectric values. These variances result in a reduction of ideal electromagnetic performance which leads to an impedance mismatch between the metamaterial unit cell and the 50 Ω input circuit modules. Overall, this results in diminished reception of electromagnetic energy due to increased reflection between the metamaterial and detector circuit. We anticipated various fabricational errors and therefore, in the design process, preemptively added a reconfigurable element to tune the impedance of the circuit layer after the metamaterial unit cell. Thus an impedance matching circuit directly following the balun compensates for MMA variances and tunes the strength and frequency of the resonance at the selected operating frequency. Due to hardware and component limitations we decided to operate at 2.5 GHz, as opposed to the simulated 2.0 GHz operational frequency.

The adjusted impedance matching circuit after measurement is shown in Fig. 5.20. The impedance of metamaterials at 2.5 GHz is tuned to 50Ω through adding this impedance

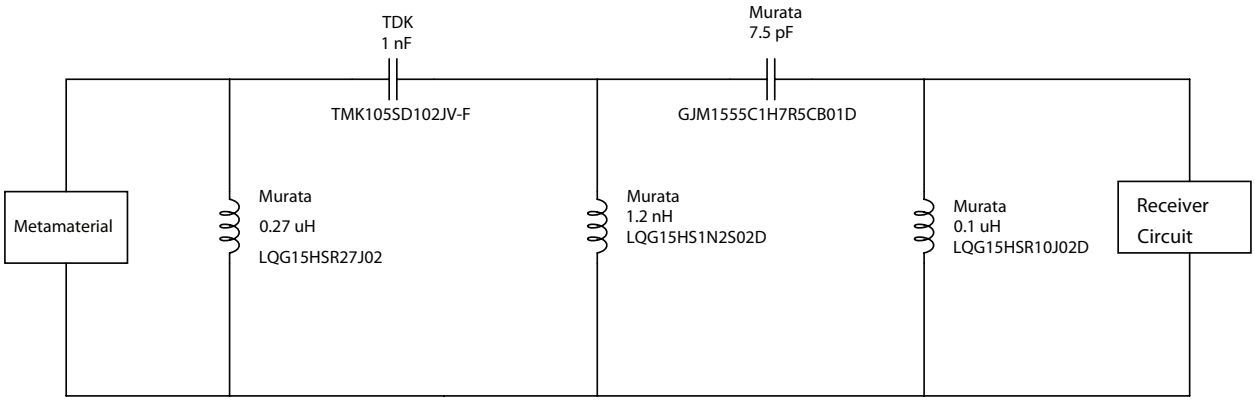

Figure 5.20: Adjusted impedance matching circuit after measurement

matching circuit.

We used a separate board to implement the impedance matching circuit and low-noise amplifier (LNA) (Board 2) and another board (Board 3) for the microwave power detector. We connected the output of Port 3 with a UMCC connector to Board 2 as shown schematically in Fig. 5.21. After the signal propagates through the impedance matching network and LNA, it passes through a SMA connector, which we call Port 4. We use the ADL5523 LNA made by Analog Device which provides a gain of approximately 15 dB at 2.5 GHz. In Fig. 5.22, the gold S_{41} curve shows over a 15 dB improvement of S_{31} at 2.5 GHz as a result of having an impedance matching circuit followed by the LNA. The microwave power detector converts the microwave output signal from port 4 into a DC voltage and is implemented using a monolithic LT5534 made by Linear Technology. The LT5534 has a 50MHz to 3GHz detected bandwidth and is capable of measuring microwave signals with over a 60dB dynamic range with a linear DC output with respect to signal amplitude in decibel scale.

The gold curve in Fig. 5.23 displays the measured mutual coupling (MC) between neighboring unit cells parallel to the electric field direction. At 2.5 GHz the MC was measured

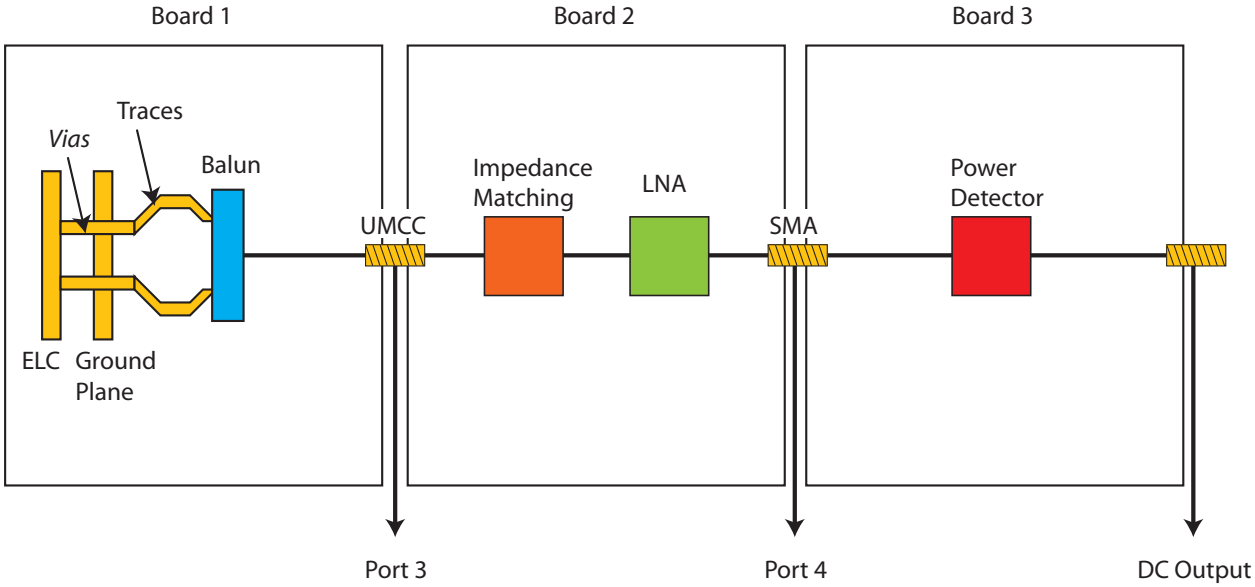

Figure 5.21: System architecture consists of three boards with board 1 which contains the metamaterial connecting through the *vias*, traces and balun out through a ultraminiature coax connector (UMCC) designated as port 3. The UMCC cable connects to board 2 containing both the impedance matching circuit and low noise amplifier (LNA) with output labeled as port 4. The third board consists of only the microwave power detector providing a DC voltage output signal.

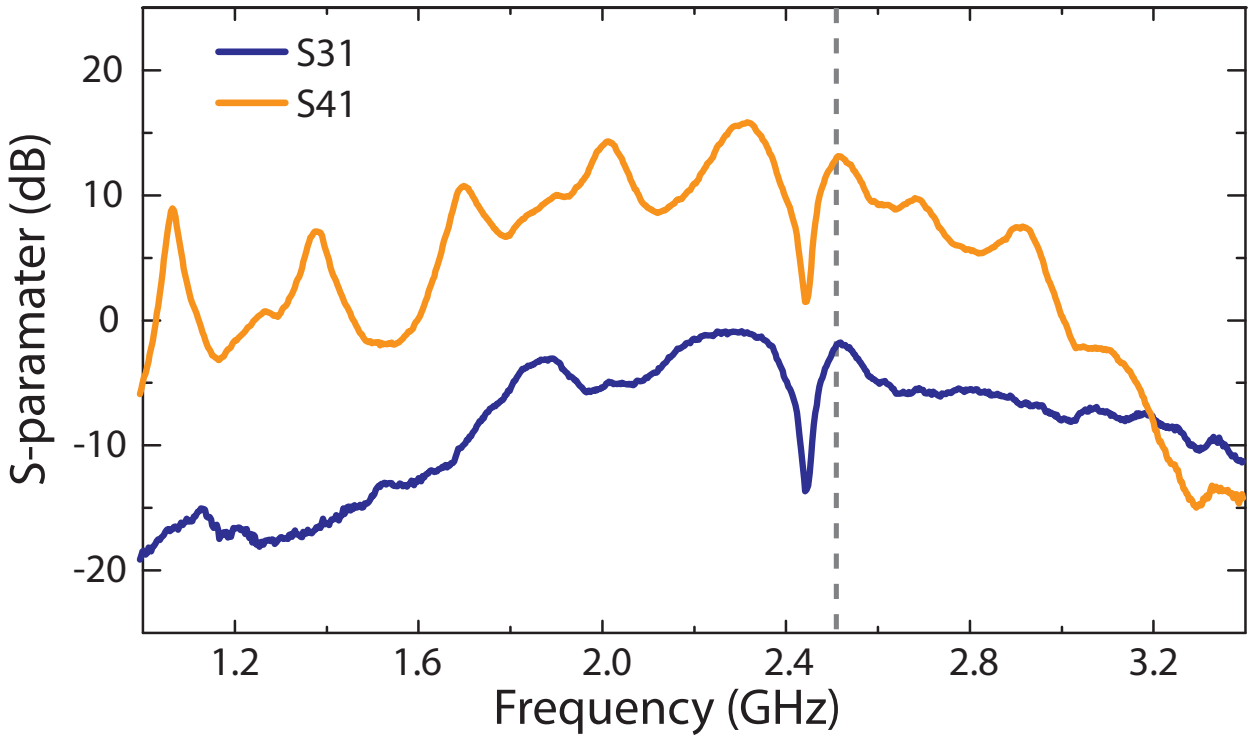

Figure 5.22: S-parameter data shows the transmission without (S_{31} blue curve) and with (S_{41} gold curve) the addition of the impedance matching and low noise amplifier (LNA) with the dashed grey line at 2.5 GHz the frequency for sensitivity and off-angle measurements.

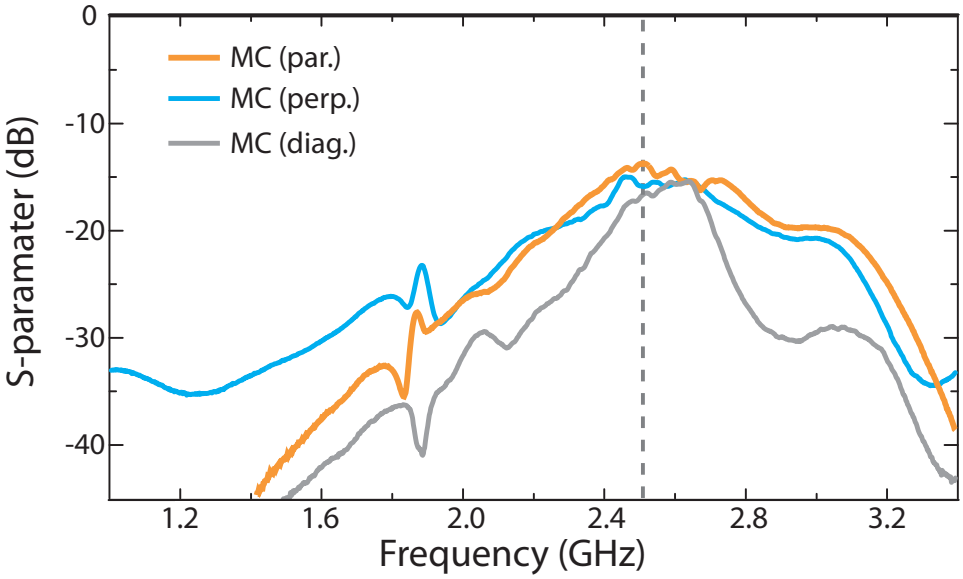

Figure 5.23: Experimental measurements in anechoic chamber for mutual coupling (MC) between neighboring metamaterial pixels located parallel (gold curve), perpendicular (blue curve), and diagonal (grey curve) with respect to the electric field polarization.

to be below -14 dB. We have also measured the MC in the perpendicular and diagonal neighboring cells and values below -15 dB were found. Values of MC are significantly low, especially considering the proximity of nearest neighbors at a lattice spacing of $\lambda/4.4$ (27.3 mm) and with edge separation of $\lambda/40$ (3.0 mm). In addition to the clear benefit toward imaging, (84, 85, 86) reducing MC is of particular importance for multiple input multiple output (MIMO) communication systems that suffer reduction in channel capacity due to these affects (109, 110).

We now turn toward characterization of the sensitivity and angular dependence of the MMA / FPA. A microwave source was fixed to operate at 2.5 GHz and fed to the horn antenna. The DC voltage output from the MMA / FPA was recorded as the horn power was swept from -50 dBm to +20 dBm as shown in Fig. 5.24. We determine an ultimate pixel sensitivity of -77 dBm, corresponding to a radiation power density of 27 nW/m^2, after calibrating for

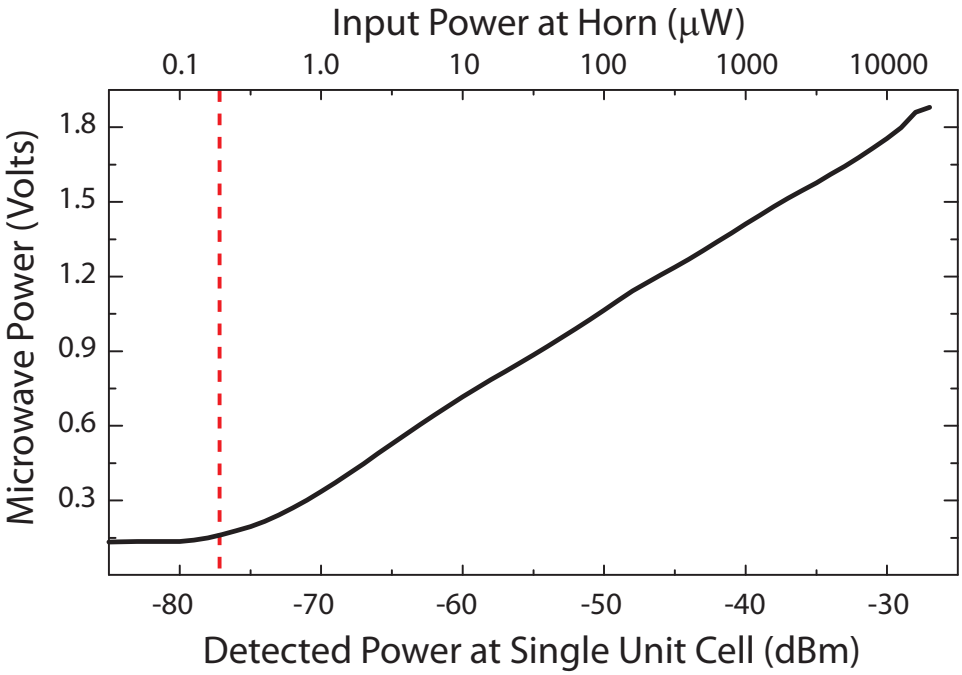

Figure 5.24: Experimental measurements in anechoic chamber for sensitivity characterization with the output of microwave power detector of single pixel as function of incident power, and is sensitive as indicated by dashed red line down to -77 dBm at 2.5 GHz.

cable and free space losses.

Fig. 5.25 shows the resulting off-angle performance characterization of the MMA / FPA at 2.5 GHz for both transverse electric (TE) and transverse magnetic (TM) polarizations. However, it should be noted that our metamaterial does not possess 90° rotational symmetry and thus we characterized TE and TM for both the "correct" polarization – as shown in Fig. 5.9(a) – the cross polarization to this. The MMA / FPA is rotated about its axis, (with the distance from the horn kept constant), in steps of 4 degrees, and the scattering parameters are recorded. The measurement results demonstrate that the MMA / FPA operates as a wide angle antenna. This is consistent with the off-angle absorption performance typical to MMAs (103). Both TE and TM cross-polarized angular dependent measurements are at

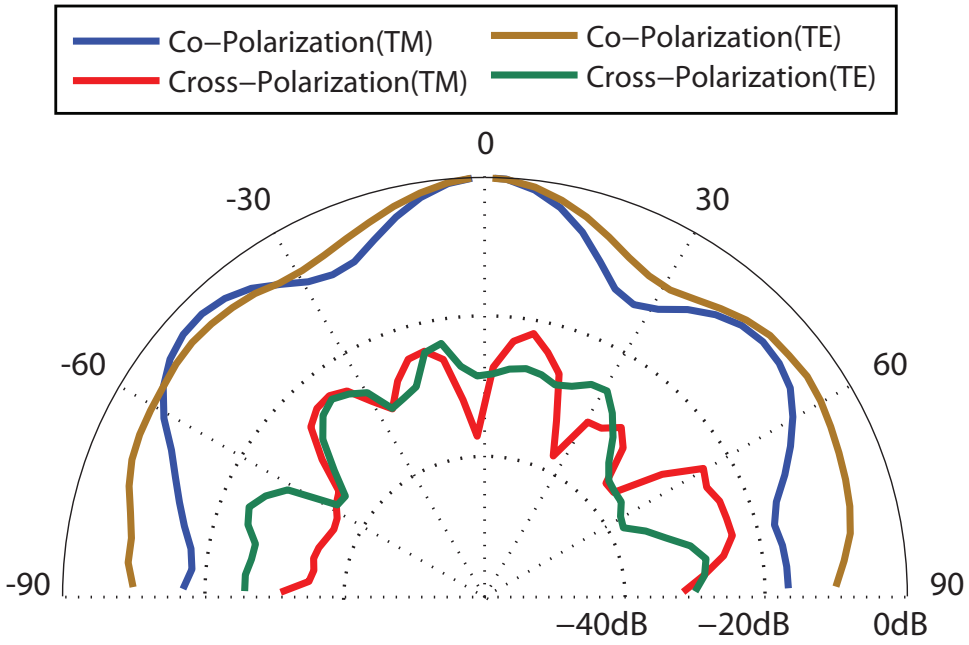

Figure 5.25: Off-angle performance characterization of the MMA / FPA at 2.5 GHz for both the electric field vector perpendicular (TE) and parallel (TM) to the floor of the chamber. The ELC resonator's are rotated between the correct polarization (E-field perpendicular the split gap) and the cross polarization (E-field parallel to the gap).

minimum of 20dB lower that the co-polarized measurements. Thus the presented MMA / FPA may be used for polarization discrimination imaging.

5.4 Summary

The characterization of our metamaterial absorber focal plane array was demonstrated to operate at 2.5 GHz and have high pixel sensitivity of -77 dBm, with low pixel to pixel coupling interference below -14 dB, good frequency selectivity and wide angular performance. We note that the FPA is not restricted to the frequency applied in this work but could prove useful at higher frequency operation from microwave to millimeter wave. Even more generally, the MMA due to its ability to capture nearly all of the incident electromagnetic energy at

design frequencies across the entire electromagnetic spectrum could serve as an excellent candidate to act as detector pixels when implemented into bolometric or semiconducting configurations. The sub-wavelength unit cell and narrow resonant spectral bandwidth can also be expanded to enable multi-color and co- and cross-polarized pixels.

6

Diode Switchable Metamaterial Reflector/Absorber

6.1 Background

Switchable metamaterial absorbers are the metamaterial based EM wave absorbers whose resonant frequency and the absorptivity at the resonant frequency are controllable through tuning of external optical, mechanical or electric signals. Switchable metamaterial absorbers are very useful in many applications. For example, switchable metamaterial absorbers have been used in microbolometer to tailor its responsivity at selected wavelength, which provide promise for hyper-spectral thermal imaging systems in the mid-IR and terahertz regime (94). Another application of switchable metamaterial absorbers is to build a beam-steerable

antenna (111), whose radiation pattern is tuned by switching on a certain pattern of metamaterial cells arranged in its substrate (111). The biggest advantage of this switchable metamaterial absorber enabled beam-steering antenna over conventional phased array based beam-steering antenna is that it does not require phase shifters and related auxiliary circuits that make them bulky and expensive.(111).

In the literature, the initial efforts made on investigating the tunable metamaterials appear in the nonlinear metamaterial area (112, 113). People have not only explored the possibility of making tunable metamaterials but also manipulating the electromagnetic radiation and harmonic generation in the research area of the nonlinear metamaterials (22). As the research of tunable metamaterials keeps progressing, a lot of methods of making metamaterials tunable have been reported in the literature such as impinging light onto the metamaterials to change the conductivity of the materials (114), changing the geometry of metamaterial unit cells using Microelectromechanical systems (MEMS) (112), embedding active or semiconductor materials into metamaterial unit cells (8), etc. All these approaches fall into three major categories (115). One is to introduce active material or semiconductor components into the metamaterial resonator or substrate in order to generate nonlinear effects so that the EM properties of the metamaterials is changed (114, 116, 117, 118). The other one is to change the structure of metamaterial using MEMS method including modifying the geometry of unit cell (112, 119), bending substrate or resonator (120, 121), rotating the lattice (122, 123, 124), etc.

The biggest advantage of introducing active nonlinear material into metamaterials over changing their structure through mechanical tuning is the high speed of tuning. The bottleneck of the speed of MEMS tuning is the the mechanical actuation time required to control

the mechanical structure of metamaterials (125). The typical actuation time of controllable mechanical actuation is more than 100μs, and thus the up limit of the modulation speed is sub-millisecond (125). In contrast, the typical response time of the active nonlinear material embedded into metamaterials to the external excitation, such as the response time of diodes or liquid crystal to the external tuning voltage, can be sub-picoseconds (126). So the speed of active nonlinear material tuning is 9 orders of magnitude faster than that of the mechanical tuning.

The third method to make metamaterials tunable is using light to change the conductivity of the substrate using photoconductive effect (112). While optical methods based on photoconductive effect are expected to be much faster, they do not lend itself to compact and portable realizations due to the need for lasers and bulky optical components. In this paper, an elegant solution is proposed to tune the metamaterial performance by embedding the diodes into strategic locations in the metamaterial array for a unique application of a thin switchable absorber/reflector. Diodes have been used to tune the performance of Frequency Selective Surfaces (127). Bayatpur *et al.* proposed to embed lumped diodes in between the adjacent square loops in the loop array of their FSS to tune the resonant frequency of FSS (127). It has also been reported that diodes incorporated in the wire grid based FSS change the resonant frequency of FSS (128).

6.2 Design and implementation

6.2.1 Principle of proposed approach

In the proposed approach, diodes are used to connect metamaterial unit cells in one column. When the diodes are turned on, they short all the unit cells in one column. This supports electromagnetic modes in an array that are different from the modes when the diodes are turned off. In essence, the electromagnetic responses of the proposed metamaterial absorber/reflector are controlled by diodes. Although the number of diodes needed is proportional to the number of unit cells in an array which could be arbitrarily large due to sub-wavelength dimensions of each unit cell and the need for large coverage, the proposed design requires only two control lines instead of N^2 control lines for an $N \times N$ array of cells to tune the entire array, making this a highly practical solution.

6.2.2 Design

The schematic of our proposed diode switchable metamaterial reflector is shown in Fig. 6.1. Each unit cell is an electrically coupled LC (ELC) resonator (38) with a ground plane on the back although many other resonator structures can also be used to realize this absorber/reflector such as split ring resonator (69). ELC resonator and the ground plane underneath it are shown in yellow and blue, respectively, in the inset of Fig. 6.1. The dimensions of the ELC resonator are shown in the inset of Fig. 6.1 as well. w_1=0.6, w_2=0.3, w_3=0.35, l_1=7.4 , l_2=4.5, g_1=0.13, a_1=9, a_2=8.4, all dimensions are in millimeter.

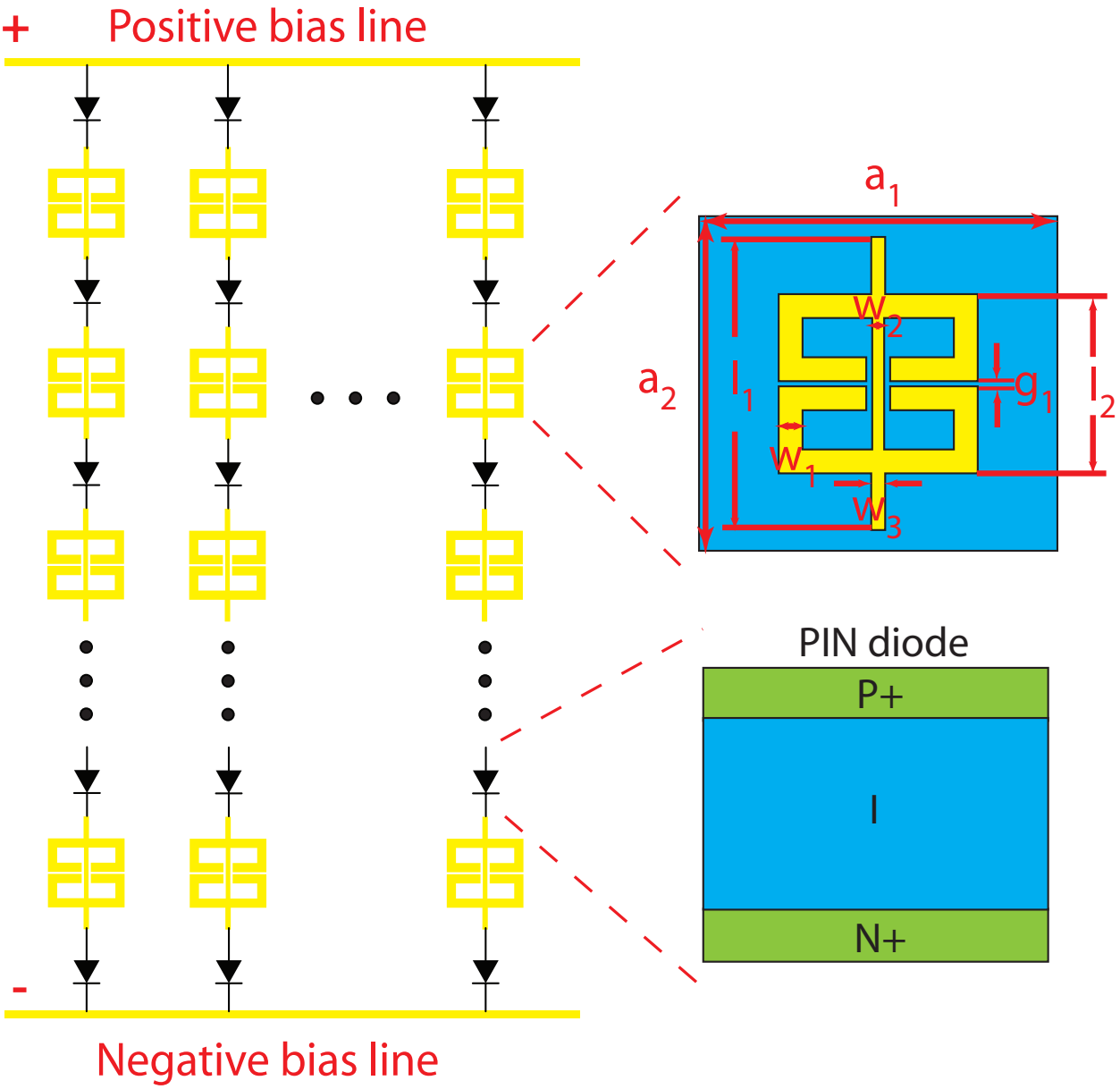

Figure 6.1: Schematic of our diode switchable MM reflector and the dimension of one unit cell. Dimensions of unit cell are in mm. w_1=0.6, w_2=0.3, w_3=0.35, l_1=7.4 , l_2=4.5, g_1=0.13, a_1=9, a_2=8.4.

As shown in Fig. 6.1, the diodes are connected in series with the anode connected to the positive bias line. In essence, each column of unit cells is essentially connected in series with diodes. The size of the diode is much smaller than that of the ELC resonator and is negligible compared to the wavelength of incident radiation. This is important because diodes should not affect the electromagnetic response of the metamaterial absorber.

The diodes used in this switchable metamaterial reflector are ″ PIN diodes, where a high resistivity intrinsic region (I region) is inserted between the P-type and N-type region″ (129). The reason of choosing this particular type of diodes is elaborated below.

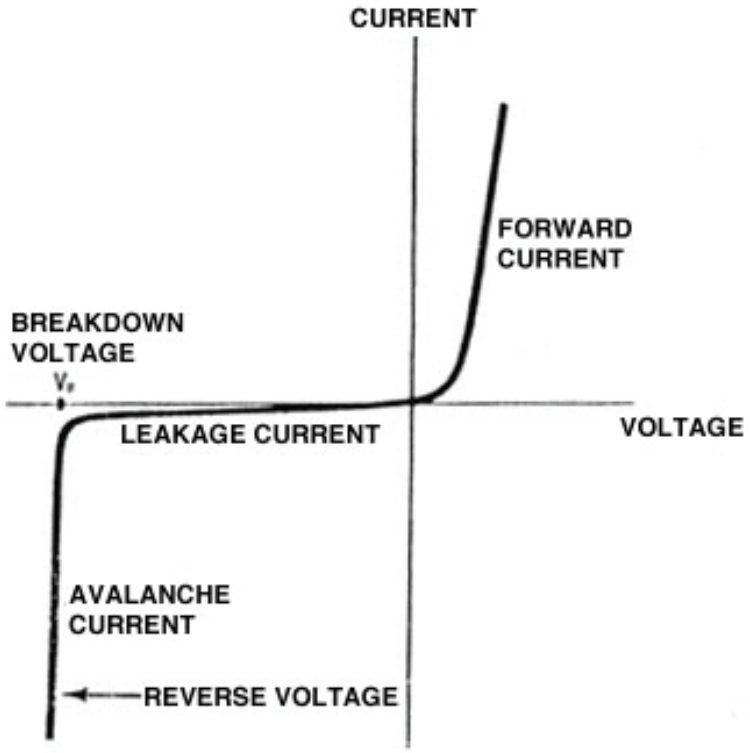

Figure 6.2: The typical I-V characteristic of diodes (130)

6.2.3 PIN diodes

Diodes are one of the most common active nonlinear components in circuits. Regular diodes such as p-n junction diodes have slow reverse recovery and cannot provide tunable resistance at high frequencies (130). Therefore regular diodes are not suitable to be used as switches at RF/microwave frequencies.

PIN diodes, on the other hand, has a unique property to show different I-V characteristic at low and high frequencies due to the lifetime of carriers (131). At low frequencies, PIN diodes behave just like regular diodes whose I-V characteristic is shown in Fig. 6.2.

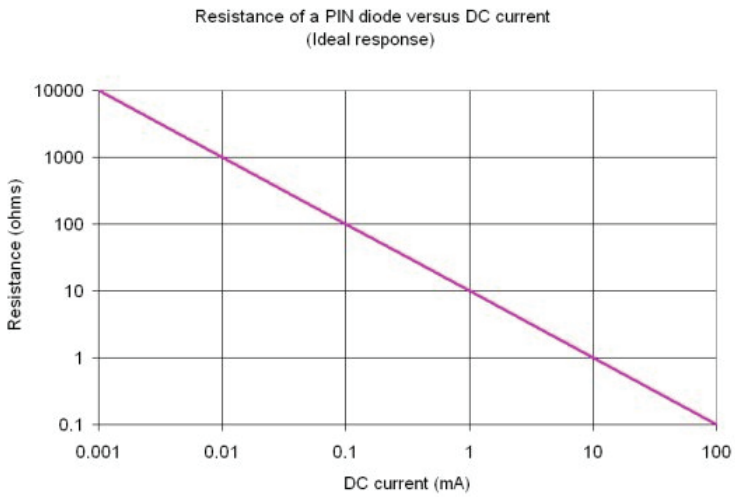

Figure 6.3: The resistance of PIN diodes versus DC bias current (131)

At high frequencies, intrinsic level of carrier concentration in the intrinsic region (I region) is much lower than the level of injected carrier concentration when positive voltage is applied across the P-type and N-type region (132). The huge discrepancy between the injected carrier concentration and the intrinsic carrier concentration in I region create a electric field that accelerates the movement of electrons and holes in the PIN diodes, which enables fast switching/tuning and makes them ideal for RF/microwave applications (132).

At high frequencies,when the PIN diode is forward biased, it appears as a small resistor between anode and cathode (129). When it is reverse biased, the PIN diode is equivalent to a capacitor and parallel resistor (129). The PIN diode is essentially a current controlled resistor (131), whose resistance can be tuned for 5 orders of magnitude (131). A plot of the resistance of PIN diodes versus DC bias current is shown in Fig. 6.3 (131).

Fig. 6.3 indicates that the resistance of PIN diodes covers a wide range, which makes PIN diodes ideal candidates to provide short, open and certain resistance (131). Therefore, PIN

diodes are widely used as switches in microwave circuits and is also the diode of choice for our application..

6.2.4 Implementation and simulation

We use PIN diodes as microwave switches in our design. In order to turn on the diodes, we have to apply a DC bias voltage across the "+" and "-" lines that exceeds the sum of threshold voltage of diodes in one column because they are connected in series. The dimensions of each metamaterial unit cell, which is the ELC resonator, are shown in the inset of Fig. 6.1. We have implemented a 10×20 metamaterial reflector array on a 2 layer printed circuit board (PCB). The top layer is metamaterial array and the bottom layer is a ground plane. The dielectric between them is FR4 and its thickness is 4mm. Both the metamterial array and ground plane are made of 1 oz copper (35 μm thick). The PIN diodes we use are Skyworks SMP1345-079LF.

We have simulated our design in CST microwave studio (133). Fig. 6.4 shows the simulated $|S_{11}|$ in dB when diodes are turned on and off in red and blue curve, respectively.

We use open and short to model the on and off state of diodes. When diodes are turned off, there is no resonance at 4.785 GHz. Instead, we observe a resonance at 4.1 GHz which we call "off resonance". When diodes are turned on, there is a strong resonance at 4.785 GHz, which we call "on resonance". Our goal is to show the ability to switch between "off resonance" and "on resonance" by turning on and off the DC bias voltage of the diode array. Fig. 6.5 shows the 2D electric field distribution on the neighboring unit cells. When

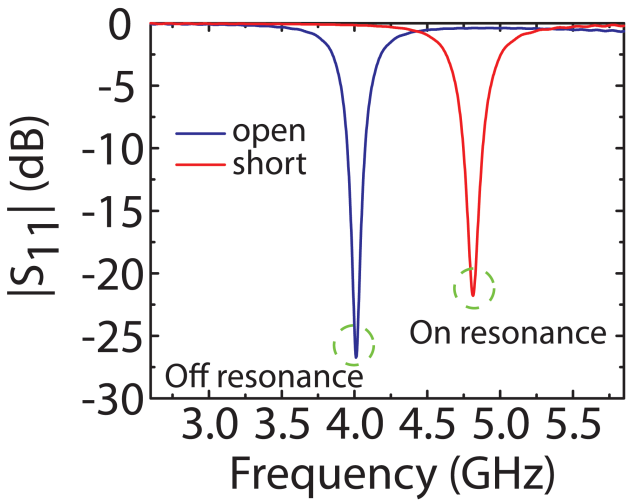

Figure 6.4: Numerical simulation of metamaterial reflector/absorber shows the reflections $|S_{11}|$ in dB. The blue curve shows the $|S_{11}|$ of metamaterial reflector when diodes are turned off while the red curve shows $|S_{11}|$ when diodes are turned on.

the diodes are turned off, as shown in Fig. 6.5 (a), we see strong electric field focused in the gap between neighboring unit cells in addition to the two gaps inside each unit cell at "off resonance" (4.1 GHz). The electric field focused in the gap between neighboring unit cells is caused by the accumulation of opposite charges between them (134, 135). In circuit terms, if the resonator is modeled as parallel RLC network, there is a large effective capacitance creating a resonance at lower frequency. When diodes are turned on, there is no strong electric field across diodes as shown in Fig. 6.5 (b). This causes a reduction in effective capacitance of the ELC resonator, shifting the resonance to a higher frequency which we term "on-resonance" (4.785 GHz). Therefore, we can tune the metamaterial reflector response between "off resonance" and "on resonane" by switching on and off the entire diode array embedded into the metamaterial. The metallic traces of the metamaterial array serve not only to provide the function of microwave reflectors/absorbers but also to provide DC bias circuit network for diodes. Our fabricated PCB is shown in Fig. 6.6.

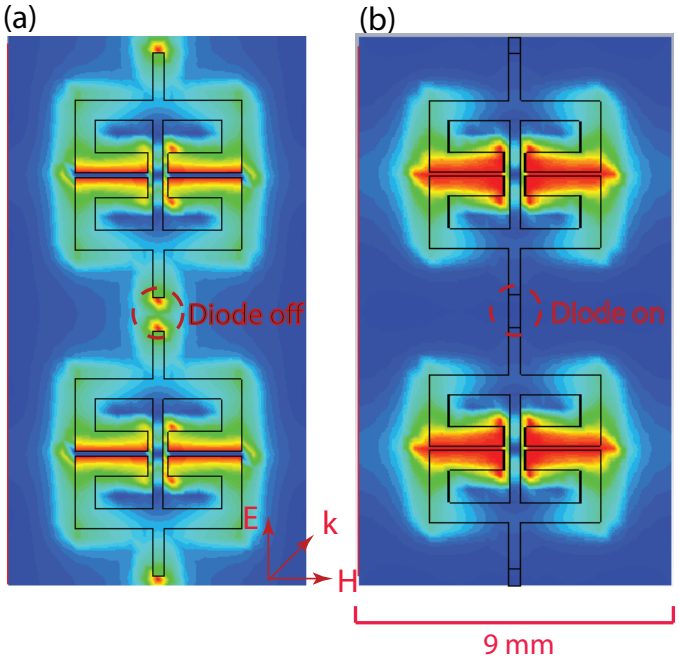

Figure 6.5: Numerical simulation of metamaterial reflector/absorber (a) shows electric field magnitude at "off resonance" (4.1 GHz) when diodes are turned off (b) shows electric field magnitude at "on resonance" (4.785 GHz) when diodes are turned on.

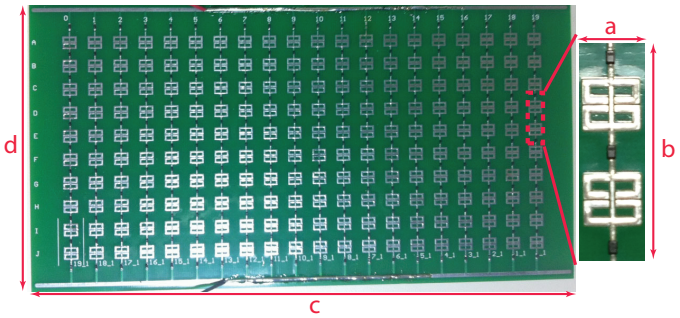

Figure 6.6: The fabricated PCB, the inset shows two neighboring unit cells and diodes connecting them. All units are in millimeter. a=9, b=21, c=199.9, d=109.98

6.3 Measurement

We used a vector network analyzer (VNA) Agilent HP8510C to perform the measurements. Waveguides are connected to port 1 of the VNA to generate the microwave radiation that is impinged on the metamaterial reflector. One waveguide we used was WR284, which covers 2.6-3.95 GHz. The other one was WR187, which covers 3.95-5.85 GHz. The waveguides are mounted directly onto the metamaterial reflector with a layer of insulation material between them to avoid shorting of diode biasing network to ground. The measurement result is shown in Fig. 6.7. The black curve shows the measured $|S_{11}|$ when there is no bias voltage applied across the metamaterial reflector array. The resonant frequency is shifted to 3.5 GHz due to parasitic components of diodes and process variation of PCB fabrication that was not accounted in design. There is also an unexpected resonance at 2.8 GHz. We expect it to be caused by coupling between neighboring ELC resonators through the diodes when they are turned off and could be accounted for in future revision of this absorber. The red curve shows the measured $|S_{11}|$ of metamaterial reflector when a 9.6 V DC voltage is applied across the positive and negative bias lines. All the diodes are turned on and the resonance frequency is around 5.6 GHz. Again, the shift of resonant frequency is incurred by the parasitic components in diodes and process variation of PCB fabrication.

6.4 Results and Summary

A diode switchable metamaterial reflector/absorber has been successfully demonstrated in 2-6 GHz frequency range through embedding of diodes within the metamaterial array. The

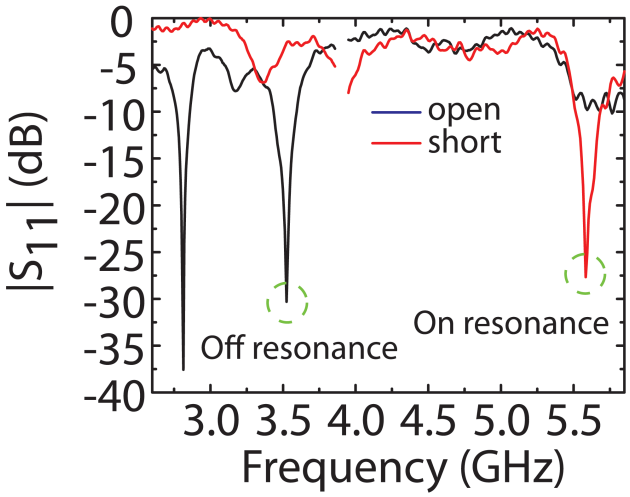

Figure 6.7: The measured $|S_{11}|$ of metamaterial reflector. The black curve shows the measured $|S_{11}|$ when there is not bias voltage applied across the metamaterial reflector array. The red curve shows the measured $|S_{11}|$ of metamaterial reflector when a 9.6 V DC voltage is applied across the positive and negative bias lines.

prior art employing diodes to tune metamaterial performance requires a complex DC bias circuit network (134, 135). The complex DC bias circuit network has to be implemented on a separate layer and requires extra routing and *via*s which increase the fabrication cost and the complexity of the design. In this paper, an elegant solution is proposed and implemented for connecting the diodes to metamaterials with minimal complexity, requiring no additional circuit layer of wiring and allowing tunability with just two control lines, making a practical realization of a large area metamaterial absorber/reflector possible. Diodes are connected in series between neighboring unit cells in single column. The metal traces to realize metamaterial also serves to bias the diodes on/off to tune the resonance frequency of this reflector/absorber. The entire array needs just two control lines to tune this frequency response. The $|S_{11}|$ of our diode switchable metamaterial reflector/absorber can be switched between "off resonance" and "on resonance", namely, 3.5 GHz and 5.5 GHz through active tuning of diodes. These frequencies can be changed by tailoring the dimension of ELC resonators

in the metamaterial array. Multi-band response is also feasible by changing the structure of the metamaterial unit cell, one example is (30). As noted, the performance is narrowband typical of metamaterial inspired designs. However, recent work in using non-foster reactive termination in antenna and metamaterial design could also be employed to realize broadband switchable reflector/absorber (136). The proposed tunable absorber/reflector can be used in a multitude of applications such an beam-steerable antennas, radomes and sensors.

It is possible to implement a spatial modulator consisting of an array of pixels, each of which is a diode switchable metamaterial reflector/absorber array. Each pixel has dedicated DC bias lines so that each pixel in the array can be modulated on/off independently.

Single detector compressive imaging at millimeter wave and terahertz frequencies can be achieved by placing this spatial modulator in front of the detector and turning on a series of designed patterns in the spatial modulator. The proposed design can be readily integrated in monolithic CMOS process. As commercial CMOS processes approach the node of several tens of nanometers (137), each unit cell of the diode switchable metamaterial reflector is scaled down to nanometer size and a larger array of pixels operating at IR/optical frequencies can be implemented on a single CMOS chip. The detector can also be fashioned on the same chip so as to make it possible to build the entire compressive image sensor on a monolithic chip.

7

CMOS Based Metamaterial - Theory, Design and Simulations

Although the initial design efforts on metamaterials (MM) focus on the microwave frequency range, it is more intriguing to demonstrate MM devices working at higher frequencies of terahertz, infrared and optical range. More advanced fabrication techniques have to be employed to implement the MMs with feature size down to a few tens or hundreds nanometers for higher frequency applications. Commonly used fabrication technique in MM community include electron-beam lithography (EBL) (138) and nano-imprint lithography (NIL) (139). EBL features very high resolution and can create patterns with feature size on the order of a few tens of nanometer (140). However, EBL is very expensive and time consuming when used to fabricate large area MM devices, which prohibit its usage for mass production. NIL is another option to fabricate nanometer feature size MM. It is simple and features

low cost, high throughput (140). But its throughput is very slow at the smallest resolution because its high resolution template patterning is performed by electron beam lithography (141). Additionally, it suffers from the problems of overlay, defects and template wear (141). All these factors render NIL unsuitable for mass production of MM devices. CMOS, which is the acronym of Complementary Metal-Oxide-Semiconductor, is a mature and standard fabrication process in the integrated circuit (IC) industry. It is the mainstream technology for mass production in industry. Moreover, CMOS foundries possess advanced UV lithography and high production-yield semiconductor processing approach. Aggressive scaling of the CMOS technology to nanometer dimensions (65) assures its ability to meet the needs of MM community for large arrays of MM devices consisting of nanometer size unit cells. CMOS technology features high yield, fast throughput and low cost, which makes it the most ideal option for mass production of MM devices.

7.1 Typical 45nm CMOS Process

It is beneficial to introduce the structure and dimensions of the commercial 45nm CMOS process. The commercial 45nm CMOS process usually have 5-12 metal layers. The 45nm CMOS technology employed in this work has 10 metal layers. The thickness of each metal layer and the dielectric between neighboring layers are fixed, which only limits the design freedom in vertical dimension when metamaterials are implemented on this CMOS process. The cross section view of the metal and dielectric layers in this 45nm CMOS process is shown in Fig. 7.1.

There are 10 metal layers in this CMOS process, which are termed M1-M10 in Fig. 7.1.

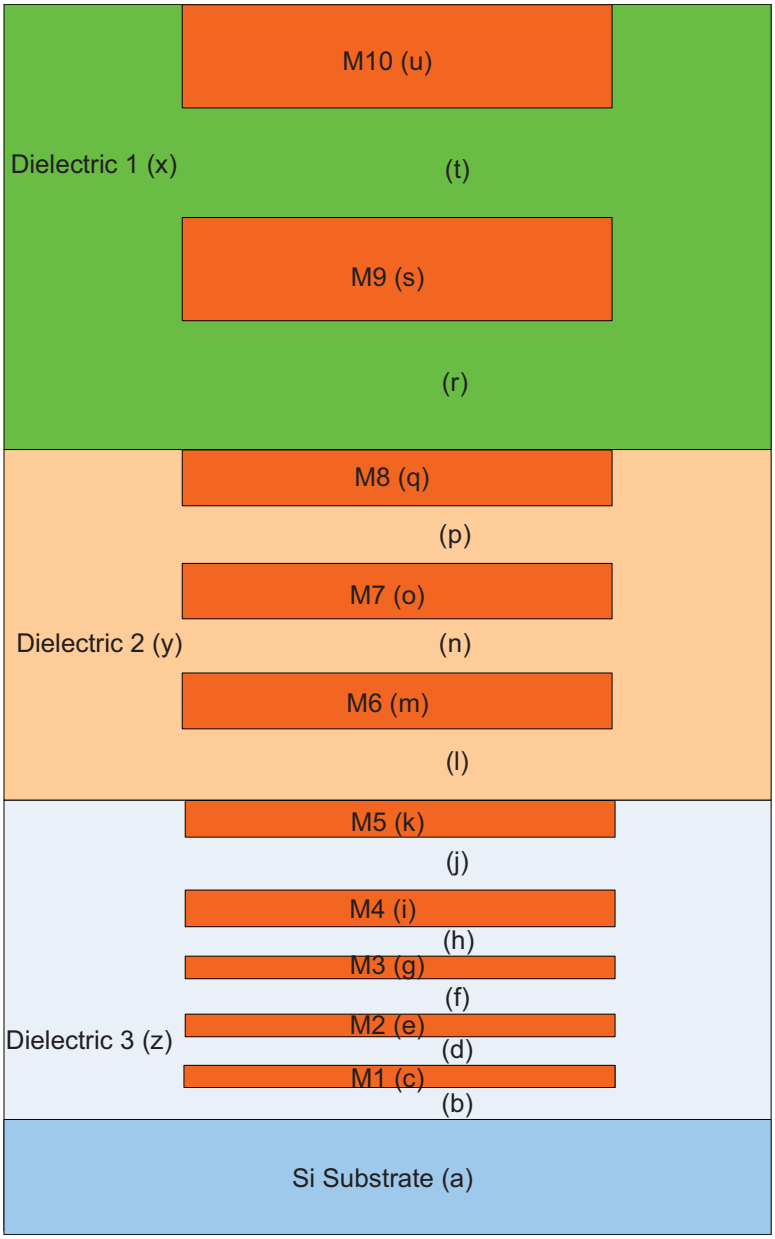

Figure 7.1: The cross section view of CMOS metal stack. The thickness of each metal and dielectric layer is named after the letter in the parenthesis and defined in table 7.1.

The thickness of each metal and dielectric layer is named after the letter in the parenthesis and defined in table 7.1. Range of values shown captures the entire feasible range of values across multiple foundries.

Name of layer	Value of thickness(nm)
a	200∼1000
b	100∼200
c	100∼200
d	50∼200
e	100∼200
f	50∼200
g	100∼200
h	50∼200
i	150∼250
j	150∼250
k	150∼250
l	250∼350
m	250∼350
n	250∼350
o	250∼350
p	250∼350
q	250∼350
r	600∼1000
s	1000∼1400
t	1300∼1900
u	1000∼1400
x	2500∼7000
y	800∼2200
z	700∼2000

Table 7.1: Vertical dimensions of metal and dielectric layers in commercial CMOS process employed

In general the lower level metal layer and dielectric spacer are thinner while the upper lever metal layer and dielectric spacer are thicker. The thickness of metal layer and dielectric spacer may vary 10%-20% due to foundry process variation.

The bottom layer in CMOS is usually a silicon handle wafer layer. It can be etched by post processing. The next layer on top of the silicon handle wafer layer is the bulk silicon layer which carries the transistors. In this work, the bulk silicon is assumed to be etched down to 200∼1000nm.

There are design rules required by the CMOS foundry limiting the minimum width of metal traces and spacing between metal traces on each metal layer. The lower metal layers have smaller minimum feature sizes while the upper metal layers have larger minimum feature sizes. So the design strategy employed in this work is to implement the higher frequency MMs on the lower metal layers and implement lower frequency MMs at higher level metal layers.

Another important design rule is the metal fill density rule on each metal layer in CMOS. Typically, the CMOS foundries require us to keep the metal fill density around 50% on each metal layer for high yield of fabrication. This will invariably restrict the kind of metamaterial geometries that can be implemented. For example, babinet metamaterial which has continuous metal layers will violate antenna rules and are not feasible.

7.1.1 Physical Properties of Metal and Dielectrics at Optical Frequencies

Conductive material such as metals have different responses to the low frequency RF/microwave radiation and IR/optics radiation. At low frequencies, metals attenuate all the incident RF/microwave radiation that is impinged on its surface because of its high conductivity. At

IR/optical frequencies, however, metals are no longer perfect conductors and the conductivity of metal is frequency dependent. Therefore, the response of metal to incident IR/optical radiation is also frequency dependent.

Metal is not a source free medium and is filled with free charge and currents. The relation between the electric flux density $\vec{D}$, current density $\vec{J}$ and the induced curl of magnetic field $\vec{H}$ when an EM radiation with frequency ω shined onto the metal is described by the Maxwell's equation as (11):

$$\nabla \times \vec{H} = \vec{J} + j\omega \ \vec{D} \tag{7.1}$$

If we assume the metal has linear dielectric property and linear conductive property, then (11)

$$\vec{D} = \epsilon \ \vec{E} \tag{7.2}$$

$$\vec{J} = \sigma \ \vec{E} \tag{7.3}$$

If the equation 7.2 and 7.3 are substituted into equation 7.1 and after we reorganize it, the following equation is obtained (11):

$$\nabla \times \vec{H} = j\omega(\epsilon + \frac{\sigma}{j\omega}) \tag{7.4}$$

The term $\epsilon + \frac{\sigma}{j\omega}$ is defined as effective permittivity ϵ_e that includes both the dielectric and conductive properties (11). It is more convenient for us to describe the response of metal to IR/optics using ϵ_e. The second term in ϵ_e, which is $\frac{\sigma}{j\omega}$, is frequency dependent (11). It is much greater than the ϵ at low frequencies and that is why metals behave like perfect conductors at low frequencies (11). When the frequency of incident radiation approaches IR/optics, $\frac{\sigma}{j\omega}$ starts to drop and at a certain frequency, it becomes zero and the metal behaves like a dielectric medium with permittivity ϵ (11).

The most suitable model to describe the frequency dependent permittivity of metal at IR is Drude model (11). The Drude model uses classical kinetic theory to describe the macroscopic behavior of electrons in solids where the EM radiation is impinged on (142).

Let us express the effective complex permittivity of dielectric as (143):

$$\epsilon_e = \epsilon_1 + i\epsilon_2 \tag{7.5}$$

The Drude model is defined as (143):

$$\epsilon_e = \epsilon_\infty - \frac{\omega_p^2}{\omega^2 + i\omega\omega_\tau} \tag{7.6}$$

where ω_p is plasma frequency, ω_τ is damping frequency (143).

The Drude model of Al and Cu, which are the most commonly used metal in CMOS, are shown in Fig. 7.2 and 7.3, respectively (143).

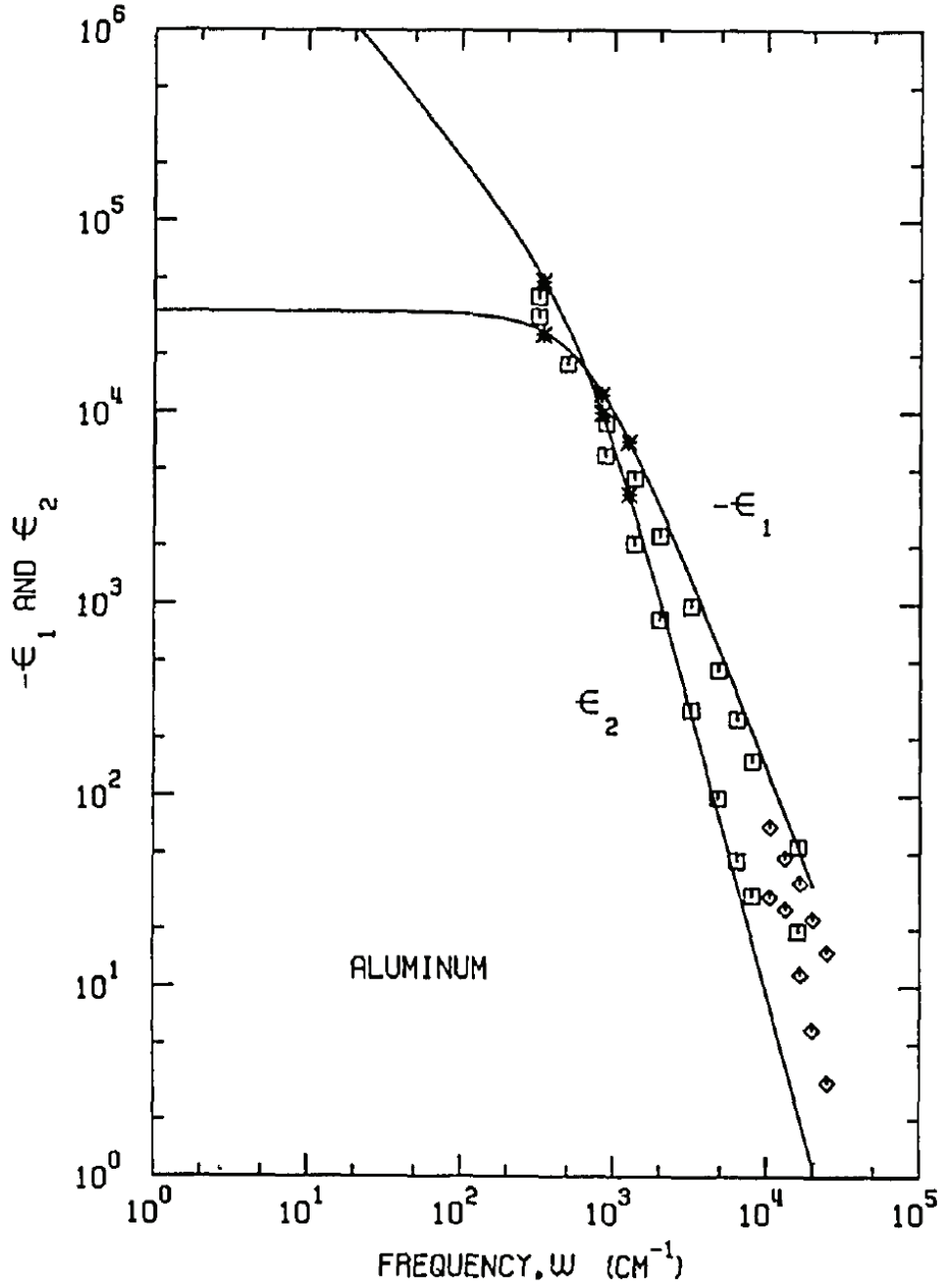

Figure 7.2: Solid lines show the Drude model of Al (143)

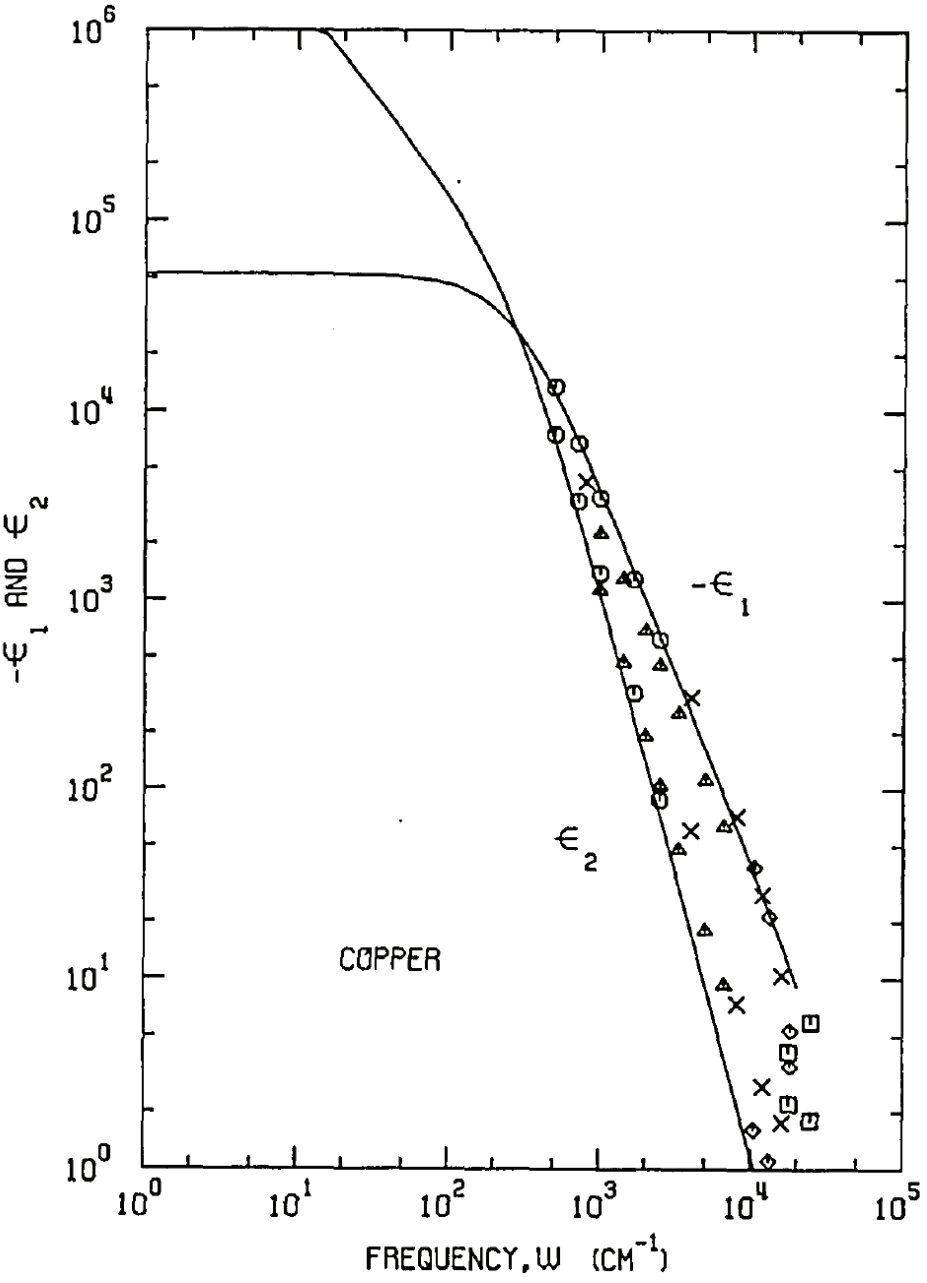

Figure 7.3: Solid lines show the Drude model of Cu (143)

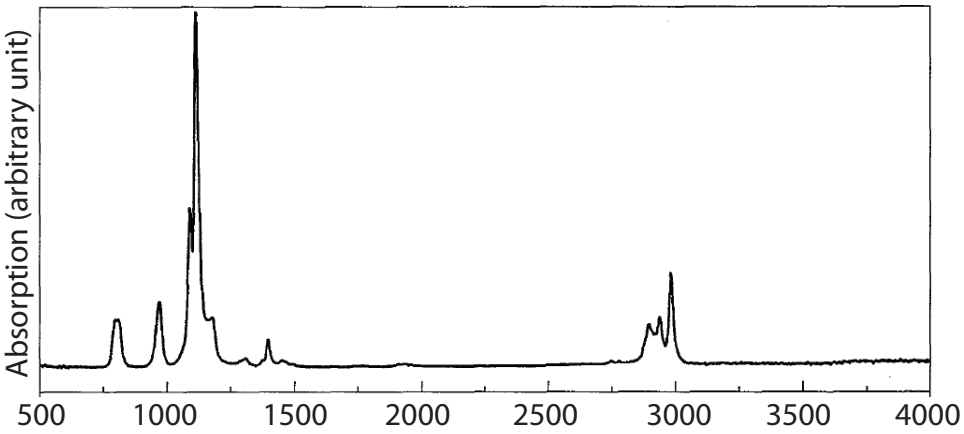

Figure 7.4: The IR absorption spectrum of TEOS. Adapted from (144)

The detailed chemical composition and material parameters of the dielectric used in the 45 nm CMOS process are not disclosed. The most common dielectrics used in CMOS processes include benzocyclobutene (BCB), SiO_2, tetraethoxysilane (TEOS), etc.

The IR absorption spectrum of tetraethoxysilane (TEOS) is shown in Fig. 7.4 (144).

The IR absorption spectrum of benzocyclobutene (BCB) shown in Fig. 7.5 (145).

The IR absorption spectrum of SiO_2 shown in Fig. 7.6 (146).

The real part of the permittivity ϵ' of the dielectric 1 is presumed to be 2.7 within band of interest. The electric tangent delta of dielectric losses of dielectric 1 is guessed to be around 0.025. ϵ' of dielectric 2 and 3 are presumed to be 2.2 and 2.7, respectively, within band of interest. Their electric tangent delta of dielectric losses are conjectured to be 0.05 and 0.025, respectively. A constant tangent delta fit are employed across the frequency range of simulation.

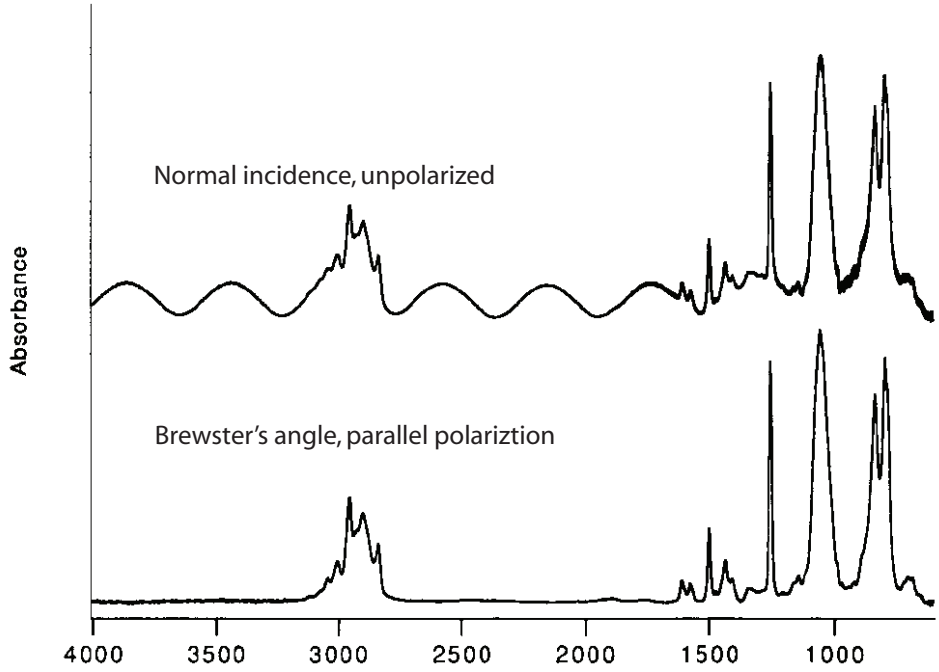

Figure 7.5: The IR absorption spectrum of BCB. Adapted from (145)

7.2 Case studies

7.2.1 Single layer metamaterial operating at 100μm

The first case investigated is a single layer metamaterial consisting of ELC resonators implemented on the top layer metal M10. ELC resonators exhibit strong coupling to applied electric field and negligible coupling to the magnetic field (3). ELC resonators have been used as a negative index material (39), dual-resonant terahertz metamaterial (40), a high speed terahertz modulator (41) and an omnidirectional EM absorber (42). Its dimensions have been carefully tuned to achieve the desired EM response to incident wave. Its dimensions are depicted in Fig. 7.7.

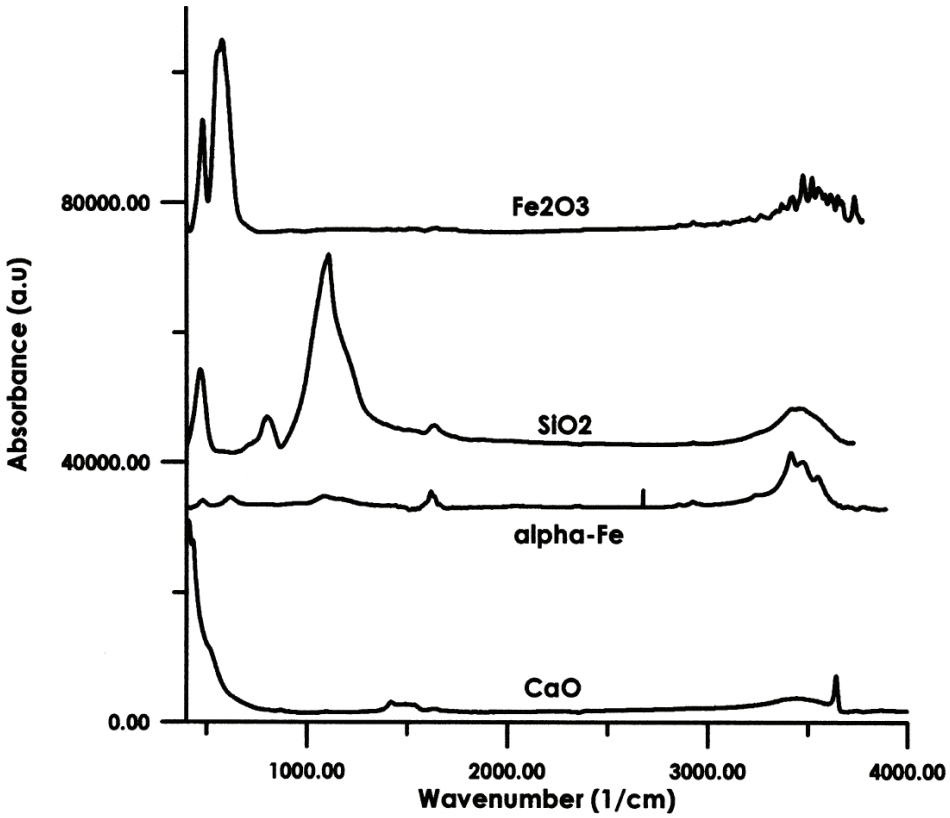

Figure 7.6: The IR absorption spectrum of SiO_2. Adapted from (146)

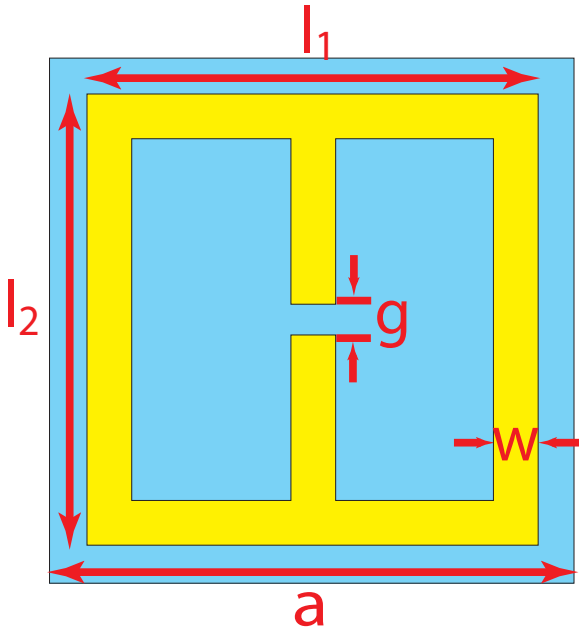

Figure 7.7: Dimensions of a ELC resonator metamaterial implemented on the top metal layer M10 in CMOS metal stack. All units are in μm. l_1=14, l_2=16, g=1.4, w=0.8, a=20

The simulated transmissivity T and reflectivity R is shown in Fig. 7.8.

At its operating frequency of 2.835THz, transmissivity T reaches -25dB and the reflectivity R is almost 0dB.

The electric field inside and around the ELC resonator at the operating frequency is shown in Fig. 7.9.

The surface current at the operating frequency is shown in Fig. 7.10.

This ELC resonator based metamaterial can be used as a spatial band-stop at THz frequencies (147). A negative index metamaterial can be achieved if it is stacked on top of magnetic metamaterials such as SRR resonator (148). The operating wavelength of this ELC resonator

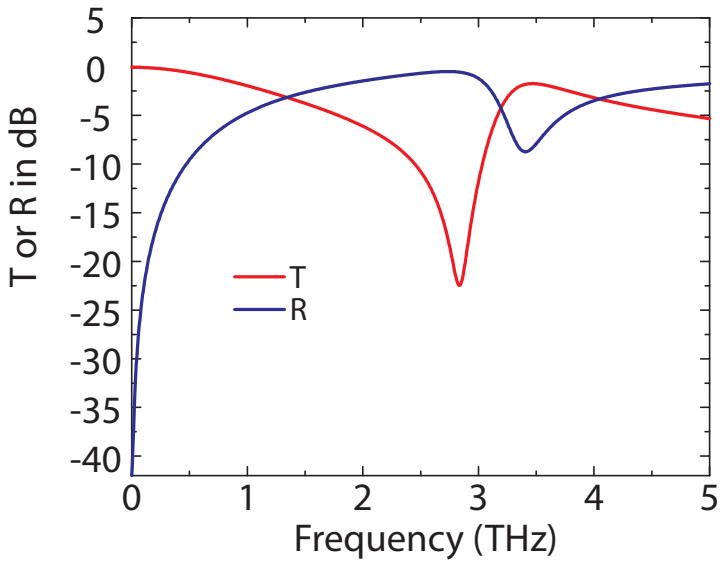

Figure 7.8: Simulated transmissivity T and reflectivity R of an ELC resonator metamaterial implemented on the top metal layer M10 in CMOS metal stack

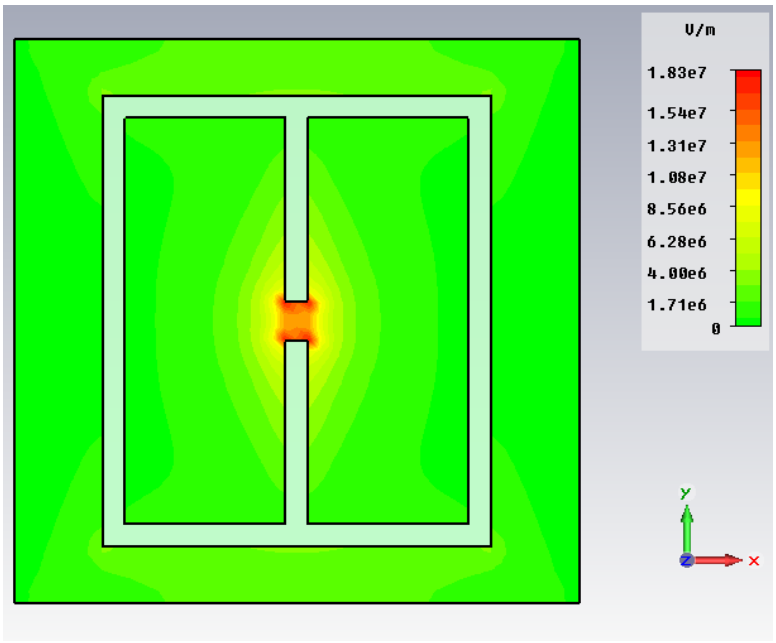

Figure 7.9: Electric field distribution of an ELC resonator metamaterial implemented on the top metal layer M10 in CMOS metal stack

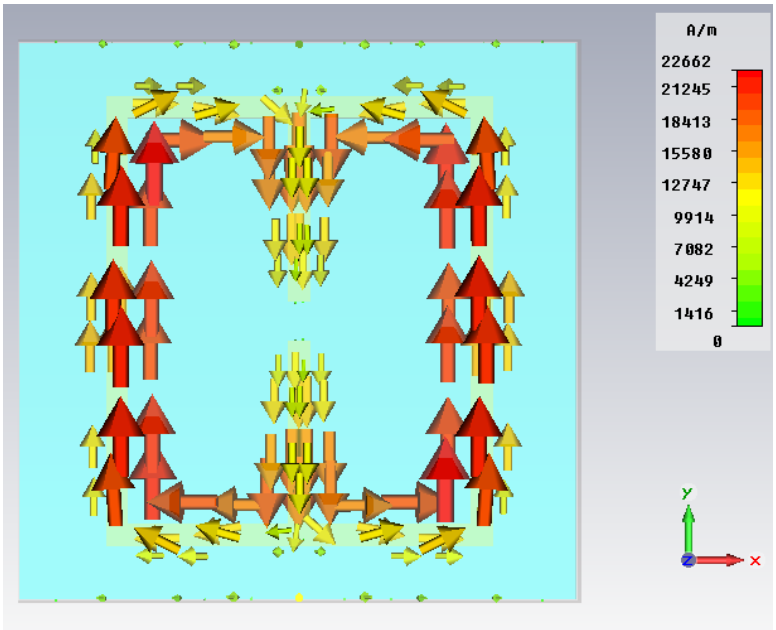

Figure 7.10: Surface current distribution of an ELC resonator metamaterial implemented on the top metal layer M10 in CMOS metal stack

based metamaterial can be decreased by scaling down its dimensions and the lower limit of its operating wavelength is constrained by the minimum line spacing and width in this metal layer. Additional protection layers on top of the metal layers fabricated by foundries may be lossy and dampen the metamaterial resonance.

7.2.2 Multi-layer metamaterial

7.2.2.1 Stacking of metamaterial layers with different architectures

One of the advantages of using CMOS process is access to multiple layers of metamaterial, so that you can implement multilayered metamaterial designs. In this case, an ELC resonator and SRR resonator are implemented on the M10 and M9 layers, respectively. They have

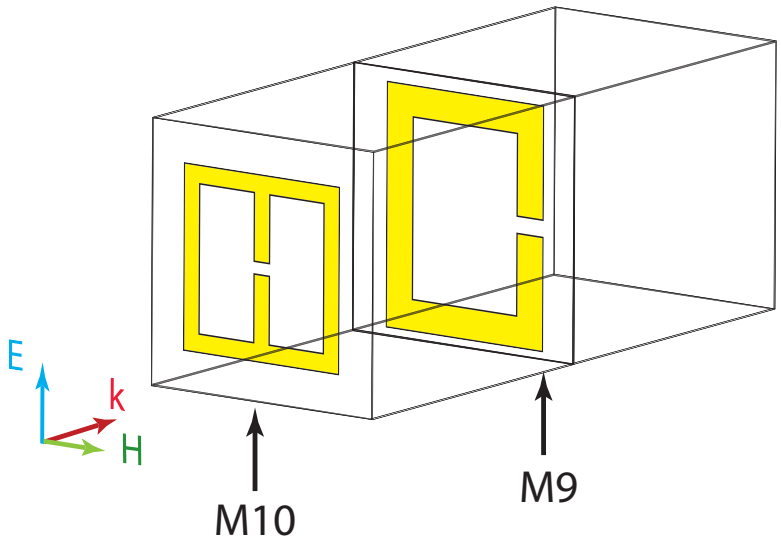

Figure 7.11: 3D view of a two-layer metamaterial composed of ELC resonator on M10 layer and SRR resonator on M9 layer

distinct resonant frequency and form a multi-band metamaterial collectively. The 3D view of this two layer MM design is shown in Fig. 7.11.

The dimensions of the ELC resonator on M10 layer is same as the single layer ELC resonator depicted in Fig. 7.7 except for the lattice parameter a, which is modified to 22μm in this case to accommodate the larger SRR underneath it.

The dimensions of the SRR resonator on M9 layer is shown in Fig. 7.12.

The transmissivity T and reflectivity R of SRR on M9 alone is shown in Fig. 7.13

As shown in Fig. 7.13, the resonant frequency of SRR on M9 is located at 1THz. The cut-wire effect cause another dip in T at around 3.5THz.

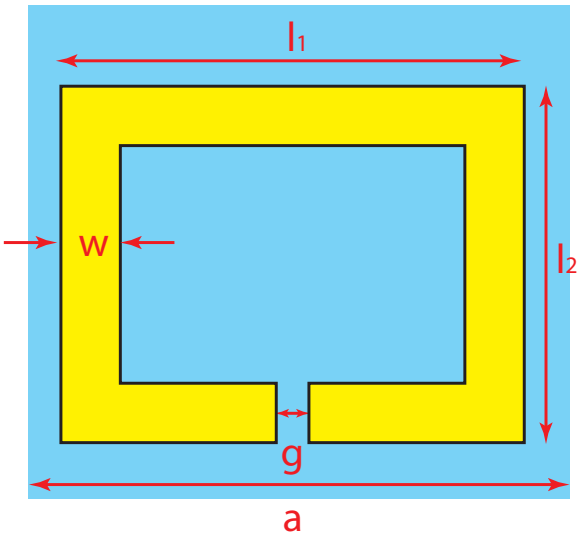

Figure 7.12: Dimensions of SRR resonator metamaterial implemented on the metal layer M9 in CMOS metal stack. All units are in μm. l_1=19, l_2=18, g=0.8, w=0.8, a=22

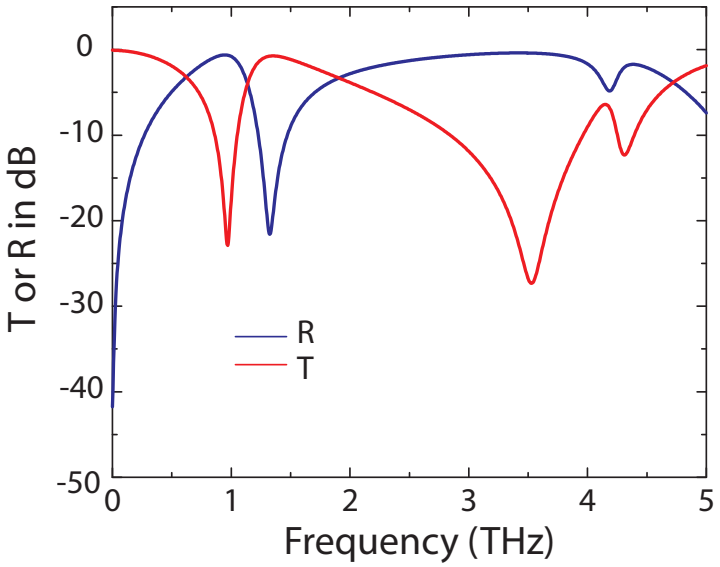

Figure 7.13: Transmissivity T and reflectivity R of SRR resonator on M9.

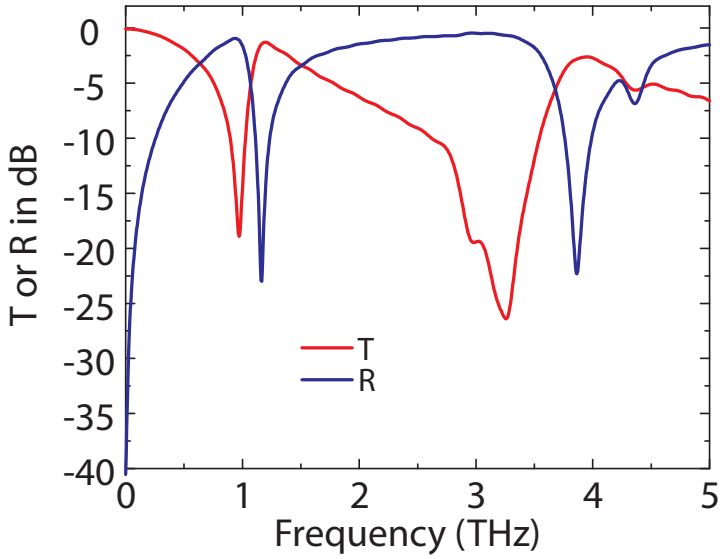

Figure 7.14: Transmissivity T and reflectivity R of a two layer metamaterial composed of ELC resonator on M10 and SRR resonator on M9.

The simulated transmissivity T and reflectivity R of the ELC resonator on M10 is shown in Fig. 7.8. Its resonant frequency is located at 2.835THz.

The transmissivity T and reflectivity R of the stack of ELC on M10 and SRR on M9 are shown in Fig. 7.14.

As depicted in Fig. 7.14, there are two operating frequency bands where T is very low and R is very high. These two frequency bands are around 1THz and 3.2THz, respectively. The resonance at 1THz is contributed by SRR on M9 layer. The resonance at 3.2THz is caused by the combination of resonance of ELC on M10 and the cut-wire effect of SRR on M9.

The alignment of two layers of metamaterial is non-trivial. Misalignment may cause additional coupling that corrupts the desired dual-band response. CMOS foundry has the

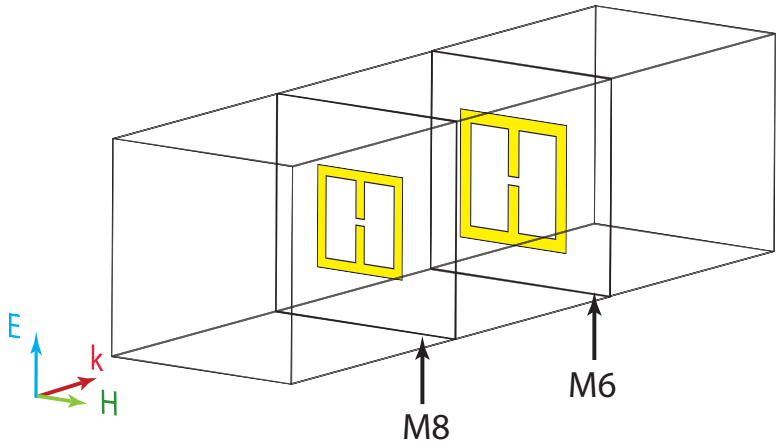

Figure 7.15: 3D view of a two-layer metamaterial composed of ELC resonator on M8 layer and ELC resonator on M6 layer

advanced technology to ensure the alignment of more than ten metal layers. It is very difficult to achieve in the university clean room environment. The dual band frequency response of this metamaterial can be utilized to build a dual band THz antenna featuring compact size and high throughput. It can also be used in hyper spectral imaging system.

7.2.2.2 Stacking of metamaterial layers with same architectures at mid-IR band

In this case, two ELC resonators with different dimensions are implemented on the M8 and M6 layers, respectively. They have distinct resonant frequencies and form a multi-band metamaterial collectively. The 3D view of this two layer MM design is shown in Fig. 7.15.

The simulated transmissivity T and reflectivity R of the single layer ELC on M8 layer is shown in Fig. 7.16.

Its resonant frequency is located at 34 THz.

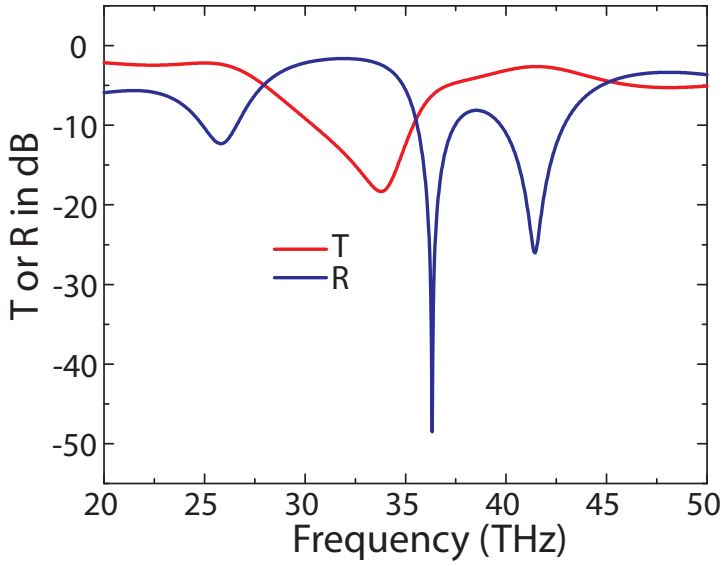

Figure 7.16: Transmissivity T and reflectivity R of a single layer metamaterial composed of ELC resonators on M8.

The simulated transmissivity T and reflectivity R of the single layer ELC on M6 layer is shown in Fig. 7.17.

Its resonant frequency is located at 23THz shown in Fig. 7.17.

The simulated transmissivity T and reflectivity R of this two layer MM is shown in Fig. 7.18.

Both the resonance of ELC resonator on M6 layer, which is located at 23THz, and the resonance of ELC resonator on M8 layer, which is located at 35THz, show up in the simulated transmissivity T and reflectivity R of this two layer MM in Fig. 7.18. The transmissivity T and reflectivity R of the stack of these two ELC resonator can be approximated as the

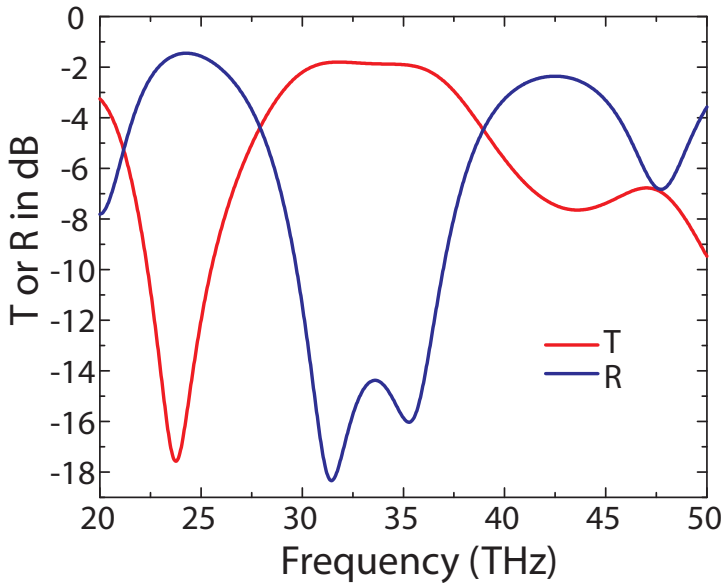

Figure 7.17: Transmissivity T and reflectivity R of a single layer metamaterial composed of ELC resonators on M6.

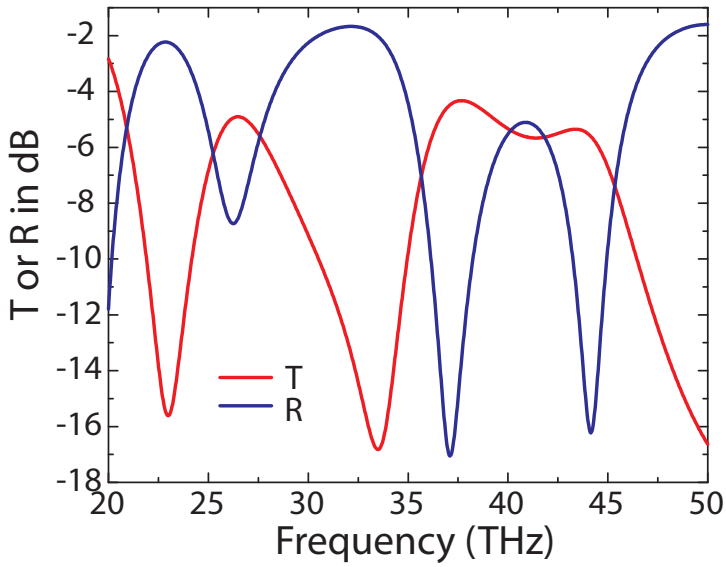

Figure 7.18: Transmissivity T and reflectivity R of a two layer metamaterial composed of a smaller ELC resonators on M8 and larger ELC resonator on M6.

superposition of the EM properties of two individual ELC resonators.

CMOS process allows stacking of over ten layers of metamterials, which offers the opportunity to build a ultra-broadband metamaterial if the resonance frequency of metamaterial on each layer is incremental with small steps. Multiple stacked layers of metamaterial can also be developed into anti-reflection coating and high-reflection coatings (149) that can reduce the undesired scattering of antenna or reflect the out-of-band signal from antenna (149).

7.2.2.3 IR absorber

In this case, the ELC resonator based metamaterial absorber is implemented on the M10 and M9 metal layers. Compared with lower metal layers, the top layers are thicker and have larger minimum feature sizes. For example, the thickness of the top two metal layers (M9 and M10) in the commercial 45nm CMOS process that we use is 1-1.4 μm while the thickness of the 3 metal layers (M8, M7, M6) immediately beneath the M9 and M10 is only 0.25-0.35μm. Moreover, the minimum feature size of M9 and M10 layer is 0.4-1.2μm while the minimum feature size of M8, M7 and M6 is 0.07-0.21μm. One advantage of thick metal layer is that the EM radiation with longer wavelength cannot penetrate through the metal because the incident EM wave decays to almost zero within the skin depth inside the metal. The skin depth is (77):

$$skin\ depth = \delta_s = \sqrt{\frac{2\rho}{2\pi\ f\mu_0\mu_r}} \tag{7.7}$$

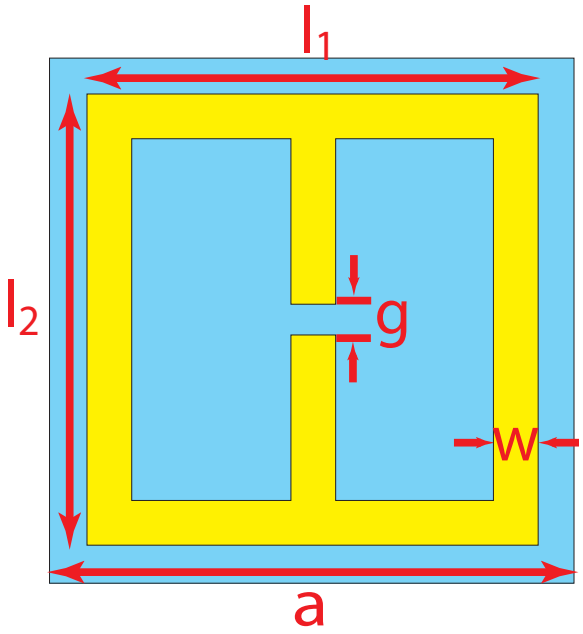

Figure 7.19: Dimensions of a metamaterial absorber implemented on the top two metal layers in CMOS metal stack. All units in μm. l_1=14, l_2=16, g=1.4, w=3, a=20

where ρ is bulk resistivity of metal, f is frequency, μ_0 is permeability constant, μ_r is relative permeability (77). This equation indicates that the lower frequency (longer wavelength) gives rise to greater skin depth.

The dimensions of the ELC resonator, shown in chapter 5 for microwave detector application, are scaled down so that its operating wavelength is shifted to 100μm.

The dimension of the metamaterial absorber is shown in Fig. 7.19

The yellow pattern shows the ELC resonator. The blue pattern shows the ground plane. All units are in μm. l_1=14, l_2=16, g=1.4, w=3, a=20. The thickness of the dielectric spacer between ELC resonator and ground plane is 1.3-1.9μm.

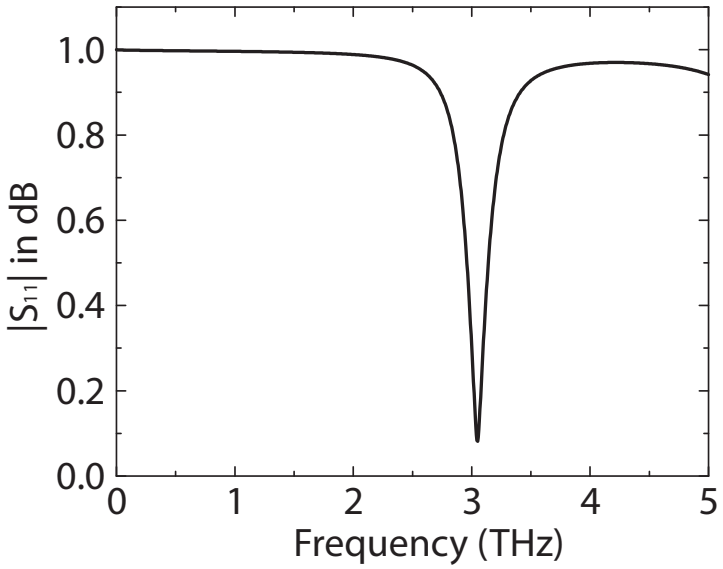

Figure 7.20: $|S_{11}|$ in dB of a metamaterial absorber implemented on the top two metal layers in CMOS metal stack

Fig. 7.20 shows the simulated $|S_{11}|$ in dB of this metamaterial absorber implemented on the top two metal layers in CMOS metal stack.

As depicted in Fig. 7.20, the resonant frequency of this metamaterial absorber is 3 THz. As we discuss in the chapter of loss compensation of metamaterials, the absorptivity A, transmissivity T and reflectivity R can be calculated from S parameters and they have the following relation (91):

$$A = 1 - T - R \tag{7.8}$$

The calculated absorptivity A, transmissivity T and reflectivity R are shown in Fig. 7.21.

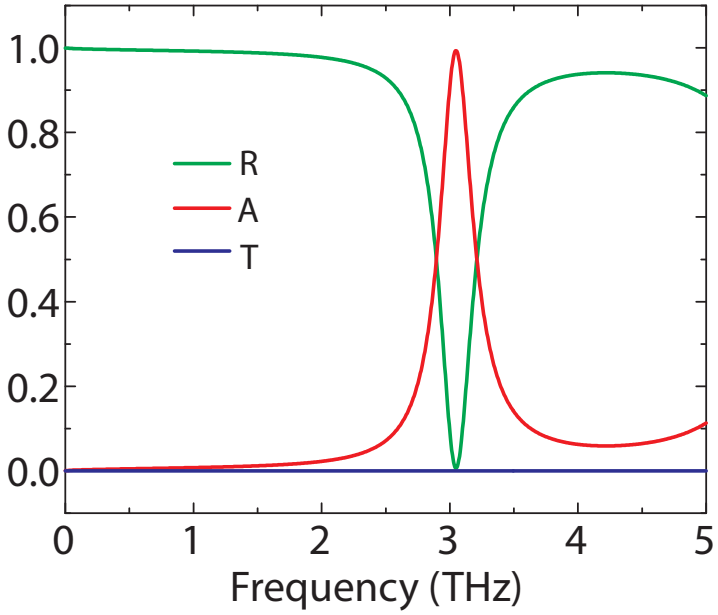

Figure 7.21: Absorptivity A, transmissivity T and reflectivity R of a metamaterial absorber implemented on the top two metal layers in CMOS metal stack

In Fig. 7.21, the absorptivity A of this absorber reaches 100% at 3THz, making it a perfect absorber.

Because of the multiple metal layers in CMOS, we have the greater design freedom of selecting the dielectric spacing between the metamaterial and ground plane through placing metamaterial on the top metal layer and moving the ground plane into any of the metal layers underneath the top metal layer. The dielectric spacing dictates the magnetic resonance response and the effective μ of the metamaterial absorber. Thus, the impedance of the metamaterial can be tuned to match that of the free space at a certain THz/infrared frequency. Multiple metamaterial absorbers with different dielectric spacing can be implemented on the same chip to build a broadband absorber. It can be used to absorb the undesirable side lobe in the antenna radiation pattern.

7.2.2.4 Twisted rod pair based circular polarizer at near infrared

The chirality of a material is defined as materials whose constituent element is different from their mirrored image (150). Chiral materials feature optical activity that can turn the polarization of an EM wave (151). Chiral metamaterials have piqued a lot of interest because they can provide negative refractive index without having negative ϵ and μ (152). Tretyakov proposed to implement a chiral metamaterial using helix as unit cell (153). It is possible to build a bulk material with negative refractive index using this helix based chiral metamaterial (154). Marques suggested a modified version that can be readily integrated in to commercial PCB (155). It has also been reported that he chirality can be achieved by a stack of gammadion (151)

The chirality can also be achieved by stacking up the rod arrays with rotated relative orientation, which is utilized to build a ″right-handed circular polarizer″ or ″left-handed circular polarizer″ (156). The right-handed circular polarizer allows ″right-handed circular polarized (RCP)″ EM wave to pass and stops the ″left-handed circular polarized (LCP)″ EM wave (152). The left-handed circular polarizer is the reverse. When the EM wave is propagating towards $+z$ (positive z direction), the vector of electric field is rotating around z axis clockwise (counterclockwise) for RCP (LCP) (152). At the resonant frequency, the E field is coupled into the two rods composing this twisted rod pair and the inter-coupling between the rods induces the chiral response that makes the twisted rod pair interact strongly to a specific handedness of light (LCP or RCP) (152).

In CST, the unit cell boundary condition is used around the twisted rod pair. The appropriate TE and TM modes are selected in the Floquet ports to excite the ″right-handed circular polarized (RCP)″ or ″left-handed circular polarized (LCP)″ EM waves (152). The unit cell boundary condition requires frequency domain solver and tetrahedral mesh for FDTD simulation.

The architecture and dimensions of this twisted rod pair based circular polarizer at near infrared are adapted from (156). The dimensions of the twisted rod pair are carefully tuned to meet the requirements of 45nm CMOS design rules and shift the its operating frequency to near infrared. The dimensions of the rod on M1 layer is shown in Fig. 7.22 (156).

All units are in μm. l=0.75, w=0.18, a=0.9.

The rod on M2 layer has the same dimensions as that on M1 layer but twisted by 60 degree

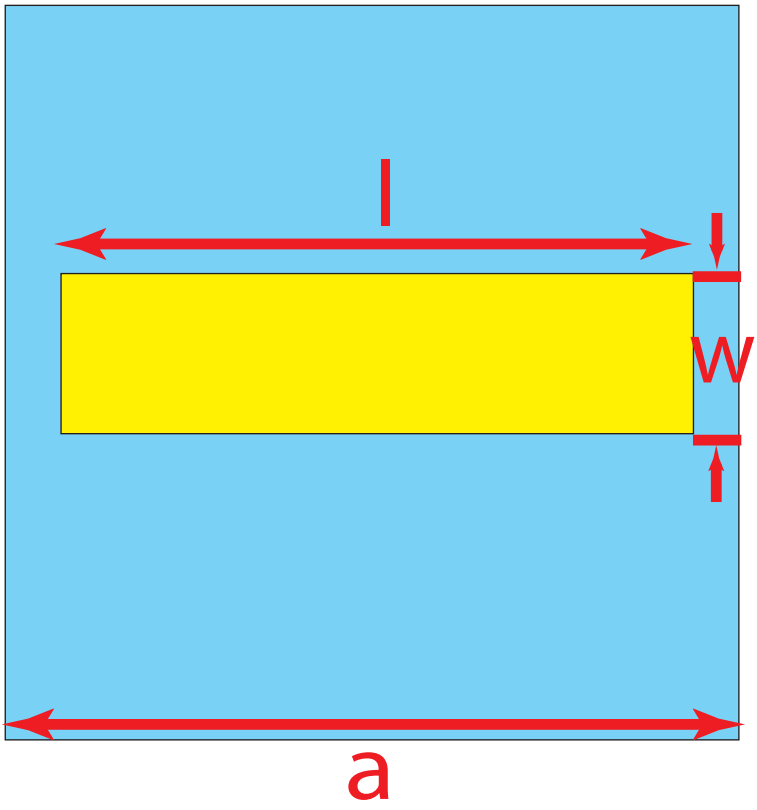

Figure 7.22: Dimensions of rod on M1 layer, All units are in μm. l=0.75, w=0.18, a=0.9 (156)

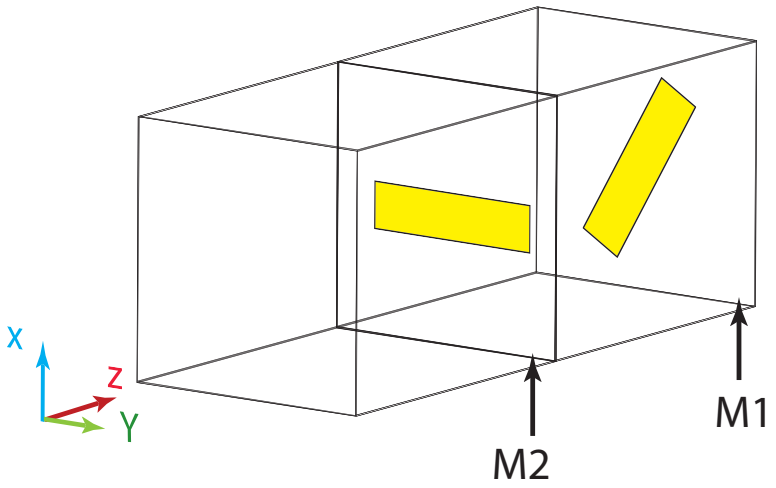

Figure 7.23: 3D view of the stacked twisted rod layers (156)

(156). The 3D view of the stacked twisted rod layers is shown in Fig. 7.23 (156).

The transmission of LCP and RCP are shown in Fig. 7.24.

At the 113.55 THz, the twisted rod pair shows chirality as it interacts strongly with RCP wave while doesn't interact with the LCP wave. Therefore, the RCP wave energy is trapped in the twisted rod pair, which causes low transmission of RCP wave. While there is very weak or no interaction between LCP wave and twisted rod pair. That is the reason why the transmission of LCP wave is high at this frequency. The reverse situation appears at 87.9 THz where twisted rod pair has strong interaction with LCP wave and weak interaction with RCP wave, as shown in Fig. 7.24.

Multiple layers of chiral metamaterial can be implemented in CMOS by stacking up a series of chiral metamaterial with incremental rotation angles. Strong optical activity can be obtained that provides large value of negative ϵ and μ and negative refractive index (151). It also has the property of polarization selectivity between left and right circular polarized EM

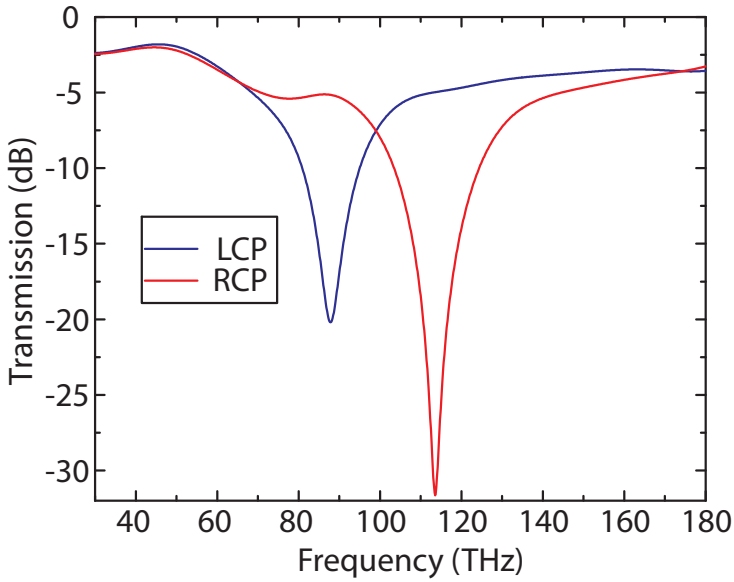

Figure 7.24: Transmission of a circular polarizer implemented on the bottom two metal layers in CMOS metal stack

wave (151). Moreover, a broadband polarization selectivity or negative refractive index can be achieved by stacking up multiple layers of chiral metamaterial and making the frequencies of cross-coupling between the neighboring layers close to each other in the band of interest.

7.2.2.5 Short wire pair based band pass filter type metamaterial

The metamaterials such as SRRs give us band stop transmission response. In many applications, metamaterials with band pass transmission response is desired. The most popular option to make such metamaterials is using complementary metamaterials based on Babinet principle (157). However, these complementary metamaterials such as complementary SRRs can only provide negative permittivity ϵ but cannot provide negative μ (157). Moreover, the incident EM wave vector must be in parallel to the complementary metamaterial plane (157),

which increases the difficulties in simulation setup and measurement characterization. Furthermore, the complementary metamaterials are composed of thin slits in continuous metal sheet, which violates the metal fill density rule of CMOS and thus cannot be implemented on CMOS. In addition to that, the continuous metal plate required in the complementary metamaterials violates the antenna rule that is common in any CMOS process.

An alternative design is used here that simplifies the simulation setup and measurement characterization, which is originally proposed in (158). A pair of short cut-wires are placed on M1 and M3 metal layer in the CMOS metal stack. We can view this short wire pair resonator as a SRR with two open gaps (159). There are displacement current flowing in the two gaps at the end of short wires which creates large capacitance C because of the thin dielectric spacer between M1 and M3 layer (158). In addition to that, there is antiparallel current induced in the short wires in response to the EM radiation with polarization as shown in Fig. 7.26, which creates an inductance L (158). A first order LC resonator is established with this L and C and the resonant frequency is $\omega = \frac{1}{\sqrt{LC}}$ (158).

A pair of continuous cut-wire is placed on both sides of the short-wire pair (158), as shown in Fig. 7.25 and Fig. 7.26, in order to move the negative ϵ frequency band closer to negative μ frequency band (158).

The dimensions of short wire pair with cut-wire on both sides is shown in Fig. 7.25. They are adapted from the design in (158) to fit into CMOS. All units are in μm. $w = 0.4$, $l = 4.1$, $a_y = 4.1$, $a_x = 3.5$, $d = 0.8$.

The 3D view of the short wire pair with cut-wire on both sides is shown in Fig. 7.26.

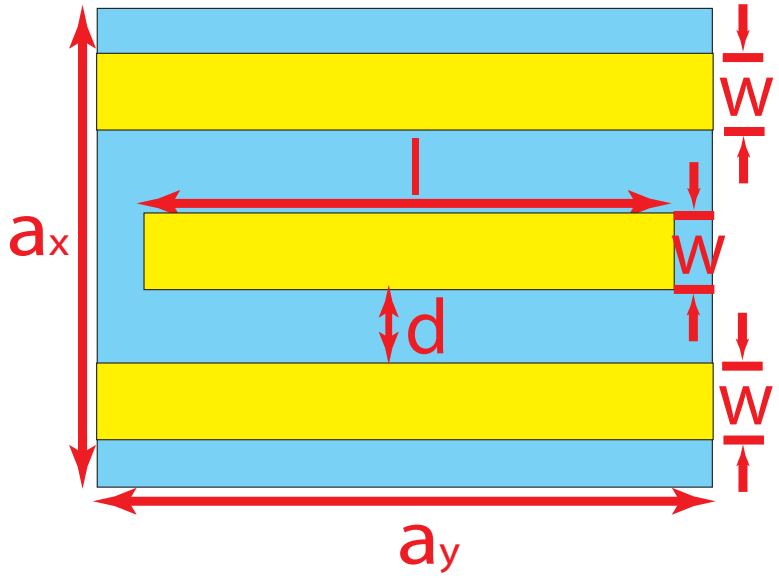

Figure 7.25: Top view of short wire pairs with cut-wires implemented on M3 and M1 metal layers in CMOS metal stack and their dimensions (158)

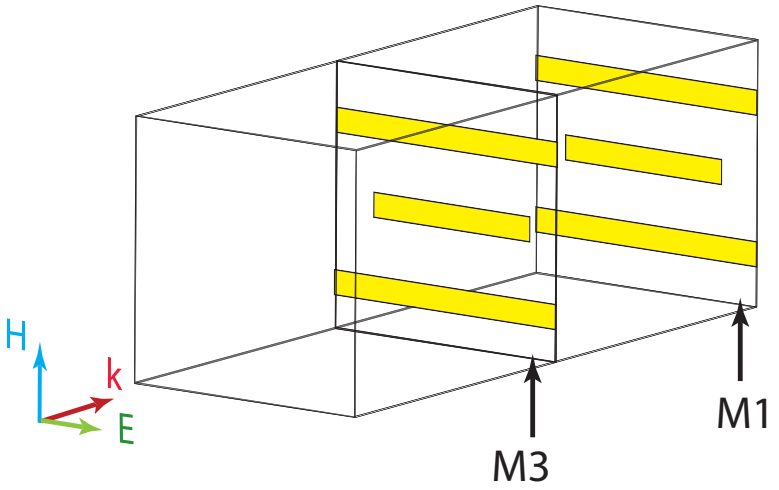

Figure 7.26: 3D view of short wire pairs with cut-wires implemented on M3 and M1 metal layers in CMOS metal stack (158)

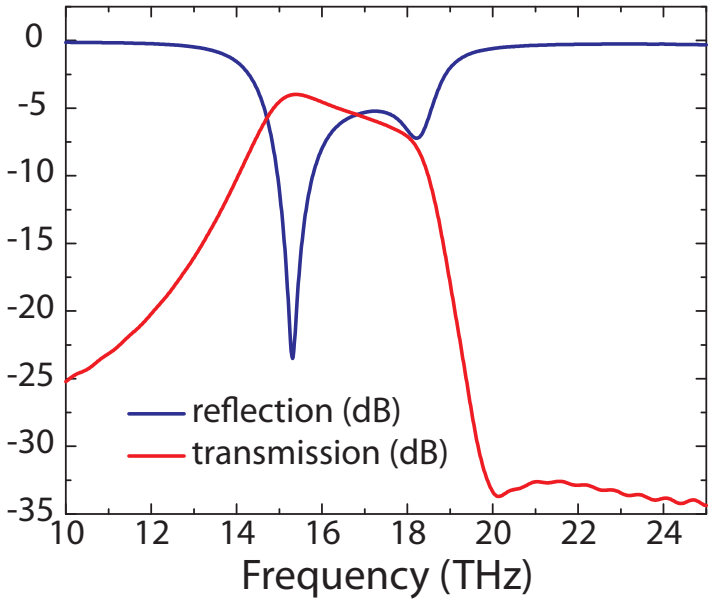

Figure 7.27: The simulated transmission and reflection in dB of short wire pair implemented on M3 and M1 metal layers in CMOS metal stack

The simulated transmission and reflection in dB are shown in Fig. 7.27.

The transmission of this short wire pair based metamaterial is very similar to that of the babinet/complementary metamaterial because it shows high transmission (low reflection) at the resonant frequency and low transmission (high reflection) in the rest of the spectrum. In contrast to babinet/complementary metamaterials, this short wire pair based metamaterial only requires normal incident EM wave to exhibit negative ϵ and μ, which simplifies the measurement setup.

Using the transmission and reflection, the ϵ and μ are extracted using the method proposed in (69, 70).

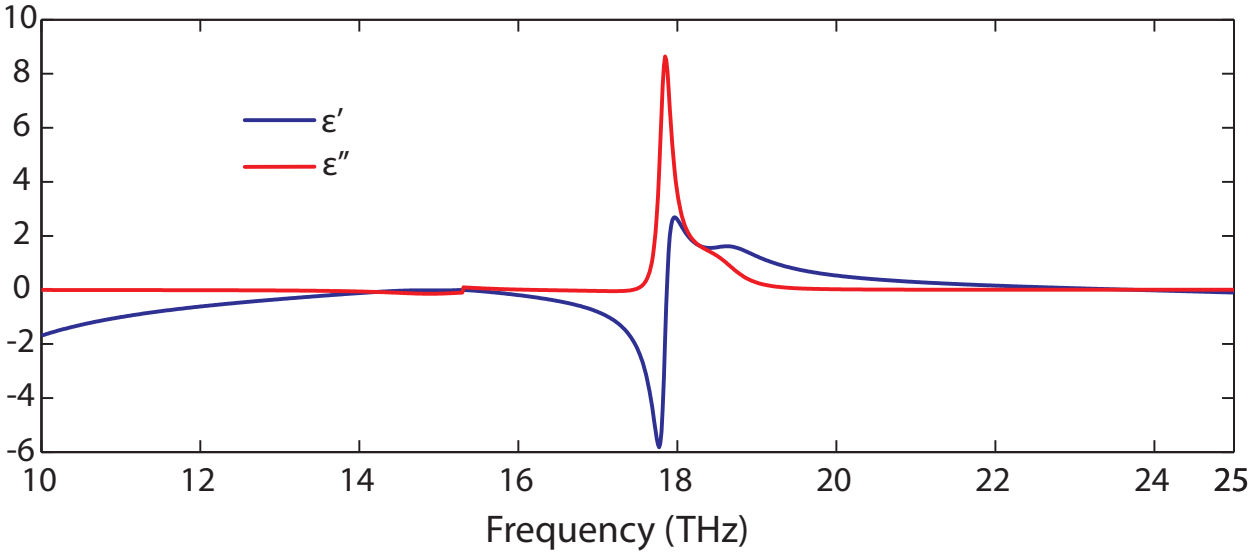

Figure 7.28: The retrieved complex permittivity $\epsilon = \epsilon' + i\epsilon''$ of short wire pair implemented on M3 and M1 metal layers in CMOS metal stack

The retrieved complex permittivity $\epsilon = \epsilon' + i\epsilon''$ is shown in Fig. 7.28.

It shows negative ϵ' from 10THz through 18THz.

The retrieved complex permeability $\mu = \mu' + i\mu''$ is shown in Fig. 7.29.

It shows negative μ' from 10THz through 14THz as well as 18THz to 24THz.

The retrieved complex refractive index $n = n' + in''$ is shown in Fig. 7.30.

In Fig. 7.30, the negative n' appears in the vicinity of 13.74THz and 17.71THz, respectively, which corresponds to the magnetic resonance frequency and electric resonance frequency, respectively. This proves that we obtain negative refractive index and left-handedness at the

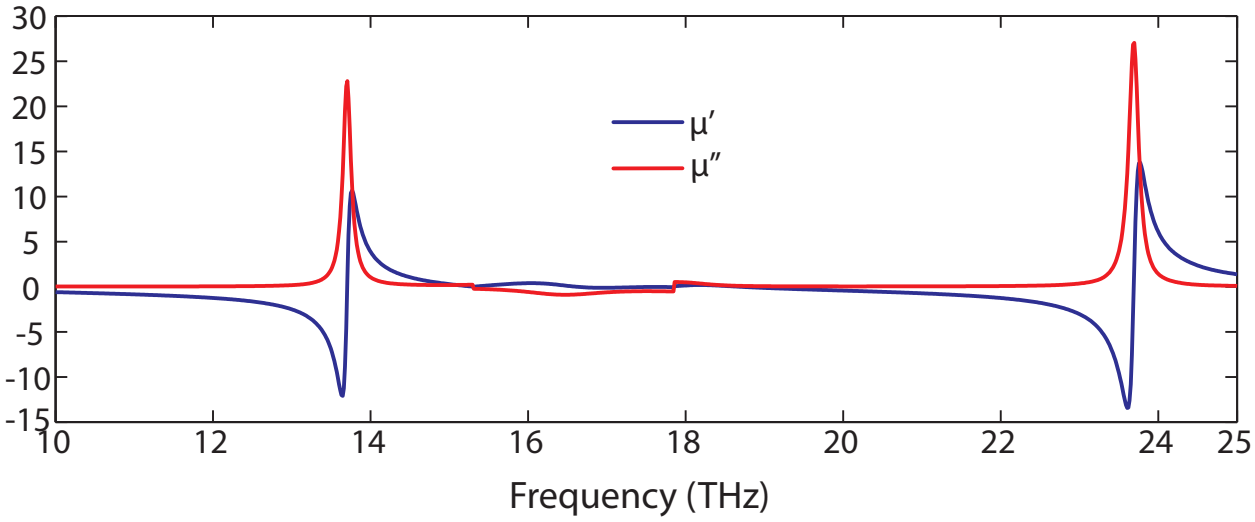

Figure 7.29: The retrieved complex permeability $\mu = \mu' + i\mu''$ of short wire pair implemented on M3 and M1 metal layers in CMOS metal stack

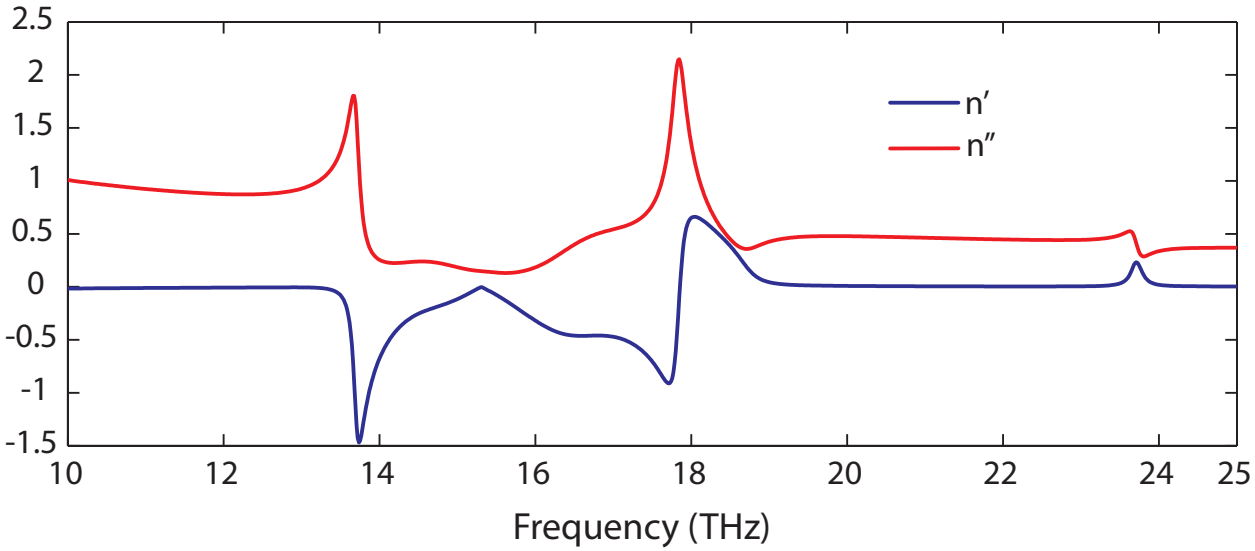

Figure 7.30: The retrieved complex refractive index $n = n' + in''$ of short wire pair implemented on M3 and M1 metal layers in CMOS metal stack

mid-IR frequency using this short-wire pair structure.

7.2.2.6 3D Metamaterial

Metamaterials must be made 3D to satisfy the requirement of bulk medium (160). 3D metamaterials are difficult to fabricate because they require many stacked layers that are aligned accurately (160). These requirements are naturally met by CMOS. Moreover, CMOS provides *via*s that can connect different metal layers in its metal stack, which is not readily available in other nanometer scale fabrication technique. The *via*s can be used as part of metamaterial inclusions, providing the opportunity of fashioning more complicated 3D metamaterial structure.

Here, one 3D metamaterial structure composed of not only metal layers but also *via*s in CMOS is explored. The structure of this 3D metamaterial is originally proposed by Wang *et al.* in (161). Its structure and dimensions have been modified to be implemented in CMOS. The perspective, top and bottom view of this 3D metamaterial is shown in Fig. 7.31 (161)

This 3D metamaterial is composed of two identical SRRs, each of which has two gaps, as shown in Fig. 7.31(b) (161). The inner radius of the SRR is 0.31 μm and the outer radius is 0.56 μm. The gap is 0.08 μm wide. The bottom SRR is implemented on M1 layer in CMOS and the top SRR is implemented on M2 layer. The SRR on M2 layer is rotated by 30 degree counter-clockwise. The upper and lower SRRs are connected by two *via*s. The simulated transmission of this 3D metamaterial is shown in Fig. 7.32.

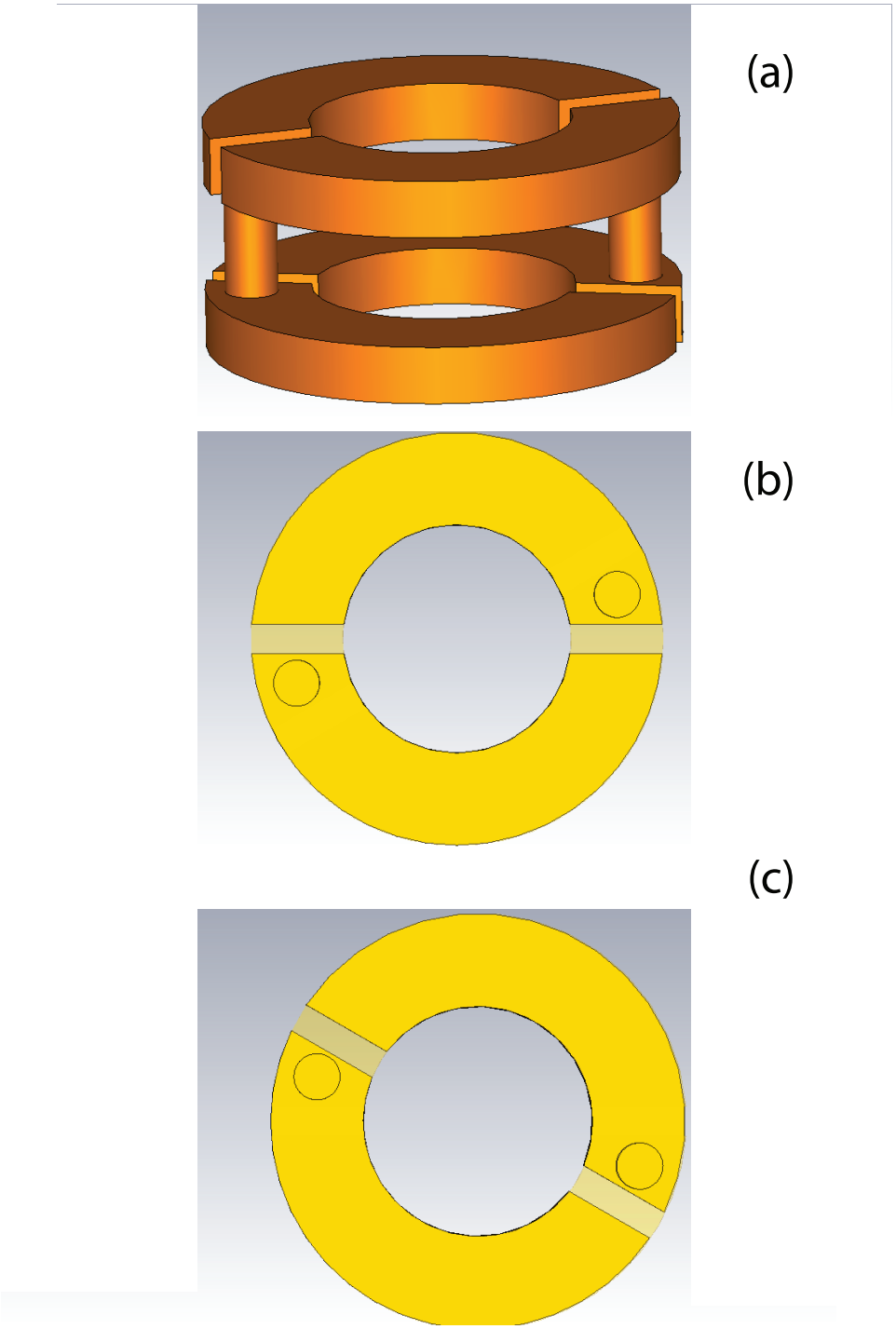

Figure 7.31: (a)Perspective (b)bottom (c)top view of 3D metamaterial in CMOS. the circle in (b) and (c) indicate the *via*s (161)

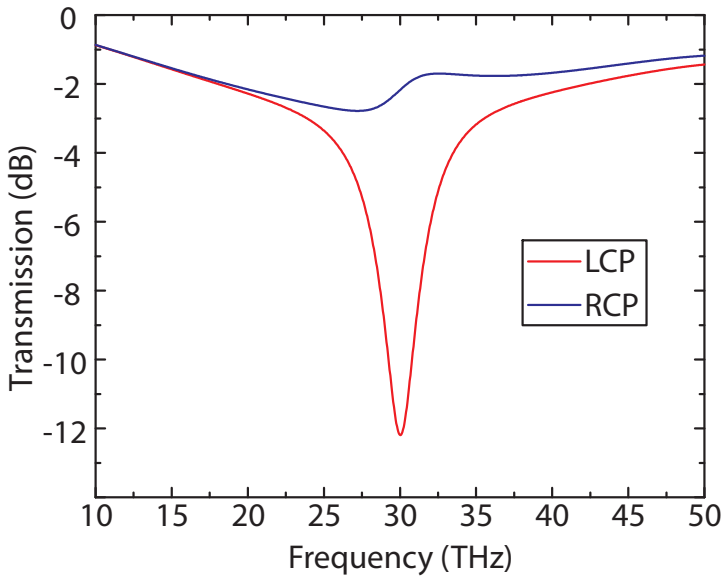

Figure 7.32: The simulated transmission of this 3D chiral metamaterial

As shown in Fig. 7.32, at the resonant frequency of 30 THz, this 3D metamaterial couples to LCP wave strongly that results in a resonant dip in the transmission of the LCP wave. In contrast, this 3D metamaterial shows very little coupling to the RCP wave. It proves that chirality has been achieved by this 3D metamaterial at mid-IR frequency.

It can be envisioned that many other 3D metamaterial can be implemented in CMOS using different combinations of metal layers and *via*s. For example, multi-band or broadband chiral metamaterials can be obtained by stacking up chiral metamaterials with distinct resonant frequencies in CMOS.

7.3 Summary

A variety of metamaterial resonators implemented on CMOS are simulated. CMOS features low cost, high yield and fast throughput, which makes it the mainstream technology for mass production of ICs. The aggressive scaling of CMOS to nanometer dimensions facilitates the fabrication of nanometer size IR and optical metamaterials. The CMOS design rules are applied to the metamaterial designs and the simulation results show that these CMOS based metamaterials have the similar EM properties as those of custom-fabricated metamaterials. This proves the feasibility of fabricating metamaterials in CMOS, making CMOS an ideal option for mass production of metamaterial devices at THz/IR/optical frequencies. The number of options for fabricating metamaterials in CMOS process is numerous, nevertheless there are restrictions imposed due to finite sizing and minimum spacing rules.

8

Metamaterial Enhanced Mid-IR Detector Array

8.1 Background

Mid-IR detectors have interested the defense industry for night vision and heat tracking applications since 1970s (162). A variety of mid-IR detector products are available in the market but the most interesting ones are the uncooled, low cost and light weight technologies for ubiquitous use. Such detectors can also find applications in consumer applications such as night vision cameras for home security and for industrial process monitoring. It has been reported that the microbolometer is the most popular uncooled IR detector technology (162). Its basic principle is to detect the change in temperature induced by the incident

IR radiation (162). The dominant microbolometers are made of vanadium oxide (163), amorphous silicon (164) and silicon diodes (165). Utilizing specialty materials often require custom fabrication processes which are expensive. Moreover, additional effort and expense is incurred in integration with readout integrated circuits. It would reduce the fabrication cost greatly if we can implement the entire IR detector including the optical absorber and sensing element on the standard CMOS process that one uses for readout integrated circuits (ROIC). One example of such single chip mid-IR detector is antenna coupled far-infrared detector implemented in 90 nm bulk CMOS (166). Authors of this work implemented a broadband, planar antenna on one of the metal layers in the metal stack of standard 90 nm CMOS as IR absorber (166). Its output is guided towards a transistor whose temperature increases when the IR radiation is impinged onto the antenna (166). The entire IR detector is implemented in the same standard CMOS process with no need of expensive pre- or post- processing and packaging (166). However, the pixel size is large in the design, which reduces the resolution of image from a focal plane array based on this pixel. These imagers are typically broadband and do not offer wavelength selectivity.

Metamaterials (MM) are artificially engineered materials composed of sub wavelength, periodic metallic inclusion on dielectric substrate. We can design the electromagnetic properties of metamaterials by tailoring the geometry of their unit cells. Metamaterials have found wide applications in demonstrating negative index of refraction (1, 2), invisible cloaking (3), and perfect lensing (4). Metamaterial resonators may provide different and better alternatives for pixel size, power transfer efficiency from free space to detector. Metamaterial unit cells have been used as perfect absorbers to absorb almost all of the incident electromagnetic (EM) radiation across the EM spectrum including IR (4, 87). One unique property of metamaterial absorber (MMA) is that its impedance can be engineered to match that of the

free space so that nearly all of the incident radiation is absorbed and dissipated as ohmic and dielectric losses around the gap where a high electric field is focused.

A metamaterial detector focal plane array have been experimentally demonstrated in Chapter 5 where the EM radiation power absorbed by each metamaterial unit cell is guided into microwave detector. Metamaterial provides the narrow-band response and high detectivity to the focal plane array. Now the same idea is employed and the metamaterial unit cell is scaled to several micrometer so that its resonant frequency is shifted to mid-IR range and it can guide the absorbed IR energy to IR detector. The advantage of implementing metamaterial devices on CMOS has been elaborated in the previous chapter. Again, the power transfer efficiency from free space to IR detector would be maximized if the impedance of the metamaterial absorber is tuned close to the impedance of free space. The received IR radiation is coupled to a small MOS transistor, heating up its channel and increasing its subthreshold drain-source current (166). This current is then measured using an integrator and readout as a signal proportional to the intensity of the IR radiation captured by this metamaterial detector. Since metamaterial are frequency selective, the output provides a wavelength selective IR output. The pitch size of the pixel is reduced greatly because the metamaterial unit cell is sub-wavelength. Sub-wavelength pixel will facilitate diffraction limited imaging.

8.2 Design

8.2.1 Architecture of Metamaterial enhanced IR detector and EM simulation of it

The cross section of the proposed metamaterial enhanced IR detector is shown in Fig. 8.1, our design is inspired by the antenna coupled THz detector proposed in (166).

The IR sensing elements consist of an ELC resonant, ground plane, a NMOS transistor biased in temperature sensitive subthreshold region and a pair of *via*s guiding the received IR signal to NMOS transistor. The two-layer wire grid polarizer is placed above the ELC resonator.

The dimensions of the ELC resonator is shown in Fig. 8.2. The yellow pattern shows the ELC resonator. The blue pattern shows the ground plane. The white rectangular in the middle represents the cutout opening in the ground plane to let the *via*s go through. All units are in μm. l_1=1.4, l_2=1.6, g=0.14, w=0.3, a=2.5

A cut-through in the ground plane was designed in order to connect the capacitive gap in the middle of the front metamaterial resonator through to the circuit layer, as depicted in Fig. 8.2 in white pattern. The opening in the ground plane was increased to minimize the coupling between *via*s and ground plane as well as tune the magnetic response. The ground plane also helps to shield any undesirable coupling effects between the circuit components and the metamaterial.

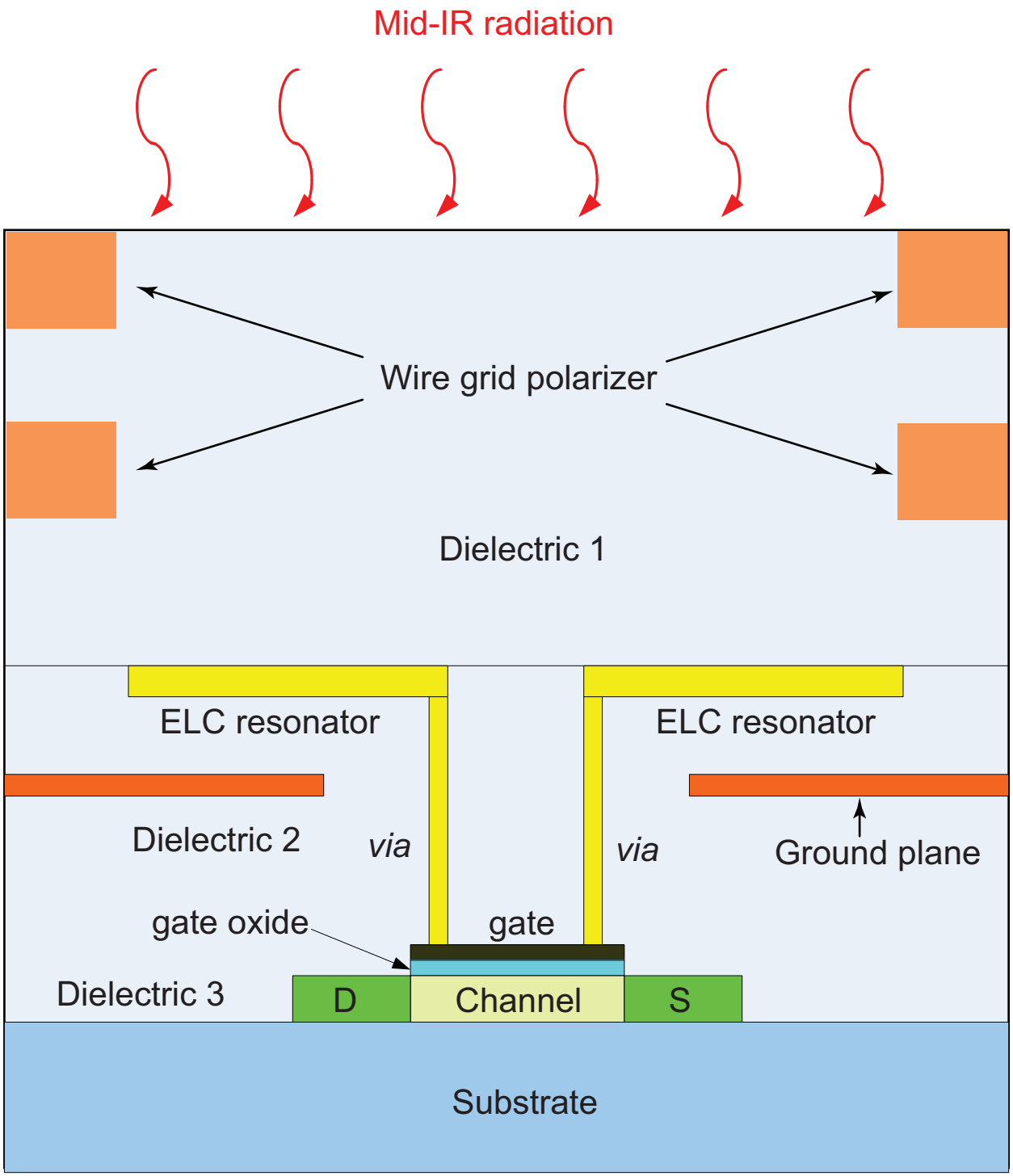

Figure 8.1: Cross section of Metamaterial (ELC resonator) enhanced mid-IR detector. Our design is inspired by the antenna coupled THz detector proposed in (166)

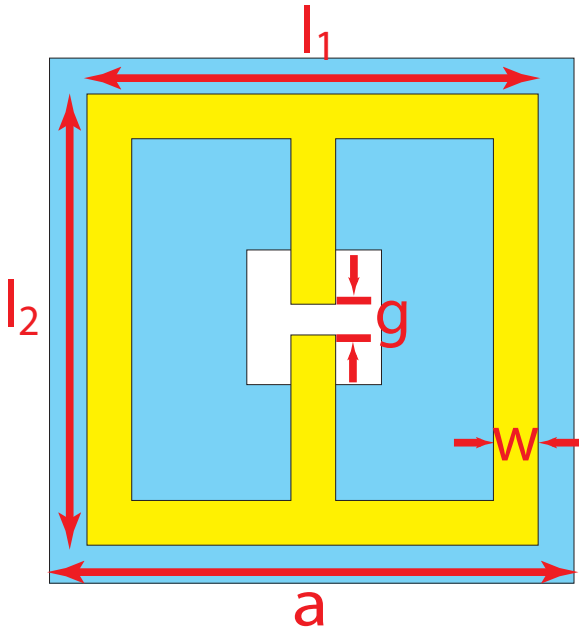

Figure 8.2: Dimensions of ELC resonator on chip. All units in μm. l_1=1.4, l_2=1.6, g=0.14, w=0.3, a=2.5

A pair of *via*s are used to guide the incident IR radiation, which is absorbed by the ELC resonator first to the gate of an NMOS (n-channel metal-oxide-semiconductor FET) transistor. Gate oxide layer isolates the channel from the gate and is made of silicon dioxide. 'D' represents the drain while 'S' denotes the source of the NMOS transistor. Both the drain and source are n^+ region.

Circuit was designed and simulated in Cadence. Metamaterial was simulated in CST microwave studio. Verification was done in both simulation and experiments.

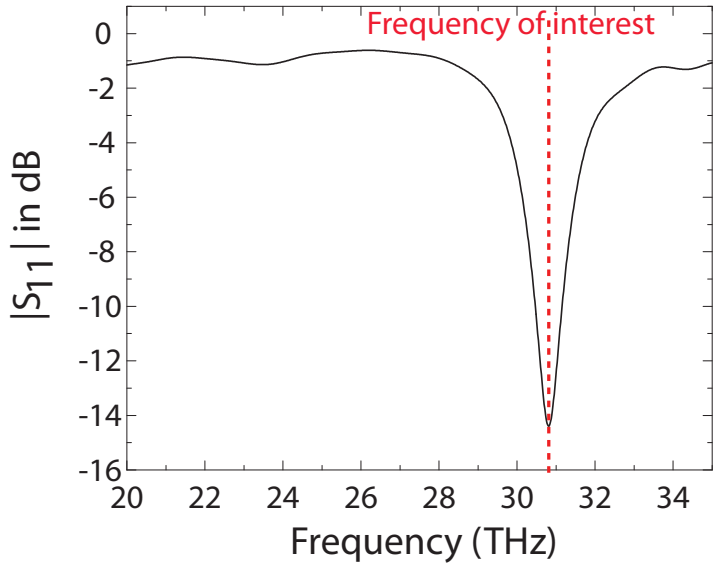

Figure 8.3: Simulation result of the magnitude of reflection | S_{11} | in dB of the ELC resonator

8.2.2 Design and Simulation of CMOS based Metamaterial Unit Cell

These material parameters are fed into CST for 3D EM simulation. Port 1 is defined as free space waveguide port that radiates the IR wave onto the metamaterial enhanced detector. Port 2 is a discrete port across the end of *via*s connecting the ELC resonator to the NMOS transistor that serves as a detector. The simulation setup is very similar to that of the microwave metamaterial detector shown in the Chapter 5.

The simulation result of the magnitude of reflection S_{11} is shown in Fig. 8.3.

The simulation result of the magnitude of power transfer from free space wave guide port (port 1) to detector (port 2) S_{21} in dB is shown in Fig. 8.4.

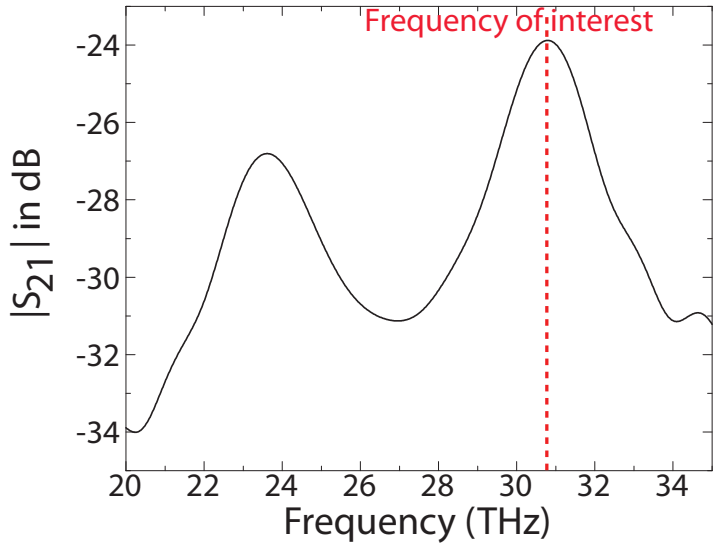

Figure 8.4: Simulation result of the magnitude of power transfer | S_{21} | of the ELC resonator

As depicted in these two figures, the resonant frequency of the metamaterial is 31 THz (9.67 μm), where the | S_{11} | reached its minimum -14dB and the | S_{21} | reaches its maximum value, which is -24dB. This means that 6.5% of the incident IR radiation is transferred to the NMOS transistor as detector and only 1.8% of the incident IR radiation is reflected back to free space at the resonant frequency of metamaterial. The rest of the incident IR radiation power, which accounts for 91.7% of the total incident IR radiation, is absorbed/dissipated in CMOS as dielectric and ohmic losses (88). The ohmic losses are caused by metallic tracies in ELC resonators and *via*s. The power flow in the IR metamaterial coupled detector at the resonant frequency is shown in Fig. 8.5.

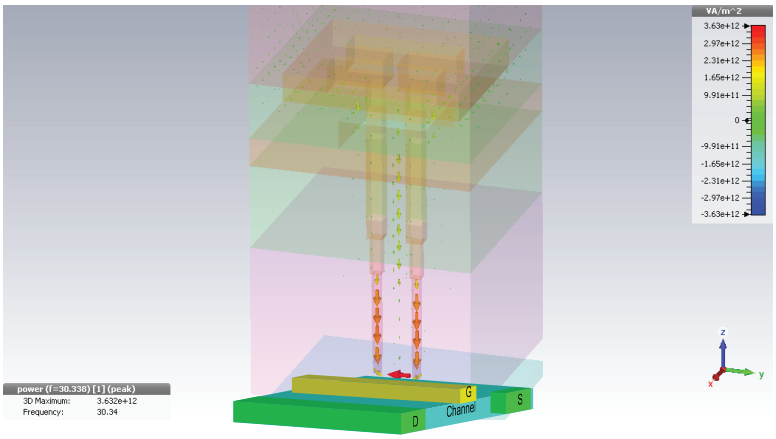

Figure 8.5: The power flow in the IR metamaterial coupled detector at the resonant frequency

8.2.3 Detector and readout circuit

The NMOS transistor is biased at 'off state' in the sense that the voltage across the gate and source, V_{gs}, is $0V$, much less than the threshold voltage (166). Therefore, there is no V_{gs} controlled current flowing through the transistor. There is only subthreshold current flowing through the transistor (166). When the IR radiation power is absorbed by the ELC resonator and guided to the gate of NMOS, it is dissipated as ohmic losses and heat up the transistor (166), as shown in Fig. 8.5. This results in a larger subthreshold current flowing through the transistor (166). The subthreshold current is converted into voltage by integrating the subthreshold current onto a capacitor using an operational transconductance amplifier (OTA), as depicted in Fig. 8.6.

Now the pixel current i_{pixel} flowing through the NMOS transistor is converted into voltage signal V_{out}. They have the following relation (68):

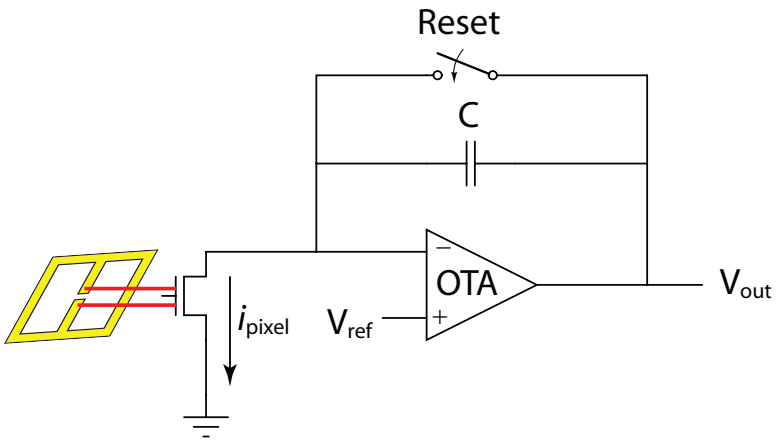

Figure 8.6: Schematic of metamaterial coupled IR detector followed by integrator

$$i_{pixel} = C\frac{dV_{out}}{dt} \tag{8.1}$$

where C is the integration capacitor around the input and output of integrator. The detected IR radiation signal is converted into the change of slope of V_{out}.

A switch is put in parallel with the capacitor C and reset periodically in order to prevent the output of integrator from saturating due to continuous charging of C. The switch is implemented by a PMOS transistor, whose gate is controlled by an off-chip signal *Reset*. The background source drain current caused by room temperature can saturate the output of integrator if the control signal *Reset* is too slow or its duty cycle is too large. The ideal output of the integrator resembles Fig. 8.7.

The frequency of *Reset* signal is 20 KHz and its duty cycle is 40%. The V_{ref} is 0.52 V and the supply voltage of the circuit is 1V.

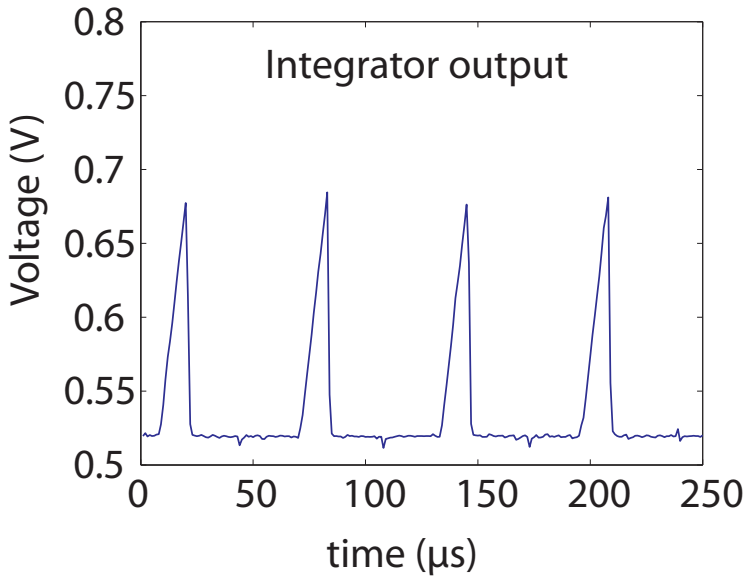

Figure 8.7: Ideal integrator output with pixel current of IR detector as input

The integrator is a closed loop feedback system whose performance relies on the OTA that provides high enough open loop gain. The OTA must provide high open-loop voltage gain, high input impedance and low output impedance to guarantee the integrator functions as desired. Our OTA design is based on the OTA proposed in (167). The schematic of the OTA is shown in Fig. 8.8 (167).

The OTA consists of two stages. The first stage is composed of a differential pair with diode-connected MOS transistor as loads. T0 and T1 are the input differential pair whose inputs V_{in+} and V_{in-} are equal and opposite. The biggest advantage of differential pair is its ability to suppress or reject common mode noise by taking the difference between the inputs V_{in+} and V_{in-} as input and amplifying the difference(168). Common mode noise refers to some interference signal or noise signal in the environment that couples to both V_{in+} and V_{in-} undesirably(168). Although both V_{in+} and V_{in-} are corrupted, the difference between them is clean (168).

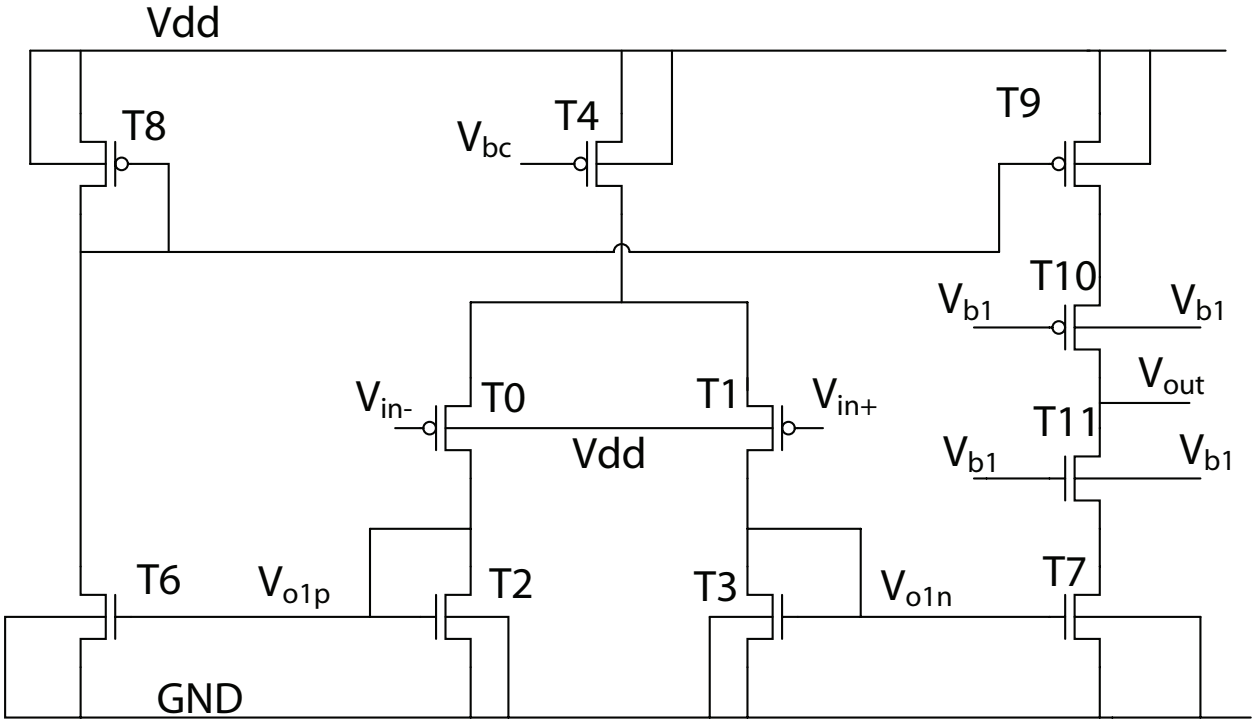

Figure 8.8: The schematic of OTA (167)

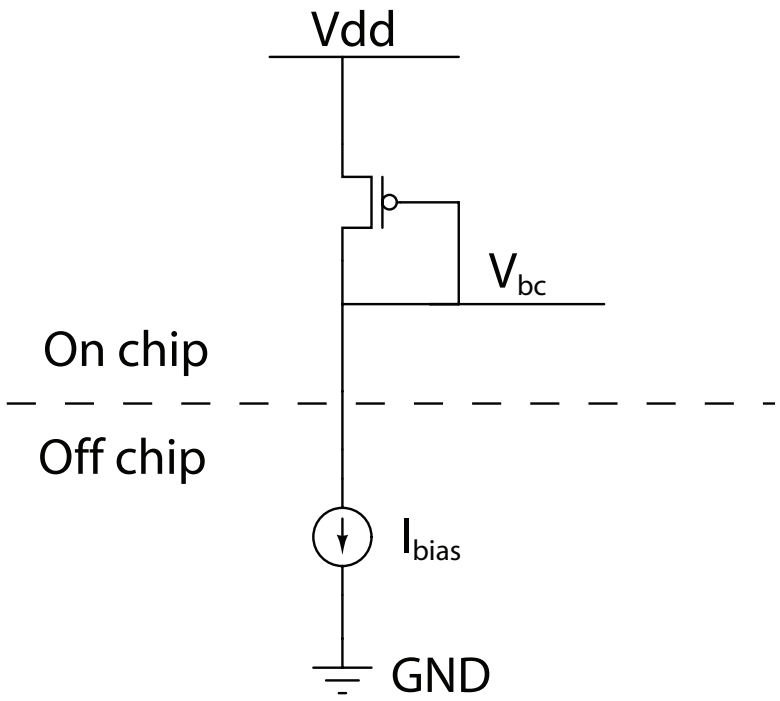

Figure 8.9: The schematic of bias voltage generator

T2 and T3 are diode-connected MOS loads of the input differential pair T0 and T1. T4 provides the bias current for the input differential pair T0 and T1. The gate of T4, which is called V_{bc} in Fig. 8.8, is connected to biasing circuit as shown in Fig. 8.9.

The DC biasing circuit is implemented on chip with external current input as shown in Fig. 8.9. In the simulation, I_{bias} is set to be 3μA. Due to the process, voltage and temperature (PVT) variation, the bias voltage required by the OTA after fabrication may be quite different from the simulated value. The bias current can be easily tuned externally to compensate for PVT variation.

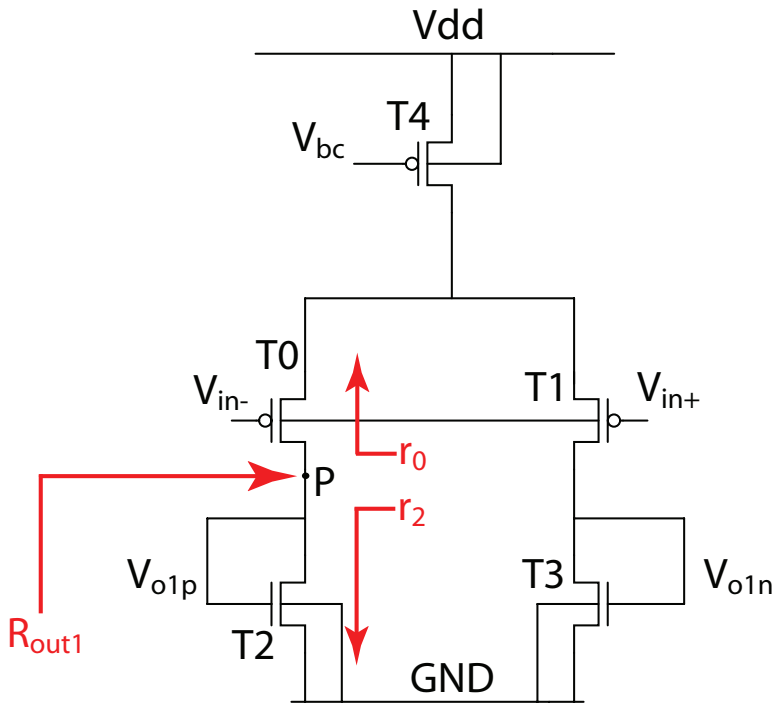

Figure 8.10: The schematic of the first stage of OTA (167)

The voltage gain of the first stage of this OTA, which is

$$A_{v1} = \frac{V_{o1p}}{V_{in-}} \tag{8.2}$$

can be obtained by analyzing half-circuit of fully differential architecture. The first stage of this OTA is shown in Fig. 8.10.

A_{v1} is determined by the transconductance g_{m0} of input transistor T0 and the output impedance R_{out1} looking into the output of the first stage, which is shown at node P in Fig. 8.10. They have the following relation:

$$A_{v1} = \frac{V_{o1p}}{V_{in-}} = -g_{m0}R_{out1} \tag{8.3}$$

The output impedance of first stage R_{out1} is composed of the output impedance r_0 of transistor T0 in parallel with the output impedance r_2 of the diode-connected transistor T2 approximately. $r_2 = \frac{1}{g_{m2}||g_{ds2}}$ for the diode-connected transistor T2. r_0 of transistor T0 is much large than the output impedance r_2 of the diode-connected transistor T2. Therefore, r_2 is dominant in the total impedance of this parallel circuit, and the gain becomes (168):

$$A_{v1} \approx -\frac{g_{m0}}{g_{m2}} \tag{8.4}$$

The transconductance g_m has the following relation with the transistor parameter (168):

$$g_m = \sqrt{2\mu_p \, C_{ox} \frac{W}{L} I_D} \tag{8.5}$$

, where μ is mobility of charge carrier in the channel, C_{ox} is the oxide capacitor formed between the gate and the channel, W and L are the width and length of the transistor, respectively, and I_D is the current flowing through the channel of the transistor (168). Among these parameter, μ and C_{ox} are constants decided by the process. W, L and I_D are controllable.

If the equation 8.5 is substituted into equation 8.4, it is obtained (168):

$$A_{v1} \approx -\sqrt{\frac{\mu_p(\frac{W}{L})_0}{\mu_n(\frac{W}{L})_2}} \tag{8.6}$$

where the μ_p is the mobility of charge carrier in the channel of PMOS transistor, μ_n is the mobility of charge carrier in the channel of NMOS transistor, $(\frac{W}{L})_0$ is the width over length ratio of transistor T0 and $(\frac{W}{L})_2$ is the width over length ratio of transistor T2 (168). Thus, the gain the of 1st stage of OTA can be tuned by tweaking the width and length of transistor T0 and T2.

A cascode architecture is used in the second stage of the OTA to increase its gain. The cascode topology is essentially a cascade of common source stage and a common gate stage (168). As depicted in Fig. 8.8, the T7 and T11 form a cascode stage. The output impedance of this cascode stage is $g_{m11}r_{o11}r_{o7}$ if we ignore the body effect. r_{o11} and r_{o7} are the intrinsic output impedance of T11 and T7, respectively. The transconductance of the cascode stage is g_{m7}. The total voltage gain provided by the cascode stage A_{v2} is approximately (168):

$$A_{v2} \approx -g_{m7}((g_{m11}r_{o11}r_{o7})||(g_{m10}r_{o10}r_{o9})) \tag{8.7}$$

, which is twice as much as the intrinsic gain of T7 (168).

The overall gain of the two stage OTA is the product of the gain of first and second stage:

$$A_v \approx \ A_{v1}A_{v2} \approx \ \frac{g_{m0}}{g_{m2}} g_{m7}((g_{m11}r_{o11}r_{o7})||(g_{m10}r_{o10}r_{o9})) \tag{8.8}$$

The AC analysis is performed on this OTA. The gain bandwidth product of the OTA is 7.3 MHz. Its DC gain is 63.34dB and its phase margin is 55 degree at the unity-gain bandwidth.

A 32 by 32 array of metamaterial enhanced detectors are populated on the chip with row column decoder and readout circuits. The schematic of the array is shown in Fig. 8.11.

Each pixel contains an ELC resonator, a NMOS transistor as IR detector and a PMOS transistor as row selection transistor. The layout of one pixel is shown in Fig. 8.12

The row selection transistor of each pixel is controlled by an on-chip 5 to 32 row decoder outside the detector array. The drain-source current of each pixels in on column are merged and fed into one of the four inputs of the integrator. The four inputs of the integrator are controlled by the 5 to 32 column decoder outside the detector array.

The microphotograph of the fabricated chip and layout of the system drawn in cadence are shown in Fig. 8.13

Focused ion beam (FIB) is used to etch the materials covering the metamaterial pixel array. A scanning electron microscope (SEM) picture showing exposed 4 by 4 metamaterial pixel array is presented in Fig. 8.14.

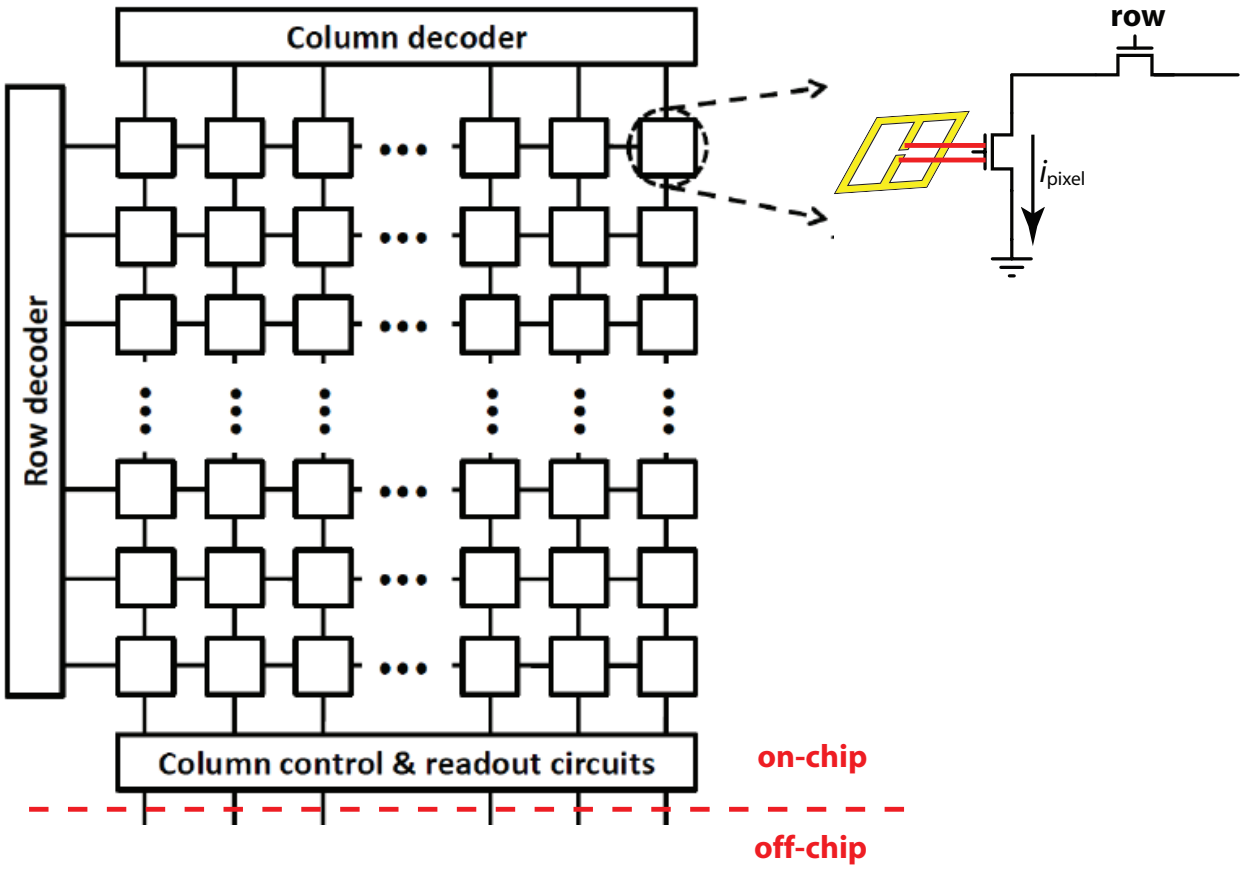

Figure 8.11: Schematic of the metamaterial enhanced IR detector array. Part of the figure is adapted from (169)

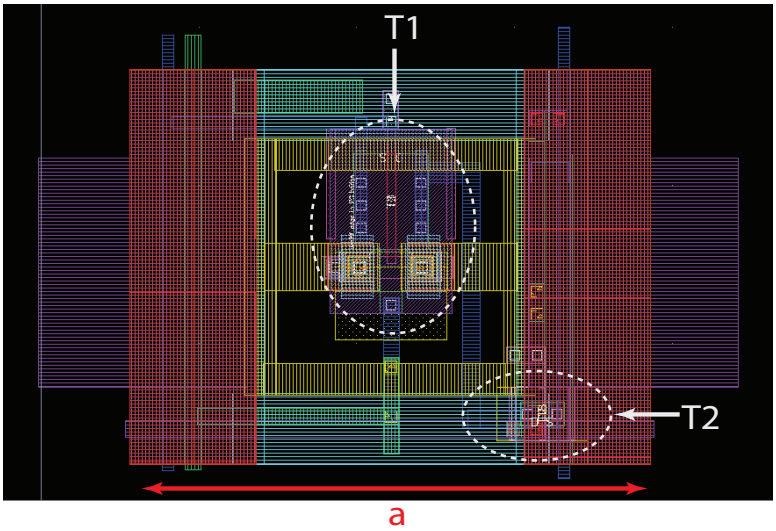

Figure 8.12: Layout of a single pixel, a is 3.3 μm. T1 is the IR detector. T2 is the row selection transistor

8.3 Measurements

8.3.1 Optical setup

In order to test the responsivity of our metamaterial enhanced IR detector, a mid-IR optical setup is custom designed and implemented. The most critical component in the optical setup is the source. We use IR blackbody source as an IR radiation source. Every object that has achieved thermodynamic equilibrium with its environment radiates electromagnetic power across the entire IR spectrum, which is termed blackbody radiation (170). The typical radiation of blackbody source over the spectrum is shown in Fig. 8.15 (171).

A black-body source with high, stable and controllable temperature is desired to provide the stable IR radiation within band of interest.

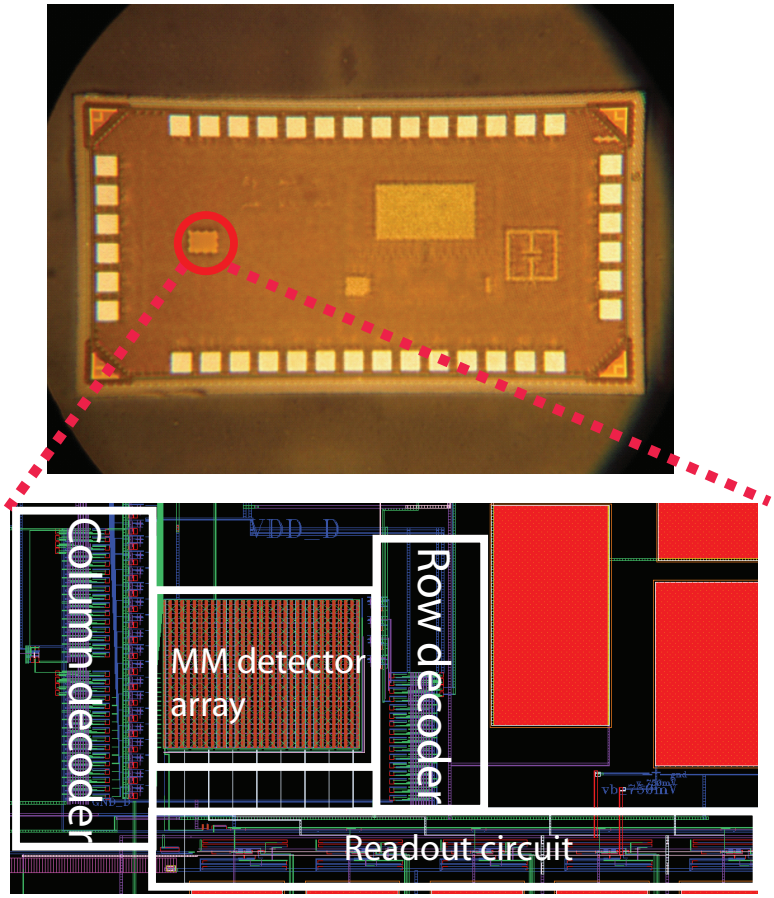

Figure 8.13: The microphotograph of the fabricated chip and layout of the system drawn in cadence

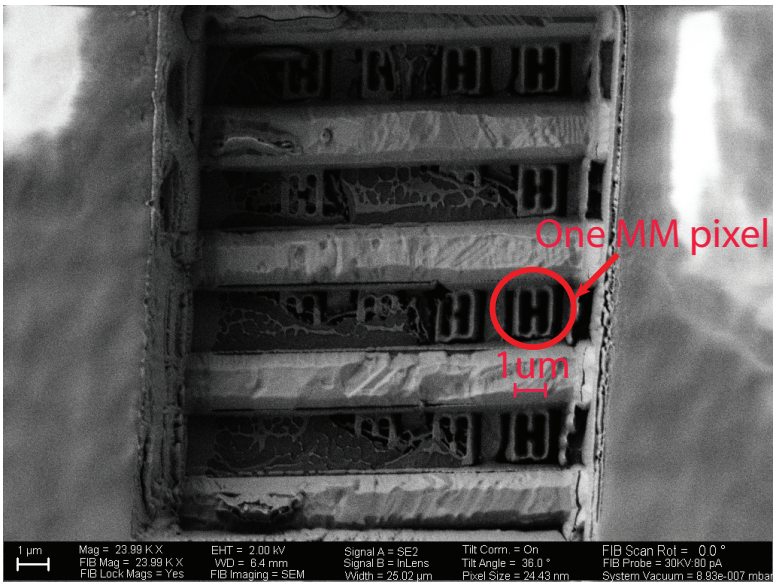

Figure 8.14: A scanning electron microscope (SEM) picture showing exposed 4 by 4 metamaterial pixel array

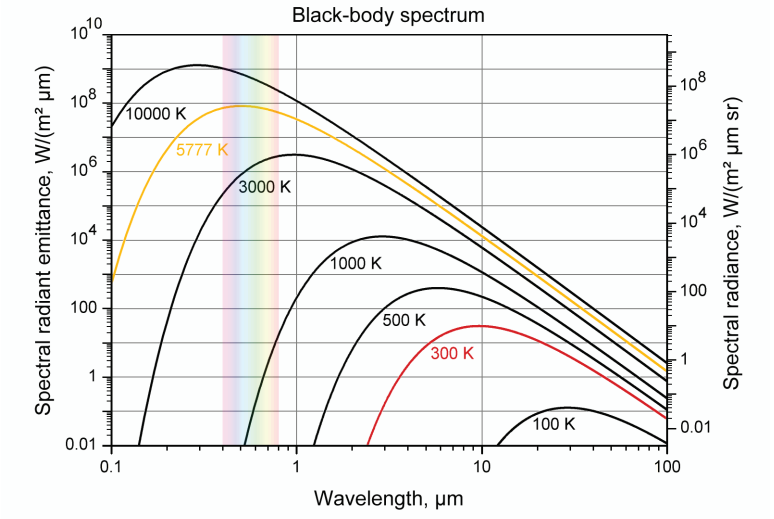

Figure 8.15: The typical radiation of blackbody source over the spectrum (171)

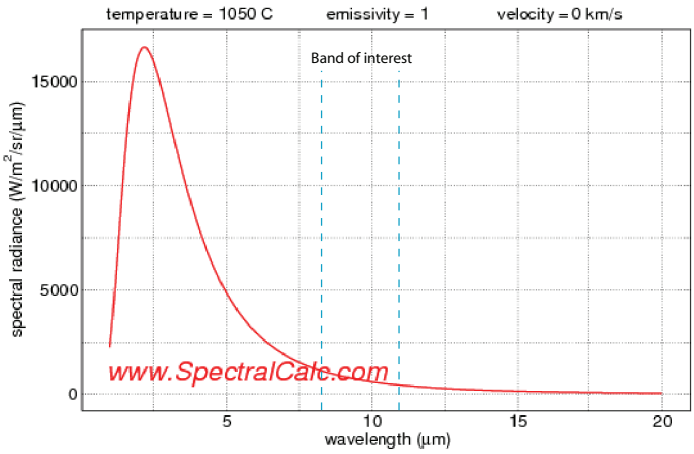

Figure 8.16: The radiation profile of blackbody source at 1050 degree (174)

The first IR source used in the measurement is the IR-518/301 Blackbody System made by Infrared Systems Development Corp. "The IR-518 Radiation Source provides an accurate, stable source of infrared radiation of known flux and spectral distribution" (172). "The IR-301 controller is a microprocessor based PID (Proportional, Integral and Derivative) system for regulating the Blackbody's Radiating Surface and controlling the temperature of the blackbody radiation source IR-518" (173).

In the measurement, the temperature of the blackbody radiation source IR-518 is set to 1050 degree Celsius, which is the upper limit of the temperature range of this blackbody radiation source (173). The radiation profile for this temperature is shown in Fig. 8.16 (174).

8.3.2 Electrical setup for image acquisition

The architecture of the hardware/software platform to read out an image from the IR image sensor is shown in Fig. 8.17. The FPGA sends scanning signal to the IR image sensor

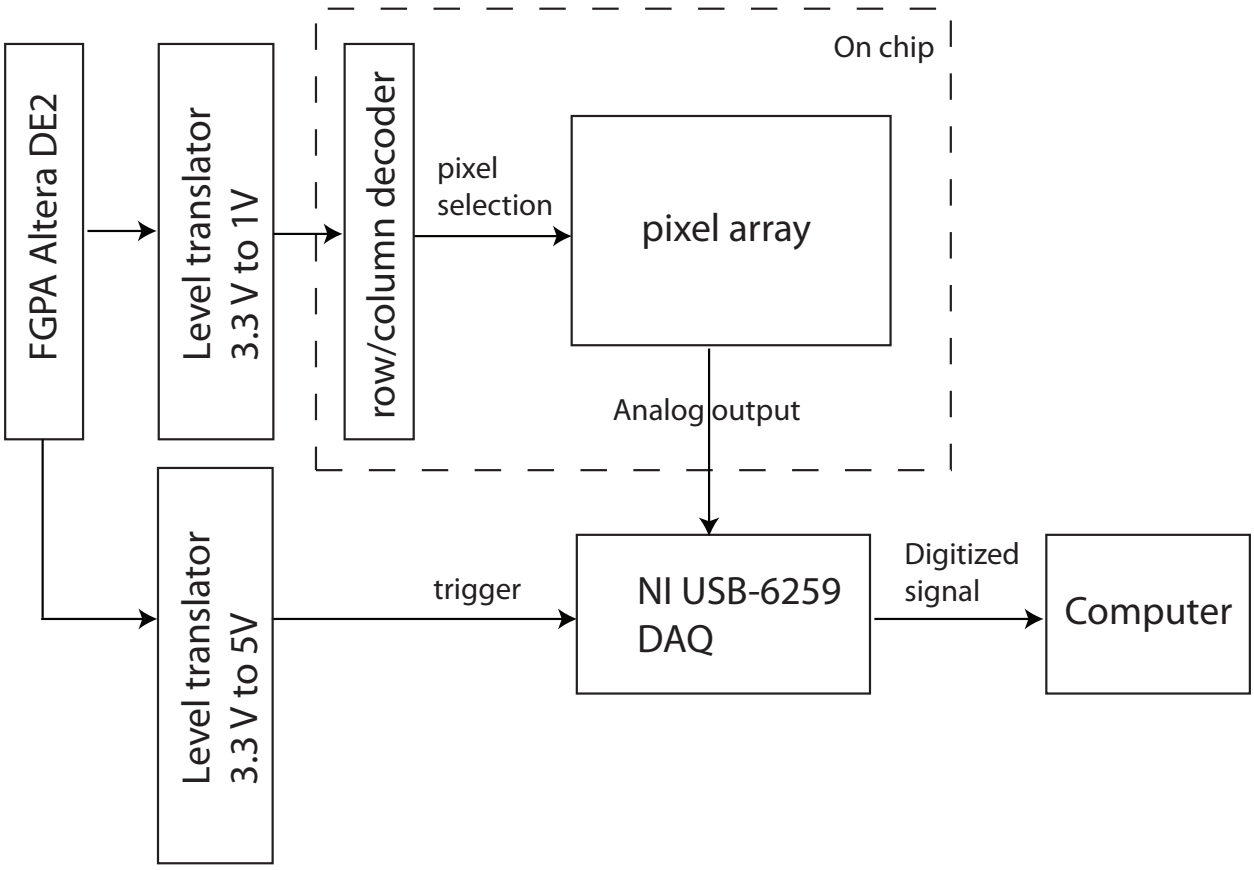

Figure 8.17: The architecture of the hardware/software platform to read out an image from the IR image sensor

through a 3.3 V to 1V level translator. Each pixel in the image sensor is accessed at the speed of 1 to 10Hz. When one pixel is selected, FPGA triggers the NI USB-6259 Data Acquisition Card (DAQ) to read out 250 samples within the period from the pixel currently selected. The number of samples read out is set to 250 because of the speed limit of this USB based DAQ. A 3.3 V to 5V voltage translator is used as an interface between FPGA and DAQ. Therefore, the scanning of pixels on chip and the DAQ card read out are synchronized.

A single metamaterial enhanced detector can be accessed by fixing the address generated by FPGA that is fed into the row/column decoder.

8.3.3 Measurement result

8.3.3.1 Blackbody source test

As mentioned earlier, the temperature of blackbody source is set to its maximum value: 1050 degree Celcius. The blackbody source is placed 15cm away from the IR detector array chip to maintain a high radiation power density on the chip. If the blackbody source is moved farther away for IR detector array, the radiation power diverges and radiation power density on the detector array drops drastically. On the other hand, if the blackbody source is placed too close to the IR detector chip, it will overheat the chip because of its high temperature and renders the chip malfunction.

The address of the detector pixel being accessed is generated by FPGA and fed into the row and column decoder on chip as shown in Fig. 8.17. Initially, the address is fixed and the output of the selected IR detector is recorded.

The output voltage V_{out} of the on-chip integrator connected to the IR detector is recorded before the IR radiation of blackbody source is impinged onto the IR detector array, which is shown in Fig. 8.18.

As discussed in subsection 8.2.3, the output voltage V_{out} of the integrator on chip is a saw tooth waveform because the capacitor around the opamp in the integrator is integrating the pixel current of the NMOS transistor based IR detector at room temperature. The amount of pixel current flowing in the IR detector can be calculated from the positive slope of the

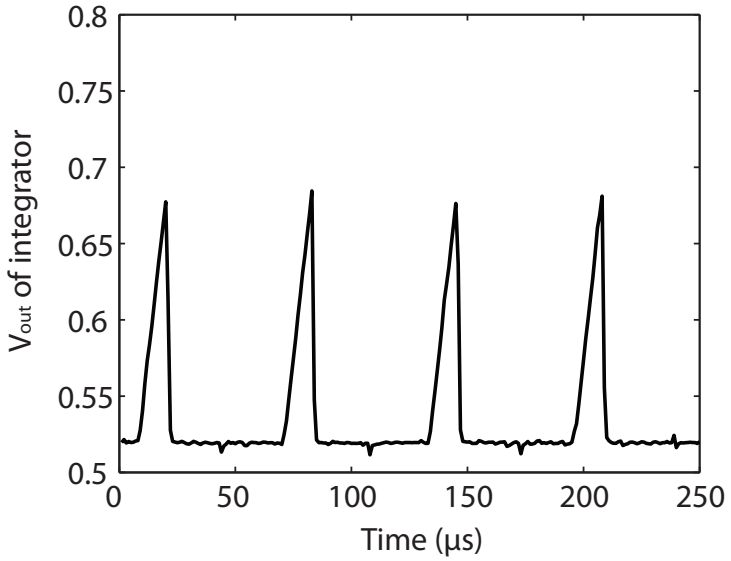

Figure 8.18: The output voltage of the integrator on-chip without IR radiation

saw-tooth waveform. Hence, the first step is to extract the slope. The following equation is used to calculate the slope of the sawtooth wave at the output of the integrator:

$$slope = \frac{V_{out,\ peak} - V_{cm}}{t_{integration}} \tag{8.9}$$

, where $V_{out,\ peak}$ is the peak value of V_{out}, V_{cm} is common mode voltage of V_{out}, $t_{integration}$ is the integration time during which the *Reset* switch around the integrator is open so that the integrator can integrate the pixel current of IR detector onto the capacitor C, as shown in Fig. 8.6. The value of peak in the saw-tooth waveform is varying because of the noise in the environment and test setup. Fluctuation in the common mode voltage of saw-tooth waveform is also observed because of the noise.

When a pixel is selected, its integrator output V_{out} is sampled 250 times, which results in a

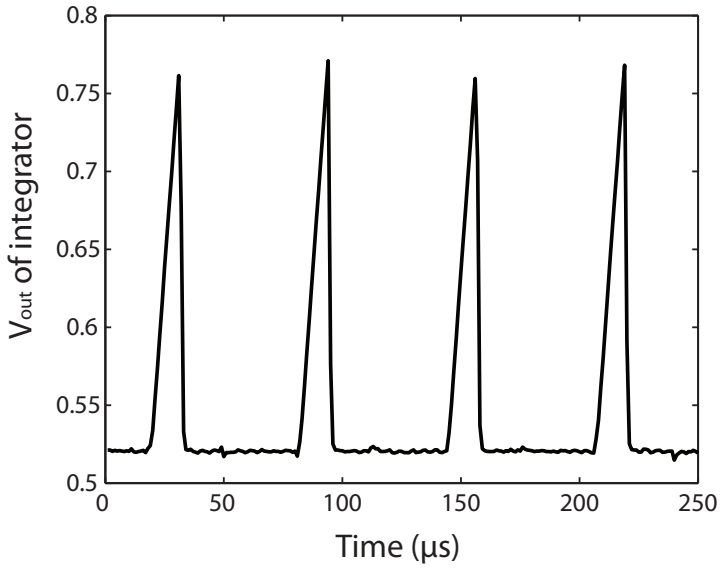

Figure 8.19: The output voltage of the on-chip integrator after the chip is exposed to IR radiation for 5 minutes

group of 250 sampled data point. The spikes in V_{out} caused by noise is removed first using median filter because these spikes have much larger slope than the slope of V_{out}. Then the slope of the V_{out} is extracted in Matlab.

The slope of V_{out} when there is no IR radiation is calculated to be 13.05mV/μs. Substituting this value into equation 8.1, the pixel current is $I_{pixel} = 130.05nA$ at room temperature.

After the IR radiation of blackbody source is impinged onto the chip, the V_{out} does not change until 3.5 min later. The slope of V_{out} keeps increasing since then and becomes saturated after 5 minutes, when the saturated output voltage V_{out} of the integrator on chip is recorded and shown in Fig. 8.19

The slope turns out to be 19.73mV/μs. Substituting this value into equation 8.1, the pixel

current is $I_{pixel} = 196.62nA$.

However, this increase in the pixel current in the NMOS transistor IR detector is not caused by the response of metamaterial coupled IR detector to the targeting 10μm IR radiation. The response time of metamaterial coupled IR detector should be in the microsecond range considering the sub-micron dimensions of the NMOS IR detector. But this increase in the pixel current in the NMOS transistor IR detector happens after 3.5 min, which means it is caused by the heated PCB carrying the chip. The PCB conducts its heat through socket and package to the chip. It takes minutes for the IR radiation to heat up the entire PCB because PCB is large compared with the chip and contains many components. And this happens to be the main source that causes the change of slope in the saw-tooth waveform. This does verify that the chip and the board are working correctly for electronic function, but does not quite work for imaging.

A series of experiments are performed to prove this hypothesis that are elaborated below.

8.3.3.2 Polarization dependent signal test

The metamaterial unit cells are ELC resonators that are polarization sensitive. For correct operation, output of the metamaterial pixel should be greater in magnitude with correct polarization than in the opposite polarization.

The most straightforward way to change the polarization of IR blackbody source is to place a polarizer in front of it and rotate it by 90 degree to change the polarization of IR radiation

orthogonally. The polarizer must have high transmission throughout the IR band. The polarizer chosen is a ZnSe Holographic Wire Grid Polarizer with item number WP50H-Z from Thorlab. Its operating wavelength range covers 2-20μm.

The polarizer is mounted in front of the IR black body source. The ELC resonators are rotated between the correct polarization (E-field perpendicular to the split gap) and the cross polarization (E-field parallel to the gap). In each cases, the same pixel is selected and its output is sampled 10000 times. After these 10000 data samples are acquired, they are divided into 40 groups, each of which consists of 250 data samples. 250 data samples contains 4 complete periods of saw-tooth wave, which makes the extracted slope of the saw-tooth more accurate. The slope is calculated for each individual 250-data-sample group and we obtain a 40 element array of slopes for both the correct and cross polarization. Let us assume the slope array for the correct polarization is $a[1, 2, ..., 40]$ and the slope array for the cross polarization is $b[1, 2, ..., 40]$. Their element-wise difference is $c[1, 2, ..., 40] = a[1, 2, ..., 40] - b[1, 2, ..., 40]$, which is also a 40 element array. The histogram of their element-wise difference array $c[1, 2, ..., 40]$ is plotted in Fig. 8.20. In the histogram, 36 out of 40 elements are 0, which shows no difference between the correct and cross polarization. The other 4 elements in the histogram are noise. The IR detector transistor does not see polarization sensitive response of the metamaterial unit cell.

8.3.3.3 High power tunable IR laser test

The blackbody source is a broadband IR source that radiates a wide-band of EM wave ranging from 0.5 - 99μm, which covers visible to far-infrared band. In addition to that, the

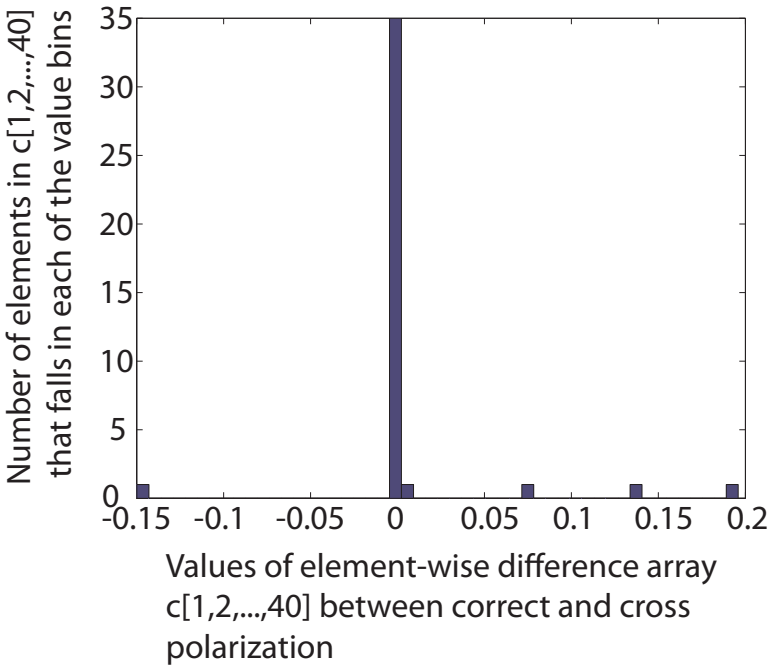

Figure 8.20: Histogram of element-wise difference array $c[1, 2, ..., 40]$ between correct and cross polarization

broadband IR source employed in the test has an 20 degree tapered - recessed - cone in the front end that diverges the emitted EM wave greatly. This may be the cause for the increase in pixel current on exposure to blackbody source, not due to metamaterial response but due to the inadvertent heating up of the rest of the chip and the PCB. This issue can be resolved by replacing the blackbody source with a coherent laser with high directivity, small beam spot size and high power. A wavelength tunable laser is more desirable because the resonant frequency of the on chip metamaterial may vary due to the process variation. A tunable laser would enables us to sweep the wavelength range to find out the real resonant frequency of the on chip metamaterial.

*Ü*ber Tuner tunable External Cavity quantum cascade Laser UT-9 (175) have all the desired features and is employed in the test. It is a tunable mid-IR pulsed laser (175). Its wavelength

can be tuned continuously from 8.3 - 9.9μm (175). Its maximum pulse repetition frequency is 100kHz (175), which is much faster than the reset frequency(reciprocal of integration time) of on chip integrator. Its beam divergence is less than 5 mrad (175), which makes the beam spot size smaller than 1mm$\times$1mm at 35 cm away from the laser (175). This is tested with a photo-chromic card. The area on the photo-chromic card impinged by the laser beam changes color and becomes brown so that the invisible mid-IR radiation becomes visible. It also facilitates the aligning of optical setup. The power of the laser beam is above 100mW across its tuning wavelength range (175). The peak power reaches 400mW at the center wavelength (175). Caution is taken to prevent the high power from damaging the chip.

In the test, the tunable mid-IR laser UT-9 is placed 35cm away from the chip and it is aligned with the chip so that the mid-IR laser beam is impinged onto the IR detector array on chip. The pulse repetition frequency is set to its maximum value, 100kHz. The duty cycle is set to its maximum value, 5% (175). The current of laser is set to its maximum allowed value, 1000mA, so that the radiation power of laser is above 100mW across the entire wavelength tuning range. At each wavelength in the tuning range of laser, the output of 40 pixels in the IR detector array are measured and 250 data points are recorded for each pixel. Then the slope of each pixel's output is extracted. The slope of each pixel's output is also acquired as reference when there is no mid-IR laser beam impinged onto the chip. The difference between the slope of each pixel's output in these two cases are calculated and plotted in the histogram. But the histogram shows that most of the pixels' output do not show any difference between laser-radiated and non-laser-radiated (reference) cases throughout the wavelength tuning range of the mid-IR laser. The histogram of 9.9 μm laser beam radiation is shown in Fig. 8.21 as an example:

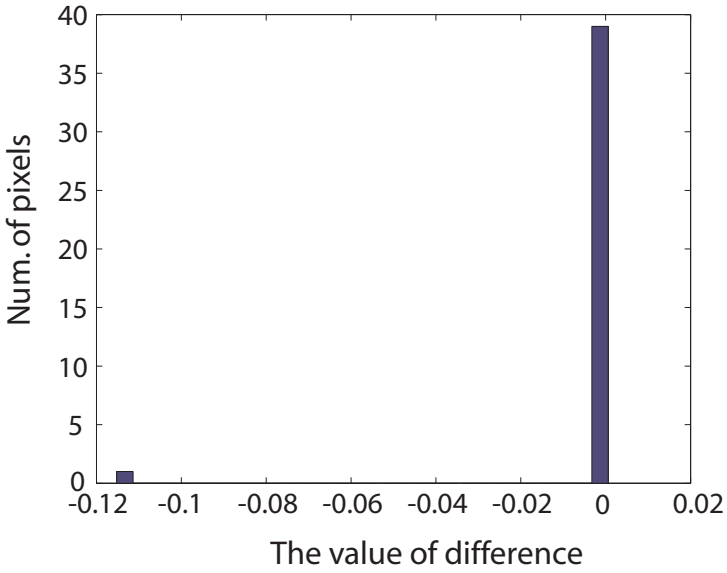

Figure 8.21: The histogram of differences in pixels' output between reference and mid-IR radiated cases

The horizontal axis in Fig. 8.21 is the differences in pixels' output between reference and mid-IR radiated cases. The vertical axis is the number of pixels that have the same value of difference between two cases. It is very conspicuous that 39 out of 40 pixels in the IR detector array show no difference with and without impinged mid-IR radiation laser (their difference value is 0). The only pixel that has non-zero difference value is interfered by the noise in the test setup. The histogram of pixels' output at other wavelength of laser radiation is very similar. The majority of pixels show no difference with and without mid-IR laser radiation. Pixels' output should have shown a large difference if the metamaterial enhanced IR detector can detect the mid-IR laser radiation because of its high power.

A polarization dependent test very similar to that in subsection 8.3.3.2 is performed assuming the detected signal is very weak due to the low detectivity of the metamaterial enhanced IR detector. The same data acquisition method is employed and the histogram of 40 pixels'

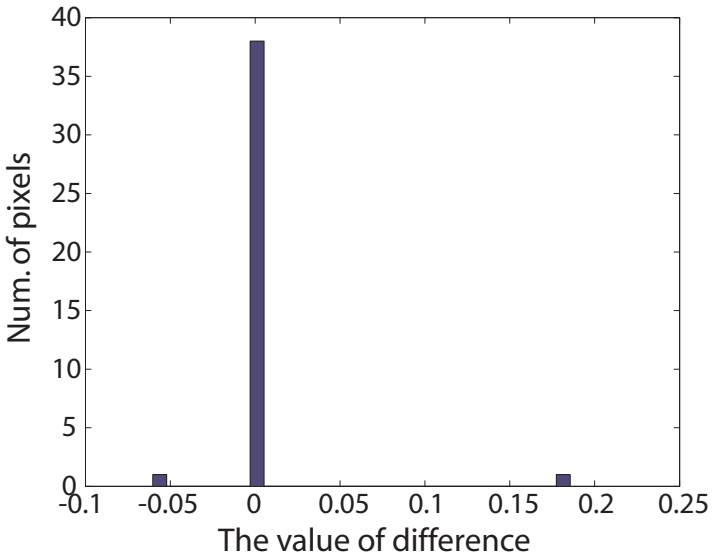

Figure 8.22: The histogram of differences in pixels' output between cross polarization and correct polarization cases

output differences between cross polarization and correct polarization is plotted for each wavelength in the laser tuning range. The histogram at 9.9 μm is shown in Fig. 8.22.

In Fig. 8.22, 38 out of 40 pixels do not show any difference at their output between correct polarization and cross polarization. Only two pixels have differences that are distributed randomly around zero, which are caused by noise in the measurement system.

The histogram of 40 pixels' output differences between cross polarization and correct polarization at other wavelength in the tuning range of the laser is very similar. The overwhelming majority of pixels among the measured 40 pixels show no difference at their output between correct polarization and cross polarization. This proves that the metamaterial enhanced IR detector cannot detect any polarization dependent signal.

The above statistical results prove that the metamaterial enhanced IR detector cannot detect this high power mid-IR radiation. The reasons could be:

- The operating wavelength of the responsivity of the metamaterial pixel is beyond the tunable range of the laser

- The input power is reflected by some material layer over the metamaterial in the CMOS stack before reaching the metamaterial layer

- The input power is lost in the dielectric between the *via*s because the length of *via*s exceeds the wavelength of incident radiation and the dielectric between is more lossy than expected

- The input power is lost in the coupling between the *via*s and cut-through opening in the ground plane because cut-through opening is smaller than expected due to CMOS process variations

- There is a slim chance that the IR signal received by the metamaterial is very weak and IR detector cannot detect it

8.3.3.4 Lock in amplifier test

It is suspected that the IR signal absorbed by the metamaterial is too weak and the signal-to-noise ratio (SNR) of the converted voltage signal is too low to be detected. A lock-in

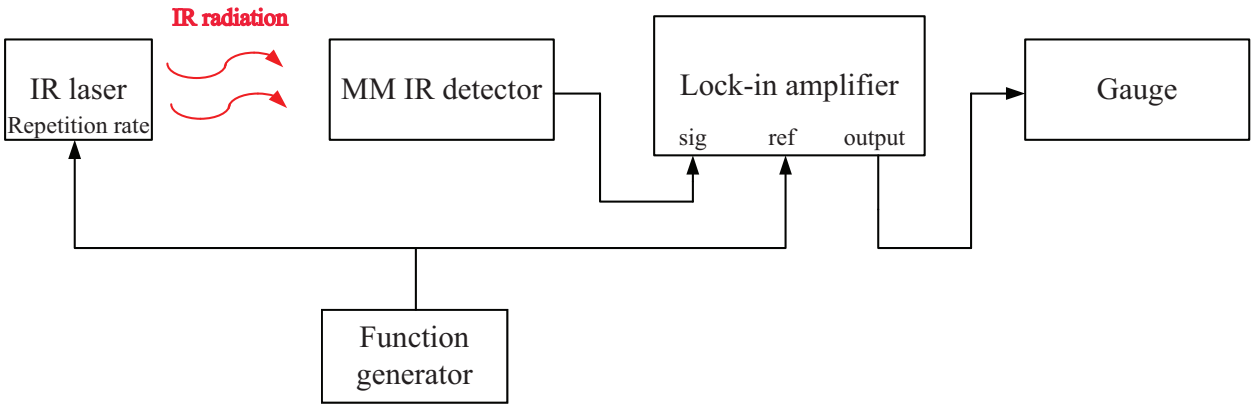

Figure 8.23: Improve the SNR by using lock-in amplifier in the IR laser test (176)

amplifier may recover the weak signal from the strong noise background (176).

The lock-in amplifier works by chopping the IR laser radiation with a reference signal, which can be generated by lock-in amplifier internally or by external instrument, and mixing the metamaterial IR detector output with the same reference signal to extract the detected IR signal (176). A block diagram illustrating this idea is shown in Fig. 8.23 (176).

In Fig. 8.23, function generator generates a 1.1KHz reference signal and feeds it to the 'ref' input of the lock-in amplifier as well as the repetition rate input of the IR laser. The repetition rate input control the speed to turn on and off the laser output pulses periodically. It is equivalent to use a mechanical chopper in front of the laser. The IR radiation impinged onto the metamaterial coupled IR detector is modulated by the repetition rate. The lock-in amplifier used is Princeton Applied Research Model 5210.

The IR radiation signal is a narrow band signal that is modulated by the reference signal first, then the output of metamaterial coupled IR detector is demodulated by the same reference signal to down-convert the detected IR signal (176). The noise in the optical setup and circuit

on-chip, however, is broadband. The noise is not periodic and is un-correlated with the pixel output, while the detected signal happens to be periodic with a fundamental frequency component at the repetition frequency of the laser. The lock in amplifier demodulates the fundamental frequency component of the detected signal back to baseband and up-converts the noise (and offset) to higher frequency.

A low pass filter is used in the lock-in amplifier to filter out the high frequency signal of noise and to preserve DC signal that is proportional to the detected IR signal power (176). If the noise in the environment is overwhelming, we can increase the SNR simply by increasing the time constant of the low pass filter (176).

If the metamaterial enhanced IR detector performs normally, it would be very sensitive to IR radiation at one wavelength and show no response for the rest of wavelength in the spectrum. When the wavelength of IR laser is swept, the amplitude of the output of lock-in amplifier is expected to be at least several millivolts when the detected IR signal at certain wavelength is locked. In the test, we have shined the IR radiation beam with the wavelength of 8.3 μm, 8.5 μm, 8.8 μm, 9μm, 9.2 μm, 9.4μm, 9.6μm, 9.8μm onto our chip. The magnitude of the output of lock in amplifier varies between 0.001mV-0.008mV for these wavelength. The time constant of lock in amplifier was set to 3s initially. It was changed to 10s, 30s later and the output still varied in the same range albeit with slower speed. Experiments conclusively prove that our metamaterial enhanced mid-IR detector cannot detect the incident IR radiation.

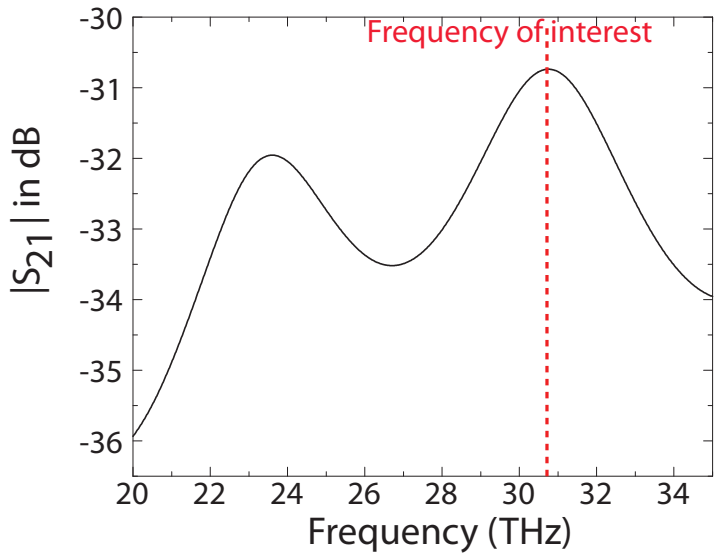

Figure 8.24: Simulation result of $|S_{21}|$ when the imaginary part of dielectrics' permittivity is doubled

8.3.4 Post-hoc analysis

One of the reasons causing the discrepancy between simulation result and measurement is the uncertainty of material parameter of the dielectric medium. For competitive reasons, CMOS foundries do not provide detailed chemical composition of the metal and dielectric used in CMOS, while they provide detailed electronic properties of circuit elements. Based on little available information, educated guesses where made on the materials used during simulation. One key source of error possibly made may be in the value of the loss tangent used for these materials. Loss tangent of dielectrics can vary as much as one order of magnitude (10 times) within mid-IR band (177). For example, the simulation result of $|S_{21}|$ of the metamaterial enhanced IR detectors drops by more than 7dB at the resonant frequency of 31 THz when the loss tangent of dielectrics is doubled, as shown in Fig. 8.24

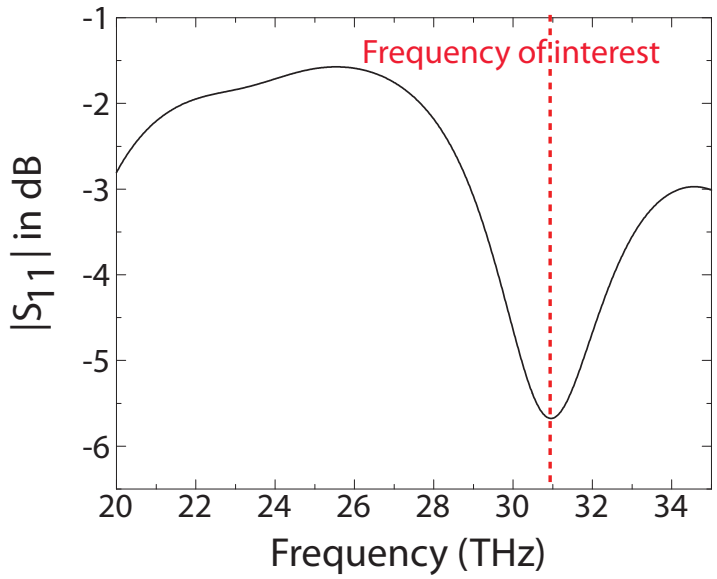

Figure 8.25: Simulation result of $|S_{11}|$ in dB when the imaginary part of dielectrics' permittivity is doubled

As shown in Fig. 8.24, $|S_{21}|$ drops to -31dB at the resonant frequency, which means only 2.9% of incident IR radiation power is delivered to the IR detector.

The simulation result of $|S_{11}|$ in this case is shown in Fig. 8.25

$|S_{11}|$ increases drastically across the band of interest. Its minimum reaches -5.8dB at the resonant frequency of MM, which means more than 51% of the incident IR radiation power is reflected back into free space.

The intensity and spectrum of black-body radiation are dictated by the temperature of the object (178, 179, 180, 181). But the intensity of the black-body radiation of the objects in the environment is very low within the band of interest, which is 8μm to 10μm, because the

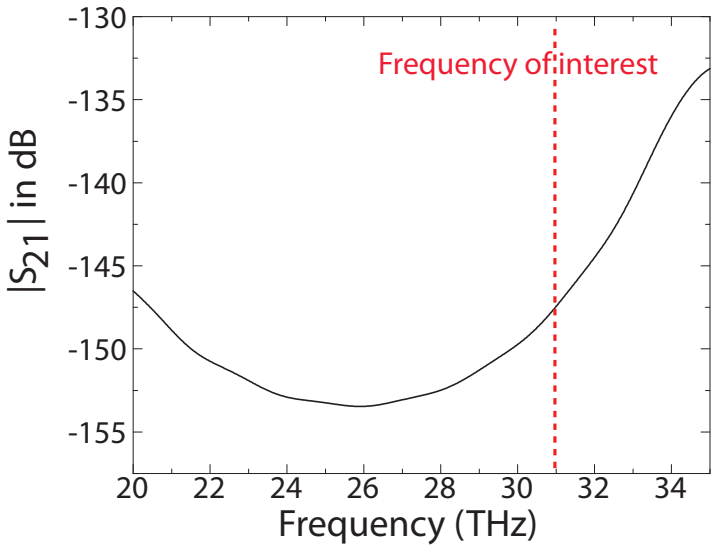

Figure 8.26: Simulation result of $|S_{21}|$ in dB when the dimensions of ELC resonator and openings in ground plane have -50% variation

temperature of the objects in the environment is about the same as the room temperature. This weak radiation intensity cannot be detected by the metamaterial enhanced IR detector. In addition, the temperature of the objects in the environment fluctuates with that of the room temperature, which adds noise into measurement.

Another factor that may corrupt the performance of MM enhanced IR detector is the variation of the lateral dimensions of MM unit cell. The commercial CMOS process we used to implement the MM enhanced IR detector array has ±50% process variation on the lateral dimension of patterns on each metal layer (182). Let us assume there is -50% variation in the metal layer where the ELC resonator is implemented. The metamaterial enhanced IR detector is simulated again under this assumption.

Fig. 8.26 shows the $|S_{21}|$ in dB when the dimensions of ELC resonator and openings in

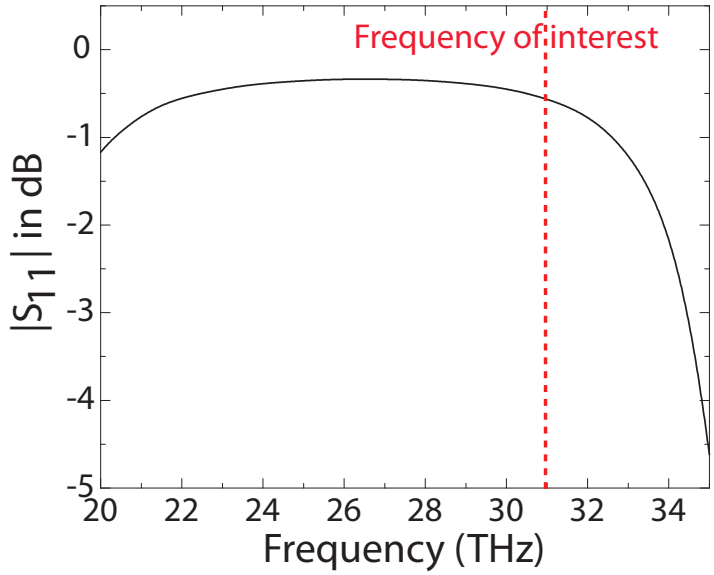

Figure 8.27: Simulation result of $|S_{11}|$ in dB when the dimensions of ELC resonator and openings in ground plane have -50% variation

ground plane have -50% variation in their dimensions. The $|S_{21}|$ across the band of interest is more than 100dB lower than the $|S_{21}|$ of ELC resonator with designed dimensions. The $|S_{21}|$ at the designed resonant frequency drops to -148dB, which means almost no incident IR radiation power is guided to the IR detector.

The $|S_{11}|$ in dB is shown in Fig. 8.27. Most of the incident IR radiation power is reflected to free space across the band of interest.

In the next version of chip, the large process variation must be accounted carefully in the design phase and different dimensions of the same MM structure should be implemented to ensure at least some of the unit cells in the array can guide the incident IR radiation onto the IR detector. The other option is to connect several MM unit cells with different dimensions

and/or structures to the same IR detector instead of connecting each MM unit cell to one IR detector. It would increase the likelihood of detection of IR signal.

We should also try to obtain more information about the dielectric material used in the process because their losses at mid-IR may be much worse than our estimation.

8.4 Summary

The metamaterial coupled detector presented in Chapter 5 is scaled down from cm to μm and implemented on CMOS process to detect the mid-IR signal. The detection scheme employed in this chapter is to convert the pixel current induced by the incident IR signal into the voltage signal. A 32 by 32 metamaterial coupled IR detector array, a row/column decoder and integrators are implemented on a 45nm CMOS chip to make a mid-IR image sensor.

The metamaterial enhanced mid-IR detector is simulated in CST using the custom designed material models of metals and dielectrics used in CMOS at mid-IR band. The simulation result verifies that metamaterial unit cell can guide the incident mid-IR radiation onto IR detector. But there are many uncertainties in the materials used in this CMOS process because the foundry does not release their detailed chemical composition. The reliability of the material models and simulation results is compromised for this reason.

A series of measurements are conducted to characterize and test the metamaterial enhanced mid-IR detector array. All the measurements show that metamaterial enhanced mid-IR

detector cannot detect any incident IR radiation. The reasons are multi-fold. One possible reason is the thick dielectric layers are much more lossy than what we expect. The other reason is the process variation of the metal layers where the metamaterial and ground plane are implemented.

One possible improvement in the next generation of this work is to illuminate the IR wave from the bottom substrate of the CMOS chip. The metamaterial can be implemented on the lowest metal layer and short *via*s can be used to guide the focused IR signal to the detector transistor. One of its advantage is that the IR radiation will not interact with any of the upper metal layers or dielectric layers. It avoids undesirable absorption of the lossy dielectric and scattering/reflection caused by metal fills in the upper metal layers. Large process variation in the upper metal layers is not a concern anymore in this case. Moreover, short *via*s eliminate the risking of losing IR signal in the *via*s.

Another suggestion is to couple multiple metamaterial resonators to the same detector transistor to improve its detectivity.

Furthermore, a variety of metamaterial resonators operating at various wavelength should be implemented on the chip. The variation in material parameters may corrupt the IR detection in one band but not the entire IR spectrum.

9

Conclusion

The main emphasis in this thesis work is to propose a synergistic embedding of active circuits into metamaterials. Active circuits are embedded into metamaterials to alleviate their inherent problems and to make innovative hybrid metamaterial devices. The example presented in the dissertation is loss compensation in metamaterials through embedding of active transistor based negative differential resistance circuit. This method can be utilized in any metamaterial with patterned metallic inclusions in a dielectric medium to compensate for their losses. The proposed loss compensation approach can be used in bulk metamaterials to make ideal absorbers, cloaks, perfect lens, modulators, phase shifters, etc., with applications in radar imaging, cellular mobile communications, satellite communications, antennas and security screening.

New metamaterial based devices are demonstrated by loading the metamaterials with active

circuits. As a first example, a microwave metamaterial enhanced detector array is presented where each metamaterial unit cell is loaded by a receiver chain. It utilizes the unique perfect absorbing properties of metamaterial absorbers and guides metamaterial-absorbed EM wave power into a detector connected to each metamaterials unit cell. Experimental results verify the improved detectivity of the proposed metamaterial coupled detector and weaker mutual coupling between neighboring pixels in the detector array. The presented metamaterial enhanced detector is an excellent candidate to act as detector pixels when implemented into bolometric or semiconducting configurations. The sub-wavelength unit cell and narrow resonant spectral bandwidth can also be expanded to enable multi-color and co- and cross-polarized pixels.

The properties of traditional metamaterials typically do not change with time and cannot be tuned. Active circuit elements implanted into metamaterials can enable time-varying response and tune their performance. The second example demonstrated in the dissertation is the diode switchable metamaterial absorber/reflector whose resonant frequency and strength are tuned by embedded diodes. The presented design allows tunability with just two control lines, making a practical realization of a large area metamaterial absorber/reflector possible. It can be used in many applications including beam-steerable antennas, radomes and single pixel compressive imaging at millimeter/terahertz frequencies.

CMOS is the ideal mainstream technology for fabricating complicated metamaterial designs because it features nanometer dimensions and has multiple layers of metal and all the circuit elements needed to implement hybrid metamaterial devices. A multitude of metamaterial devices on CMOS operating at terahertz/IR/optcial frequencies are designed and simulated. Simulation results prove the idea is rational and feasible. It paves the way towards fabricating

nanometer scale metmaterial devices on CMOS with low cost, high yield and fast throughput in the future.

In this spirit of implementing metamaterials in semiconductor processes, an IR metamaterial enhanced detector array with readout circuit is implemented on a commercial 45nm CMOS process. Preliminary electrical test proves the electronic circuit is functioning. But the optical test shows the detector cannot detect the incident IR radiation. The reason is the detailed chemical composition of the dielectric in CMOS is not provided and their material parameters are quite different from our expectation. This issue is taken into account and fixed in the next version of this chip, which is being developed by another member of the group.

A possible extension of this dissertation might be implementing a broad band metamaterial by embedding non-Foster elements into each unit cell (136). The exotic EM properties of metamaterials, such as negative refractive index or perfect absorption, only exist around their sharp resonance, which limit their practical operating bandwidth (136). Many applications require metamarials with wide-band EM response. Non-Foster elements are active circuits that provide negative capacitance and inductance, which may cancel the intrinsic L and C of metamaterial unit cell so that the resonant-type response of a metamaterial is broadened in bandwidth (136). However, non-Foster elements are potentially unstable and may trigger resonance of metamaterials (136). The design of non-Foster elements must be very careful to prevent the instability of metamaterials (136). This could be a focus on comprehensive future effort in making broadband metamaterials with active circuits.

In conclusion, active circuits, both discrete and integrated in CMOS, embedded into meta-

materials are shown to be a novel method to profoundly enhance the performance and capabilities of metamaterial devices and enable many new functions for diverse applications.

Bibliography

[1] RA Shelby, DR Smith, and S. Schultz. **Experimental verification of a negative index of refraction**. *Science*, **292**(5514):77–79, 2001. xi, 1, 15, 16, 21, 59, 165

[2] DR Smith, W.J. Padilla, DC Vier, S.C. Nemat-Nasser, and S. Schultz. **Composite medium with simultaneously negative permeability and permittivity**. *Physical review letters*, **84**(18):4184–4187, 2000. 1, 2, 15, 37, 165

[3] D. Schurig, JJ Mock, BJ Justice, S.A. Cummer, JB Pendry, AF Starr, and DR Smith. **Metamaterial electromagnetic cloak at microwave frequencies**. *Science*, **314**(5801):977–980, 2006. 1, 19, 21, 25, 37, 41, 135, 165

[4] J.B. Pendry. **Negative refraction makes a perfect lens**. *Physical Review Letters*, **85**(18):3966–3969, 2000. 1, 2, 37, 165

[5] V.G. Veselago. **The electrodynamics of substances with simultaneously negative values of ε and μ**. *Physics-Uspekhi*, **10**(4):509–514, 1968. 1, 10, 12, 37

[6] JB Pendry, AJ Holden, DJ Robbins, and WJ Stewart. **Magnetism from conductors and enhanced nonlinear phenomena**. *Microwave Theory and Techniques, IEEE Transactions on*, **47**(11):2075–2084, 1999. 2, 13, 37

[7] Andrew C. Strikwerda. *Metamaterial Enchanced Coupling*. ProQuest Dissertations and Theses (PQDT), 2012. 2

[8] A.D. Boardman, V.V. Grimalsky, Y.S. Kivshar, S.V. Koshevaya, M. Lapine, N.M. Litchinitser, V.N. Malnev, M. Noginov, Y.G. Rapoport, and V.M. Shalaev. **Active and tunable metamaterials**. *Laser & Photonics Reviews*, **5**(2):287–307, 2011. 2, 111

[9] A. Scott. *Active and nonlinear wave propagation in electronics*. Wiley-Interscience New York, 1970. 2

[10] AD Boardman, RC Mitchell-Thomas, NJ King, and YG Rapoport. **Bright spatial solitons in controlled negative phase metamaterials**. *Optics Communications*, **283**(8):1585–1597, 2010. 2

[11] B.E.A. Saleh and M.C. Teich. **Fundamentals of photonics**. 2007. 6, 7, 9, 56, 129, 130

[12] André Vander Vorst, Arye Rosen, and Youji Kotsuka. **Fundamentals of Electromagnetics**. *RF/Microwave Interaction with Biological Tissues*, pages 7–62, 2006. 7, 8

[13] **Permittivity**. http://en.wikipedia.org/w/index.php?title=\Permittivity&oldid=531154899, January 2013. Page Version ID: 531154899. 8

[14] **Permeability (electromagnetism)**. http://en.wikipedia.org/w/index.php?title=Permeability_(electromagnetism)&oldid=532514665, January 2013. Page Version ID: 532514665. 8

[15] www4.ncsu.edu/~rsmith/DonovanAMGSSBeamer.pdf. xi, 9, 10

[16] J. Zhou. *Study of left-handed materials*. PhD thesis, Iowa State University, 2008. 9, 10, 11, 12

[17] R. Marqués, F. Martín, and M. Sorolla. *Metamaterials with negative parameters: theory, design and microwave applications*, **183**. Wiley-Interscience, 2008. xi, 10, 11, 12, 13

[18] R.W. Ziolkowski and E. Heyman. **Wave propagation in media having negative permittivity and permeability**. *Physical review E*, **64**(5):056625, 2001. 12

[19] I.V. Lindell, SA Tretyakov, KI Nikoskinen, and S. Ilvonen. **BW mediaMedia with negative parameters, capable of supporting backward waves**. *Microwave and Optical Technology Letters*, **31**(2):129–133, 2001. 12

[20] http://www.ihf.uni-stuttgart.de/forschung/forschungsgebiete/metamaterials/index.en.html. xi, 13, 14

[21] Uday K Chettiar, Alexander V Kildishev, Hsiao-Kuan Yuan, Wenshan Cai, Shumin Xiao, Vladimir P Drachev, and Vladimir M Shalaev. **Double Negative Index Metamaterial: Simultaneous Negative Permeability and Permittivity at 812 nm**. In *Photonic Metamaterials: From Random to Periodic*. Optical Society of America, 2007. xi, 13, 14

[22] F. Capolino. *Metamaterials handbook*. CRC Press, 2009. 13, 111

[23] F. Capolino. *Theory and phenomena of metamaterials*, **1**. CRC, 2009. 13

[24] Nikolay I Zheludev. **The road ahead for metamaterials**. *Science*, **328**(5978):582–583, 2010. xi, 15, 16, 17

[25] H. Chen, CT Chan, and P. Sheng. **Transformation optics and metamaterials**. *Nature Materials*, **9**(5):387–396, 2010. 16

[26] A.V. Kildishev and V.M. Shalaev. **Transformation optics and metamaterials**. *Physics-Uspekhi*, **54**:53, 2011. 16

[27] X. Zhang and S.R. Forrest. **Theory of the perfect lens**. *Physical Review B*, **84**(4):045427, 2011. 16

[28] X. Zhou and G. Hu. **Superlensing effect of an anisotropic metamaterial slab with near-zero dynamic mass**. *Applied Physics Letters*, **98**(26):263510–263510, 2011. 16

[29] N. Zhu, R.W. Ziolkowski, and H. Xin. **A metamaterial-inspired, electrically small rectenna for high-efficiency, low power harvesting and scavenging at the global positioning system L1 frequency**. *Applied Physics Letters*, **99**:114101, 2011. 16

[30] P.K. Singh, K.A. Korolev, M.N. Afsar, and S. Sonkusale. **Single and dual band 77/95/110 GHz metamaterial absorbers on flexible polyimide substrate**. *Applied Physics Letters*, **99**(26):264101–264101, 2011. 16, 123

[31] J. Zhou, H.T. Chen, T. Koschny, A.K. Azad, A.J. Taylor, C.M. Soukoulis, and J.F. O'Hara. **Application of metasurface description for multilayered**

metamaterials and an alternative theory for metamaterial perfect absorber. *Arxiv preprint arXiv:1111.0343*, 2011. 16

[32] M.K. Hedayati, M. Javaherirahim, B. Mozooni, R. Abdelaziz, A. Tavassolizadeh, V.S. Kiran Chakravadhanula, V. Zaporojtchenko, T. Strunkus, F. Faupel, and M. Elbahri. **Design of a perfect black absorber at visible frequencies using plasmonic metamaterials**. *Advanced Materials*, 2011. 16

[33] RJ Langley and EA Parker. **Double-square frequency-selective surfaces and their equivalent circuit**. *Electronics Letters*, **19**(17):675–677, 1983. 19

[34] Farhad Bayatpur. *Metamaterial-inspired frequency-selective surfaces*. PhD thesis, The University of Michigan, 2009. 19, 28

[35] MF Wu, FY Meng, Q Wu, J Wu, and LW Li. **A compact equivalent circuit model for the SRR structure in metamaterials**. In *Microwave Conference Proceedings, 2005. APMC 2005. Asia-Pacific Conference Proceedings*, **1**, pages 4–pp. IEEE, 2005. 19

[36] Hongsheng Chen, Lixin Ran, Jiangtao Huangfu, Tomasz M Grzegorczyk, and Jin Au Kong. **Equivalent circuit model for left-handed metamaterials**. *Journal of applied physics*, **100**(2):024915–024915, 2006. 19, 28

[37] R. Marques, F. Mesa, J. Martel, and F. Medina. **Comparative analysis of edge- and broadside- coupled split ring resonators for metamaterial design - theory and experiments**. *IEEE Transactions on Antennas and Propagation*, **51**(10):2572 – 2581, October 2003. xi, 19, 20

[38] D. Schurig, JJ Mock, and DR Smith. **Electric-field-coupled resonators for negative permittivity metamaterials**. *Applied physics letters*, **88**:041109, 2006. 19, 21, 59, 72, 92, 113

[39] Ruopeng Liu, Aloyse Degiron, Jack J. Mock, and David R. Smith. **Negative index material composed of electric and magnetic resonators**. *Applied Physics Letters*, **90**(26):263504–263504–3, June 2007. 21, 41, 135

[40] Yu Yuan, Christopher Bingham, Talmage Tyler, Sabarni Palit, Thomas H. Hand, Willie J. Padilla, Nan Marie Jokerst, and Steven A. Cummer. **A dual-resonant terahertz metamaterial based on single-particle electric-field-coupled resonators**. *Applied Physics Letters*, **93**(19):191110–191110–3, November 2008. 21, 41, 135

[41] D. Shrekenhamer, S. Rout, A.C. Strikwerda, C. Bingham, R.D. Averitt, S. Sonkusale, and W.J. Padilla. **High speed terahertz modulation from metamaterials with embedded high electron mobility transistors**. *Optics Express*, **19**(10):9968–9975, 2011. 21, 40, 41, 135

[42] Qiang Cheng, Tie Jun Cui, Wei Xiang Jiang, and Ben Geng Cai. **An omnidirectional electromagnetic absorber made of metamaterials**. *New Journal of Physics*, **12**(6):063006, June 2010. 21, 41, 135

[43] Filiberto Bilotti, Alessandro Toscano, Lucio Vegni, Koray Aydin, Kamil Boratay Alici, and Ekmel Ozbay. **Equivalent-circuit models for the design of metamaterials based on artificial magnetic inclusions**. *Microwave Theory and Techniques, IEEE Transactions on*, **55**(12):2865–2873, 2007. xi, 21, 22, 23

[44] L. Setian. *Practical Communication Antennas with Wireless Applications*. Prentice Hall PTR, 1998. 23, 24

[45] G. Gonzalez. *Microwave transistor amplifiers: analysis and design*, **2**. Prentice hall New Jersey, 1997. 24

[46] Jiang Zhu. *Compact Antennas and Superlenses Using Transmission-line Metamaterials*. PhD thesis, 2011. 26

[47] Farhad Bayatpur and Kamal Sarabandi. **Single-layer high-order miniaturized-element frequency-selective surfaces**. *Microwave Theory and Techniques, IEEE Transactions on*, **56**(4):774–781, 2008. xii, 30, 31, 32

[48] B.I. Popa and S.A. Cummer. **An architecture for active metamaterial particles and experimental validation at RF**. *Microwave and Optical Technology Letters*, **49**(10):2574–2577, 2007. 37, 38

[49] http://en.wikipedia.org/wiki/Superlens. 37

[50] Xiang Zhang and Zhaowei Liu. **Superlenses to overcome the diffraction limit**. *Nature materials*, **7**(6):435–441, 2008. 37

[51] D.R. Smith, D. Schurig, M. Rosenbluth, S. Schultz, S.A. Ramakrishna, and J.B. Pendry. **Limitations on subdiffraction imaging with a negative refractive index slab**. *Applied Physics Letters*, **82**(10):1506–1508, 2003. 37

[52] B.I. Popa and S.A. Cummer. **Direct measurement of evanescent wave enhancement inside passive metamaterials**. *Physical Review E*, **73**(1):016617, 2006. 37

[53] Z.G. Dong, H. Liu, T. Li, Z.H. Zhu, S.M. Wang, J.X. Cao, S.N. Zhu, and X. Zhang. **Optical loss compensation in a bulk left-handed metamaterial by the gain in quantum dots**. *Applied Physics Letters*, **96**:044104, 2010. 38

[54] S.A. Ramakrishna and J.B. Pendry. **Removal of absorption and increase in resolution in a near-field lens via optical gain**. *Physical Review B*, **67**(20):201101, 2003. 38

[55] **Active laser medium**, December 2012. Page Version ID: 514828649. 38

[56] C.M. Soukoulis and M. Wegener. **Optical metamaterialsmore bulky and less lossy**. *Science*, **330**(6011):1633, 2010. 38

[57] Y. Yuan, B.I. Popa, and S.A. Cummer. **Zero loss magnetic metamaterials using powered active unit cells**. *Optics express*, **17**(18):16135–16143, 2009. 38

[58] L. Jelinek and J. Machac. **An FET-Based Unit Cell for an Active Magnetic Metamaterial**. *Antennas and Wireless Propagation Letters, IEEE*, (99):1–1, 2011. 38, 64

[59] F. Auzanneau and R.W. Ziolkowski. **Artificial composite materials consisting of nonlinearly loaded electrically small antennas: operational-amplifier-based circuits with applications to smart skins**. *Antennas and Propagation, IEEE Transactions on*, **47**(8):1330–1339, 1999. 38

[60] S. A. Tretyakov. **Meta-materials with wideband negative permittivity and permeability**. *Microwave and Optical Technology Letters*, **31**(3):163165, 2001. 38

[61] Silvio Hrabar, Igor Krois, Ivan Bonic, and Aleksandar Kiricenko. **Neg-**

ative capacitor paves the way to ultra-broadband metamaterials. *Applied Physics Letters*, **99**(25):254103 –254103–4, December 2011. 38

[62] A. D. Boardman, Yu. G. Rapoport, N. King, and V. N. Malnev. **Creating stable gain in active metamaterials**. *Journal of the Optical Society of America B*, **24**(10):A53–A61, October 2007. 38

[63] J. Craninckx and M.S.J. Steyaert. **A 1.8-GHz low-phase-noise CMOS VCO using optimized hollow spiral inductors**. *Solid-State Circuits, IEEE Journal of*, **32**(5):736–744, 1997. 40

[64] B. Razavi. *RF microelectronics*. Prentice Hall, 2011. 40

[65] J.D. Albrecht, M.J. Rosker, H.B. Wallace, and T.H. Chang. **THz electronics projects at DARPA: Transistors, TMICs, and amplifiers**. In *Microwave Symposium Digest (MTT), 2010 IEEE MTT-S International*, pages 1118–1121. IEEE, 2010. 40, 125

[66] http://www.triquint.com/. 48

[67] M.R. Brozel and GE Stillman. *Properties of gallium arsenide*. Number 16. Inspec/Iee, 1996. 48

[68] A.S. Sedra and K.C. Smith. *Microelectronic circuits*, **1**. Oxford University Press, USA, 1998. 48, 62, 64, 172

[69] DR Smith, DC Vier, T. Koschny, and CM Soukoulis. **Electromagnetic parameter retrieval from inhomogeneous metamaterials**. *Physical Review E*, **71**(3):036617, 2005. xiv, 53, 54, 55, 56, 57, 58, 67, 113, 157

[70] L. Li Hou, J.Y. Chin, X.M. Yang, X.Q. Lin, R. Liu, F.Y. Xu, and T.J. Cui. **Advanced parameter retrievals for metamaterial slabs using an inhomogeneous model**. *Journal of Applied Physics*, **103**(6):064904–064904, 2008. 53, 157

[71] Th Koschny, P Markoš, EN Economou, DR Smith, DC Vier, and CM Soukoulis. **Impact of inherent periodic structure on effective medium description of left-handed and related metamaterials**. *Physical Review B*, **71**(24):245105, 2005. 53

[72] C.A. Kyriazidou, HE Contopanagos, W.M. Merrill, and NG Alexopoulos. **Artificial versus natural crystals: effective wave impedance of printed photonic bandgap materials**. *Antennas and Propagation, IEEE Transactions on*, **48**(1):95–106, 2000. 53

[73] W.B. Weir. **Automatic measurement of complex dielectric constant and permeability at microwave frequencies**. *Proceedings of the IEEE*, **62**(1):33–36, 1974. 56

[74] AM Nicolson and GF Ross. **Measurement of the intrinsic properties of materials by time-domain techniques**. *Instrumentation and Measurement, IEEE Transactions on*, **19**(4):377–382, 1970. 56

[75] X. Chen, T.M. Grzegorczyk, B.I. Wu, J. Pacheco Jr, and J.A. Kong. **Robust method to retrieve the constitutive effective parameters of metamaterials**. *Physical Review E*, **70**(1):016608, 2004. 56, 67

[76] DR Smith, R. Dalichaouch, N. Kroll, S. Schultz, SL McCall, and

PM Platzman. **Photonic band structure and defects in one and two dimensions**. *JOSA B*, **10**(2):314–321, 1993. 56

[77] D.M. Pozar. *Microwave engineering*. John Wiley & Sons, 2009. xv, 57, 74, 75, 76, 146, 147

[78] http://en.wikipedia.org/wiki/Inverse_trigonometric_function. 58

[79] B. Wang, J. Zhou, T. Koschny, and C. M. Soukoulis. **Nonlinear properties of split-ring resonators**. *Opt. Express*, **16**(20):16058–16063, 2008. 61, 64

[80] W.C. Chen, C.M. Bingham, K.M. Mak, N.W. Caira, and W.J. Padilla. **Extremely subwavelength planar magnetic metamaterials**. *Physical Review B*, **85**(20):201104, 2012. 64

[81] Larry Yujiri, Merit Shoucri, and Philip Moffa. **Passive millimeter wave imaging**. *Microwave Magazine, IEEE*, **4**(3):39–50, 2003. 71

[82] Soichi Oka, Hiroyoshi Togo, Naoya Kukutsu, and Tadao Nagatsuma. **Latest trends in millimeter-wave imaging technology**. *Progress In Electromagnetics Research Letters*, **1**:197–204, 2008. 71

[83] R. Appleby and R.N. Anderton. **Millimeter-wave and submillimeter-wave imaging for security and surveillance**. *Proceedings of the IEEE*, **95**(8):1683–1690, 2007. 71

[84] J.P. Weem and Z. Popovic. **A method for determining noise coupling in a phased array antenna**. In *Microwave Symposium Digest, 2001 IEEE MTT-S International*, **1**, pages 271–274. IEEE, 2001. 72, 106

[85] C. Craeye, B. Parvais, and X. Dardenne. **MoM simulation of signal-to-noise patterns in infinite and finite receiving antenna arrays**. *Antennas and Propagation, IEEE Transactions on*, **52**(12):3245–3256, 2004. 72, 106

[86] K.F. Warnick and M.A. Jensen. **Effects of mutual coupling on interference mitigation with a focal plane array**. *Antennas and Propagation, IEEE Transactions on*, **53**(8):2490–2498, 2005. 72, 106

[87] NI Landy, S. Sajuyigbe, JJ Mock, DR Smith, and WJ Padilla. **Perfect metamaterial absorber**. *Physical review letters*, **100**(20):207402, 2008. xvi, 72, 81, 83, 84, 85, 165

[88] Hu Tao, CM Bingham, AC Strikwerda, D Pilon, D Shrekenhamer, NI Landy, K Fan, and X Zhang. **Highly flexible wide angle of incidence terahertz metamaterial absorber: Design, fabrication, and characterization**. *PHYSICAL REVIEW B Phys Rev B*, **78**(241103):241103, 2008. 72, 171

[89] AN Yusoff, MH Abdullah, SH Ahmad, SF Jusoh, AA Mansor, and SAA Hamid. **Electromagnetic and absorption properties of some microwave absorbers**. *Journal of Applied Physics*, **92**(2):876–882, 2002. 73

[90] W. Irnich, L. Batz, R. MÜLLER, and R. Tobisch. **Electromagnetic interference of pacemakers by mobile phones**. *Pacing and clinical electrophysiology*, **19**(10):1431–1446, 1996. 73

[91] C.M. Watts, X. Liu, and W.J. Padilla. **Metamaterial Electromagnetic Wave Absorbers**. *Advanced Materials*, 2012. xv, 73, 74, 78, 79, 80, 81, 82, 148

[92] B.A. Munk. **Frequency selective surfaces**. *New York*, 2000. 73

[93] W.H. Emerson. **Electromagnetic wave absorbers and anechoic chambers through the years**. *IEEE Transactions on Antennas and Propagation*, **21**:484–490, 1973. 73, 77

[94] T. Maier and H. Brückl. **Wavelength-tunable microbolometers with metamaterial absorbers**. *Optics letters*, **34**(19):3012–3014, 2009. 73, 110

[95] J. Hao, J. Wang, X. Liu, W.J. Padilla, L. Zhou, and M. Qiu. **High performance optical absorber based on a plasmonic metamaterial**. *Applied Physics Letters*, **96**(25):251104–251104, 2010. 73

[96] G.T. Ruck, D.E. Barrick, W.D. Stuart, and C.K. Krichbaum. *Radar cross section handbook*, **1**. Plenum Press New York, 1970. 74, 76

[97] http://www.ecnmag.com/sites/ecnmag.com/files/legacyfiles/ECN/Absorbers_White_Paper.pdf. 74

[98] YJ Sung, M. Kim, and YS Kim. **Harmonics reduction with defected ground structure for a microstrip patch antenna**. *Antennas and Wireless Propagation Letters, IEEE*, **2**(1):111–113, 2003. 76

[99] W.J. Padilla, D.N. Basov, and D.R. Smith. **Negative refractive index metamaterials**. *Materials Today*, **9**(7):28–35, 2006. 77

[100] X. Liu, T. Starr, A.F. Starr, and W.J. Padilla. **Infrared spatial and frequency selective metamaterial with near-unity absorbance**. *Physical review letters*, **104**(20):207403, 2010. 77, 78, 81, 85

[101] R. Huang, Z.W. Li, L.B. Kong, L. Liu, and S. Matitsine. **Analysis and**

design of an ultra-thin metamaterial absorber. *Progress In Electromagnetics Research B*, **14**:407–429, 2009. 81

[102] J.E. Raynolds, B.A. Munk, J.B. Pryor, and R.J. Marhefka. **Ohmic loss in frequency-selective surfaces**. *Journal of applied physics*, **93**(9):5346–5358, 2003. 84

[103] Hu Tao, C. M. Bingham, A. C. Strikwerda, D. Pilon, D. Shrekenhamer, N. I. Landy, K. Fan, X. Zhang, W. J. Padilla, and R. D. Averitt. **Highly flexible wide angle of incidence terahertz metamaterial absorber: Design, fabrication, and characterization**. *Phys. Rev. B*, **78**:241103, Dec 2008. 85, 107

[104] http://www.qsl.net/yo4hfu/Files/MATCHING/LC_comp.gif. xvii, 94, 95

[105] http://en.wikipedia.org/. xvii, 96, 97

[106] http://en.wikipedia.org/. 98

[107] http://www.edn.com/file/19256-159688.pdf. xvii, 100

[108] http://www.johansontechnology.com/technical-notes/rf-capacitors-a-inductors/s-parameter-accuracy.html. 100

[109] M.A. Jensen and J.W. Wallace. **A review of antennas and propagation for MIMO wireless communications**. *Antennas and Propagation, IEEE Transactions on*, **52**(11):2810–2824, 2004. 106

[110] C.Y. Chiu, C.H. Cheng, R.D. Murch, and C.R. Rowell. **Reduction of mutual coupling between closely-packed antenna elements**. *Antennas and Propagation, IEEE Transactions on*, **55**(6):1732–1738, 2007. 106

[111] **Technology | Kymeta**. http://www.kymetacorp.com/technology/. 111

[112] M. Lapine, D. Powell, M. Gorkunov, I. Shadrivov, R. Marqués, and Y. Kivshar. **Structural tunability in metamaterials**. *Applied Physics Letters*, **95**(8):084105–084105, 2009. 111, 112

[113] A.A. Zharov, I.V. Shadrivov, and Y.S. Kivshar. **Nonlinear properties of left-handed metamaterials**. *Physical review letters*, **91**(3):37401, 2003. 111

[114] P.V. Kapitanova, S.I. Maslovski, I.V. Shadrivov, P.M. Voroshilov, D.S. Filonov, P.A. Belov, and Y.S. Kivshar. **Controlling split-ring resonators with light**. *Applied Physics Letters*, **99**(25):251914–251914, 2011. 111

[115] AQ Liu, WM Zhu, DP Tsai, and NI Zheludev. **Micromachined tunable metamaterials: a review**. *Journal of Optics*, **14**(11):114009, 2012. 111

[116] I.V. Shadrivov, A.B. Kozyrev, D.W. van der Weide, and Y.S. Kivshar. **Nonlinear magnetic metamaterials**. *Optics Express*, **16**(25):20266–20271, 2008. 111

[117] I. Gil, J. Bonache, J. Garcia-Garcia, and F. Martin. **Tunable metamaterial transmission lines based on varactor-loaded split-ring resonators**. *Microwave Theory and Techniques, IEEE Transactions on*, **54**(6):2665–2674, 2006. 111

[118] I.V. Shadrivov, A.B. Kozyrev, D.W. Van Der Weide, and Y.S. Kivshar. **Tunable transmission and harmonic generation in nonlinear metamaterials**. *Applied Physics Letters*, **93**(16):161903–161903, 2008. 111

[119] M. Lapine, I.V. Shadrivov, D.A. Powell, and Y.S. Kivshar. **Magnetoelastic metamaterials**. *Nature Materials*, 2011. 111

[120] J.Y. Ou, E. Plum, L. Jiang, and N.I. Zheludev. **Reconfigurable photonic metamaterials**. *Nano letters*, **11**(5):2142, 2011. 111

[121] H. Tao, AC Strikwerda, K. Fan, WJ Padilla, X. Zhang, and RD Averitt. **Reconfigurable terahertz metamaterials**. *Physical review letters*, **103**(14):147401, 2009. 111

[122] D.A. Powell, K. Hannam, I.V. Shadrivov, and Y.S. Kivshar. **Near-field interaction of twisted split-ring resonators**. *Physical Review B*, **83**(23):235420, 2011. 111

[123] H. Liu, YM Liu, T. Li, SM Wang, SN Zhu, and X. Zhang. **Coupled magnetic plasmons in metamaterials**. *physica status solidi (b)*, **246**(7):1397–1406, 2009. 111

[124] F. Hesmer, E. Tatartschuk, O. Zhuromskyy, A.A. Radkovskaya, M. Shamonin, T. Hao, C.J. Stevens, G. Faulkner, D.J. Edwards, and E. Shamonina. **Coupling mechanisms for split ring resonators: Theory and experiment**. *physica status solidi (b)*, **244**(4):1170–1175, 2007. 111

[125] AQ Liu and XM Zhang. **A review of MEMS external-cavity tunable lasers**. *Journal of Micromechanics and Microengineering*, **17**(1):R1, 2006. 112

[126] Y. Liu, X. Hu, D. Zhang, B. Cheng, D. Zhang, and Q. Meng. **Subpicosecond optical switching in polystyrene opal**. *Applied Physics Letters*, **86**(15):151102–151102, 2005. 112

[127] F. Bayatpur and K. Sarabandi. **Tuning performance of metamaterial-based frequency selective surfaces**. *Antennas and Propagation, IEEE Transactions on*, **57**(2):590–592, 2009. 112

[128] Christos Mias. **Varactor-tunable frequency selective surface with resistive-lumped-element biasing grids**. *Microwave and Wireless Components Letters, IEEE*, **15**(9):570–572, 2005. 112

[129] http://www.skyworksinc.com/uploads/documents/Design_With_PIN_Diodes_200312D.pdf, 2003. 115, 117

[130] http://http://en.wikipedia.org/wiki/Diode. xix, 116

[131] http://www.microwaves101.com/encyclopedia/diodes_PIN.cfm. xix, 116, 117

[132] http://en.wikipedia.org/wiki/PIN_diode#Characteristics. 117

[133] http://www.cst.com, 2012. 118

[134] B. Zhu, Y. Feng, J. Zhao, C. Huang, and T. Jiang. **Switchable metamaterial reflector/absorber for different polarized electromagnetic waves**. *arXiv preprint arXiv:1010.4377*, 2010. 119, 122

[135] B. Zhu, Y. Feng, J. Zhao, C. Huang, Z. Wang, and T. Jiang. **Polarization modulation by tunable electromagnetic metamaterial reflector/absorber**. *Optics Express*, **18**(22):23196–23203, 2010. 119, 122

[136] S. Hrabar, I. Krois, I. Bonic, and A. Kiricenko. **Basic concepts of active dispersionless metamaterial based on non-foster elements**. In *ICECom, 2010 Conference Proceedings*, pages 1–4. IEEE, 2010. 123, 207

[137] http://en.wikipedia.org/wiki/22_nanometer. 123

[138] V.M. Shalaev, W. Cai, U.K. Chettiar, H.K. Yuan, A.K. Sarychev, V.P.

Drachev, and A.V. Kildishev. **Negative index of refraction in optical metamaterials**. *Optics Letters*, **30**(24):3356–3358, 2005. 124

[139] W. Wu, E. Kim, E. Ponizovskaya, Y. Liu, Z. Yu, N. Fang, Y.R. Shen, A.M. Bratkovsky, W. Tong, C. Sun, et al. **Optical metamaterials at near and mid-IR range fabricated by nanoimprint lithography**. *Applied Physics A: Materials Science & Processing*, **87**(2):143–150, 2007. 124

[140] N. Dutta, S. Shi, and D. Prather. **Large Area Near-IR Optical Fishnet-Metamaterials**. In *CLEO: Science and Innovations*. Optical Society of America, 2011. 124, 125

[141] http://en.wikipedia.org/wiki/Nanoimprint_lithography. 125

[142] http://en.wikipedia.org/wiki/Drude_model. 130

[143] MA Ordal, LL Long, RJ Bell, SE Bell, RR Bell, RW Alexander, CA Ward, et al. **Optical properties of the metals al, co, cu, au, fe, pb, ni, pd, pt, ag, ti, and w in the infrared and far infrared**. *Applied Optics*, **22**(7):1099–1119, 1983. xix, xx, 130, 131, 132, 133

[144] MGM Van Der Vis, EHP Cordfunke, and RJM Konings. **The thermodynamic properties of tetraethoxysilane (TEOS) and an infrared study of its thermal decomposition**. *Le Journal de Physique IV*, **3**(C3):C3–75, 1993. xx, 134

[145] Philip E Garrou, Robert H Heistand, Mitchell G Dibbs, TA Manial, CE Mohler, TM Stokich, PH Townsend, GM Adema, MJ Berry, and I Turlik. **Rapid thermal curing of BCB dielectric**. *Components, Hybrids, and Manufacturing Technology, IEEE Transactions on*, **16**(1):46–52, 1993. xx, 134, 135

[146] S Atalay, HI Adiguzel, and F Atalay. **Infrared absorption study of Fe¡ sub¿ 2¡/sub¿ O¡ sub¿ 3¡/sub¿–CaO–SiO¡ sub¿ 2¡/sub¿ glass ceramics**. *Materials Science and Engineering: A*, **304**:796–799, 2001. xx, 134, 136

[147] He-Xiu Xu, Guang-Ming Wang, and Qing Peng. **Fractal-shaped complementary electric-LC resonator for bandstop filter**. *Progress In Electromagnetics Research C*, **23**:205–217, 2011. 137

[148] Ruopeng Liu, Aloyse Degiron, Jack J Mock, and David R Smith. **Negative index material composed of electric and magnetic resonators**. *Applied Physics Letters*, **90**(26):263504–263504, 2007. 137

[149] Haim Cory and C Zach. **Wave propagation in metamaterial multi-layered structures**. *Microwave and Optical Technology Letters*, **40**(6):460–465, 2004. 146

[150] Ismo V Lindell. *Electromagnetic waves in chiral and Bi-isotropic media*. Artech House on Demand, 1994. 150

[151] E Plum, J Zhou, J Dong, VA Fedotov, Th Koschny, CM Soukoulis, and NI Zheludev. **Metamaterial with negative index due to chirality**. *Physical Review B*, **79**(3):035407, 2009. 150, 153, 154

[152] Bingnan Wang, Jiangfeng Zhou, Thomas Koschny, Maria Kafesaki, and Costas M Soukoulis. **Chiral metamaterials: simulations and experiments**. *Journal of Optics A: Pure and Applied Optics*, **11**(11):114003, 2009. 150, 151

[153] Sergei Tretyakov, Igor Nefedov, Ari Sihvola, Stanislav Maslovski, and Constantin Simovski. **Waves and energy in chiral nihility**. *Journal of electromagnetic waves and applications*, **17**(5):695–706, 2003. 150

[154] IV Semchenko, SA Khakhomov, and SA Tretyakov. **Chiral metamaterial with unit negative refraction index**. *The European Physical Journal Applied Physics*, **46**(03), 2009. 150

[155] Ricardo Marqués, Lukas Jelinek, and Francisco Mesa. **Negative refraction from balanced quasi-planar chiral inclusions**. *Microwave and Optical technology Letters*, **49**(10):2606–2609, 2007. 150

[156] Y Zhao, MA Belkin, and A Alù. **Twisted optical metamaterials for planarized ultrathin broadband circular polarizers**. *Nature Communications*, **3**:870, 2012. xxi, 151, 152, 153

[157] Lei Zhang, Thomas Koschny, and Costas M Soukoulis. **Creating double negative index materials using the Babinet principle with one metasurface**. *Physical Review B*, **87**(4):045101, 2013. 154

[158] Jiangfeng Zhou, Lei Zhang, Gary Tuttle, Thomas Koschny, and Costas M Soukoulis. **Negative index materials using simple short wire pairs**. *Physical Review B*, **73**(4):041101, 2006. xxi, 155, 156

[159] G Dolling, C Enkrich, M Wegener, JF Zhou, Costas M Soukoulis, and S Linden. **Cut-wire pairs and plate pairs as magnetic atoms for optical metamaterials**. *Optics letters*, **30**(23):3198–3200, 2005. 155

[160] Costas M Soukoulis and Martin Wegener. **Past achievements and future challenges in the development of three-dimensional photonic metamaterials**. *Nature Photonics*, **5**(9):523–530, 2011. 160

[161] Bingnan Wang, Jiangfeng Zhou, Thomas Koschny, and Costas M Soukoulis. **Nonplanar chiral metamaterials with negative index**. *Applied Physics Letters*, **94**(15):151112–151112, 2009. xxii, 160, 161

[162] A. Rogalski. **Progress in focal plane array technologies**. *Progress in Quantum Electronics*, 2012. 164, 165

[163] N. Oda, H. Yoneyama, T. Sasaki, M. Sano, S. Kurashina, I. Hosako, N. Sekine, T. Sudoh, and T. Irie. **Detection of terahertz radiation from quantum cascade laser using vanadium oxide microbolometer focal plane arrays**. In *Proc. SPIE*, **6940**, page 69402Y, 2008. 165

[164] AJ Syllaios, TR Schimert, RW Gooch, WL McCardel, BA Ritchey, and JH Tregilgas. **Amorphous silicon microbolometer technology**. In *Materials Research Society Symposium Proceedings*, **609**, pages 14–14. Cambridge Univ Press, 2001. 165

[165] D.S. Tezcan, S. Eminoglu, and T. Akin. **A low-cost uncooled infrared microbolometer detector in standard CMOS technology**. *Electron Devices, IEEE Transactions on*, **50**(2):494–502, 2003. 165

[166] T. Morf, J. Weiss, L. Kull, H. Rothuizen, T. Toifl, M. Kossel, C. Menolfi, G. von Bueren, T. Brunschwiler, and M. Schmatz. **Antenna coupled far-infrared/THz detector in CMOS**. *Electronics letters*, **45**(25):1321–1323, 2009. xxii, 165, 166, 167, 168, 172

[167] Reid R Harrison and Cameron Charles. **A low-power low-noise CMOS amplifier for neural recording applications**. *Solid-State Circuits, IEEE Journal of*, **38**(6):958–965, 2003. xxii, 174, 175, 177

[168] B. Razavi. **Design of analog CMOS integrated circuits**. 2001. 174, 178, 179

[169] Jian Guo. *Design and Implementation of a CMOS Digital Phase Imager for Time-Resolved Luminescence Imaging Applications*. ProQuest Dissertations and Theses (PQDT), 2012. xxii, 181

[170] http://en.wikipedia.org/wiki/Black-body_radiation, 2012. 182

[171] http://commons.wikimedia.org/wiki/File:BlackbodySpectrum_loglog_150dpi_en.png. xxiii, 182, 184

[172] http://www.infraredsystems.com/Products/blackbody518.html, 2012. 185

[173] http://www.infraredsystems.com/Products/ir301.html, 2012. 185

[174] http://www.spectralcalc.com/blackbody_calculator/blackbody.php. xxiii, 185

[175] http://www.daylightsolutions.com/, 2013. 192, 193

[176] http://en.wikipedia.org/wiki/Lock-in_amplifier, 2013. xxiii, 197, 198

[177] David Shelton. *Tunable Infrared Metamaterials*. PhD thesis, University of Central Florida Orlando, Florida, 2010. 199

[178] R. Loudon. *The quantum theory of light*. Oxford University Press, USA, 2000. 200

[179] L. Mandel and E. Wolf. *Optical coherence and quantum optics*. Cambridge university press, 1995. 200

[180] S.K. Lin. **Modern Thermodynamics: From Heat Engines to Dissipative Structures.** *Entropy*, **1**(4):148–149, 1999. 200

[181] P.T. Landsberg. *Thermodynamics and statistical mechanics*. Dover Publications, 1991. 200

[182] Wei Zhao and Yu Cao. **New generation of predictive technology model for sub-45 nm early design exploration**. *Electron Devices, IEEE Transactions on*, **53**(11):2816–2823, 2006. 201